The effect of inertia on the equilibration of non-linear $\alpha\omega$ and $\alpha^2\omega$ dynamo models.

by

Shona Margaret Maclean

A thesis submitted to the

Faculty of Information and Mathematical Sciences

at the University of Glasgow

for the degree of

Doctor of Philosophy

June 2005

The layout of this thesis is as follows. In Chapter 1, we introduce the background theory of the geodynamo and the relevant established results. In Chapter 2, we introduce our physical model. In Chapter 3 we consider the $\alpha\omega$-type dynamo model, which then provides us with a reference case for Chapter 4, where we consider the effect of inertia on this model. In Chapter 5 we consider the $\alpha^2\omega$-type dynamo model and then extend this in Chapter 6 to include the effect of inertia. Chapter 7 summarises the main results of each of these chapters and ties all the material together. For completeness, in Appendix A we include proofs of well established results, and finally in Appendix B we include a description of the codes used.

To my Parents;

without whose love, support and encouragement,

I would never have gotten this far.

"Can't resist the strange attraction,

From that giant dynamo,

Lots to take and lots to give,

Time to breathe and time to live."

B. Andersson/B. Ulvaeus

Statement.

This thesis is submitted in accordance with the regulations for the degree of Doctor of Philosophy in the University of Glasgow. It is the record of research carried out at the University of Glasgow between October 2001 and May 2005. No part of it has been submitted by me for a degree at any other university. The results contained in this thesis are claimed as original except where indicated in the text.

Acknowledgement

I would like to begin by thanking my supervisor Prof. David R. Fearn, for the opportunity to continue my studies at the University of Glasgow. It has been a great privilege to have been able to work under his supervision. I'd also like to thank Dr. Rainer Hollerbach, for use of his numerical code and the helpful discussions we've had over my time as a postgraduate student. Many thanks also go to my friend and colleague Dr. Md. Mansur Rahman, for all his help on getting me started with the numerical codes and introducing me to the graphics package. Finally, I'd like to thank the E.P.S.R.C. for funding me through the past 3 years.

On a personal note, I'd like to thank Mum, Dad, Alison and Catherine, for their love, support and encouragement over the past 3 and a half years. To Neil, thanks for your love, support and patience over the last few months, especially in keeping me company on many weekends spent in the department writing up. In the course of working for my PhD, I have made some wonderful friends, and many thanks go to them for making my life as a PhD student as enjoyable as it has been.

Contents

List of Figures

List of Tables

Chapter 1

Introduction

1.1 Background.

1.1.1 The history of the Earth's magnetic field.

The Earth's magnetic field has been a source of considerable interest over the past two millennia. One of the first major achievements in understanding the source of the magnetic field, came from the ancient Chinese, who were responsible for inventing the magnetic compass and discovered declination – the angle between magnetic and geographic North. The angle of inclination – a measure of the dip of the magnetic field – was discovered in the 16th century. The inclination and declination as well as the strength of the field characterise the measurable aspects of the magnetic field. These features are known to vary slowly with time – a fact first discovered by Henry Gellibrand in 1634, in his observations of the magnetic declination. This was the first observed feature of the so-called Geomagnetic Secular Variation (GSV), which is the slow change in the observed magnetic field with time. Since the first detailed observations, measurements of the declination and inclination of the Earth's field have been recorded, providing us with a detailed record of the Earth's field over the past few hundred years.

In addition to the direct measurements of the Earth's magnetic field which have been kept since the 16th century, the behaviour of the Earth's field has been found indirectly through paleomagnetic measurements which give a record of the Earth's field going back some 3 billion years, (see for example, Merrill *et al* 1996). Short timescale behaviour ($t \sim 0.1\text{year} - 1k\text{year}$), is obtained

from the study of volcanic rocks, which contain small amounts of magnetic particles (typically iron oxide), released during eruptions. These magnetic particles naturally align themselves with the local magnetic field, so that when the lava from the volcano solidified, these small magnetic particles were trapped in the rock, thus preserving the strength and direction of the magnetic field at that moment in time. Longer timescale behaviour is found from studies of sedimentary rocks, which contain traces of iron oxides, which became embedded during their formation.

From these records of the field, it is well established that the Earth's magnetic field has remained at approximately its present strength for the past 3×10^9 years. However we note that recent work by Macouin *et al* (2004) does show evidence that there has been a small increase in the observed magnetic field strength over the past 1 billion years, possibly associated with the formation of the inner core. The ohmic decay time of the core is estimated to be

$$\tau_\eta = \frac{\mathcal{L}^2}{\eta} \approx 3 \times 10^5 \text{ years.}$$

where $\mathcal{L}$ is a typical lengthscale (e.g. the radius of the core, $\mathcal{L} = 3.485 \times 10^6$m) and η is the magnetic diffusivity. A derivation of the magnetic diffusion time τ_η is given in Chapter 2. Clearly, since the field strength has been approximately constant for a time many orders of magnitude longer than the time over which the field would be expected to decay, there must be some mechanism maintaining the Earth's magnetic field. Another aspect of the Earth's magnetic field which is apparent from the GSV record, is the ability of the dominantly dipolar field to change direction in an unpredictable fashion. This is further evidence that the Earth's magnetic field can not be a fossil field present from its birth. The Earth's field also can not be a permanent magnet as below a depth of the order of a hundred kilometers the temperature inside the Earth exceeds the Curie temperature; the temperature at which permanent magnetism disappears. Therefore the only feasible mechanism by which the Earth's field may be maintained is the dynamo. The dynamo as a mechanism for generating and maintaining the Earth's magnetic field was first suggested in 1919 by Sir Joseph Larmor. The dynamo mechanism works on the principle that the motion of the conducting fluid induces from the prevailing magnetic field an electromotive force, creating currents which generate the inducing magnetic field. At first sight this concept, seems very much like a perpetual motion machine, but in fact there is really no conflict as energy is conserved. The energy lost through ohmic diffusion, is compensated for by the rate at which fluid motions generate electromagnetic

energy.

1.1.2 The Interior of the Earth.

To understand how such a dynamo might operate within the Earth to enable the maintenance and reversal of the field, we need to examine the interior structure of the Earth. The interior of the Earth is composed of 3 main layers; in the centre there is the spherical core of radius 3485km, this is surrounded by a thick layer of rock called the mantle of radius 6370km, and then this is finally encased in a thin layer of rock called the crust. The mantle is a good electrical insulator, (except perhaps close to the core-mantle boundary), and so the only possible source of electromagnetic induction lies in the core. In the core, we have two distinct regions; the inner core and the outer core. The inner core is a sphere of radius 1215km and is composed almost entirely of solid iron at temperatures of $\gtrsim$ 5000K. The outer core forms a fluid shell between the inner core and the mantle and is composed primarily of iron. In addition to the iron in the fluid outer core there is evidence of compounds of iron with some lighter elements, possibly oxygen, silicon or sulphur. See for example, Jacobs (1993) or Poirer (1994), for further details. The core is the focus of the dynamo mechanism in the Earth as the fluid motions in the outer core interact with the magnetic field to regenerate and maintain the Earth's field.

1.2 The Induction equation.

The magnetic induction equation, which is derived from Maxwell's equations governing electromagnetic theory, and can be found in any introductory text on dynamo theory (see for example, Roberts 1994), is

$$\frac{\partial \widetilde{\mathbf{B}}}{\partial \widetilde{t}} = \widetilde{\nabla} \times (\widetilde{\mathbf{U}} \times \widetilde{\mathbf{B}}) + \eta \widetilde{\nabla}^2 \widetilde{\mathbf{B}}, \tag{1.1}$$

where $\widetilde{\mathbf{B}}$ is the magnetic field, $\widetilde{\mathbf{U}}$ is the fluid velocity and η is the magnetic diffusivity. From Maxwell's equations we have

$$\widetilde{\nabla} \cdot \widetilde{\mathbf{B}} = 0 \tag{1.2}$$

which, whilst not independent of (1.1), (as this is used in the derivation of the induction equation) can prove a useful condition on the field.

The induction equation may be non-dimensionalised using the ohmic diffusion timescale $\tau_\eta = \mathcal{L}^2/\eta$ as the timescale, $\mathcal{L}$ as the typical lengthscale, and $\mathcal{U}$ as the typical velocity. Full details of the non-dimensionalisation is given in Chapter 2. The non-dimensionalised induction equation may be written as,

$$\frac{\partial \mathbf{B}}{\partial t} = R\nabla \times (\mathbf{U} \times \mathbf{B}) + \nabla^2 \mathbf{B} \tag{1.3}$$

where the dimensionless parameter R is called the magnetic Reynolds number and is defined as the ratio of the advection term to the magnetic diffusion term. Thus

$$R = \frac{\mathcal{U}\mathcal{L}}{\eta} \tag{1.4}$$

where $\mathbf{B}, \mathbf{U}$ are now dimensionless quantities.

1.2.1 Alfven's frozen flux theorem.

If we consider the idealised case in which we have a perfect conductor, then $\eta = 0$, and the induction equation in (1.1) reduces to

$$\frac{\partial \mathbf{B}}{\partial \widetilde{t}} = \widetilde{\nabla} \times (\widetilde{\mathbf{U}} \times \widetilde{\mathbf{B}}) \tag{1.5}$$

from which it can be shown that the magnetic field lines are material curves. A proof may be found in almost any MHD textbook; see for example Roberts (1967). This means that the magnetic field lines move and evolve with the fluid and so a helpful visualisation is to consider the magnetic field lines as being frozen into the fluid.

The magnetic Reynolds number, R, defined in (1.4), gives a measure of the extent to which this idealisation holds, so that the perfectly conducting limit, $\eta \to 0$, is characterised by $R \to \infty$.

1.2.2 Dynamo conditions.

In addition to satisfying equations (1.1) and (1.2), there are an additional two conditions that a dynamo must satisfy which solutions to (1.1) and (1.2) need not obey.

First Dynamo Condition.

All fields and currents must be created by fluid motion; none must be supplied by other sources external or internal (for example, thermoelectric and thermochemical sources, i.e., batteries, must be excluded).

Second Dynamo Condition.

The field and currents must persist indefinitely (or for a time long compared with τ_η, where it is assumed that the energy sources powering the motions are maintained during that time).

1.2.3 Cowling's theorem.

An alternative approach to finding solutions which satisfy the dynamo conditions (Section 1.2.2), is the approach taken to find *anti-dynamo* theorems, which allow us to rule out whole classes of solutions. Cowling's theorem (given below) was one of the earliest and most significant anti-dynamo theorems.

Cowling's theorem (1934) states that; "An axisymmetric magnetic field can not be maintained by fluid motions". This means that the dynamo process is inevitably three dimensional. As a result, the dynamo process is a complex and numerically intensive problem. We present a sketch proof of this theorem in Appendix A.

1.3 The Momentum equation.

In the outer core, our induction equation (1.1) is coupled to the momentum equation,

$$\rho\left(\frac{\partial\tilde{\mathbf{U}}}{\partial\tilde{t}}+(\tilde{\mathbf{U}}\cdot\tilde{\nabla})\tilde{\mathbf{U}}\right)+2\rho\tilde{\mathbf{\Omega}}\times\tilde{\mathbf{U}}+\rho\tilde{\mathbf{\Omega}}\times(\tilde{\mathbf{\Omega}}\times\tilde{\mathbf{r}})=-\tilde{\nabla}\tilde{p}^{*}+\rho\nu\tilde{\nabla}^{2}\tilde{\mathbf{U}}+\frac{1}{\mu_o}(\tilde{\nabla}\times\tilde{\mathbf{B}})\times\tilde{\mathbf{B}}+\rho\tilde{\mathbf{g}} \quad (1.6)$$

in a reference frame rotating with angular velocity $\tilde{\mathbf{\Omega}}$, where $\rho\left(\frac{\partial\tilde{\mathbf{U}}}{\partial\tilde{t}}+(\tilde{\mathbf{U}}\cdot\tilde{\nabla})\tilde{\mathbf{U}}\right)$ is the fluid inertia, $2\rho\tilde{\mathbf{\Omega}}\times\tilde{\mathbf{U}}$ is the Coriolis force, $\rho\tilde{\mathbf{\Omega}}\times(\tilde{\mathbf{\Omega}}\times\tilde{\mathbf{r}})$ is the centrifugal force, $\tilde{\nabla}\tilde{p}^{*}$ is the pressure gradient, $\rho\nu\tilde{\nabla}^{2}\tilde{\mathbf{U}}$ is the viscous force, $\frac{1}{\mu_o}(\tilde{\nabla}\times\tilde{\mathbf{B}})\times\tilde{\mathbf{B}}$ is the Lorentz force and finally $\rho\tilde{\mathbf{g}}$ is the buoyancy force.

Through standard vector relations we may rewrite the centrifugal force $\rho\tilde{\mathbf{\Omega}} \times (\tilde{\mathbf{\Omega}} \times \tilde{\mathbf{r}})$ as $-\tilde{\nabla}(\frac{\rho}{2}(\tilde{\mathbf{\Omega}} \times \tilde{\mathbf{r}})^2)$, which may be absorbed into the pressure gradient term, provided ρ is constant, to give a modified pressure $\tilde{p} = \tilde{p}^* + \frac{\rho}{2}(\tilde{\mathbf{\Omega}} \times \tilde{\mathbf{r}})^2$. Alternatively, the centrifugal force may be included in the buoyancy force to give a modified gravity term. We then have

$$\rho\left(\frac{\partial\tilde{\mathbf{U}}}{\partial\tilde{t}} + (\tilde{\mathbf{U}}\cdot\tilde{\nabla})\tilde{\mathbf{U}}\right) + 2\rho\tilde{\mathbf{\Omega}} \times \tilde{\mathbf{U}} = -\nabla\tilde{p} + \rho\nu\tilde{\nabla}^2\tilde{\mathbf{U}} + \frac{1}{\mu_o}(\tilde{\nabla} \times \tilde{\mathbf{B}}) \times \tilde{\mathbf{B}} + \rho\tilde{\mathbf{g}} \tag{1.7}$$

The buoyancy force $\rho\tilde{\mathbf{g}}$ appearing in the momentum equation, (1.7) drives thermal convection (which we will discuss further in Section 1.4.1) in the fluid outer core and is typically modelled by

$$\frac{\partial\tilde{T}}{\partial\tilde{t}} + (\tilde{\mathbf{U}}\cdot\tilde{\nabla})\tilde{T} = \kappa\tilde{\nabla}^2\tilde{T} + h' \tag{1.8}$$

where $\tilde{T}$ is the temperature, κ is the thermal diffusivity and h' represents local sources of heating. Assuming a linear temperature gradient of typical magnitude β, we may write the temperature $\tilde{T}$ as

$$\tilde{T} = \beta\mathcal{L}(T_o + T), \tag{1.9}$$

where T_o is a reference temperature and T is a measure of the deviation from the adiabatic temperature. In the Earth's core, the effects of compressibility are not believed to be of primary importance in the dynamics of the core, and therefore we adopt the Boussinesq approximation. The Boussinesq approximation assumes that the density in the fluid core, can be treated as constant ($\rho = \rho_o$) in all terms of the momentum equation except in the buoyancy force, where the linear relation between density and temperature is used:

$$\rho = \rho_o[1 - \alpha(\tilde{T} - \beta\mathcal{L}T_o)], \tag{1.10}$$

where α is the coefficient of thermal expansion. Assuming the electrically conducting fluid in the outer core to be incompressible, we have the condition

$$\tilde{\nabla}\cdot\tilde{\mathbf{U}} = 0 \tag{1.11}$$

and therefore the momentum equation is

$$\rho_o\left(\frac{\partial\tilde{\mathbf{U}}}{\partial\tilde{t}} + (\tilde{\mathbf{U}}\cdot\tilde{\nabla})\tilde{\mathbf{U}}\right) + 2\rho_o\Omega\mathbf{k} \times \tilde{\mathbf{U}} = -\tilde{\nabla}\tilde{p} + \rho_o\nu\tilde{\nabla}^2\tilde{\mathbf{U}} + \frac{1}{\mu_o}(\tilde{\nabla} \times \tilde{\mathbf{B}}) \times \tilde{\mathbf{B}} - \rho g_o\tilde{\mathbf{r}} \tag{1.12}$$

where we have written $\widetilde{\mathbf{g}} = -g_o\widetilde{\mathbf{r}}$ and $\widetilde{\mathbf{\Omega}} = \Omega\mathbf{k}$, where $\mathbf{k}$ is the unit vector in the direction of the rotation axis. Now for some of the subsequent analysis we present in this chapter, it is helpful to have the momentum equation in a non-dimensionalised form. As we present full details of the non-dimensionalisation we have used which is specific to our model in Chapter 2, we simply state the non-dimensionalised equations here and give the appropriate scalings.

We have non-dimensionalised on the ohmic diffusion timescale, $\tau_\eta = \mathcal{L}^2/\eta$ and a lengthscale, $\mathcal{L}$. We scale the magnetic field with $(\Omega\mu_o\rho_o\eta)^{1/2}$ and velocity with $\mathcal{U} = \frac{\mathcal{L}}{\tau_\eta}$. Therefore the non-dimensionalised equation (1.12) is

$$Ro\left(\frac{\partial \mathbf{U}}{\partial t} + (\mathbf{U}\cdot\nabla)\mathbf{U}\right) + 2\mathbf{k}\times\mathbf{U} = -\nabla p + E\nabla^2\mathbf{U} + (\nabla\times\mathbf{B})\times\mathbf{B} + qRaT\mathbf{r} \tag{1.13}$$

where $\mathbf{r}$ is the non-dimensional radial vector. The non-dimensionalised equation (1.8) is

$$\frac{\partial T}{\partial t} + (\mathbf{U}\cdot\nabla)T = q\nabla^2 T + h \tag{1.14}$$

where h is now the non-dimensionalised heat source. The dimensionless parameters are the Rossby number (sometimes called the magnetic Ekman number) Ro, the Ekman number E, the (modified) Rayleigh number Ra and the Roberts number q.

$$Ro = \frac{\eta}{\Omega\mathcal{L}^2}, \quad E = \frac{\nu}{\Omega\mathcal{L}^2}, \quad Ra = \frac{g_o\alpha\beta\mathcal{L}^2}{\Omega\kappa}, \quad q = \frac{\kappa}{\eta} \tag{1.15}$$

1.4 Energy sources driving fluid flow.

As we discussed in Section 1.1.1, the Earth's magnetic field would be expected to decay on the ohmic diffusion timescale of $\sim 3\times10^5$years. However, the Earth's magnetic field has been observed at approximately its present strength for the past 3×10^9years and so the loss in energy through magnetic diffusion is being compensated for by the advection term $\widetilde{\nabla}\times(\widetilde{\mathbf{U}}\times\widetilde{\mathbf{B}})$ in (1.1). However, there must be some energy source which is providing the kinetic energy to drive the fluid motions $\widetilde{\mathbf{U}}$.

We can obtain an estimate of the typical power requirement of such an energy source by considering the induction equation (1.1) and setting $\widetilde{\mathbf{U}} = 0$. Taking the scalar product with $\widetilde{\mathbf{B}}/\mu_o$ and integrating over all space V we find

$$P = \frac{d}{dt}\int_V \frac{B^2}{2\mu_o}dV = -\int_V \frac{J^2}{\sigma}dV \tag{1.16}$$

where we have used the divergence theorem and the standard vector identities;

$$\begin{aligned}
\nabla \times (\mathbf{e} \times \mathbf{f}) &= \mathbf{f} \cdot (\nabla \times \mathbf{e}) - \mathbf{e} \cdot (\nabla \times \mathbf{f}) \\
\nabla \times (\nabla \times \mathbf{e}) &= \nabla(\nabla \cdot \mathbf{e}) - \nabla^2 \mathbf{e} \\
\nabla(\mathbf{e} \cdot \mathbf{f}) &= (\mathbf{e} \cdot \nabla)\mathbf{f} + (\mathbf{f} \cdot \nabla)\mathbf{e} + \mathbf{e} \times (\nabla \times \mathbf{f}) + \mathbf{f} \times (\nabla \times \mathbf{e})
\end{aligned}$$

to obtain this expression. For an insulating mantle, the current J vanishes outside the core. The left hand side of (1.16) is the rate of change of magnetic energy. Since $\mu_o \tilde{\mathbf{J}} = \tilde{\nabla} \times \tilde{\mathbf{B}}$, the ohmic power dissipation can be estimated from the right hand side of (1.16) as

$$P \approx \frac{4}{3} \pi r_o^3 \frac{\mathcal{B}^2}{\sigma \mu_o^2 \mathcal{L}^2} \tag{1.17}$$

where $\mathcal{B}$ is a typical field strength and $\mathcal{L}$ is an appropriate lengthscale. Choosing a lengthscale of the order of the radius of the Earth's core, say $\mathcal{L} = 10^6$m, then we may estimate that the power dissipation would be $\sim 1.8 \times 10^{14} \mathcal{B}^2$W. So, for a typical magnetic field strength of say 10mT, the power dissipation would be of the order 2×10^{10}W. Obviously this estimate depends on our rather arbitrary choice of lengthscale $\mathcal{L}$; a shorter lengthscale producing more power dissipation and a longer lengthscale less dissipation. Loper and Roberts (1983) reviewed the various estimates and found values of $P/\mathcal{B}^2$ ranging from 0.7×10^{14} to 200×10^{14}WT^{-2}, favouring a value somewhere in-between. Therefore for a field strength of 10mT, a ballpark figure for the power requirement of the dynamo simply to overcome the effects of dissipation is approximately 10^{11}W.

Another important consideration in determining a suitable energy source for the dynamo, is the efficiency with which this energy may be converted into useful fluid motions. The energy lost through ohmic dissipation is compensated for by the kinetic energy of flow $\tilde{\mathbf{U}}$ through the term $\tilde{\nabla} \times (\tilde{\mathbf{U}} \times \tilde{\mathbf{B}})$ in equation (1.1). The possible sources responsible for driving the flow are mainly: thermal convection, compositional convection and precessional driving, with effects such as radiogenic heating and the release of latent heat and light constituents contributing to convection. Precessional driving of core flows is generated by the gravitational torques exerted on the Earth by the Sun and the Moon. Thermal convection and composition convection are described in more detail in Sections 1.4.1 and 1.4.2.

In Section 1.3, we introduced a buoyancy force to the momentum equation of the form $\rho\tilde{\mathbf{g}}$, where $\tilde{\mathbf{g}}$ is the gravitational acceleration. This buoyancy force is responsible for driving the fluid motions in the outer core. The exact nature of the convection in the Earth's core is not precisely known, but is believed to be a combination of thermal convection and compositional convection. Typically in dynamo models, the buoyancy force drives thermal convection, since this process is better understood and easier to model mathematically. However on efficiency grounds compositional convection is favoured as a driving force for the fluid flow. Modelling compositional convection is difficult, despite the considerable amount of progress that has been made in understanding this complex process.

1.4.1 Thermal convection.

Thermal convection, arises through the temperature gradient in the core, and is typically modelled through an equation like (1.14). In Section 1.3 we stated that h appearing in (1.14) represented local sources of heating. We will now describe the possible heat sources that exist within the Earth which could contribute to this term. The source of the heating within the core may be distributed evenly throughout the core, or else concentrated at the inner core boundary (ICB). From a modelling perspective, the idea of a heat source which is distributed evenly throughout the core proved popular especially in purely spherical models which do not include an inner core (see for example, Roberts 1968). In such models, the source may be generated by radiogenic heating and through the release of specific heat as the core cools. For heating which is focussed at the ICB, the main contribution to the generation of thermal convection comes from the latent heat released on the crystallisation of the inner core as the core cools.

1.4.2 Compositional convection.

The fluid which makes up the Earth's outer core, is composed of iron plus iron compounds of lighter elements such as silicon, sulphur and oxygen (see for example, Poirier 1994). As the Earth cools with age, the inner core is gradually growing outwards into the fluid outer core through the preferential freezing out of the iron from these iron compounds. The boundary between the solid inner core and fluid outer core is not a solid boundary as used in the dynamo models, but is in fact a freezing interface called a mushy zone. Compositional convection arises as a result of the freezing

out of the iron in the iron compounds in the fluid outer core at the inner core boundary (see for example, Loper and Roberts 1981).

The understanding of the physical processes underlying compositional convection is gleaned from experiments using metallic alloys. Through these experiments it is believed that the iron component becomes frozen into the mushy zone in the form of dendrites, whilst the remaining component is left behind in the surrounding melt. This remaining component is significantly less dense than the surrounding fluid, as it is undersaturated in iron, and so is naturally more buoyant and rises through the dendritic layer in narrow chimneys. As the fluid parcel of compositionally buoyant material rises, it may remelt any encompassed dendrites, thus producing a solid free chimney. Over most of the rest of the surface of the mushy zone there is a slow downwelling of fluid from the fluid layer above.

Whilst this is believed to be the process which is present in the Earth, the non-linear processes in the mushy zone that cause this structure are extremely complicated and questions exist over whether convection takes this form at the ICB if the effects of rotation and a magnetic field are included. Work by Bergman and Fearn (1994) suggest that these effects may in fact cause chimney formation to be inhibited.

1.5 Taylor's constraint and the Geostrophic flow.

As given in Section 1.3, we defined the dimensionless parameters Ro and E, the Rossby number and the Ekman number, which determine the relative size of the inertial and viscous terms to the dominant Coriolis force, respectively. Now, within the Earth, the angular velocity of the mantle, $\Omega = 7.29 \times 10^{-5}\mathrm{s}^{-1}$ and the lengthscale, $\mathcal{L}$ chosen for the non-dimensionalisation, are both well determined. Typically, the non-dimensionalised lengthscale, $\mathcal{L}$ is chosen as the gap width $r_o - r_i = 2.314 \times 10^6\mathrm{m}$ (Merrill *et al* 1996), which we adopt in our model presented in Chapter 2. Alternatively, the outer core radius, $r_o = 3.485 \times 10^6\mathrm{m}$ is chosen as the lengthscale $\mathcal{L}$; we will adopt this scaling in the analysis that follows. However, η and ν, the magnetic diffusivity and fluid viscosity are not so well determined. Recent estimates, give $\eta \approx 1.3\mathrm{m}^2\mathrm{s}^{-1}$ (Merrill *et al* 1996) and $\nu \approx 10^{-6}\mathrm{m}^2\mathrm{s}^{-1}$ (de Wijs *et al* 1998). These values mean that $Ro = O(10^{-9})$ and $E = O(10^{-15})$.

These estimates for Ro and E, suggest that both inertial and viscous effects are small and so may be negligible. Setting $Ro = E = 0$ in (1.13) we obtain,

$$2\mathbf{k} \times \mathbf{U} = -\nabla p + (\nabla \times \mathbf{B}) \times \mathbf{B} + qRaT\mathbf{r}. \tag{1.18}$$

This is called the magnetostrophic approximation. If we take the ϕ-component of (1.18), we have

$$2U_s = -\frac{1}{s}\frac{\partial p}{\partial \phi} + ((\nabla \times \mathbf{B}) \times \mathbf{B})_\phi, \tag{1.19}$$

and integrating it over the whole surface of the cylinder $C(s)$ (pictured in Figure 1.1) of radius s, coaxial with the rotation axis, we obtain

$$2\int_{C(s)} U_s dS = \int_{C(s)} ((\nabla \times \mathbf{B}) \times \mathbf{B})_\phi dS. \tag{1.20}$$

The cylinder $C(s)$ intersects the outer sphere ($r = r_o = 1$) at $z = z_T, z_B$ where $z_T = -z_B = \sqrt{1 - s^2} (= \cos\theta)$. The LHS of (1.20) is the net flow out of the cylindrical surface. If the viscosity is zero throughout the core, as we assumed, then the cylinder extends to the boundaries of the outer core, and so there can be no flow into or out of the ends of the cylinder. Therefore, for an incompressible fluid, the LHS of equation (1.20) must be zero, and hence

$$\int_{C(s)} ((\nabla \times \mathbf{B}) \times \mathbf{B})_\phi dS = 0 \tag{1.21}$$

This is Taylor's constraint, (Taylor 1963).

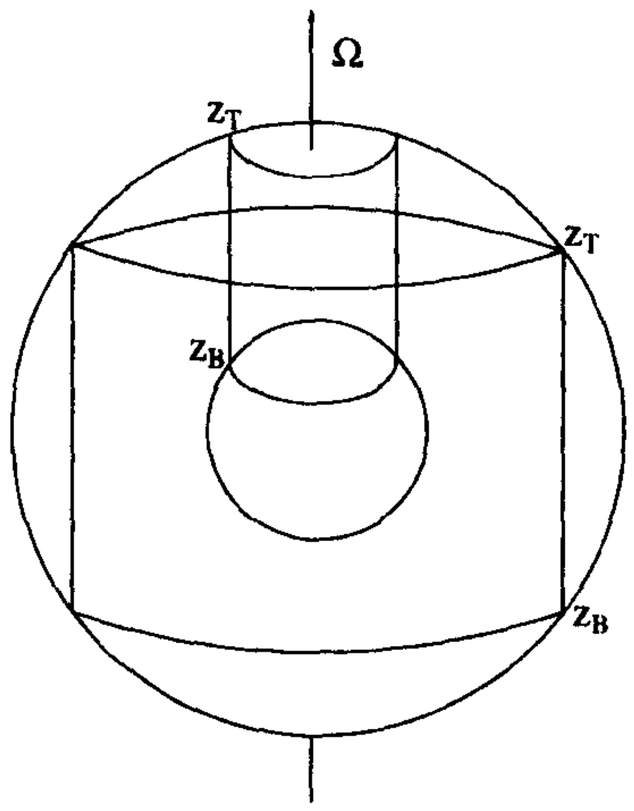

Figure 1.1: The Taylor cylinder $C(s)$, illustrated for the cases (a) where the cylinder intersects the inner core, and (b) where $s > r_{ib}$. The cylinder extends from $z = z_T = \sqrt{1 - s^2}$ to z_B, where (a) $z_B = \sqrt{r_{ib}^2 - s^2}$ and (b) $z_B = -z_T$. From Fearn (1994).

The system has the freedom to satisfy Taylor's constraint through a component of the azimuthal flow that is otherwise undetermined. Now if we begin by taking the curl of (1.18) to eliminate the pressure gradient, and applying the incompressibility condition $\nabla \cdot \mathbf{U} = 0$, we have

$$-2\frac{\partial \mathbf{U}}{\partial z} = \nabla \times ((\nabla \times \mathbf{B}) \times \mathbf{B}) + qRa(\nabla T \times \mathbf{g})$$

Taking the axisymmetric part of this equation integrating with respect to z

$$-2\overline{\mathbf{U}} = \int_z^{z_T} \langle \nabla \times ((\nabla \times \mathbf{B}) \times \mathbf{B}) \rangle \, dz' + qRa \int_z^{z_T} \langle (\nabla T \times \mathbf{g}) \rangle \, dz' + F(s)$$

where $F(s)$ is an arbitrary function of integration, and for any function $f = f(r, \theta, \phi)$,

$$\bar{f}(r, \theta) \equiv < f > \equiv \frac{1}{2\pi} \int_0^{2\pi} f \, d\phi$$

is the azimuthal averaged (or mean or axisymmetric) part of f. For a spherical geometry, the no-normal flow conditions at $z = z_T, z_B$ determine F_s and F_z. In non-axisymmetric systems, the remaining component is determined from the incompressibility condition, however in an axisymmetric system F_ϕ remains undetermined. It is this factor we term the geostrophic flow. Thus

$$\overline{U}_\phi = U_M + U_T + U_G \tag{1.22}$$

where

$$U_M = \int_z^{z_T} < \nabla \times ((\nabla \times \mathbf{B}) \times \mathbf{B}) > dz' \tag{1.23}$$

is the magnetic wind, and

$$U_T = qRa \int_z^{z_T} < (\nabla T \times \mathbf{g}) > dz' \tag{1.24}$$

is the thermal wind. Note that with our choice of integration limits, $U_M = U_T = 0$ at $z = z_T$, and so the geostrophic flow is therefore, $U_G = \overline{U}_\phi|_{z_T}$.

The geostrophic flow, U_G is therefore determined by the system, and it is through this term that the system may satisfy Taylor's constraint. The mechanism to adjust the magnetic field and so satisfy Taylor's constraint, is to adjust the differential rotation (ω-effect) of the system by varying the geostrophic flow, U_G. The differential rotation generates toroidal field from poloidal field through the stretching out of field lines. By varying U_G, B_ϕ can be adjusted, possibly enabling

(1.21) to be satisfied. This mechanism determines U_G in a very complicated implicit manner. The extent to which Taylor's constraint is satisfied depends on the importance of Ekman suction in the system. States in which Taylor's constraint is satisfied are termed Taylor states. When Taylor's constraint is not satisfied, the system is still in the viscously limited regime in which Ekman suction remains important, and these states are termed Ekman states.

Fearn and Proctor (1987) explored the problem of the determination of the geostrophic flow, by choosing U_G to minimise the absolute value of the RHS of (1.21) for a given poloidal magnetic field and a flow which is prescribed (apart from the geostrophic flow). This method, proved very successful for certain choices of fields and flows, but produced poor results for others.

1.6 Classification of dynamos.

Dynamo models generally fall into two broad categories; Kinematic models or Hydrodynamic models, with many intermediate models in a variety of geometries falling somewhere in-between. In the following sections we attempt to summarise the main characteristics of each of these types of models, and then finally describe the approach we adopt.

1.6.1 Kinematic Models.

The kinematic dynamo, involves solving the magnetic induction equation for $\mathbf{B}$ for a given flow $\mathbf{U}$. If we initially suppose that the flow is steady, then equation (1.3) admits solutions of the form

$$\mathbf{B} \propto e^{\lambda t}, \tag{1.25}$$

where the growth rate λ is an eigenvalue. Equation (1.3) therefore becomes,

$$\lambda \mathbf{B} = R\nabla \times (\mathbf{U} \times \mathbf{B}) + \nabla^2 \mathbf{B}$$

The spectrum of λ is discrete, with limit point at $-\infty$ (Roberts 1994). Greatest interest lies with the value of λ which has greatest real part, $\lambda_{\max}$ say. Adopting this eigenvalue decomposition, means that we also have eigenfunctions $\mathbf{B}_\gamma$ for each λ_γ. This decomposition allows us to write, any arbitrary field $\mathbf{B}$ in terms of the eigenfunctions $\mathbf{B}_\gamma$,

$$\mathbf{B} = \sum_\gamma \mathbf{B}_\gamma(\mathbf{x}) \exp(\lambda_\gamma t)$$

If the flow is unsteady, the problem becomes significantly more difficult to solve, as equation (1.25) no longer holds. A common approach is to assume a periodic flow variation of period P,

$$\mathbf{U}(\mathbf{x}, t+P) \equiv \mathbf{U}(\mathbf{x}, t), \qquad \forall\ \mathbf{x} \text{ and } t.$$

In this case, $\mathbf{B}$ behaves in the same way as $t \to \infty$, and the dynamo conditions simply requires that $\lambda \geq 0$, where

$$\lambda = \frac{1}{P} \ln \left[\lim_{t \to \infty} \frac{B(t+P)}{B(t)} \right]$$

where B is any component of $\mathbf{B}$ at any $\mathbf{x}$. In general $\mathbf{U}$ may be a chaotic solution of the non-linear MHD equations, which requires a generalised form of the above equation for λ.

The main advantage of the kinematic approach is that it avoids the obvious complication caused by the inclusion of the momentum equation in the system of equations, and the difficulties posed by the relative smallness of the Ekman and Rossby numbers. Another linear approach to the dynamo problem is through mean-field models, which we discuss in Section 1.6.4.

1.6.2 3D/Hydrodynamic Models.

The hydrodynamic dynamo model involves solving the full 3D coupled system of equations, i.e. equations (1.3), (1.13), (1.14) for $\mathbf{B}, \mathbf{U}, T$. However, as discussed earlier, the difficulty with this problem is caused by the comparative smallness of the fluid inertia and viscosity terms, which even at physically unrealistic parameter values for both Ro and E, is an extremely numerically expensive and intensive problem.

The first 3D calculations were performed by Zhang and Busse (1989,1990). Due to computational limitations they considered a single mode analysis, assuming solutions of the form $\exp(\phi - ct)$, and assuming stress free boundary conditions. The first 3D timestepped model was produced by Glatzmaier and Roberts (1995a,b), who found the trend that for fixed values of q, the Rayleigh number required to maintain dynamo action, Ra, increased as q is decreased. This trend was reinforced by Jones' work in 2.5D models described in the next section. An important feature of this work was that it included a field reversal. Since then, and as computing power has increased, many groups now have fully 3D timestepping dynamo models, which use a similar (spectral) numerical

approach, see for example Hollerbach (2000). This has allowed different groups to focus on different aspects important to the dynamo mechanism, such as the presence of a finitely conducting inner core, the effect of inertia, the buoyancy distribution and the boundary conditions, see Fearn (1998) or Jones (2000) for a review.

As result of the stiffness of this problem, simpler problems have also been investigated which focus on different aspects of the dynamo and help to further our physical understanding of the dynamo mechanism.

1.6.3 2.5D Models.

The 2.5D models are models which solve the convectively driven system of equations: (1.3), (1.13), (1.14) for $\mathbf{B}, \mathbf{U}, T$ as in the 3D or hydrodynamic model described above, resolving fully in radius r and colatitude θ, but which had very limited resolution in azimuth ϕ. Due to the intense numerical computations required in the 3D dynamo described above, the 2.5D model is a much more manageable problem with a moderate use of computing resources. Recall from Cowling's theorem that an axisymmetric field can not be maintained by fluid motions. Therefore including just one non-axisymmetric mode will provide the required interaction between the axisymmetric and non-axisymmetric components of the system, therefore enabling dynamo action to be maintained.

The 2.5D models (see for example, Jones *et al* 1995) have so far produced field and flows of approximately the correct magnitude for the Earth in line with estimates of the Earth's field and flow determined from the GSV. The results obtained using the 2.5D models have been extremely useful in elucidating results obtained in the 3D models, and reinforcing trends observed in the 3D models.

1.6.4 Mean-field Theory.

The approach adopted in linear mean-field theory, is to simply consider only the induction equation as in kinematic models, but here, include only the mean or axisymmetric part of the field, neglecting the asymmetric contribution to the field.

Linear $\alpha^2\omega$ Models.

Decomposing the field and flow into axisymmetric and non-axisymmetric parts as follows,

$$\begin{aligned}\mathbf{B} &= \overline{\mathbf{B}} + \mathbf{B}' \\ \mathbf{U} &= \overline{\mathbf{U}} + \mathbf{U}'\end{aligned}$$

where an overbar indicates axisymmetric quantities and a dash indicates non-axisymmetric quantities. Applying this decomposition to (1.3) (where $R = 1$[1]), yields

$$\frac{\partial}{\partial t}(\overline{\mathbf{B}} + \mathbf{B}') = \nabla \times [(\overline{\mathbf{U}} + \mathbf{U}') \times (\overline{\mathbf{B}} + \mathbf{B}')] + \nabla^2(\overline{\mathbf{B}} + \mathbf{B}')$$

which upon expanding out, decouples into two equations; an axisymmetric equation and a non-axisymmetric equation. Thus

$$\begin{aligned}\frac{\partial}{\partial t}\overline{\mathbf{B}} &= \nabla \times [(\overline{\mathbf{U}} \times \overline{\mathbf{B}}) + \overline{(\mathbf{U}' \times \mathbf{B}')}] + \nabla^2\overline{\mathbf{B}} \\ \frac{\partial}{\partial t}\mathbf{B}' &= \nabla \times [\overline{\mathbf{U}} \times \mathbf{B}' + \mathbf{U}' \times \overline{\mathbf{B}} + (\mathbf{U}' \times \mathbf{B}')'] + \nabla^2\mathbf{B}'\end{aligned}$$

Now in our model, for simplicity, we consider only the axisymmetric equation, however as given in Section 1.2.3, Cowling's theorem states that,"no fluid flow exists which can maintain an axisymmetric magnetic field". Therefore in order to circumvent this difficulty, we replace the azimuthal average of the interaction of the non-axisymmetric field and flow with a parametrisation of the effects of small scale non-axisymmetric flows. So

$$\overline{(\mathbf{U}' \times \mathbf{B}')} = \overline{\boldsymbol{\mathcal{E}}} \simeq \alpha\overline{\mathbf{B}}.$$

This, now standard, approach of prescribing the effects of small scale non-axisymmetric flows, was first justified by Steenbeck and Krause (1966), see Section 2.6 for more details. So we are simply required to solve the axisymmetric equation,

$$\frac{\partial \mathbf{B}}{\partial t} = \nabla \times (\mathbf{U} \times \mathbf{B} + \alpha\mathbf{B}) + \nabla^2\mathbf{B}$$

where we have now dropped the overbars.

---

[1]The case $R = 1$, occurs when we assume (as we do in Chapter 2) that in the non-dimensionalisation, the fluid velocity, scales as $\mathcal{U} = \frac{\mathcal{L}}{\tau} = \frac{\mathcal{L}}{\tau_\eta}$

If we now further decompose our field and flow into poloidal and toroidal components,

$$\begin{aligned}\mathbf{B} &= \mathbf{B}_p + \mathbf{B}_\phi = \nabla \times [A(r,\theta,t)\mathbf{e}_\phi] + B(r,\theta,t)\mathbf{e}_\phi \\ \mathbf{U} &= \mathbf{U}_p + \mathbf{U}_\phi = \nabla \times [\psi(r,\theta,t)\mathbf{e}_\phi] + v(r,\theta,t)\mathbf{e}_\phi\end{aligned}$$

we obtain the following,

$$\frac{\partial A}{\partial t} + \frac{1}{s}\mathbf{U}_p \cdot \nabla(sA) = \left(\nabla^2 - \frac{1}{(r\sin\theta)^2}\right) A + \overline{\mathcal{E}}_\phi \tag{1.26}$$

$$\frac{\partial B}{\partial t} + s\mathbf{U}_p \cdot \nabla\left(\frac{B}{s}\right) = \left(\nabla^2 - \frac{1}{(r\sin\theta)^2}\right) B + s\mathbf{B}_p \cdot \nabla\left(\frac{v}{s}\right) + (\nabla \times \overline{\boldsymbol{\mathcal{E}}})_\phi \tag{1.27}$$

This system of equations, (1.26) and (1.27), describes what is known as an $\alpha^2\omega$ dynamo by virtue of the product of the 3 driving terms; $\overline{\mathcal{E}}_\phi$, $(\nabla \times \overline{\boldsymbol{\mathcal{E}}})_\phi$ and $s\mathbf{B}_p \cdot \nabla\left(\frac{v}{s}\right)$. The first two terms are the α-effect terms, introduced to parametrise the effects of a small-scale non-axisymmetric flow. The final term is the ω-effect term. This term arises from the effect of differential rotation in the system. In Appendix A, we show the details of the analysis of the mean-field equations, which indicate that the only terms which are capable of generating magnetic energy are the thermal wind and the prescribed α-effect term. The α-effect is discussed further in Section 2.6. The $\alpha^2\omega$ model has two natural limiting cases; the α^2 case, arising when $(\nabla \times \overline{\boldsymbol{\mathcal{E}}})_\phi \gg s\mathbf{B}_p \cdot \nabla\left(\frac{v}{s}\right)$ and the $\alpha\omega$-case, arising when $(\nabla \times \overline{\boldsymbol{\mathcal{E}}})_\phi \ll s\mathbf{B}_p \cdot \nabla\left(\frac{v}{s}\right)$. These limiting cases have quite different characteristics and are described in more detail in Section 2.8, when we discuss the specifics of our own model.

Linear models are useful for determining characteristics of the system at the onset of dynamo action, see for example Roberts (1972). The onset is determined as the value of α_o in the α^2 case, or $\alpha_o\omega_o$ in the $\alpha\omega$ case (where α_o and ω_o are the magnitudes of the prescribed α and ω-effects respectively), which yields a zero growth rate for the fastest growing mode. Beyond the onset of dynamo action, in the supercritical regime, a seed field will grow without bound. Therefore in order to gain some ideas about the system beyond onset, it is necessary to include some non-linearity into the system, which will act to equilibrate the system at some finite amplitude and prevent the solution blowing up.

Non-linear $\alpha^2\omega$ dynamo models.

For forcing just above critical through the α and/or ω parameters, the first non-linear effect important for equilibrating the geodynamo is the geostrophic flow. In this case, the magnetic

field strength is dependent on the Ekman number, E ($|\mathbf{B}| \sim O(E^{1/4})$ and so the system lies in a viscously limited Ekman state. As the forcing is further increased, the system evolves to a state where Taylor's constraint is satisfied and the system is equilibrated at a higher amplitude (typically of $O(1)$) by other non-linear effects; viscosity no longer plays an important role in the balance of the system. The evolution of the system from an Ekman state at just beyond critical, to a state in which Taylor's constraint is satisfied, is the scenario envisaged by Malkus and Proctor (1975), however the way in which this evolution occurs is model dependent. If the only non-linear effect included in a model is the geostrophic flow then, once Taylor's constraint (1.21) is satisfied, the solution is no longer viscously controlled, and since there are no other non-linear effects in the model to act to equilibrate the system, the solutions will grow without bound.

The modelling equations have been solved in a variety of geometries. Simpler geometries such as the plane layer, allow significant simplifications to the modelling equations. The infinite plane layer has been considered for the α^2 case by Soward and Jones (1983), and the $\alpha\omega$ case was investigated by Abdel-Aziz and Jones (1988). Bounding the plane layer model to form a duct, was a more realistic extension of Jones' (1991) plane-layer $\alpha\omega$ model. This extension by Jones and Wallace (1992) removes the unsatisfactory feature that plane layer dynamo waves propagate forever. The consideration of planar models provides a means of testing various physical parametrisations, without the additional complication of a spherical geometry. However they have the obvious drawback that they are unable to represent global modes. Therefore, many models have been used which adopt a spherical geometry, for example Proctor (1977), Hollerbach and Ierley (1991), Barenghi (1992, 1993) and Hollerbach and Jones (1993, 1995). The models we use in our investigations presented in this thesis, extend the $\alpha\omega$-type dynamo model first presented by Hollerbach and Jones. In the next section we outline the main characteristics of our models and the structure of the remainder of the thesis.

Our Model.

The dynamo models we present here, are in a sense intermediate models, as they combine aspects of both the kinematic and hydrodynamic models. These models fall into the category of non-linear mean-field $\alpha^2\omega$ dynamos, where we focus on the behaviour of the axisymmetric field and

flow, and prescribe the effects of non-axisymmetric flows via a so-called α-effect. We simplify the hydrodynamic system of equations by replacing the dynamically determined buoyancy force with a prescribed buoyancy term $\Theta\mathbf{r}$, as first considered by Hollerbach and Jones (1993b). This simplification then enables us to neglect the feedback from the heat equation in the system. We include the more realistic effects of a parametrised buoyancy force, which will drive a meridional circulation as well as a differential rotation (ω-effect) in the system, rather than simply prescribing an ω-effect. This approach therefore allows a natural feedback between the induction and momentum equations, including the key non-linear interactions deemed important to the dynamo mechanism. For clarity we will refer to these kinds of models as being "α^2-type", "$\alpha\omega$-type" or "$\alpha^2\omega$-type" dynamo models, to make the distinction with traditional α^2, $\alpha\omega$ and $\alpha^2\omega$ models which are kinematic models with prescribed flows. We describe the $\alpha^2\omega$-type model in more detail in Chapter 2, but will sketch out the main ideas below.

The dynamo is modelled by the following equations

$$\frac{\partial \mathbf{B}}{\partial t} = \nabla \times (\mathbf{U} \times \mathbf{B} + \alpha \mathbf{B}) + \nabla^2 \mathbf{B}$$

$$Ro\left(\frac{\partial \mathbf{U}}{\partial t} + (\mathbf{U}\cdot\nabla)\mathbf{U}\right) + 2\mathbf{k}\times\mathbf{U} = -\nabla p + E\nabla^2\mathbf{U} + (\nabla\times\mathbf{B})\times\mathbf{B} + \Theta\mathbf{r}$$

where we additionally assume that our fluid is incompressible. We consider both $\alpha\omega$ and $\alpha^2\omega$-type models, with and without the effects of inertia. Fearn and Rahman (2004a,b,c) investigated the α^2-type model first in the absence of inertia, then later extending these results to include inertial effects. In this way we are able to cover a substantial region of parameter space and from these four models, draw conclusions about the similarities and differences between the solutions found using each of these models. The following section describes the presentation of the remainder of this thesis.

1.7 Area of Investigation.

Our motivation for the study of the 2D non-linear mean-field models we present here – when the ability to now produce well resolved, fully 3D dynamo models, such as those by Glatzmaier and Roberts, has been possible for around 10years now – lies in the fact that the 3D calculations are incredibly numerically intensive and expensive to run. The consideration of non-linear mean-field

dynamos, which allows us to focus in on specific aspects of the dynamo mechanism, enables us to obtain a better understanding of the underlying physical processes.

Malkus and Proctor (1975) were the first to explore analytically the non-linear aspects of their α^2 dynamo model in a rotating sphere. Their investigations revealed two regimes in which the dynamo operated. The solutions could remain in the low amplitude, viscously limited regime (Ekman states) or in a higher amplitude, invisid regime where equilibration is achieved through ohmic dissipation (Taylor states). These results fuelled interest in these types of models, and numerous problems were investigated numerically, by for example Proctor (1977), Hollerbach and Ierley (1991), Barenghi (1992, 1993), Hollerbach and Jones (1993a,b,1995).

The analysis of the problem investigated analytically by Malkus and Proctor (1975) was extended by Proctor (1977), who studied the problem numerically. Proctor included the effects of viscosity and inertia and applied stress-free boundary conditions at the core mantle boundary. He concluded from his studies that the form of α could not be constant, as adopted in the earlier Malkus and Proctor (1975) paper, as it is physically unrealistic for the α-effect to be independent of z. He considered an α of the form $\alpha_o \cos\theta$, and examined the global effects of induced velocity fields. He concluded from the limited range in Ekman number he considered ($5 \times 10^{-3} \leq E \leq 1$), that the viscous and inertial forces are unimportant in the final equilibrated state. This result is challenged by recent work by Fearn and Rahman (2004a,b), who given significant improvements in numerical capabilities in recent years have been able to investigate thoroughly the dependence of inertia and viscosity on their α^2-type model and find that mean-field models are strongly affected by both.

Hagee and Olson (1991) investigated the time dependence of spherical $\alpha^2\omega$ dynamo models. Their model includes a toroidal shear (ω-effect) into the flow and incorporates a non-linear α-quenching which acts to equilibrate their kinematic dynamo model. They consider the cases of isotropic and anisotropic forms for their α-effect, the anisotropy incorporated was in the radial direction to simulate the effects of density statification. They found solutions with a steady dipole component coexisting with an oscillating quadrupole component, which well represented the ob-

served geosecular variation.

Jones and Wallace (1992) consider an $\alpha\omega$ dynamo in a duct. They make the rapid rotation approximation neglecting inertia and including viscous effects only in narrow boundary layers. The non-linearity in the model arises from the inclusion of a magnetically driven geostrophic flow and meridional circulation. For the two forms of α-effect they consider, they investigate the circumstances under which a Taylor state can arise. In their first model, $\alpha = z$, they find oscillatory solutions, which reverse far too frequently to be characteristic of the geodynamo, but are unable to obtain any clear-cut Taylor states. In the second model, they adopt $\alpha = \sin(\pi z)\sin(\pi(1-2x))$, so that the sign of the α-effect changes upon crossing the equator. These solutions are initially steady at onset, but quickly become oscillatory. Taylor states are obtained, and the model, has regions of reversing and non-reversing regimes, exhibiting behaviour which is more characteristic of the geodynamo.

Barenghi (1993) investigated the behaviour of an $\alpha^2\omega$ model, as it was hoped that including a second α-effect would help to stabilise the rapid timescale behaviour of $\alpha\omega$ dynamos. Solving his non-linear kinematic model in a spherical shell, neglecting inertial effects and including viscosity only in narrow boundary layers, he varied the form used for his α-effect, in order to obtain an idea of general characteristics of such models. He found that the onset of dynamo action is steady if the strength of the ω-effect is sufficiently weak, becoming time dependent at a value of the ω-effect Reynolds number $R_\omega \approx 100$, in all the models he considered. Beyond onset, he examined the transition from a weak field Ekman state to a strong field Taylor state, as the strength of the α-effect is increased. He found the oscillatory solutions in the strong field regime, to be slow and consistent with the observed intervals between reversals of the geodynamo.

Hollerbach and Jones (1993a) investigated the solutions obtained using a spherical shell α^2-type dynamo model, in which they incorporated a finitely conducting inner core. Their results found at $\alpha_o = 5.5$ and $\alpha_o = 8.0$, represent solutions in the slightly supercritical and supercritical regimes respectively. The slightly supercritical solutions are representative of solutions in a transition from an Ekman state to a Taylor state. The supercritical solutions lie in a Taylor state, where (by defini-

tion) Taylor's constraint is satisfied. Later papers by Hollerbach and Jones (1993b, 1995) focussed instead on an $\alpha\omega$-type dynamo model, where an ω-effect was generated through the prescribed buoyancy force. These papers also focussed on the influence a finitely conducting inner core had on the dynamics of the dynamo mechanism. They concluded that the diffusive timescale of the inner core – which is long compared with the most rapid advective timescales of the outer core – the field in the inner core effectively averages over these very rapid timescales, thus acting to stabilise the dynamo process.

More recently, Fearn and Rahman (2004a) investigated the α^2-type model of Hollerbach and Jones (1993a). Through their investigations using this model they find that the evolution of the mean-field is strongly dependent on the form of α or the value of Ekman number used, and the role of Taylor's constraint on the solutions. They also investigate the influence of inertia on solutions, (see Fearn and Rahman 2004b) and find for their model that inertia actually acts to facilitate dynamo action, contrary to the results found in 2.5D and 3D models. They compare their results with the 2.5D model investigated by Fearn and Morrison (2001). In their discussion they compare these two studies and attempt to gain some insight into aspects of the dynamo mechanism. Through this comparison, they suggest that the reason Fearn and Rahman's α^2-type model does not fail as the Rossby number is increased, lies in the fact that the non-axisymmetric α-effect which is responsible for the field generation process is unaffected by inertia. They suggest that the shutting off mechanism exhibited in the Fearn and Morrison model and other 2.5D models, may be related to the effect of differential rotation. However, given the complexity, of 2.5D and 3D models and the interdependence of parameters on particular quantities, makes it difficult to pinpoint the exact reasons for the failure of dynamos with increasing Rossby number, or decreasing Roberts number. This therefore suggested that an interesting study would be to explore the effect of inertia on a non-linear $\alpha\omega$-type model.

In Chapter 2 we introduce the general model used in all four subsequent chapters, and outline the differences between each of the models used. As we are interested in the effect of inertia in $\alpha\omega$-type models, it is important to consider first the model in the absence of inertia. Chapter 3 focusses on the non-linear $\alpha\omega$-type model, allowing us a comparison with earlier models and providing us

with a reference case for our later inertia studies, presented in Chapter 4. As a link between the α^2-type model considered by Fearn and Rahman (2004a,b), and the $\alpha\omega$-type model considered in Chapters 3 and 4, we consider the more general and intermediate case of an $\alpha^2\omega$-type model. Chapter 5 investigates the effect of increasing the strength of the imposed differential rotation (or ω-effect) on the α^2-type model, in the absence of inertia. We then include the effect of inertia, and through varying the strength of this term in the momentum equation, we alter the balance of terms in the system and see how the equilibration of the system changes. Finally, in Chapter 7 we compare and contrast each of these models and also consider earlier work by Fearn and Rahman on an α^2-type model with and without the inclusion of inertial effects, enabling us to draw some key conclusions about the parameter space we have explored.

Chapter 2

The Physical Model & Governing Equations.

2.1 Introduction.

In this chapter we present the model and governing equations relevant in the following four chapters. The model is fairly similar in each case we consider, so it makes sense to present the general model once and then indicate the differences between each of the cases presented. An advantage of the similarity between all of these models is that it allows us to draw conclusions regarding the global effect of certain parameters on the system. We will comment on these similarities and differences in our conclusions in Chapter 7. The numerical method used to solve our models is discussed in Appendix B.

2.2 The Non-dimensionalisation.

It is standard practice within applied mathematics to non-dimensionalise a differential equation. This practice is useful as it introduces dimensionless parameters, whose size give a measure of the relative importance of the terms they multiply in the equation. We apply this procedure to the induction equation (1.1) and the momentum equation (1.7) introduced in Chapter 1.

We have

$$\frac{\partial \widetilde{\mathbf{B}}}{\partial \widetilde{t}} = \widetilde{\nabla} \times (\widetilde{\mathbf{U}} \times \widetilde{\mathbf{B}}) + \eta \widetilde{\nabla}^2 \widetilde{\mathbf{B}} \tag{2.1}$$

and

$$\rho_o \left(\frac{\partial \widetilde{\mathbf{U}}}{\partial \widetilde{t}} + (\widetilde{\mathbf{U}} \cdot \widetilde{\nabla}) \widetilde{\mathbf{U}} \right) + 2\rho_o \widetilde{\mathbf{\Omega}} \times \widetilde{\mathbf{U}} = -\widetilde{\nabla} \widetilde{p} + \rho_o \nu \widetilde{\nabla}^2 \widetilde{\mathbf{U}} + \frac{1}{\mu_o} (\widetilde{\nabla} \times \widetilde{\mathbf{B}}) \times \widetilde{\mathbf{B}} + \widetilde{\Theta} \widetilde{\mathbf{r}} \tag{2.2}$$

where $\widetilde{}$ is present on all variables to indicate that they are dimensional quantities. Now the buoyancy term in (2.2) differs from that given in (1.7). Here we choose to include a generic term to represent the buoyancy force, since in our model, which we present in Section 2.3, we prescribe this force and so it is convenient to introduce this simplification here.

Now, to non-dimensionalise these equations, we let

$$\widetilde{\nabla} = \frac{1}{\mathcal{L}} \nabla, \quad \frac{\partial}{\partial \widetilde{t}} = \frac{1 \partial}{\tau \partial t}$$

where $\mathcal{L} = (r_o - r_i)$ is a typical lengthscale and where τ is a typical timescale. Here we scale length with the gap width $r_o - r_i$, where r_o is the outer core radius and r_i is the inner core radius.

Let $\widetilde{\mathbf{U}} = \mathcal{U}\mathbf{U}$ where $\mathcal{U} = \frac{\mathcal{L}}{\tau}$ is a typical fluid velocity, $\widetilde{\mathbf{B}} = \mathcal{B}\mathbf{B}$ where $\mathcal{B}$ is a typical magnetic field strength, $\widetilde{p} = \mathcal{P}p$ where $\mathcal{P}$ is a typical magnitude of pressure and $\widetilde{\mathbf{\Omega}} = \Omega \mathbf{k}$ where $\mathbf{k}$ is the unit vector in the direction of the axis of rotation and Ω is the angular velocity of the mantle. $\widetilde{\Theta}\widetilde{\mathbf{r}} = \vartheta \Theta \mathbf{r}$, where ϑ is a typical magnitude of the now dimensionless buoyancy force $\Theta \mathbf{r}$.

Beginning by considering the induction equation in the absence of a fluid flow and applying these scalings we have

$$\begin{aligned}
\frac{\partial \widetilde{\mathbf{B}}}{\partial \widetilde{t}} &= \eta \widetilde{\nabla}^2 \widetilde{\mathbf{B}} \\
\Rightarrow \frac{\mathcal{B}}{\tau} \frac{\partial \mathbf{B}}{\partial t} &= \eta \frac{\mathcal{B}}{\mathcal{L}^2} \nabla^2 \mathbf{B} \\
\Rightarrow \frac{1}{\tau} \frac{\partial \mathbf{B}}{\partial t} &= \eta \frac{1}{\mathcal{L}^2} \nabla^2 \mathbf{B} \\
\rightarrow \tau &= \frac{\mathcal{L}^2}{\eta}
\end{aligned}$$

$\tau (= \tau_\eta)$ is the length of time it would take for the magnetic field to decay by a factor e in the absence of a flow acting to prevent it. We call τ_η the magnetic diffusion time.

Now non-dimensionalising equations (2.1) and (2.2) we find

$$\begin{aligned}
\frac{\partial \widetilde{\mathbf{B}}}{\partial \widetilde{t}} &= \widetilde{\nabla} \times (\widetilde{\mathbf{U}} \times \widetilde{\mathbf{B}}) + \eta \widetilde{\nabla}^2 \widetilde{\mathbf{B}} \\
\Rightarrow \frac{\mathcal{B}}{\tau}\frac{\partial \mathbf{B}}{\partial t} &= \frac{\mathcal{U}\mathcal{B}}{\mathcal{L}} \nabla \times (\mathbf{U} \times \mathbf{B}) + \eta \frac{\mathcal{B}}{\mathcal{L}^2} \nabla^2 \mathbf{B} \\
\Rightarrow \frac{\mathcal{B}}{\tau}\frac{\partial \mathbf{B}}{\partial t} &= \frac{\mathcal{B}}{\tau} \nabla \times (\mathbf{U} \times \mathbf{B}) + \eta \frac{\mathcal{B}}{\mathcal{L}^2} \nabla^2 \mathbf{B} \\
\Rightarrow \frac{\partial \mathbf{B}}{\partial t} &= \nabla \times (\mathbf{U} \times \mathbf{B}) + \nabla^2 \mathbf{B}
\end{aligned}$$

since we choose to non-dimensionalise the system on the ohmic diffusion timescale; $\tau_\eta = \frac{\mathcal{L}^2}{\eta}$.

Similarly,

$$\begin{aligned}
\rho_o \left(\frac{\partial \widetilde{\mathbf{U}}}{\partial \widetilde{t}} + (\widetilde{\mathbf{U}} \cdot \widetilde{\nabla})\widetilde{\mathbf{U}} \right) + 2\rho_o \widetilde{\mathbf{\Omega}} \times \widetilde{\mathbf{U}} &= -\widetilde{\nabla}\widetilde{p} + \rho_o \nu \widetilde{\nabla}^2 \widetilde{\mathbf{U}} + \frac{1}{\mu_o}(\widetilde{\nabla} \times \widetilde{\mathbf{B}}) \times \widetilde{\mathbf{B}} + \widetilde{\Theta}\widetilde{\mathbf{r}} \\
\Rightarrow \rho_o \frac{\mathcal{U}}{\tau}\frac{\partial \mathbf{U}}{\partial t} + \rho_o \frac{\mathcal{U}^2}{\mathcal{L}}(\mathbf{U} \cdot \nabla)\mathbf{U} + 2\rho_o \Omega \mathcal{U}(\mathbf{k} \times \mathbf{U}) &= -\frac{\mathcal{P}}{\mathcal{L}}\nabla p + \rho_o \nu \frac{\mathcal{U}}{\mathcal{L}^2}\nabla^2 \mathbf{U} + \frac{1}{\mu_o}\frac{\mathcal{B}^2}{\mathcal{L}}(\nabla \times \mathbf{B}) \times \mathbf{B} + \vartheta \Theta \mathbf{r}
\end{aligned}$$

now dividing through by $\rho_o \Omega \mathcal{U}$ and simplifying, we obtain

$$\Rightarrow \frac{\eta}{\Omega \mathcal{L}^2}\left(\frac{\partial \mathbf{U}}{\partial t} + (\mathbf{U} \cdot \nabla)\mathbf{U} \right) + 2(\mathbf{k} \times \mathbf{U}) = -\frac{\mathcal{P}}{\rho_o \Omega \mathcal{U}\mathcal{L}}\nabla p + \frac{\nu}{\Omega \mathcal{L}^2}\nabla^2 \mathbf{U} + \frac{\mathcal{B}^2}{\mu_o \rho_o \Omega \eta}(\nabla \times \mathbf{B}) \times \mathbf{B} + \frac{\vartheta}{\rho_o \Omega \mathcal{U}}\Theta \mathbf{r}$$

where we may choose $\mathcal{P}$ to be $\rho_o \Omega \mathcal{U}\mathcal{L}$ and ϑ to be $\rho_o \Omega \mathcal{U}$. In addition, for the Earth, we expect the Coriolis and Lorentz forces to be comparable in magnitude, so we choose $\mathcal{B} = (\rho_o \mu_o \eta \Omega)^{1/2}$ in keeping with this assumption. This leads us to the following

$$Ro\left(\frac{\partial \mathbf{U}}{\partial t} + (\mathbf{U} \cdot \nabla)\mathbf{U} \right) + 2(\mathbf{k} \times \mathbf{U}) = -\nabla p + E\nabla^2 \mathbf{U} + (\nabla \times \mathbf{B}) \times \mathbf{B} + \Theta \mathbf{r}$$

Now we have defined two parameters from this non-dimensionalisation. The first one, appearing in front of the inertia term, is called the Rossby number or magnetic Ekman number, $Ro = \eta/\Omega\mathcal{L}^2$. As we saw from the non-dimensionalisation this term is simply the ratio of the inertia term to the Coriolis force and within the Earth, recent estimates of this parameter give a value of around $O(10^{-9})$. The second parameter arising from the non-dimensionalisation appears in front of the viscous term and is called the Ekman number, $E = \nu/\Omega\mathcal{L}^2$ and is the ratio of the viscous term to the Coriolis force. In the Earth, this term is estimated to be $O(10^{-15})$. The smallness of these two

parameters compared with the other terms in the equation are among the main sources of difficulty associated with this problem. For further details on the estimation of these parameters, see Section 1.5.

2.3 The Modelling Equations.

In the following four chapters, we consider a spherical shell model, with inner core of radius, r_i and outer core of radius, r_o, which is rotating about its axis with angular velocity, Ω. The inner core is free to rotate about this same axis with angular velocity Ω_i. We consider the inner core to be finitely conducting and of equal conductivity to the fluid outer core. The outer core is then bounded by the insulating mantle.

We introduced in Section 1.6.4 the main ideas of mean-field dynamo models and outlined briefly the approach we would adopt in our own models. In our discussion of mean-field models, we introduced the concepts of the α and ω-effects and how they are they are capable of generating and maintaining dynamo action in axisymmetric models. We show in Appendix A.2, that these two effects are the only terms present in the governing equations which are capable of producing an increase in magnetic energy. However, in the Earth, it is believed that field generation only occurs in the fluid outer core, with the inner core (perhaps) playing a stabilising role (Hollerbach and Jones (1993b, 1995)). It is believed that the field diffuses on the magnetic diffusion timescale, into the solid inner core.

The scaled mean-field induction equations are

$$\frac{\partial \hat{\mathbf{B}}}{\partial t} = \nabla^2 \hat{\mathbf{B}} + \nabla \times (\mathbf{u}_i \times \hat{\mathbf{B}}) \tag{2.3}$$

in the inner core, and

$$\frac{\partial \mathbf{B}}{\partial t} = \nabla^2 \mathbf{B} + \nabla \times (\alpha \mathbf{B}) + \nabla \times (\mathbf{U} \times \mathbf{B}) \tag{2.4}$$

in the outer core, where $\mathbf{B}$ is the large-scale axisymmetric magnetic field, $\mathbf{U}$ is the large-scale axisymmetric fluid flow and $\mathbf{u}_i = \Omega_i r \sin\theta \mathbf{e}_\phi$ where Ω_i denotes the inner core angular velocity. In our model we choose the axis of rotation of the inner and outer cores to be the same. Here the superscript $\hat{}$ is used to denote inner core quantities. In the outer core, our induction equation (2.4)

is coupled to the momentum equation,

$$Ro\left(\frac{\partial \mathbf{U}}{\partial t} + (\mathbf{U}\cdot\nabla)\mathbf{U}\right) + 2\mathbf{k}\times\mathbf{U} = -\nabla p + E\nabla^2\mathbf{U} + (\nabla\times\mathbf{B})\times\mathbf{B} + \Theta\mathbf{r} \tag{2.5}$$

we also assume that our fluid is incompressible, so the equation of mass continuity gives us $\nabla\cdot\mathbf{U} = 0$.

2.4 Poloidal and Toroidal decomposition.

Since the dynamo problem we are considering here is inherently spherical and we have the conditions that both

$$\nabla\cdot\mathbf{B} = 0 \quad \text{and} \quad \nabla\cdot\mathbf{U} = 0$$

we are able to separate our field and flow into poloidal and toroidal parts. The poloidal and toroidal components are mutually orthogonal vectors, which means that the curl of a toroidal vector is a poloidal vector and vice-versa. This poloidal-toroidal decomposition also lends itself to spectral methods a means of solving the system of equations. The programs used for both the inertia and inertialess models are included in Appendix B and further details on the method are given there.

Beginning with the poloidal-toroidal decomposition; (2.6) and (2.7)

$$\mathbf{B} = \nabla\times A\mathbf{e}_\phi + B\mathbf{e}_\phi \tag{2.6}$$

$$\mathbf{U} = \nabla\times\psi\mathbf{e}_\phi + v\mathbf{e}_\phi \tag{2.7}$$

applied to equation (2.4) we obtain the following

$$\begin{aligned}
\frac{\partial}{\partial t}(\nabla\times A\mathbf{e}_\phi + B\mathbf{e}_\phi) &= \nabla^2(\nabla\times A\mathbf{e}_\phi + B\mathbf{e}_\phi) + \nabla\times(\alpha(\nabla\times A\mathbf{e}_\phi + B\mathbf{e}_\phi)) \\
&+ \nabla\times((\nabla\times\psi\mathbf{e}_\phi + v\mathbf{e}_\phi)\times(\nabla\times A\mathbf{e}_\phi + B\mathbf{e}_\phi)) \\
\Rightarrow \nabla\times\left(\frac{\partial A}{\partial t}\mathbf{e}_\phi\right) + \frac{\partial B}{\partial t}\mathbf{e}_\phi &= \nabla\times\nabla^2(A\mathbf{e}_\phi) + \nabla^2 B\mathbf{e}_\phi + \nabla\times(\alpha(\nabla\times A\mathbf{e}_\phi)) \\
&+ \nabla\times(\alpha B\mathbf{e}_\phi) + \nabla\times((\nabla\times\psi\mathbf{e}_\phi)\times(\nabla\times A\mathbf{e}_\phi)) \\
&+ \nabla\times((\nabla\times\psi\mathbf{e}_\phi)\times(B\mathbf{e}_\phi)) + \nabla\times((v\mathbf{e}_\phi)\times(\nabla\times A\mathbf{e}_\phi)) \\
&+ \nabla\times((v\mathbf{e}_\phi)\times(B\mathbf{e}_\phi))
\end{aligned} \tag{2.8}$$

we see that the final term on the RHS of equation (2.8) will drop out by standard vector calculus, and the rest of the terms in the equation will decouple into either poloidal terms (i.e. terms which

are $\sim \nabla \times \mathbf{e}_\phi$) or toroidal terms (i.e. terms which are $\sim \mathbf{e}_\phi$). Therefore, the equation decouples into a poloidal equation and a toroidal equation, thus

$$\nabla \times \left(\frac{\partial A}{\partial t}\mathbf{e}_\phi\right) = \nabla \times \nabla^2(A\mathbf{e}_\phi) + \nabla \times (\alpha B\mathbf{e}_\phi) + \nabla \times ((\nabla \times \psi\mathbf{e}_\phi) \times (\nabla \times A\mathbf{e}_\phi)) \quad (2.9)$$

$$\begin{aligned}\frac{\partial B}{\partial t}\mathbf{e}_\phi &= \nabla^2 B\mathbf{e}_\phi + \nabla \times (\alpha(\nabla \times A\mathbf{e}_\phi)) + \nabla \times ((\nabla \times \psi\mathbf{e}_\phi) \times (B\mathbf{e}_\phi)) \\ &+ \nabla \times ((v\mathbf{e}_\phi) \times (\nabla \times A\mathbf{e}_\phi)) \quad (2.10)\end{aligned}$$

Now, 'uncurling' equation (2.9) and then taking the dot product with $\mathbf{e}_\phi$ and taking the dot product of (2.10) with $\mathbf{e}_\phi$, we obtain

$$\frac{\partial A}{\partial t} = D^2 A + \alpha B + N(\psi, A) \quad (2.11)$$

$$\frac{\partial B}{\partial t} = D^2 B + \mathbf{e}_\phi \cdot \nabla[\alpha \nabla \times (A\mathbf{e}_\phi)] + M(v, A) - M(B, \psi) \quad (2.12)$$

where

$$\begin{aligned}\frac{\partial}{\partial z} &= \cos\theta \frac{\partial}{\partial r} - \frac{\sin\theta}{r}\frac{\partial}{\partial \theta} \\ D^2 &= \nabla^2 - (r\sin\theta)^{-2} \\ N(X, Y) &= \mathbf{e}_\phi \cdot [\nabla \times (X\mathbf{e}_\phi) \times \nabla \times (Y\mathbf{e}_\phi)] \\ M(X, Y) &= \mathbf{e}_\phi \cdot \nabla \times [X\mathbf{e}_\phi \times \nabla \times (Y\mathbf{e}_\phi)]\end{aligned}$$

This decomposition was first introduced by Proctor(1977).

Before we may apply the poloidal-toroidal decomposition, it is helpful to rewrite the inertia term $(\mathbf{U} \cdot \nabla)\mathbf{U}$ using a standard vector identity as,

$$(\mathbf{U} \cdot \nabla)\mathbf{U} = \mathbf{U} \times (\nabla \times \mathbf{U}) - \frac{1}{2}\nabla U^2$$

Applying the poloidal-toroidal decomposition to the momentum equation then gives,

$$\begin{aligned}Ro\left[\nabla \times \left(\frac{\partial \psi}{\partial t}\mathbf{e}_\phi\right) + [\nabla^2 \psi\mathbf{e}_\phi \times (\nabla \times \psi\mathbf{e}_\phi)] + [v\mathbf{e}_\phi \times (\nabla \times v\mathbf{e}_\phi)] - \frac{1}{2}\nabla((\nabla \times \psi)^2 + v^2)\right] - 2v\mathbf{e}_s \\ = -\nabla p + E\nabla \times \nabla^2 \psi\mathbf{e}_\phi - [\nabla^2 A\mathbf{e}_\phi \times (\nabla \times A\mathbf{e}_\phi)] - [B\mathbf{e}_\phi \times (\nabla \times B\mathbf{e}_\phi)] + \Theta r\mathbf{e}_r \quad (2.13)\end{aligned}$$

$$Ro\left[\frac{\partial v}{\partial t}\mathbf{e}_\phi + [(\nabla \times \psi\mathbf{e}_\phi) \times (\nabla \times v\mathbf{e}_\phi)]\right] - 2\frac{\partial \psi}{\partial z}\mathbf{e}_\phi = E\nabla^2 v\mathbf{e}_\phi + [(\nabla \times B\mathbf{e}_\phi) \times (\nabla \times A\mathbf{e}_\phi)] \quad (2.14)$$

The toroidal equation (2.14) can then be easily dealt with by taking the dot product with $\mathbf{e}_\phi$. Thus,

$$Ro\left[\frac{\partial v}{\partial t}+\mathbf{e}_\phi\cdot[(\nabla\times\psi\mathbf{e}_\phi)\times(\nabla\times v\mathbf{e}_\phi)]\right]-2\frac{\partial\psi}{\partial z} = E\nabla^2 v+\mathbf{e}_\phi\cdot[(\nabla\times B\mathbf{e}_\phi)\times(\nabla\times A\mathbf{e}_\phi)]$$

$$\text{i.e.}\quad Ro\left[\frac{\partial v}{\partial t}-N(v,\psi)\right]-2\frac{\partial\psi}{\partial z} = E\nabla^2 v+N(B,A) \tag{2.15}$$

Now to deal with the poloidal equation, we begin by taking the curl of (2.13), in order to eliminate the pressure gradient term and the gradient term that appears as part of the inertia. This gives,

$$Ro\left[\nabla\times\left(\nabla\times\left(\frac{\partial\psi}{\partial t}\mathbf{e}_\phi\right)\right)+\nabla\times[\nabla^2\psi\mathbf{e}_\phi\times(\nabla\times\psi\mathbf{e}_\phi)]+\nabla\times[v\mathbf{e}_\phi\times(\nabla\times v\mathbf{e}_\phi)]\right]-2\frac{\partial v}{\partial z}\mathbf{e}_\phi$$

$$=-\nabla p+E\nabla\times(\nabla\times\nabla^2\psi\mathbf{e}_\phi)-\nabla\times[\nabla^2 A\mathbf{e}_\phi\times(\nabla\times A\mathbf{e}_\phi)]-\nabla\times[B\mathbf{e}_\phi\times(\nabla\times B\mathbf{e}_\phi)]-\frac{\partial\Theta}{\partial\theta}\mathbf{e}_\phi$$

$$\text{i.e.}\quad Ro\left[\frac{\partial\nabla^2\psi}{\partial t}\mathbf{e}_\phi-\nabla\times[\nabla^2\psi\mathbf{e}_\phi\times(\nabla\times\psi\mathbf{e}_\phi)]-\nabla\times[v\mathbf{e}_\phi\times(\nabla\times v\mathbf{e}_\phi)]\right]+2\frac{\partial v}{\partial z}\mathbf{e}_\phi$$

$$=E\nabla^2(\nabla^2\psi\mathbf{e}_\phi)+\nabla\times[\nabla^2 A\mathbf{e}_\phi\times(\nabla\times A\mathbf{e}_\phi)]+\nabla\times[B\mathbf{e}_\phi\times(\nabla\times B\mathbf{e}_\phi)]+\frac{\partial\Theta}{\partial\theta}\mathbf{e}_\phi \tag{2.16}$$

Finally taking the dot product of (2.16) with $\mathbf{e}_\phi$ gives,

$$Ro\left(\frac{\partial D^2\psi}{\partial t}-M(D^2\psi,\psi)-M(v,v)\right)+2\frac{\partial v}{\partial z}=E(D^2)^2\psi+M(D^2A,A)+M(B,B)+\frac{\partial\Theta}{\partial\theta} \tag{2.17}$$

2.5 Boundary Conditions.

2.5.1 The magnetic field boundary conditions.

Since we have a finitely conducting inner core, we require that we have continuity of the magnetic field components and continuity of the tangential components of the associated electric field across the inner core boundary, $r=r_i$. This yields the following,

$$\hat{\mathbf{B}}=\mathbf{B}\quad\text{and}\quad\hat{\mathbf{E}}_\perp=\mathbf{E}_\perp\qquad\text{on}\quad r=r_i \tag{2.18}$$

We also assume the mantle is a perfect insulator, and so no current flows in the mantle. This allows us to apply at the core mantle boundary, $r=r_o$, the insulating boundary condition,

$$\mathbf{B}=\mathbf{B}^{(e)}\qquad\text{on}\quad r=r_o \tag{2.19}$$

where $\mathbf{B}^{(e)}$ is the external potential field.

2.5.2 The velocity boundary conditions.

For the fluid confined to the outer core, we assume that on the inner core boundary at $r = r_i$ and at the core mantle boundary at $r = r_o$, that we have no slip. Additionally, we allow our inner core to freely rotate relative to the mantle and thus we have the conditions that

$$U_r, U_\theta = 0 \quad , \quad U_\phi = \Omega_i r \sin\theta \qquad \text{at} \quad r = r_i \tag{2.20}$$

$$U_r, U_\theta, U_\phi = 0 \qquad \text{at} \quad r = r_o \tag{2.21}$$

where Ω_i is the solid body rotation of the inner core and is to be determined as part of the solution.

Now in order to determine Ω_i, we require that the total torque in the inner core vanishes. This balance is discussed further below. The implementation of these boundary conditions is described in detail in Appendix B.

Torque Balance on the inner core boundary.

Now in order to determine Ω_i, we require that the total axial torque, Γ is given by,

$$CRo\frac{\partial \Omega_i}{\partial t} = \Gamma \tag{2.22}$$

where $C = \frac{8}{15}\pi r_i^5$ (for inner and outer cores of equal density) and Ro is the Rossby number. $CRo = 5.86 \times 10^{34} kgm^2$ is the polar moment of inertia of the inner core. The total torque on the inner core is balanced by the sum of electromagnetic and viscous torques, thus

$$\Gamma = \Gamma_B + \Gamma_\nu \tag{2.23}$$

where

$$\Gamma_B = 2\pi r_i^3 \int_0^\pi B_\phi B_r \Big|_{r=r_i} \sin^2\theta d\theta \quad \text{, is the electromagnetic torque and}$$

$$\Gamma_\nu = E2\pi r_i^3 \int_0^\pi r\frac{\partial}{\partial r}\left(\frac{U_\phi}{r}\right)\Big|_{r=r_i} \sin^2\theta d\theta \quad \text{is the viscous torque.}$$

Including Inertia.

Thus, on the inner core boundary we have the following torque balance

$$E2\pi r_i^3 \int_0^\pi r\frac{\partial}{\partial r}\left(\frac{U_\phi}{r}\right)\Big|_{r=r_i} \sin^2\theta d\theta + 2\pi r_i^3 \int_0^\pi B_\phi B_r\Big|_{r=r_i} \sin^2\theta d\theta = CRo\frac{\partial \Omega_i}{\partial t} \tag{2.24}$$

which now needs to timestepped along with the momentum equation to determine Ω_i.

Neglecting Inertia.

In the absence of inertia, the integrated viscous torque, must be balanced by the electromagnetic torque,

$$E2\pi r_i^3 \int_0^\pi r\frac{\partial}{\partial r}\left(\frac{U_\phi}{r}\right)\Big|_{r=r_i} \sin^2\theta d\theta + 2\pi r_i^3 \int_0^\pi B_\phi B_r\Big|_{r=r_i} \sin^2\theta d\theta = 0 \tag{2.25}$$

i.e.

$$E\int_0^\pi r\frac{\partial}{\partial r}\left(\frac{U_\phi}{r}\right)\Big|_{r=r_i} \sin^2\theta d\theta = -\int_0^\pi B_\phi B_r\Big|_{r=r_i} \sin^2\theta d\theta \tag{2.26}$$

It is through this electromagnetic coupling between the inner and outer cores that the inner core actively becomes involved in the outer core fluid flow.

2.6 The α-effect.

The α that appears in equation (2.4), is a parametrisation of the small-scale non-axisymmetric flow, introduced in the mean-field theory of Steenbeck and Krause (1966). In our axisymmetric model, the presence of this term is crucial in generating a dynamo, as Cowling's Theorem (1934) states that an axisymmetric magnetic field can not be maintained by dynamo action (see also Section 1.2.3. Appendix A includes a sketch proof of this theorem.). Introducing this parametrisation of a non-axisymmetric flow into the equation successfully circumvents Cowling's Theorem.

Therefore as described in the mean-field theory introduced in Section 1.6.4, we may write the axisymmetric part of the product of the non-axisymmetric field and flow as;

$$\overline{(\mathbf{U}' \times \mathbf{B}')} = \overline{\mathcal{E}} \simeq \alpha\overline{\mathbf{B}}$$

Through the studies of Steenbeck and Krause (1966), we know that the effects of rotation and stratification acting alone can not produce an α-effect. Considering an expansion of $\overline{\mathcal{E}}$, which includes the effects of rotation and stratification, we can write (see Roberts 1994)

$$\overline{\mathcal{E}} = -\beta_o \nabla \times \overline{\mathbf{B}} + \alpha_1(\mathbf{\Omega}\cdot\mathbf{x})\overline{\mathbf{B}} + \alpha_2\mathbf{x}(\mathbf{\Omega}\cdot\overline{\mathbf{B}}) + \alpha_3\mathbf{\Omega}(\mathbf{x}\cdot\overline{\mathbf{B}}) \tag{2.27}$$

where we assume the effects of rotation and stratification are small and so retain only terms which are linear in $\mathbf{x}$ and linear in $\mathbf{\Omega}$. The final 2 terms on the RHS of (2.27) are non-isotropic and are

generally neglected in mean-field models. From (2.27) we see that we will obtain an α-effect of the form

$$\alpha = \alpha_o(r)\cos\theta.$$

as the first term on the RHS of (2.27) generates a turbulent diffusion term, which may be combined with the magnetic diffusion term in the induction equation.

The precise form of α is therefore variable and many studies have considered different forms for the radial variation. However, Steenbeck and Krause (1966) adopted the simplest case and took α independent of r. In order to facilitate comparisons between different models, many studies followed this choice, in particular Hollerbach and Jones' (1993b,1995) $\alpha\omega$-type model. The form of this α-effect however, does not naturally satisfy the boundary conditions at the inner core boundary, and so they neglect the effect of the α-effect here.

In the models we investigate, we follow Fearn and Rahman (2004a,b,c) and include a radial structure to this variation, taking the more realistic form $\alpha = \alpha_o \cos\theta \sin(\pi(r - r_i))$, so that this automatically satisfies the boundary conditions at the inner core.

In all the models we present here, as in Hollerbach and Jones (1993a,b,1995), the α-term is taken to be a tensor. In Chapters 3 and 4, we include only the component which acts to regenerate poloidal from toroidal field. However, in Chapters 5 and 6 we allow the α-term to act on all components of the magnetic field, thus not only generating poloidal from toroidal field, but additionally regenerating toroidal from poloidal field.

2.7 The Buoyancy Force, Θ.

In determining the specific form our parametrised buoyancy force, Θ, should take, we begin by considering the linear momentum equation in the inertialess and inviscid limit. This is,

$$2\mathbf{k} \times \mathbf{U} = -\nabla p + \Theta \mathbf{r} \tag{2.28}$$

If we then take the curl of this equation in order that we may eliminate the pressure term, we find

$$2\nabla \times (\mathbf{k} \times \mathbf{U}) = \nabla \times (\Theta \mathbf{r}) \tag{2.29}$$

which gives

$$2\frac{\partial U_\phi}{\partial z} \approx \frac{\partial \Theta}{\partial \theta} \tag{2.30}$$

where $\frac{\partial}{\partial z} = \cos\theta \frac{\partial}{\partial r} - \frac{\sin\theta}{r}\frac{\partial}{\partial \theta}$. This shows that the buoyancy term essentially drives a thermal wind. Therefore, this thermal wind then acts to regenerate toroidal field from poloidal field via the ω-effect. The specific form of the parametrised buoyancy force, Θ, is chosen so that we have a differential rotation of the form $\omega_\phi = \omega_o r$, which is independent of the colatitude θ. This therefore generates a thermal wind $U_\phi = \omega_o r^2 \sin\theta$, so that $\dfrac{\partial U_\phi}{\partial z} = \omega_o r \sin\theta\cos\theta$ and so we see that choosing $\Theta = -\Theta_o r\cos^2\theta$, will give this. Figure 2.1 shows the form of the prescribed flow at the onset of dynamo action for $\Theta_o = \pm 200$.

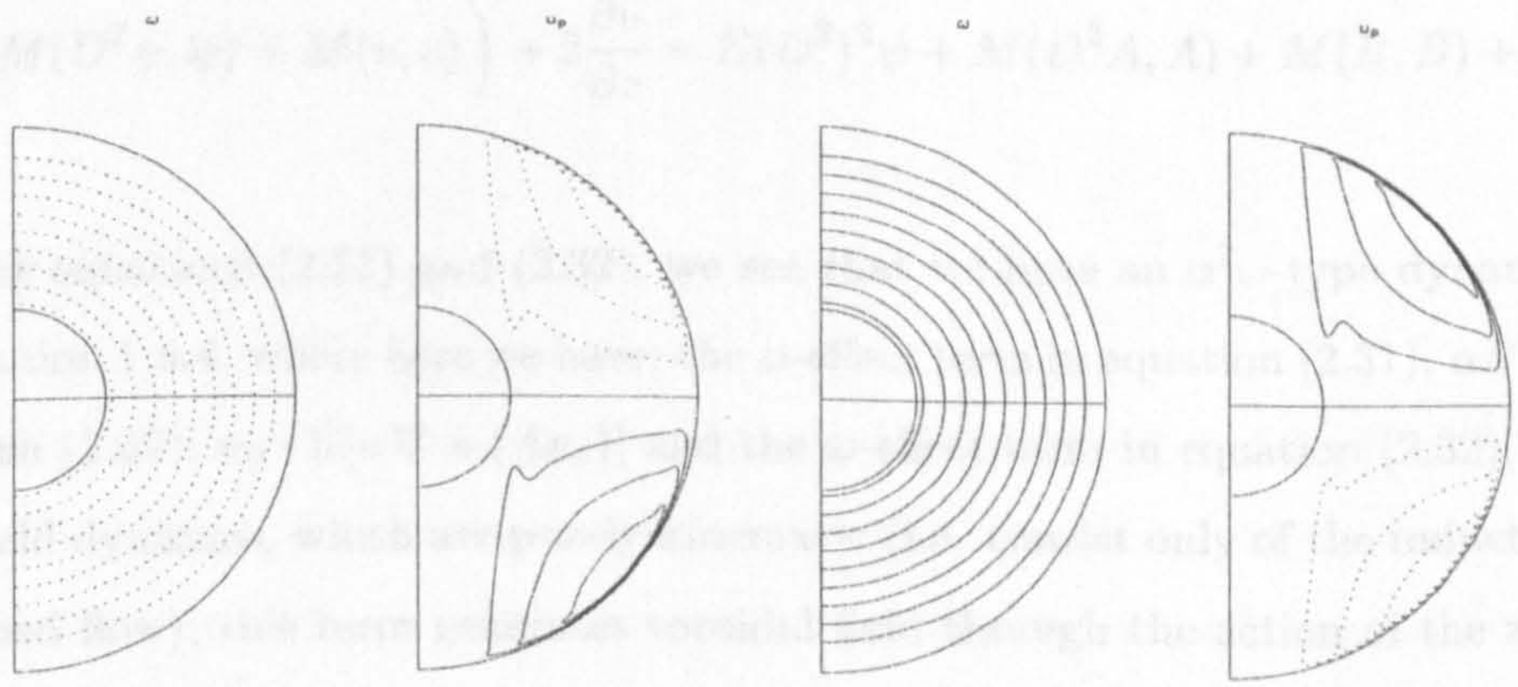

Figure 2.1: The above snapshots show the components of the velocity at onset. These contours do not change with time. From the left we have the following; the angular velocity, and meridional circulation contours for $\Theta_o = 200$, followed by the angular velocity and meridional circulation for $\Theta_o = -200$. The Ekman number, $E = 1\times10^{-4}$ in both cases. The angular velocity contour interval is 20, whilst the meridional circulation contour interval is 0.01. Here solid lines indicate positive contours and dashed lines represent negative contours.

This particular form of the buoyancy term has been used extensively in dynamo models (e.g. Hollerbach and Jones (1993b, 1995) and Hollerbach and Glatzmaier (1998)), but the influence of the specific form of this term has not been fully investigated. In later Chapters, we investigate the effects of changing the magnitude and direction of this term.

2.8 Our $\alpha^2\omega$-dynamo model.

Gathering together the decoupled governing equations from Section 2.4 we have

The Induction equation.

$$\frac{\partial A}{\partial t} = D^2 A + \alpha B + N(\psi, A) \tag{2.31}$$

$$\frac{\partial B}{\partial t} = D^2 B + \mathbf{e}_\phi \cdot \nabla[\alpha \nabla \times (A\mathbf{e}_\phi)] + M(v, A) - M(B, \psi) \tag{2.32}$$

The Momentum equation.

$$Ro\left(\frac{\partial v}{\partial t} - N(v, \psi)\right) - 2\frac{\partial \psi}{\partial z} = ED^2 v + N(B, A) \tag{2.33}$$

$$Ro\left(\frac{\partial D^2\psi}{\partial t} + M(D^2\psi, \psi) + M(v, v)\right) + 2\frac{\partial v}{\partial z} = E(D^2)^2\psi + M(D^2 A, A) + M(B, B) + \frac{\partial \Theta}{\partial \theta}. \tag{2.34}$$

From examining equations (2.31) and (2.32), we see that we have an $\alpha^2\omega$-type dynamo like those discussed in Section 1.6.4, where here we have; the α-effect term in equation (2.31), αB, the α-effect term in equation (2.32), $\mathbf{e}_\phi \cdot \nabla[\alpha \nabla \times (A\mathbf{e}_\phi)]$ and the ω-effect term in equation (2.32), $M(v, A)$. In simple mean field dynamos, which are purely kinematic (i.e. consist only of the induction equation with a prescribed flow), this term generates toroidal field through the action of the zonal flow on the poloidal field component. In our model, the induction equation is coupled to the momentum equation, and so the zonal flow, v is driven by the prescribed buoyancy force, Θ, as we see from equation (2.34). This method of generating a flow is more realistic. There are two natural limiting cases of this general $\alpha^2\omega$-type dynamo; the α^2-type dynamo and the $\alpha\omega$-type dynamo. The $\alpha\omega$-type dynamo arises when

$$M(v, A) \gg \mathbf{e}_\phi \cdot \nabla[\alpha \nabla \times (A\mathbf{e}_\phi)]$$

allowing the $\mathbf{e}_\phi \cdot \nabla[\alpha \nabla \times (A\mathbf{e}_\phi)]$ term in (2.32) to be neglected. This is the limit which we adopt in Chapters 3 and 4. The other extreme case is the α^2-type dynamo, and this arises when

$$M(v, A) \ll \mathbf{e}_\phi \cdot \nabla[\alpha \nabla \times (A\mathbf{e}_\phi)]$$

allowing us to neglect the $M(v, A)$ term. This model is investigated by Fearn and Rahman (2004a,b,c).

The term "strong field" dynamos is sometimes used to describe $\alpha\omega$ dynamos, since the toroidal component of the field is greater than the poloidal component. In α^2 dynamos this is not the case, with the poloidal field comparable with the toroidal component of the field and so these are named "weak field" dynamos. In the Earth, only the poloidal component of the field may be inferred from outside observations, but it is believed that the total field strength greatly exceeds the magnitude of the poloidal component and so it it believed that the Earth's dynamo is of the $\alpha\omega$ type.

2.8.1 Equilibration of α^2 versus $\alpha\omega$ dynamos.

The problems of the α^2-type dynamo and $\alpha\omega$-type dynamo models are quite different. Let us consider the governing equations as presented in (2.4) and (2.5). We have

$$\frac{\partial \mathbf{B}}{\partial t} = \nabla^2\mathbf{B} + \nabla \times (\alpha\mathbf{B}) + \nabla \times (\mathbf{U} \times \mathbf{B}) \tag{2.35}$$

$$Ro\left(\frac{\partial \mathbf{U}}{\partial t} + (\mathbf{U}\cdot\nabla)\mathbf{U}\right) + 2\mathbf{k} \times \mathbf{U} = -\nabla p + E\nabla^2\mathbf{U} + (\nabla \times \mathbf{B}) \times \mathbf{B} + \Theta\mathbf{r} \tag{2.36}$$

There are therefore 4 dimensionless parameters in our model; Ro and E which arose from the non-dimensionalisation of the equations in Section 2.2, and α_o and Θ_o which have arisen from our parametrisation of our α and ω-effects introduced in Sections 2.6 and 2.7, respectively.

The α^2-type model.

At the onset of dynamo action, the problem reduces to simply solving the induction equation, (2.35), in the absence of a flow, $\mathbf{U}$. The remaining equation is then a linear eigenvalue problem which may then be solved for the eigenvalue, α_c. Beyond onset as α_o is increased, the α-effect is then able to act on all components of the magnetic field through the induction equation, resulting in an increase in $\mathbf{B}$. In the absence of inertia (and of course buoyancy), the increase in magnetic field, $\mathbf{B}$ feeds into the momentum equation via the Lorentz force. The now stronger Lorentz force then acts to drive a flow in the momentum equation, which is damped by effect of viscosity. The flow generated through the balance in the momentum equation then feeds back into the induction equation via the advection term, which acts to equilibrate the dynamo.

The $\alpha\omega$-type model.

At onset, the $\alpha\omega$-type model is a quite different problem to the α^2-type model, as, from the outset, we have a flow appearing in the induction equation, generated by the prescribed buoyancy force $\Theta\mathbf{r}$ in (2.36). It is also different with the α-effect restricted to act only on the toroidal component of the field. The onset of dynamo action then occurs when the strength of the α-effect is large enough, with the flow driven by the buoyancy force feeding into the advection term in the induction equation. Beyond onset, as α_o is increased (at fixed Θ_o), the strength of the magnetic field is increased, which then feeds into the Lorentz force term appearing in the momentum equation. As in the α^2-type model, the Lorentz force drives a flow in the momentum equation, but now that we have a prescribed buoyancy force in the equation, this also acts to drive a flow in the momentum equation. As we discussed in Section 2.7, the form of the buoyancy force is chosen so that it primarily drives a zonal flow, $U_\phi = \Theta_o r^2 \sin\theta$. Therefore, the zonal flow generated through the buoyancy force competes with zonal flow driven by the Lorentz force. In the absence of inertia, the damping in the system arises through the viscous term in the momentum equation. The generated flow then feeds back into the induction equation via the advection term, acting to equilibrated the dynamo.

Including Inertial effects.

Including the full inertia term in the momentum equation modifies the balance of the momentum equation in both models. Inertia when strong enough, replaces the role of viscosity at leading order in the momentum equation balance, which as we will see in later chapters modifies the behaviour of the solutions as the strength of inertia is increased.

2.9 The Linear Dynamo number, $\mathcal{D}$.

In Section 1.6.4 we described the linear kinematic $\alpha^2\omega$ dynamo models. In this Section we are specifically interested in the $\alpha\omega$ limit of this general case. From the analysis of such models, a key parameter was identified as the product of the magnitudes of the α and ω-effects; $\mathcal{D} = \alpha_o\omega_o$. For our model, where an ω-effect is generated through the prescribed buoyancy force, we see that from Section 2.7, $\omega_o \equiv \Theta_o$. This parameter, $\mathcal{D}$, is called the dynamo number, see for example Roberts

(1972).

In this section, we examine the governing equations for the $\alpha\omega$-type dynamo and explore the balance of these equations at the onset of dynamo action, when the magnetic field is small, and investigate whether the equations scale with the dynamo number.

2.9.1 A linear kinematic $\alpha\omega$ dynamo model.

As discussed in Section 1.6.4, a typical kinematic model consisted of prescribing the flow $\mathbf{U}$ and then solving the (now linear) induction equation for $\mathbf{B}$. Therefore, such a model would be of the form,

$$\frac{\partial A}{\partial t} = D^2 A + \alpha B \tag{2.37}$$

$$\frac{\partial B}{\partial t} = D^2 B + M(v, A) \tag{2.38}$$

where we prescribe the α and ω-effects generally as

$$\alpha = \alpha_o f(r, \theta) \text{ and } \omega = \Theta_o g(r, \theta)$$

where f and g are prescribable functions of r and θ and $v = r\omega$.

Now, from equations (2.37) and (2.38) above, it can be shown that the equations scale with $\mathcal{D} = \alpha_o \Theta_o$. Linear systems may be characterised simply by the dynamo number $\mathcal{D}$, with the individual values of α_o and Θ_o being unimportant, (see for example, Roberts 1972). However once non-linearities are included in the system, it turns out that this is no longer the case, and that both α_o and Θ_o, must be specified independently.

2.9.2 Our non-linear $\alpha\omega$ models.

Now let us consider our non-linear system of equations. From Section 2.8, our modelling equations in the $\alpha\omega$ limit are

$$\frac{\partial A}{\partial t} = D^2 A + \alpha B + N(\psi, A) \tag{2.39}$$

$$\frac{\partial B}{\partial t} = D^2 B + M(v, A) - M(B, \psi) \tag{2.40}$$

$$Ro\left(\frac{\partial v}{\partial t} - N(v,\psi)\right) - 2\frac{\partial \psi}{\partial z} = ED^2 v + N(B,A) \tag{2.41}$$

$$Ro\left(\frac{\partial D^2\psi}{\partial t} + M(D^2\psi,\psi) + M(v,v)\right) + 2\frac{\partial v}{\partial z} = E(D^2)^2\psi + M(D^2A,A) + M(B,B) + \frac{\partial \Theta}{\partial \theta} \tag{2.42}$$

Through examining the above system of equations, we can see that the non-linear modelling equations do not scale with $\mathcal{D}$. However, $\mathcal{D}$ could still prove to be a useful parameter.

The inertialess case.

Considering the case in the absence of inertia first. At the onset of dynamo action the magnetic field will be small, and so we may neglect the Lorentz force components in (2.42) and (2.41). Examining the reduced equations,

$$\frac{\partial A}{\partial t} = D^2 A + \alpha B + N(\psi, A) \tag{2.43}$$

$$\frac{\partial B}{\partial t} = D^2 B + M(v, A) - M(B, \psi) \tag{2.44}$$

$$2\frac{\partial \psi}{\partial z} = -ED^2 v \tag{2.45}$$

$$2\frac{\partial v}{\partial z} = E(D^2)^2\psi + \frac{\partial \Theta}{\partial \theta} \tag{2.46}$$

we see that the system of equations does still not scale with $\mathcal{D}$, with the difficulty lying between the scaling of the flow coefficients v and ψ. Now, in the Earth, the Ekman number is estimated to be $O(10^{-15})$. Therefore in the limit of $E \to 0$, $\frac{\partial \psi}{\partial z} \to 0$ and this difficulty is removed. Equation (2.46) then reduces to

$$2\frac{\partial v}{\partial z} \simeq \frac{\partial \Theta}{\partial \theta}$$

which allows the equations to then scale with $\mathcal{D}$.

Now in order that our system of equations scales with the dynamo number, we have effectively eliminated the terms associated with the meridional circulation in the flow through adopting the inviscid limit. Therefore, the smaller the value of E we are able to use, the more able the equations are to scale with $\mathcal{D}$. The magnitude of E therefore determines the extent to which the meridional

circulation is present in the system.

For solutions beyond onset, the Lorentz force is no longer negligible; in these cases the non-linearity causes the system not to scale exactly with $\mathcal{D}$.

Including inertial effects.

Through examining equations (2.39)-(2.42) we see that the non-linearity in the inertial terms further complicates the equations and makes an exact scaling with $\mathcal{D}$ impossible, even if we neglect terms in ψ, which will be small at onset.

Since we have shown that even at onset, our $\alpha\omega$-type dynamo model (with and without the effects of inertia) does not scale exactly with $\mathcal{D}$, due to the effects of meridional circulation in the system, it will be necessary to state both α_o and Θ_o separately, as this analysis shows that a single parameter ($\mathcal{D}$) is not sufficient. However, the dynamo number still remains a useful parameter in the analysis of $\alpha\omega$-type dynamos, as is shown in Chapters 3 and 4.

2.10 Energy Calculations.

The magnetic energy that we calculate is

$$\widetilde{E}_m = \frac{1}{2\mu_o}\int_V |\widetilde{\mathbf{B}}|^2 dV \tag{2.47}$$

$$= [\rho_o \Omega \eta \mathcal{L}^3]\frac{1}{2}\int_V |\mathbf{B}|^2 dV \tag{2.48}$$

$$= [\rho_o \Omega \eta \mathcal{L}^3] E_m \tag{2.49}$$

where V is the volume of the inner and outer cores, and $\widetilde{\mathbf{B}}$ is the dimensional magnetic field.

The kinetic energy that we calculate in the models which include inertia is

$$\widetilde{E}_k = \frac{\rho_o}{2}\int_{V_o} |\widetilde{\mathbf{U}}|^2 dV \tag{2.50}$$

$$= [\rho_o \Omega \eta \mathcal{L}^3]\frac{1}{2} Ro \int_{V_o} |\mathbf{U}|^2 dV \tag{2.51}$$

$$= [\rho_o \Omega \eta \mathcal{L}^3] E_k \tag{2.52}$$

where V_o is the volume of the outer core and $\widetilde{\mathbf{U}}$ is the dimensional fluid velocity.

The non-dimensionalisation reveals that the scaling of the magnetic and kinetic energies is the same, with the constant factor $[\rho_o \Omega \eta \mathcal{L}^3]$ appearing in both cases, thus these energies are comparable. As the system is timestepped forward using the numerical scheme described in Appendix B, the magnetic and kinetic energies are calculated from the spectral coefficients as required. This therefore allows us to follow the behaviour of the magnetic and kinetic energies as they evolve with time and provides us with a means of determining the equilibration of the system. We use the variation of the magnetic and kinetic energies with time, instead of the variation of a single spectral coefficient, as energy of the system is a global quantity and a more reliable means of determining the stability of the system.

2.11 Summary of Model Differences.

In this Chapter, I have tried to indicate where differences arise in the models due to the effect of inertia; which is present in Chapters 4 and 6 or through the dynamo mechanism, be it an $\alpha\omega$-type model or an $\alpha^2\omega$-type model.

The dynamo mechanism is generated via an $\alpha\omega$-type dynamo in Chapters 3 and 4 and an $\alpha^2\omega$-type dynamo in Chapters 5 and 6. In the $\alpha^2\omega$-type dynamos the α-effect is allowed to act on all components of the field, as opposed to just the ϕ component in the $\alpha\omega$-type model.

The differences in the models due to the effect of inertia, apply throughout the model and is not such a minor alteration to the numerical code, as switching from $\alpha\omega$ to $\alpha^2\omega$-type dynamos. A separate 'inertia' code is used, based on the original 'inertialess' code, but which now additionally requires the flow coefficients to be timestepped forward in time as well as the field coefficients. For further details on both of these codes, see Appendix B. The other difference due to the consideration of inertia in the problem, is the torque balance on the inner core boundary and the way in which the inner core rotation rate is determined. Details of this balance were given in Section 2.5.2.

Chapter 3

$\alpha\omega$-dynamos without inertia.

3.1 Introduction.

In this chapter, we consider the $\alpha\omega$-type dynamo model described in Chapter 2. The results found using this model provide us with a reference case, which will prove useful in the subsequent chapters. In addition, this model also allows us to compare our findings with earlier $\alpha\omega$ models, and in particular the results of Hollerbach and Glatzmaier (1998). The Hollerbach and Glatzmaier paper, whose results are summarised in the Section 3.2, use an α-effect of the form $\alpha = \alpha_o \cos\theta$. This form for the α-effect was chosen in order to facilitate comparisons with other models. However using this form for α leads to difficulties with the boundary conditions at the inner core boundary, as discussed in Section 2.6. Therefore in our models, we consider a more realistic form for the prescribed α-effect, and include a radial dependence that naturally satisfies the boundary conditions; $\alpha = \alpha_o \cos\theta \sin(\pi(r - r_i))$.

In parallel studies to these $\alpha\omega$-type models, Hollerbach and Jones (1993a) considered an α^2-type model (see Section 1.6.4 for a discussion on mean-field dynamo models, the differences between $\alpha\omega$ and α^2 models and their respective merits). In Hollerbach and Jones' model, they adopted the simpler form of $\alpha = \alpha_o \cos\theta$ which yielded only steady solutions. Hollerbach and Ierley (1991) considered a modal α^2 model in a spherical shell and adopted an α-effect of the form $\alpha = \alpha_o \cos\theta f(r)$. Through varying $f(r)$ they found that some choices of α yielded steady solutions whilst others produced time dependent solutions. Fearn and Rahman (2004a) extended Hollerbach and Jones

(1993a) model and considered the more realistic form $\alpha = \alpha_o \cos\theta \sin(\pi(r - r_i))$. They found an unusual spiky periodic behaviour, similar to that found by Hollerbach and Ierley, developed just beyond the onset of dynamo action arising from the radial dependence in α. The differences in the behavior caused by the introduction of a realistic radial dependent α-effect suggested that applying this form for α in our $\alpha\omega$-type model could provide us with some interesting results. In adopting this form for the α-effect, we enable direct comparisons with their model, which will prove especially constructive in later chapters.

In Section 3.3, we investigate the variation of the onset of dynamo action with the Ekman number. In Section 3.4, we examine the onset of dynamo action and its dependence on the individual parameters α_o and Θ_o. In Sections 3.5 and 3.6, we investigate the evolution of the solutions with an increase in the forcing. Finally in Section 3.9 we compare our findings with other $\alpha\omega$ models and comment on the similarities and differences. We conclude this chapter in Section 3.10, by summarising the main findings of our study of this $\alpha\omega$-type model.

3.2 Background.

In this section we review the main results of $\alpha\omega$ dynamos, with which we will compare our results in later sections.

Roberts (1972) investigated the steadying effect of a meridional circulation applied to a linear kinematic dynamo model solved in a conducting sphere. Before tackling the effects of meridional circulation, he considered linear $\alpha\omega$ dynamos, establishing some general characteristics about these models. These studies then also provide a basis for the later investigations involving the meridional circulation.

In his studies of $\alpha\omega$ dynamos, he begins by examining Steenbeck and Krause's (1966) model which solves the induction equation

$$\Omega\mathbf{B} = R\nabla \times (\mathbf{U} \times \mathbf{B} + \alpha\mathbf{B}) + \nabla^2\mathbf{B}$$

in a sphere of radius 1. R is the magnetic Reynolds number, which we introduced in Section 1.2

and since he seeks normal mode solutions, the time derivative in (1.3) is replaced by Ω which is the (complex) growth rate of the solutions. The α and ω-effects are prescribed as

$$\alpha = \alpha_o \cos\theta \text{ and } \omega = \omega_o' r.$$

Despite the non-analytic nature of the α-effect at the centre of the sphere, this choice enabled a comparison with Steenbeck and Krause (1966). Roberts also considers an additional two $\alpha\omega$ models which adopt different forms for the prescribed α and ω-effects. These are,

$$\text{model 2:} \quad \alpha = \frac{729}{16}\alpha_o r^8(1-r^2)^2\cos\theta \ , \ \omega = -\frac{19683}{40960}\omega_o'(1-r^2)^5$$

$$\text{model 3:} \quad \alpha = 24\sqrt{3}\alpha_o r^2(1-r)^2\cos\theta\sin^2\theta \ , \ \omega = -\frac{3\sqrt{3}}{8}\omega_o'(1-r^2)^2$$

Roberts chose α and ω such that α and ω' (where $\omega' = d\omega/dr$) had maximum values α_o and ω_o' respectively, within the sphere of radius 1. The second model here was chosen to address the question raised by Steenbeck and Krause (1966, 1969) that suggested that $\alpha\omega$ dynamos function most efficiently when the regions of greatest shear were separated from the those of the maximum α-effect. Using this model, Roberts found that there was no evidence of the dynamo being easier to excite, however investigating this dynamo model in a spherical shell, his findings lend support to this issue of region separation.

The common characteristics of these models were that $\alpha\omega$ models are generally periodic dynamos. At the onset of dynamo action when $\alpha\omega' > 0$, the solution has quadrupole parity and the dynamo wave solutions generated drift from the equator towards the poles. For $\alpha\omega' < 0$, solutions are dipolar in nature, with the dynamo wave solutions propagating from the poles towards the equator.

Roberts then considers the effect of prescribed meridional circulation on the $\alpha\omega$ dynamos, controlling the strength of this effect through a parameter m which is varied between ± 1. Roberts considered 4 different models, as well as a model considered by Braginsky (1964b) as a check on his results. Typically solutions were found to be steady provided $|m|$ is sufficiently large and he noted that the most easily excited solutions for $\alpha\omega' > 0$ had dipole parity. For $\alpha\omega' < 0$ the most easily excited solutions had quadrupole parity – this is opposite parity to the $\alpha\omega$ dynamos which were found for the case without the inclusion of meridional circulation. The variation in the behaviour

of the models with m, depended on the model. In the Braginsky model and model 1, which we consider in more detail in Section 3.9.1, dynamo action is greatly facilitated for m negative in the $\alpha\omega' > 0$ case but inhibited for m positive. For the $\alpha\omega' < 0$ case, the areas in which dynamo action is assisted or impeded are switched around, with m positive facilitating dynamo action, and m negative impeding it. In model 1 at small values of m, in the $\alpha\omega' > 0$ case, oscillatory quadrupole solutions are more easily excited than the unsteady dipole solutions as shown in Figure 3.26. This situation is reversed in the $\alpha\omega' < 0$ case which is shown in Figure 3.27. In model 2 the values of m for which these most favourable solutions are obtained is opposite that of the models discussed above. In models 3 and 4, the solutions obtained are quite different from the other models considered. In these cases, ω is now a function of r and θ (instead of simply r as in the early models). This leads to slightly different behaviour. In model 3, he finds that in the case of $\alpha\omega' > 0$, dipole solutions are most easily excited as before and dynamo action is assisted for $m > 0$, with no solutions obtained for $m < 0$. In the case of $\alpha\omega' < 0$, he finds quadrupole solutions excited first, with dynamo action assisted for $m < 0$. For model 4, he finds that in both cases dipole solutions are obtained and $m > 0$ assists the solutions in both cases, no solutions being found for $m < 0$ in the $\alpha\omega' > 0$, similar to model 3.

In the $\alpha\omega$-type dynamo papers of Hollerbach and Jones (1993b, 1995), they focussed on the role the finitely conducting inner core has on the dynamics of the system. They follow the bifurcation pattern of the system as α_o is increased having imposed a strong differential rotation ($\Theta_o = 200$) on the system. For their dipole-imposed-symmetry solutions, onset occurs for $\alpha_o = \alpha_c \sim 8$, as dynamo waves which propagate with a zero time-average from the equator to the poles. The system undergoes a bifurcation at $\alpha_o \sim 12$ to dynamo waves with a non-zero time-average. Solutions at low values of $\alpha_o (> \alpha_c)$ produce the same bifurcation results as previous results found for a model which had no inner core. When the system is highly supercritical, they find that the core forms two dynamically distinct regions: inside and outside the tangent cylinder – a pattern which is supported by observational evidence. They find that inside the tangent cylinder, the long diffusion time of the inner core causes the poloidal field to remain fairly constant, as there is no mechanism here for generating toroidal field. The dynamically active region appears outside the tangent cylinder where dynamo action is achieved through the interaction of the large zonal flow with the poloidal

field to generate toroidal field, which in turn generates poloidal field through the imposed α-effect. This process is shown to be particularly inefficient however, as the contours are so closely aligned. Between these two papers, they reduce the Ekman number down from a value of 1×10^{-3} to 5×10^{-4} and find very little difference in the solutions between the two values for E.

In the Hollerbach and Glatzmaier (1998) paper, they solve this same system of equations allowing for both dipole and quadrupole parity solutions. They find at onset ($\alpha_c \sim 6$) that dynamo wave solutions are produced and have quadrupole parity, with a zero time-average. The solutions bifurcate at $\alpha_o \sim 11$ to mixed parity solutions with a non-zero time-average. These solutions also exhibit a form of symmetry; they find that the solutions have a half period dipole symmetry; meaning that solutions which are half a period apart, have the same equatorial symmetry that a purely dipolar solution would have without the half-period shift in time. Around $\alpha_o \sim 30$ the solutions undergo a bifurcation to mixed parity steady solutions. From their subsequent analysis, it is clear that very different behaviour is obtained when the system is not restricted to a particular parity and they note that despite the considerable extra computational expense incurred, it is safest not to restrict attention to pure-parity models.

3.3 The onset of Dynamo action and the Ekman number.

We began by finding the value of α_o for the onset of dynamo action at varying values of the Ekman number, and for fixed Θ_o ($= 200$). The graph in Figure 3.1 shows a plot of the critical α_o, α_c against the log of the Ekman number.

At the onset of dynamo action, the main balance of the momentum equation lies between the Coriolis force and the buoyancy force, with viscous effects only significant in boundary layers close to the inner core and core-mantle boundaries. We anticipate that as the Ekman number is decreased towards zero, (and as we see in the simulations), the thickness of these boundary layers decreases and resolution of these narrow boundary layers becomes more difficult. Figure 3.1 shows, as the Ekman number is decreased, the value of α_c also decreases until $E \sim 2 \times 10^{-5}$ where the graph appears to begin levelling off. This behaviour is in fact what we might expect, since as E is decreased, the thickness of the viscous boundary layers decreases (as we see in Section 2.7, so

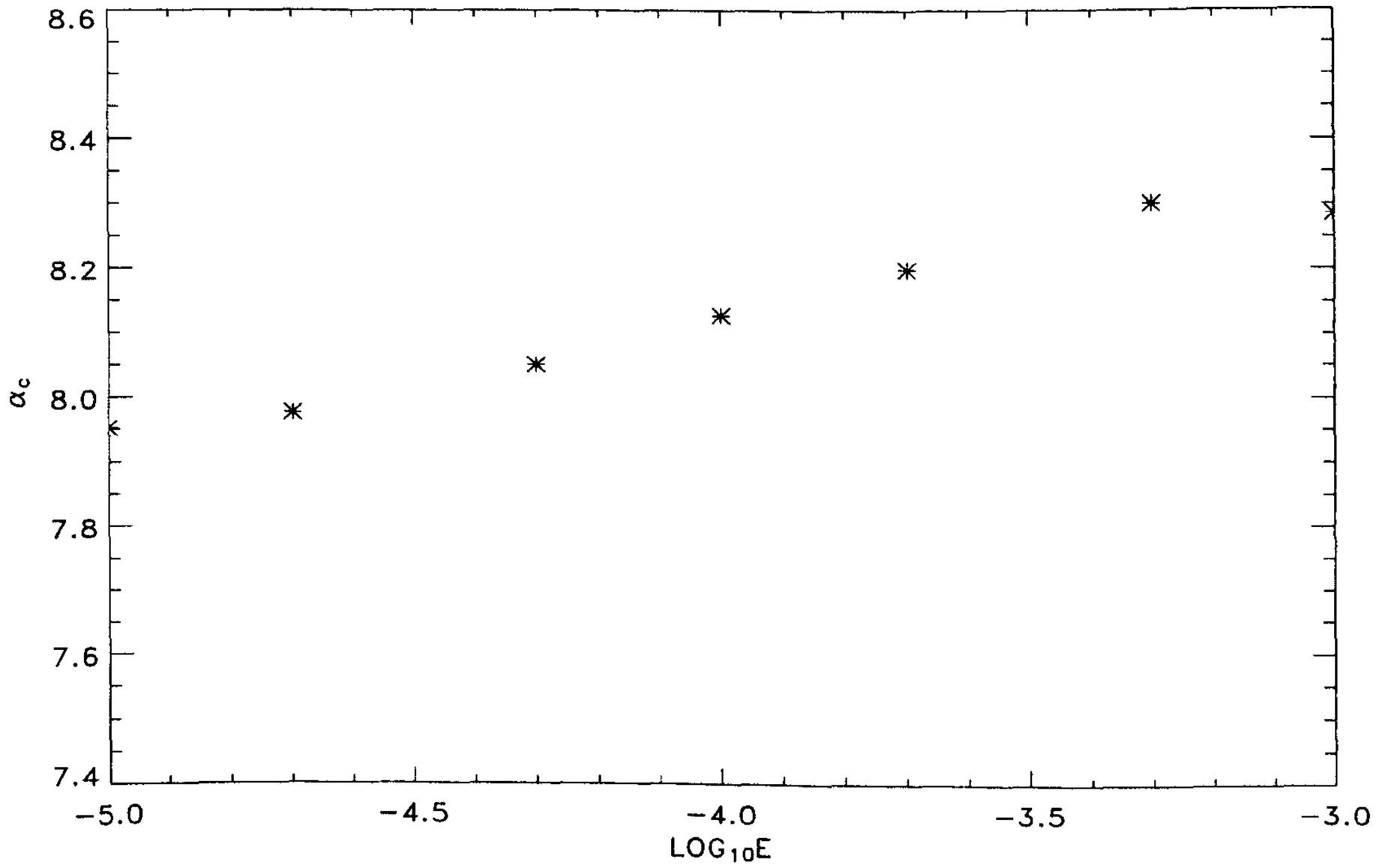

Figure 3.1: The variation of α_c with Ekman number for $\alpha = \alpha_o \cos\theta \sin(\pi(r - r_i))$ and $\Theta_o = 200$.

that successive plots of the angular velocity appear more and more like the inviscid limit solution; $U_\phi \sim \Theta_o r^2 \sin\theta$). We see that as E decreases towards zero, the results are consistent with α_c approaching a constant (non-zero) value.

For all further simulations in this chapter we choose $E = 10^{-4}$, as this is the limit of computational capabilities for moderate truncation of the solutions.

3.4 Dependence on α_o and Θ_o.

As we showed in our discussion in Section 2.9, our system of equations do not scale exactly with the dynamo number, $\mathcal{D}$. In this section we aim to investigate the extent to which this remains a reasonable measure of the system, and the validity of simply considering the product of our two forcing terms, α_o and Θ_o.

We begin by considering the onset of dynamo action, as this is when the system will be linear. We showed that due to the presence of meridional circulation in the system at onset, the equations

do not scale with the dynamo number $\mathcal{D}$. However as a test of the extent to which the equations scale with $\mathcal{D}$, or perhaps more accurately the extent to which the meridional circulation is playing a role in the equilibration of the dynamo at onset, we considered 4 different values of Θ_o and found the corresponding value of α_c. In Table 3.1, we show the values of α_c found for each Θ_o respectively. For each pair their product, $\mathcal{D}_c = \alpha_c \Theta_o$, is calculated.

Examining the data in Table 3.1 we find that the values of $\mathcal{D}_c$ we obtain are similar. Another important aspect of $\alpha\omega$ dynamos, is that the cases of positive and negative $\mathcal{D}$ are different, and we see that this is apparent even at onset. Therefore treating the cases of $\mathcal{D} > 0$ and $\mathcal{D} < 0$ separately, we see that we have good agreement between the values of $\mathcal{D}_c$. This implies that the equations are close to scaling with $\mathcal{D}_c$ and so the effect of meridional circulation in the equilibration of the dynamo at onset is small. This fact is further illustrated by the plot of this set of data in Figure 3.2 where we show α_c versus Θ_o.

α_c	Θ_o	$\mathcal{D}_c$
8.12	+200	1624
16.4	+100	1640
15.2	−100	−1520
7.57	−200	−1514

Table 3.1: The data set for Figure 3.2. This shows the value of α_c to 3 significant figures, and the corresponding value of $\mathcal{D}_c$.

Examining Figure 3.2, we see the negative Θ_o solutions produced onset values consistently lower than their positive Θ_o counterparts. These solutions in fact turned out to have dipole parity, with the positive Θ_o solutions having quadrupole parity. Both types of solution were oscillatory with a period of ~ 0.24. This aspect of parity selection for $\alpha\omega$ dynamos was also found by Roberts (1972) in his consideration of linear $\alpha\omega$ dynamos. Another interesting aspect which arises from this data set in Table 3.1 which is worth noting, is the suggestion that the onset of dynamo action occurs at a lower value of $|\mathcal{D}_c|$ for larger values $|\Theta_o|$.

We then investigated, for each of these values of Θ_o, the variation in the solutions as α_o is increased beyond critical. Figure 3.3 shows the variation of the magnetic energy with the dynamo

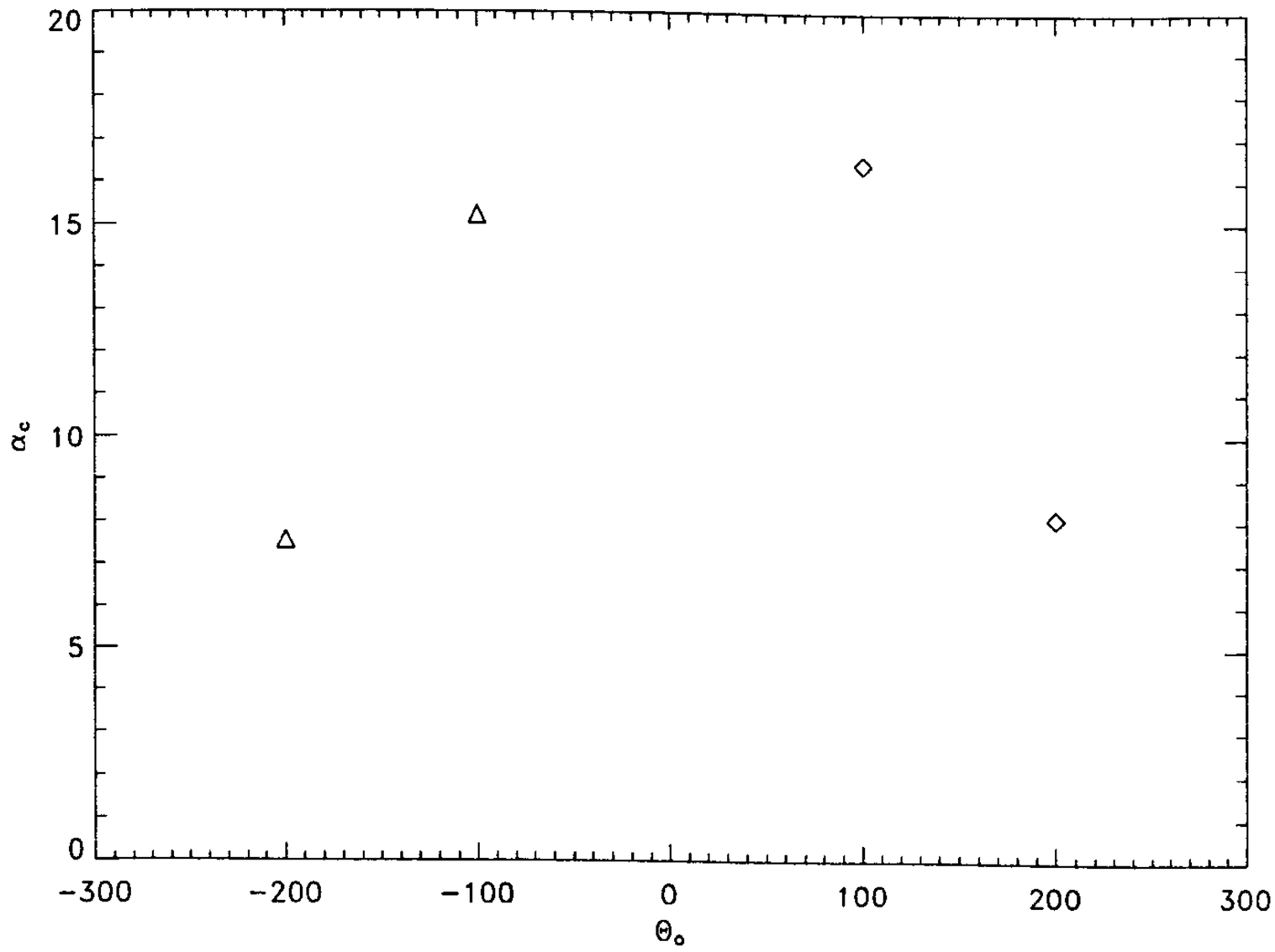

Figure 3.2: Here we show the value of α_c for each Θ_o considered. Δ's denote dipole parity solutions and $\diamond$'s denote quadrupole parity solutions.

number. Whilst we have shown that the dynamo number is not specifically a key parameter in this model, using $|\mathcal{D}|$ as our scale on the x-axis proves useful as it allows us to easily compare the solutions at different values of Θ_o and therefore obtain some global information about the system.

As $|\mathcal{D}|$ is increased (through fixing Θ_o and increasing the strength of α_o) beyond onset, we see that for $\mathcal{D}$=2500, the dependence on the sign of Θ_o (and so $\mathcal{D}$) becomes evident. For $\mathcal{D} > 0$ the magnetic energy changes rapidly with the gradient of the curve quickly steepening as $|\mathcal{D}|$ is increased. For $\mathcal{D} < 0$ the magnetic energy changes much more slowly, allowing $|\mathcal{D}|$ to be increased all the way up to 10000. For the $\mathcal{D} > 0$ solutions, it became too difficult to increase $|\mathcal{D}|$ beyond 4400, as the magnetic energy of the solutions between consecutive values of α_o, for a fixed Θ_o, changed so steeply. However the shape of the curve remains clear, and the difference between $\mathcal{D} > 0$ and $\mathcal{D} < 0$ is obvious. Since we generate these two cases, by changing the sign of Θ, we explore the effect of the buoyancy force further in Section 3.8, where we aim to try and understand the mechanisms at work to produce these differences and the actual physical interpretation of the prescribed buoyancy force.

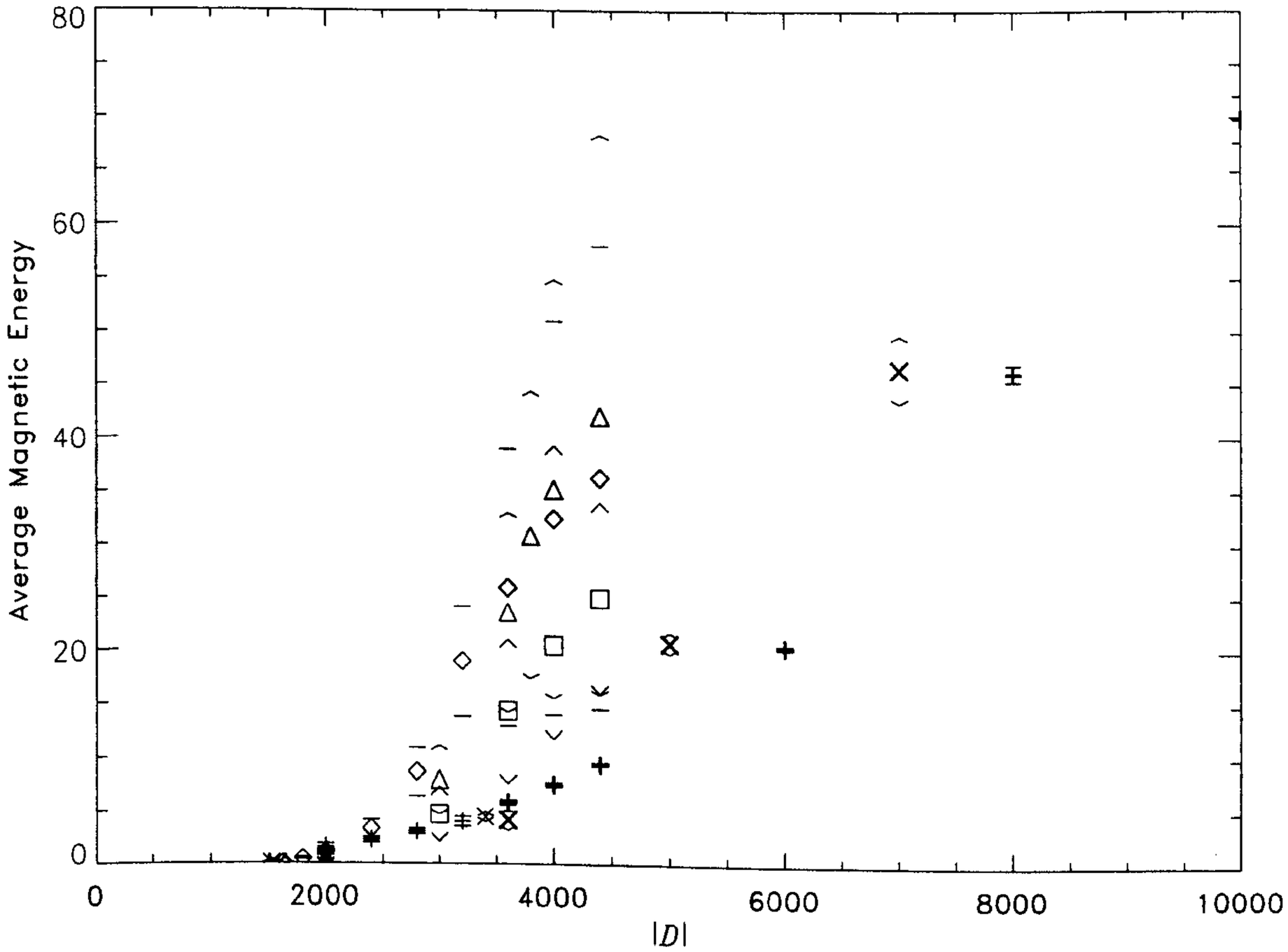

Figure 3.3: The following show the values of the average magnetic energy at the respective values of Θ_o.+ : $\Theta_o = -200$, × : $\Theta_o = -100$, □ : $\Theta_o = 50$, △ : $\Theta_o = 100$, ◇ : $\Theta_o = 200$. The error bars indicate the maximum and minimum amplitudes of the magnetic energy. The symbols in bold show the solutions which have undergone bifurcations to different behaviour.

From Figure 3.3, we also note that the solutions all undergo bifurcations to different behaviour (exact details are given later). These bifurcations see a difference in the time evolution of the magnetic energy for $\Theta_o > 0$ solutions, and for $\Theta_o < 0$, the bifurcation results in the solutions changing from dipole parity to becoming mixed. These are the solutions shown in bold in Figure 3.3 and it is evident that these occur around the same value of $|\mathcal{D}|$ for the solutions at $\Theta_o = 200, -200, -100$. We notice that the solutions at $\Theta_o = 100$ bifurcate slightly later and for $\Theta_o = 50$ we find the solutions for as far as we considered them, have yet to bifurcate. Examining Figure 3.3 suggests that there may exist a threshold energy which solutions must reach before the nature of the solutions change. This however shows that the system can not be characterised by a single parameter; both α_o and Θ_o must be specified. The exact nature of the solutions and how they evolve with increasing $|\mathcal{D}|$ is described in more detail in Sections 3.5 and 3.6 for $\mathcal{D} > 0$ and $\mathcal{D} < 0$,

respectively.

3.5 Solutions for $\Theta_o > 0$.

For $\Theta_o = 200$, we investigated the bifurcations of the solutions as α_o is gradually increased from its onset value of $\alpha_c = 8.12$ up to $\alpha_o = 30$. For $\alpha_c \leq \alpha_o \leq 16$, the solutions have a quadrupole parity and vascillate sinusoidally in time with a period, $T \simeq 0.24$. The variation with time over one cycle of the magnetic energy is shown in Figures 3.5 and 3.6(a) for $\alpha_o = \alpha_c = 8.12$ and $\alpha_o = 14$, respectively, where we see that the length of a cycle has remained approximately constant, decreasing only slightly as α_o is increased. The variation of the field and flow may be examined by following the snapshots of the solution over a cycle of the magnetic energy. These are shown in Figure 3.7 for $\alpha_o = \alpha_c = 8.12$ and Figure 3.8 for $\alpha_o = 14$. Examining the contour plots reveals that the solutions are reversing and complete half a period over one cycle of the magnetic energy. Comparing Figures 3.7 and 3.8 we see that the evolution of magnetic field contours with time is very much the same despite the differences in the strength of the field. The flow contours vary slightly differently. The contours of the flow at the onset of dynamo action (shown in Figure 2.1) do not change with time, however once the solution is beyond onset as shown in Figure 3.8 for $\alpha_o = 14$, we see that the flow contours also evolve with time.

As α_o is increased to 18, we find a bifurcation in the behaviour of the solution. The time evolution of the magnetic energy is no longer sinusoidal and has instead developed a variation which exhibits an alternating peak/trough height. This is shown more clearly in Figure 3.6(b). As before, we plot snapshots of the solution over a cycle of the magnetic energy and these are shown in Figure 3.9. These solutions reveal that the quadrupole nature of the solutions has been maintained and has reversing features similar to those found in Figure 3.8. We find that following the evolution of solutions over a cycle of its magnetic energy, results in the solutions completing a period of its variation. In this way the evolution is slightly different to the solutions found prior to the bifurcation which had only completed half a period over a cycle of magnetic energy. As α_o is further increased, the solutions parity remains quadrupolar and the magnetic energy variation remains qualitatively the same. The only observed difference is a decrease in the period of the solutions as α_o is increased.

As discussed in Section 3.4, we found that the critical dynamo numbers were fairly similar, so we wondered if the bifurcation from sinusoidal behaviour to the periodic alternating peak height solution, would also occur around the same value of $\mathcal{D}$. For $\Theta_o = 100$ and 50 we looked to see if there is the same bifurcation pattern as found for $\Theta_o = 200$.

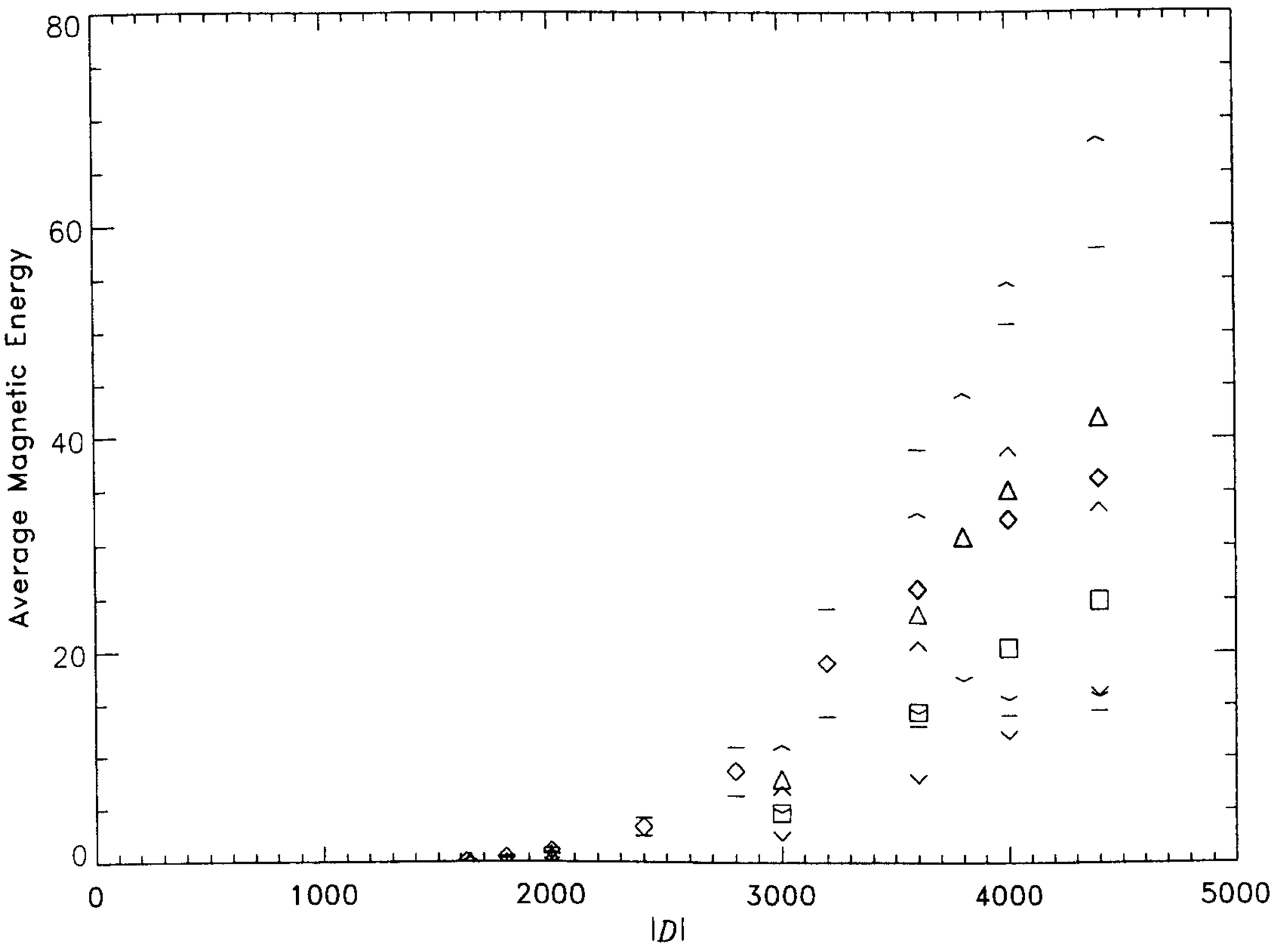

Figure 3.4: As Figure 3.3, but for $\Theta_o > 0$ only. $\Box : \Theta_o = 50$, $\triangle : \Theta_o = 100$, $\Diamond : \Theta_o = 200$.

The bifurcation for $\Theta_o = 200$, occurred at $\alpha_o \simeq 18$, which gives a dynamo number of $\mathcal{D} = 3600$. If the bifurcation for $\Theta_o = 100$ were to occur at the same value of $\mathcal{D}$, then this suggests that the bifurcation should occur around $\alpha_o = 36$. Following the $\Theta_o = 100$ branch of solutions as we increase α_o from its onset value of $\alpha_c = 16.4$, we initially find the solutions exhibit similar behaviour to that found when $\Theta_o = 200$, with solutions produced which are quadrupolar in nature and whose period of evolution is $T \simeq 0.24$. Paying particular attention to the solution at $\alpha_o = 36$, we find that the quadrupole parity solution vacillates sinusoidally with time, indicating that the system had not yet bifurcated to the different time behaviour solution. Increasing α_o to 38, the solution retained its quadrupole parity and exhibits the same time behaviour as shown in Figure 3.6(b). This means

the dynamo number for the point of the bifurcation is $\mathcal{D} \approx 3800$.

Following the bifurcation pattern for $\Theta_o = 50$, we see the same bifurcation pattern as found before. Now, we see that the bifurcation does not occur until beyond $\alpha_o = 88$, as we have yet to find a periodic alternating peak height solution for $\Theta_o = 50$. This confirms that the bifurcation of the solutions depends on both α_o and Θ_o and can not simply be characterised by their product $\mathcal{D}$. The graph in Figure 3.4, shows clearly the bifurcation points in each of the branches of the solutions we considered, the bifurcated solutions being shown in bold. This graph (Figure 3.4) suggests that the bifurcation of the solutions may instead be dependent on the magnitude of the magnetic energy, there being a threshold energy beyond which the solutions are of the periodic alternating peak type.

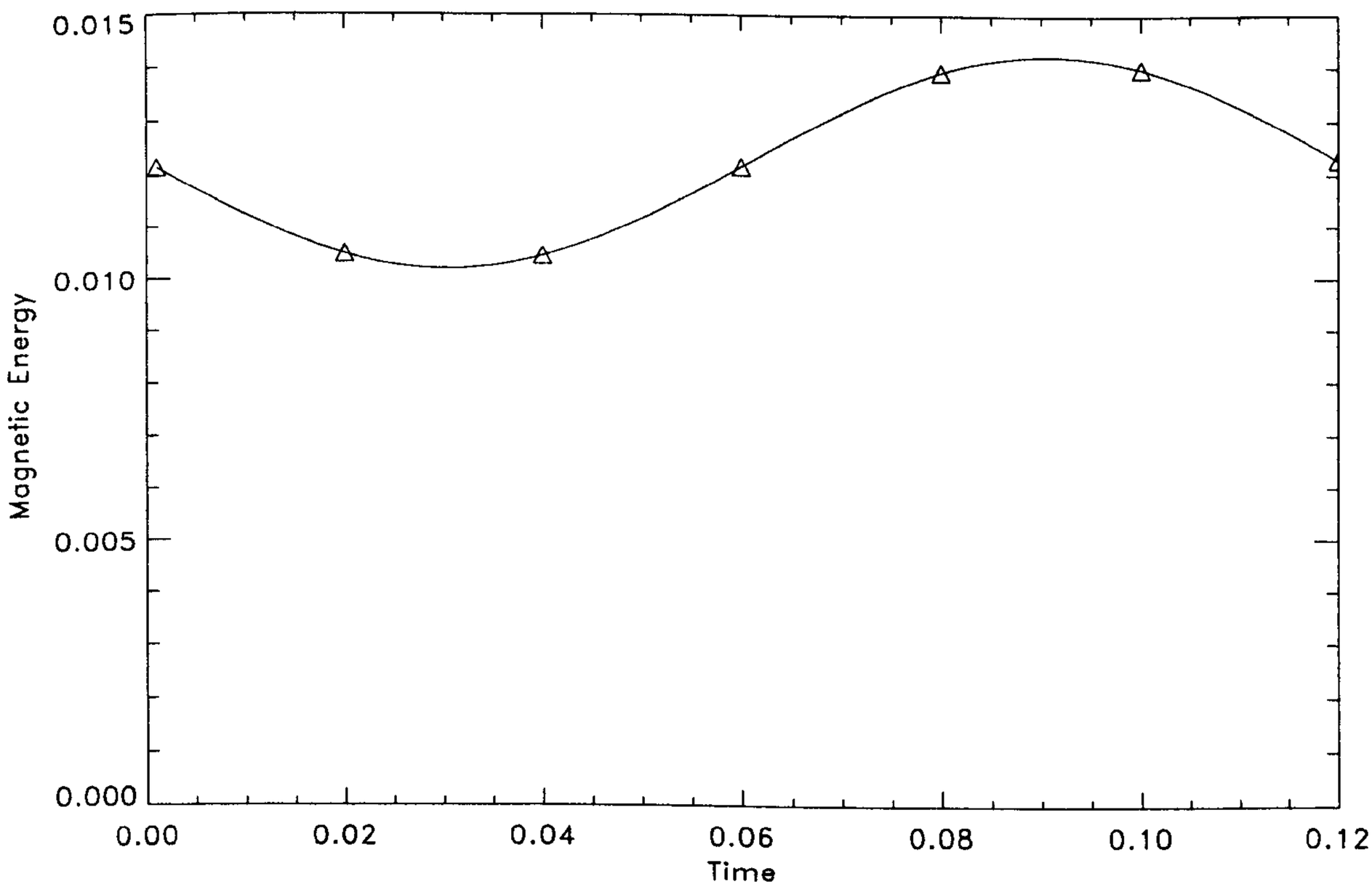

Figure 3.5: The evolution of the magnetic energy over a cycle at the onset of dynamo action; $\alpha_c = 8.12$ and $\Theta_o = 200$. The Δ's indicate the points through the cycle which have been plotted and are shown in Figure 3.7. The flow contours, which do not change with time, are shown in Figure 2.1.

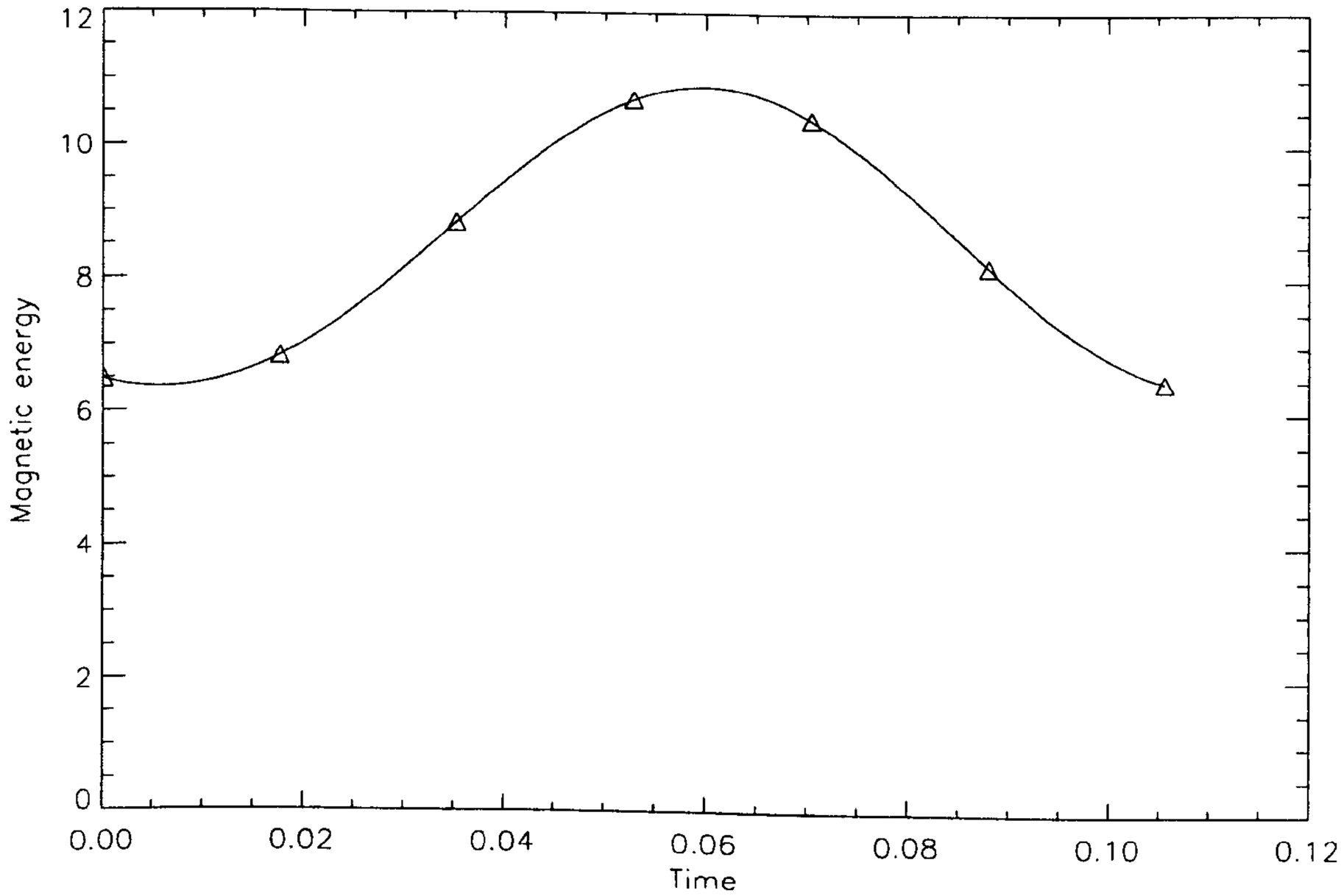

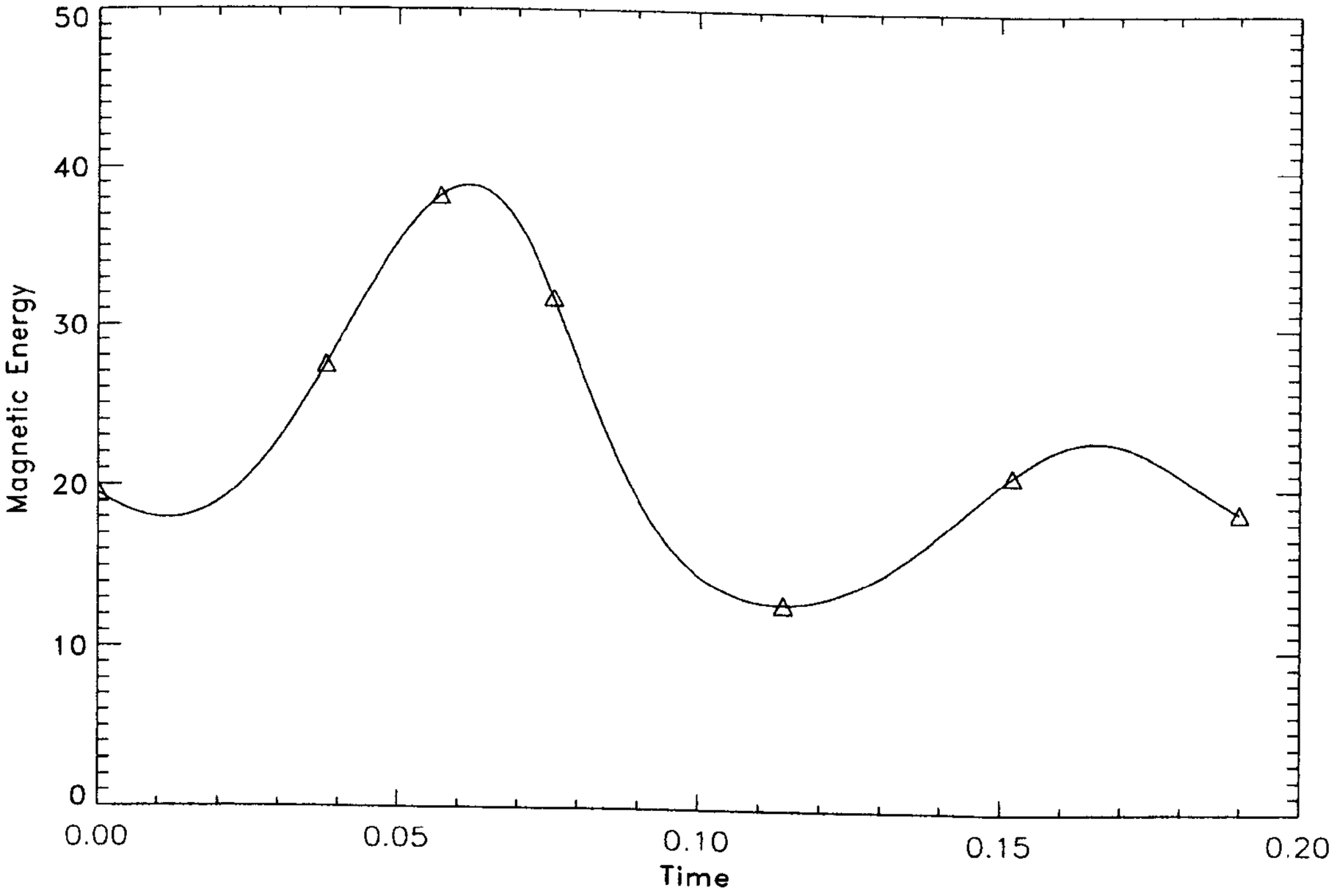

Figure 3.6: As Figure 3.5, but for (top to bottom) (a) $\alpha_o = 14$ and (b) $\alpha_o = 18$, with $\Theta_o = 200$.

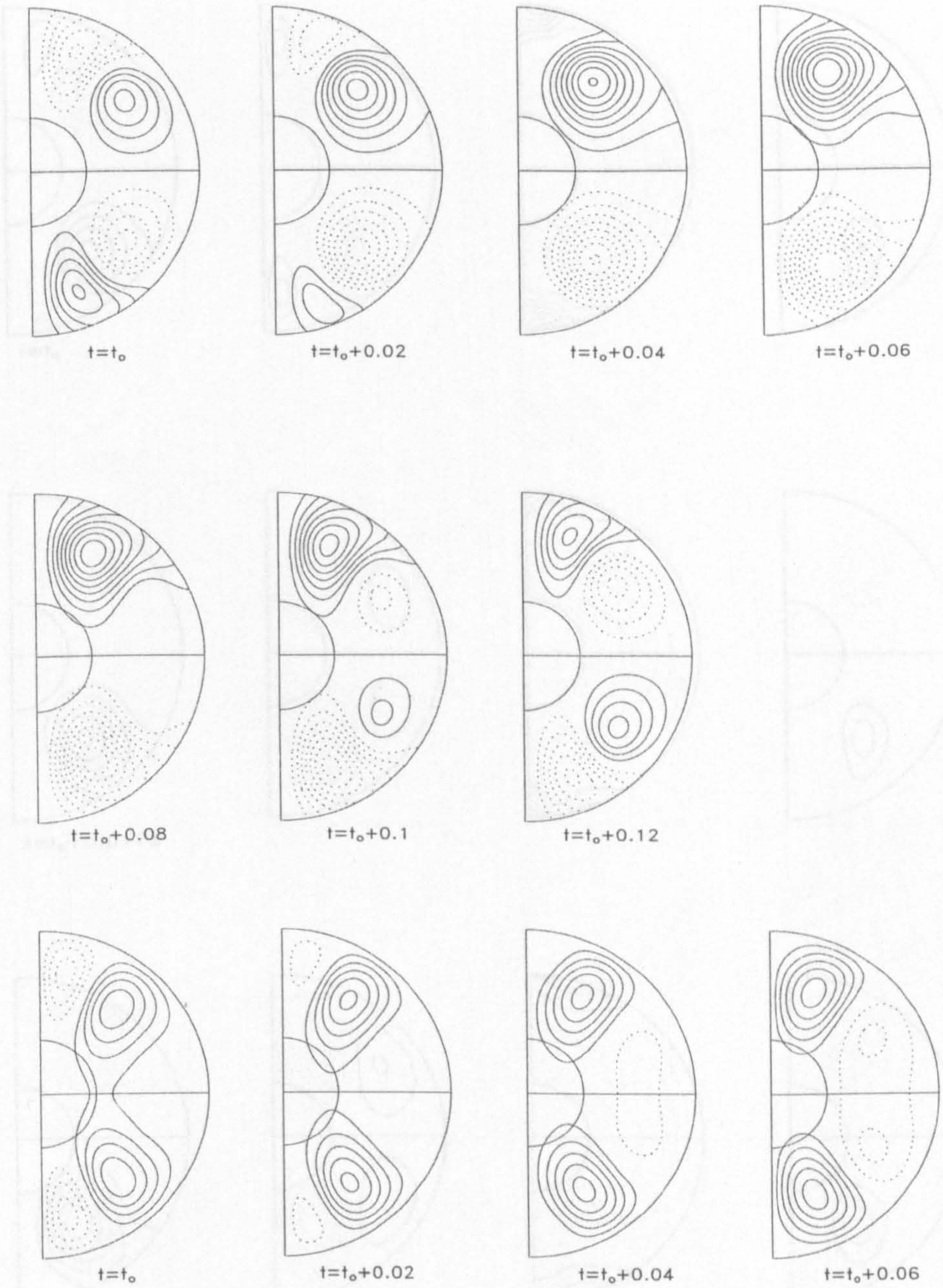

Figure 3.7: The above snapshots show the evolution of the solution over a cycle of magnetic energy at onset ($\alpha_o = \alpha_c$) for $\Theta_o = 200$. The first two rows show the poloidal magnetic field at a contour interval of 0.001. The toroidal magnetic field is shown in the second two rows at a contour interval of 0.02. Here solid lines

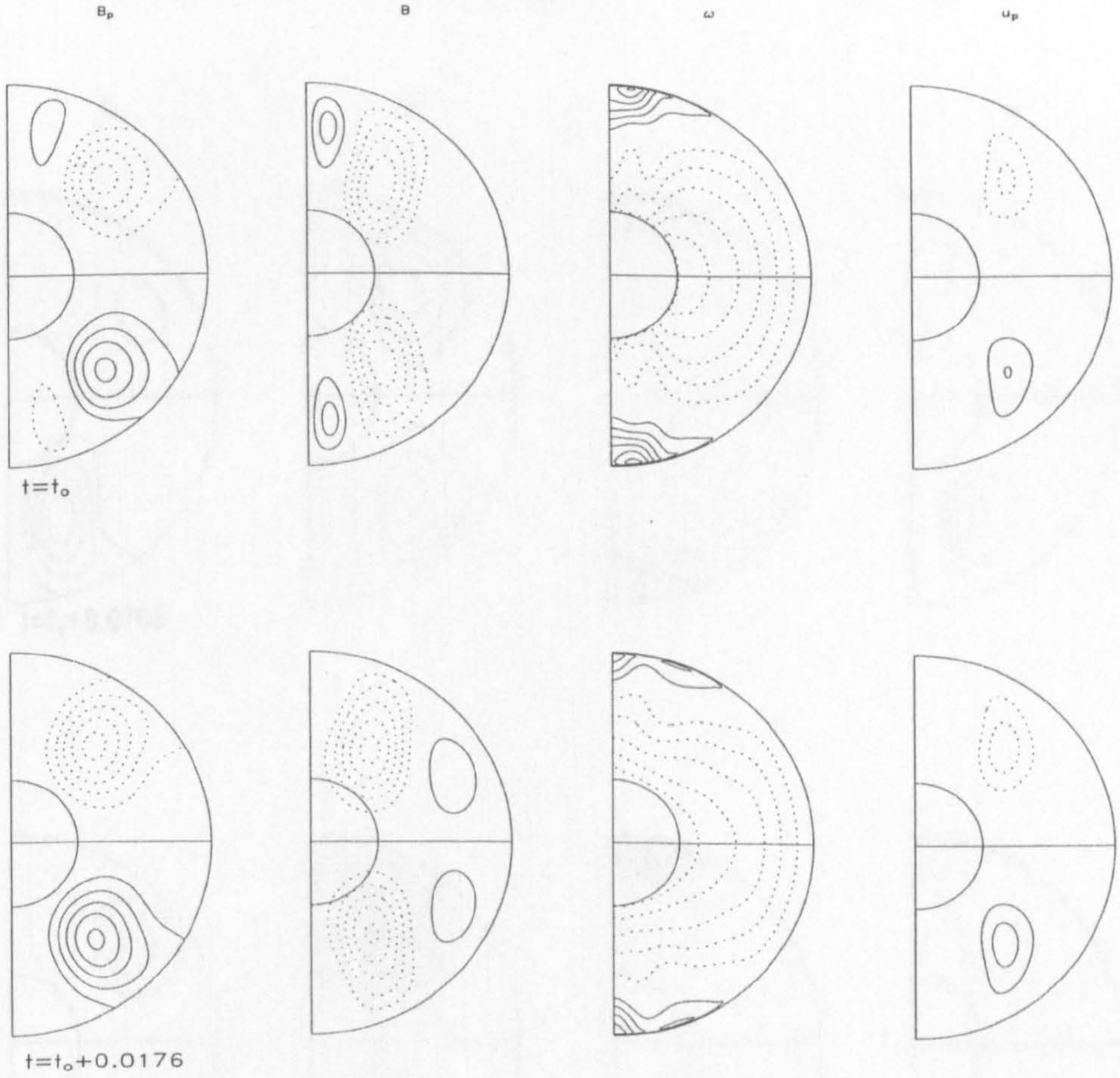

Figure 3.8: Here we show for $\alpha_o = 14$ and $\Theta_o = 200$ (from left to right) the poloidal field, toroidal field, angular velocity and meridional circulation contours using contour intervals of 0.05, 0.5, 25, 0.25, respectively. This shows the evolution of the solution over a half period, $\frac{T}{2} = 0.1056$.

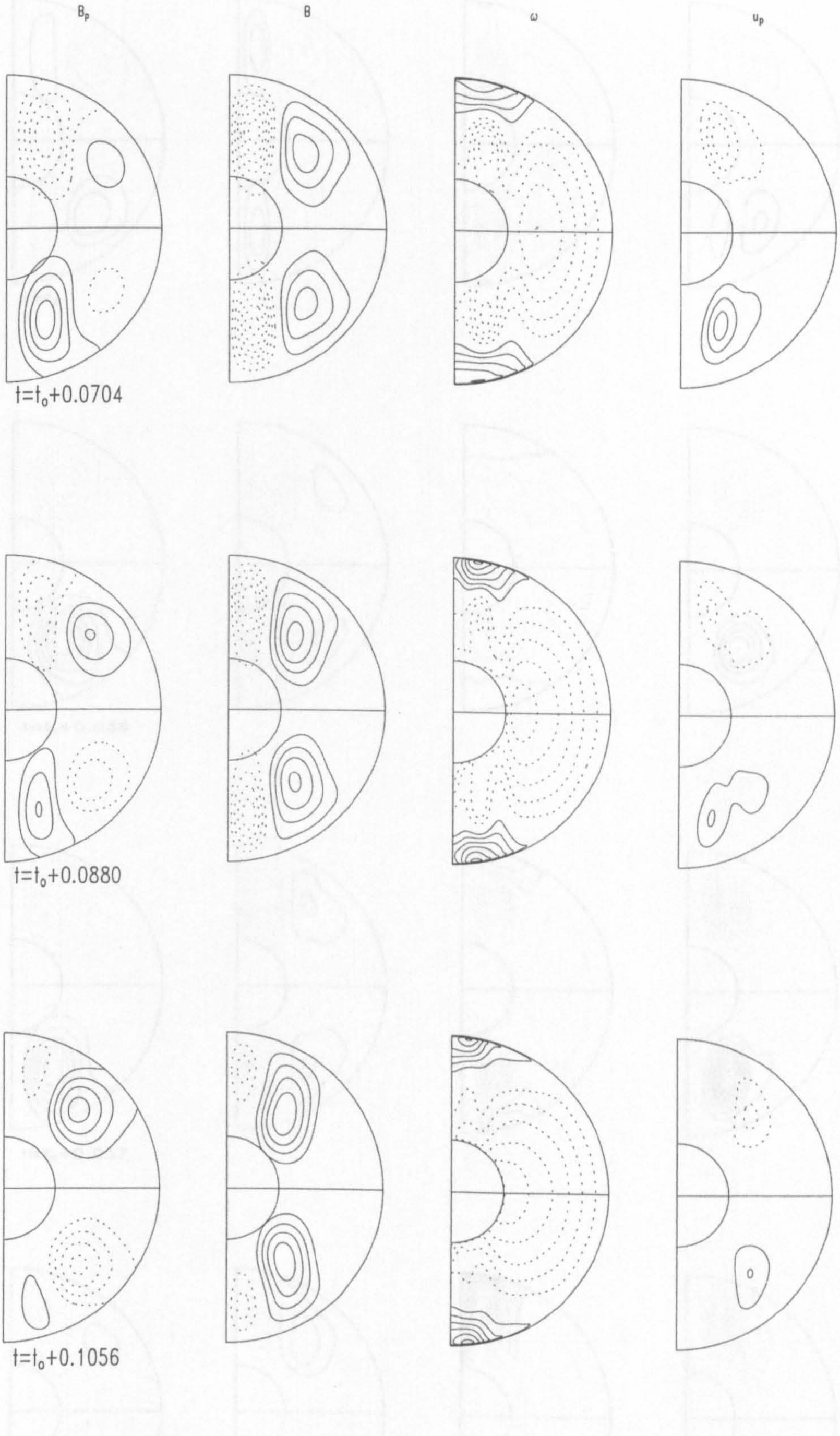

Figure 3.8 continued.

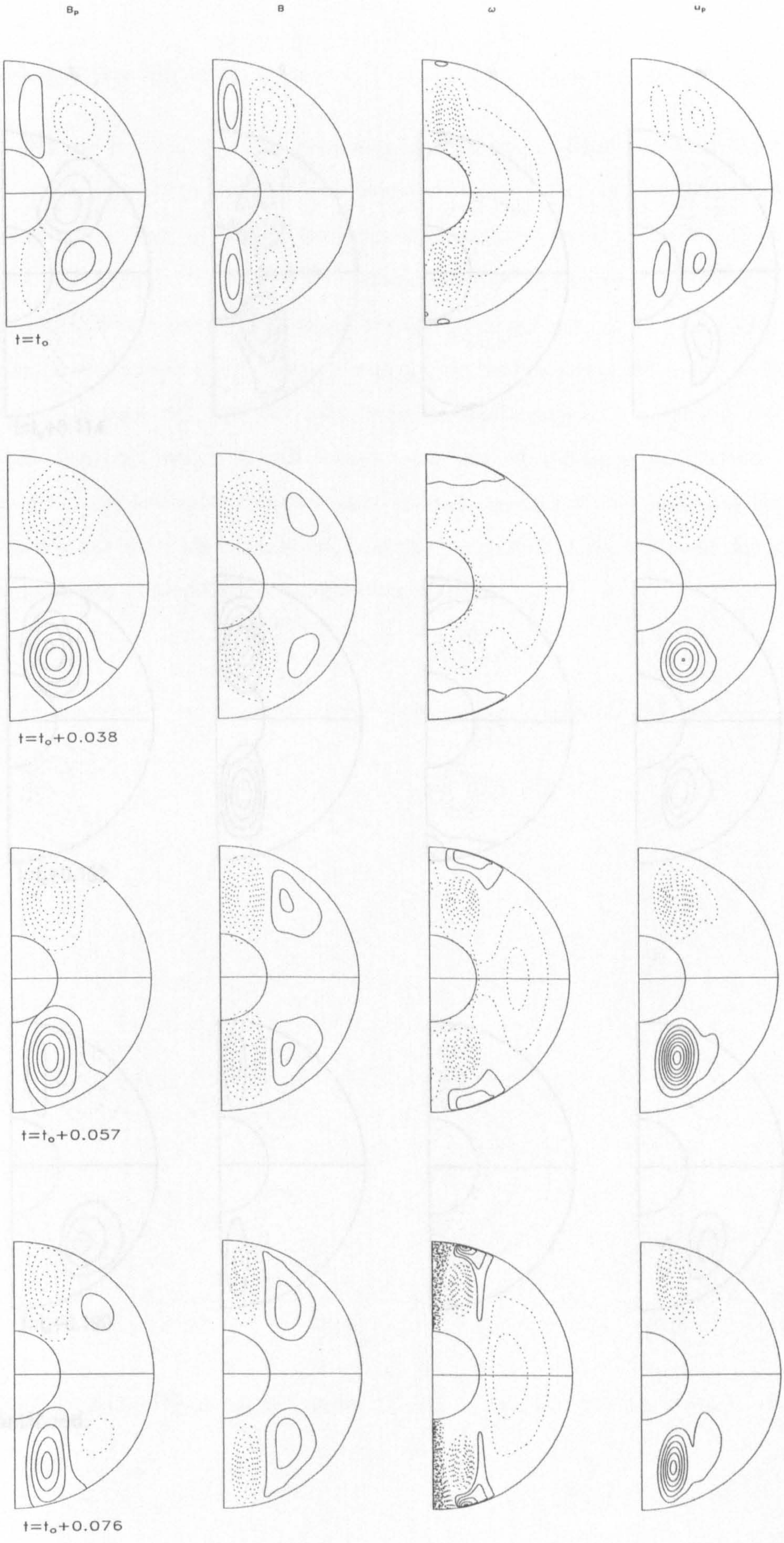

Figure 3.9: As Figure 3.8, but for $\alpha_o = 18$ and $\Theta_o = 200$. Here we use contour intervals of 0.1, 1 , 50 , 0.5. This shows the evolution of the solutions over a period, $T = 0.19$.

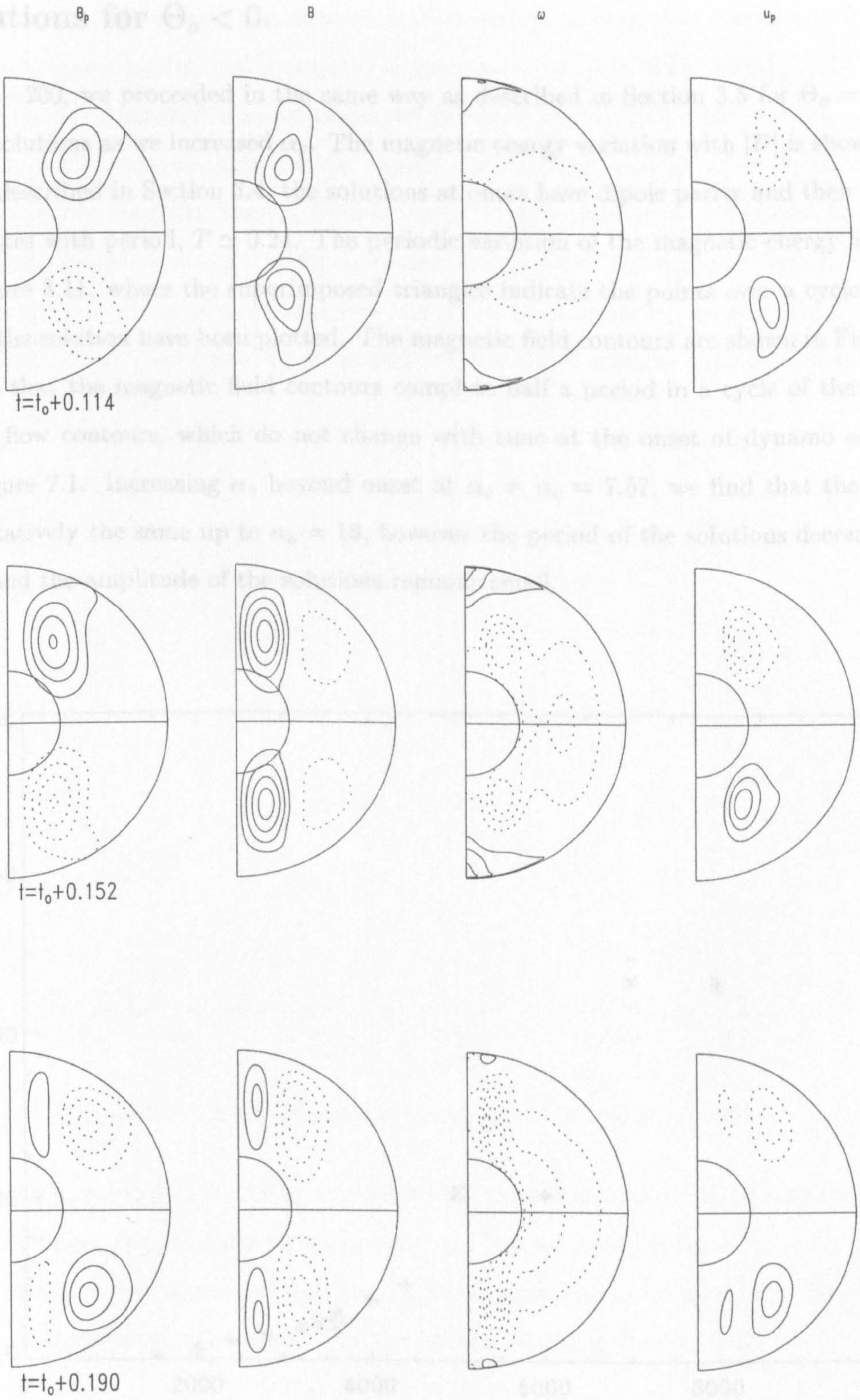

Figure 3.9 continued.

3.6 Solutions for $\Theta_o < 0$.

For $\Theta_o = -200$, we proceeded in the same way as described in Section 3.5 for $\Theta_o = 200$, and followed the solutions as we increased α_o. The magnetic energy variation with $|\mathcal{D}|$ is shown in Figure 3.10. As described in Section 3.4, the solutions at onset have dipole parity and their magnetic energy vacillates with period, $T \simeq 0.24$. The periodic variation of the magnetic energy at onset is shown in Figure 3.11, where the superimposed triangles indicate the points over a cycle at which snapshots of the solution have been plotted. The magnetic field contours are shown in Figure 3.12, where we see that the magnetic field contours complete half a period in a cycle of the magnetic energy. The flow contours, which do not change with time at the onset of dynamo action, are shown in Figure 2.1. Increasing α_o beyond onset at $\alpha_o = \alpha_c = 7.57$, we find that the solutions remain qualitatively the same up to $\alpha_o = 18$, however the period of the solutions decreases as α_o is increased and the amplitude of the solutions remains small.

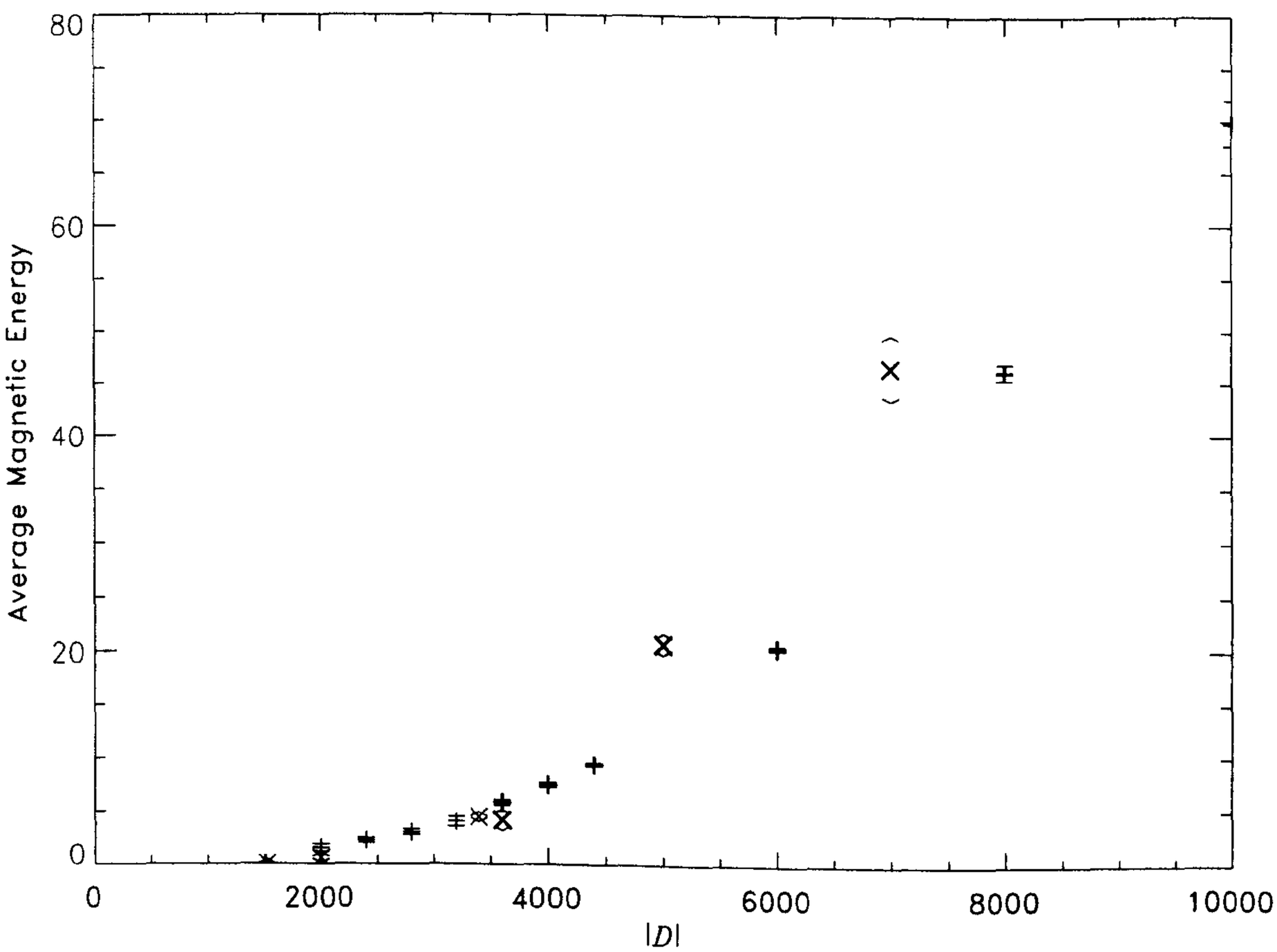

Figure 3.10: As for Figure 3.3, but for $\Theta_o < 0$ only. $+ : \Theta_o = -200$, and $\times : \Theta_o = -100$.

At $\alpha_o = 18$, we find the system has undergone a bifurcation and the solutions change from being of dipole parity to mixed parity, as shown in the snapshots over a cycle in Figure 3.13. The magnetic energy maintains the sinusoidal time variation, as shown in Figure 3.14. Through examining the evolution of the mixed solution over a cycle, we see that the magnetic field has completed half a period in a cycle of the magnetic energy. Interestingly, the flow appears to have completed a period over a cycle of the magnetic energy. Given the small amplitude of the magnetic energy vacillation and the gentle increase in the average magnetic energy as we increase α_o, as shown in Figure 3.10, we can with relative ease increase α_o up to 50 and find the mixed solution behaviour is maintained.

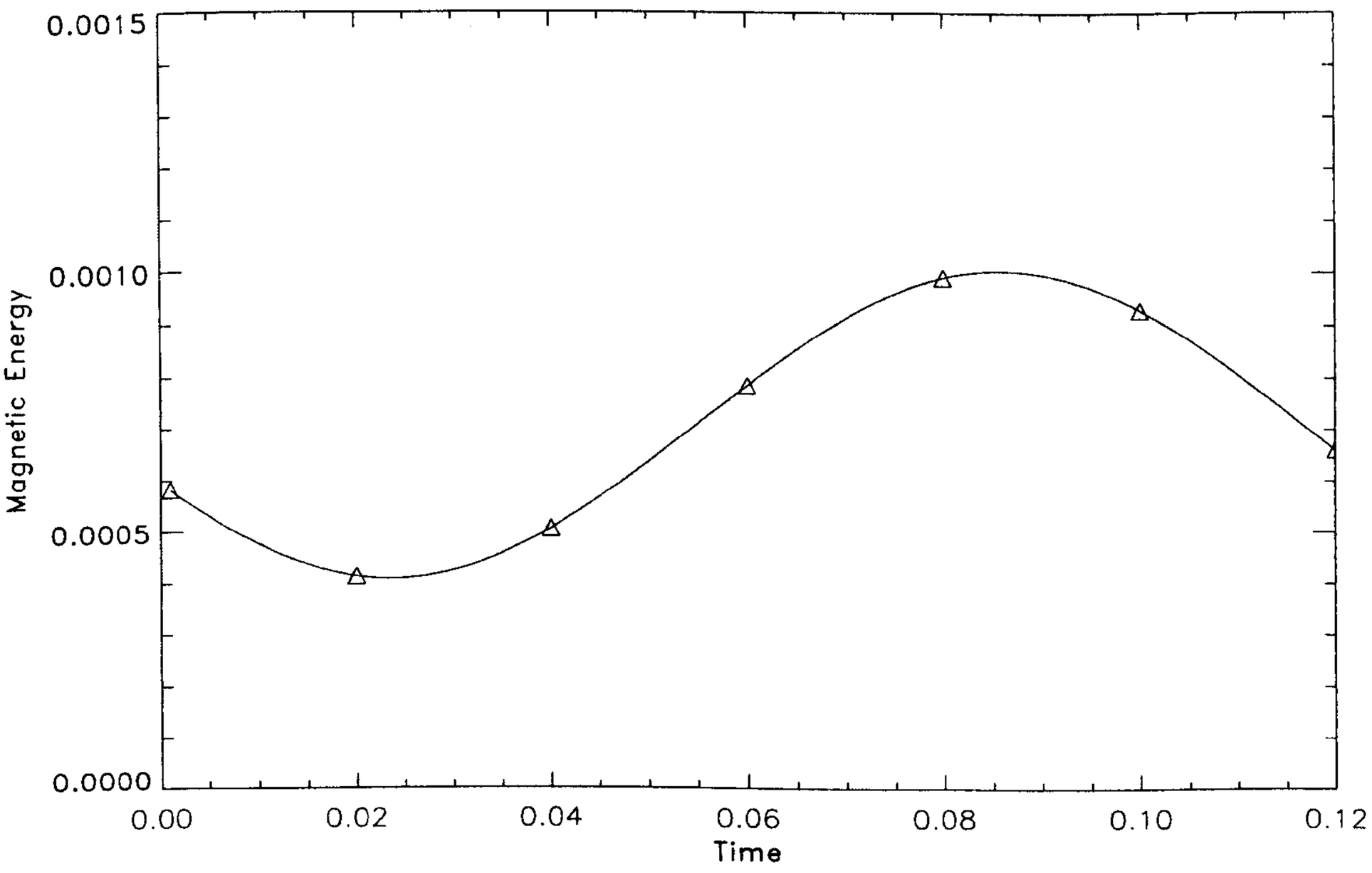

Figure 3.11: As for Figure 3.5, but for $\alpha_c = 7.57$ and $\Theta_o = -200$.

For $\Theta_o = -100$, we expect a similar variation with magnetic energy, which enables us to take fewer points to follow the solutions as we increase α_o beyond onset at $\alpha_o = \alpha_c = 15.2$. We find qualitatively similar behaviour as we increase α_o; small amplitudes and increasing frequency with increasing α_o. The bifurcation to mixed parity solutions occurs around $\alpha_o = 36$.

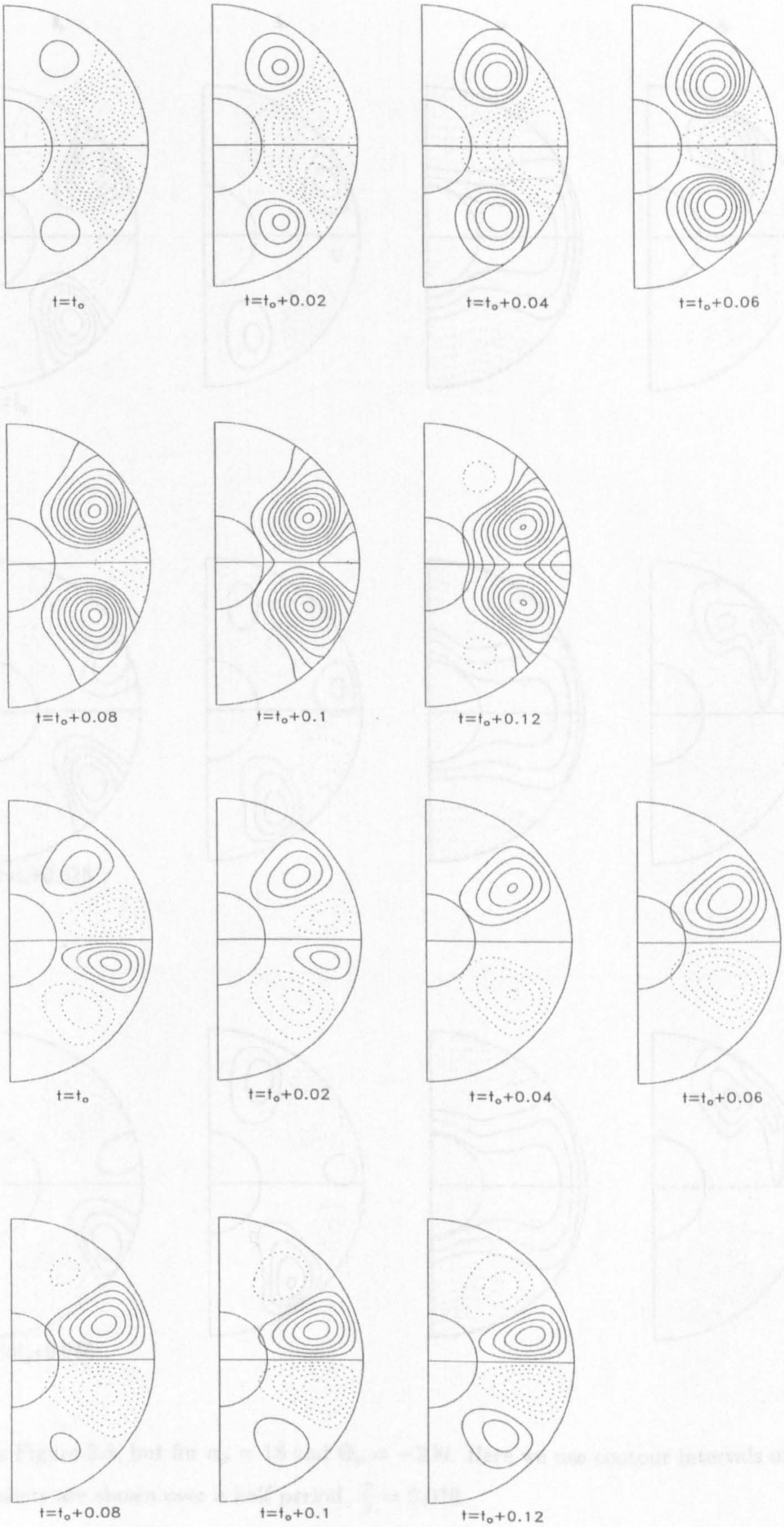

Figure 3.12: As Figure 3.7, but for onset ($\alpha_c \sim 7.57$) for $\Theta_o = -200$. Here the contour interval is 0.0002 for the poloidal field (top two rows) and 0.005 for the toroidal field (bottom two rows).

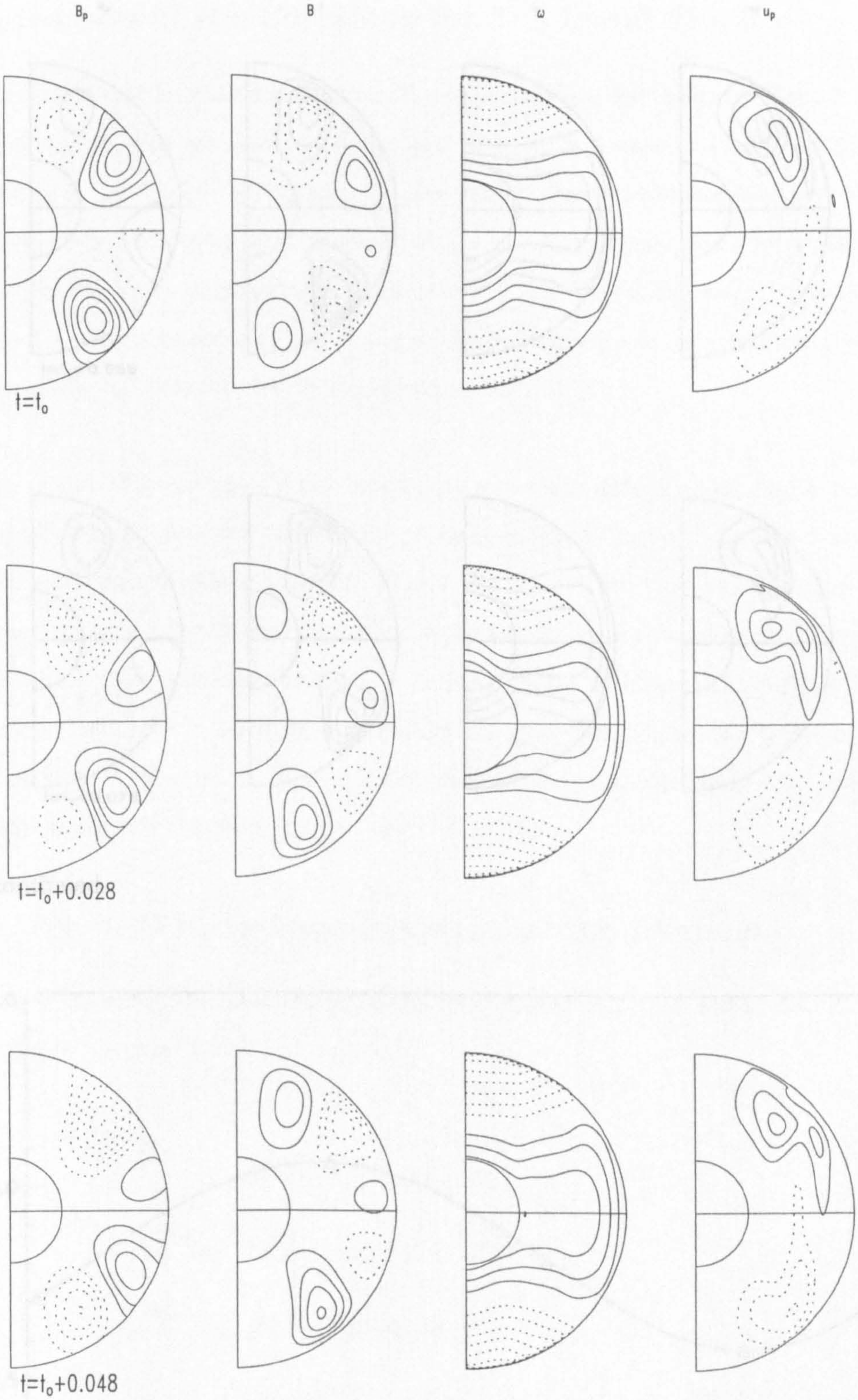

Figure 3.13: As Figure 3.8, but for $\alpha_o = 18$ and $\Theta_o = -200$. Here we use contour intervals of 0.05, 0.5, 20, 0.2. The 5 snapshots are shown over a half period, $\frac{T}{2} = 0.078$.

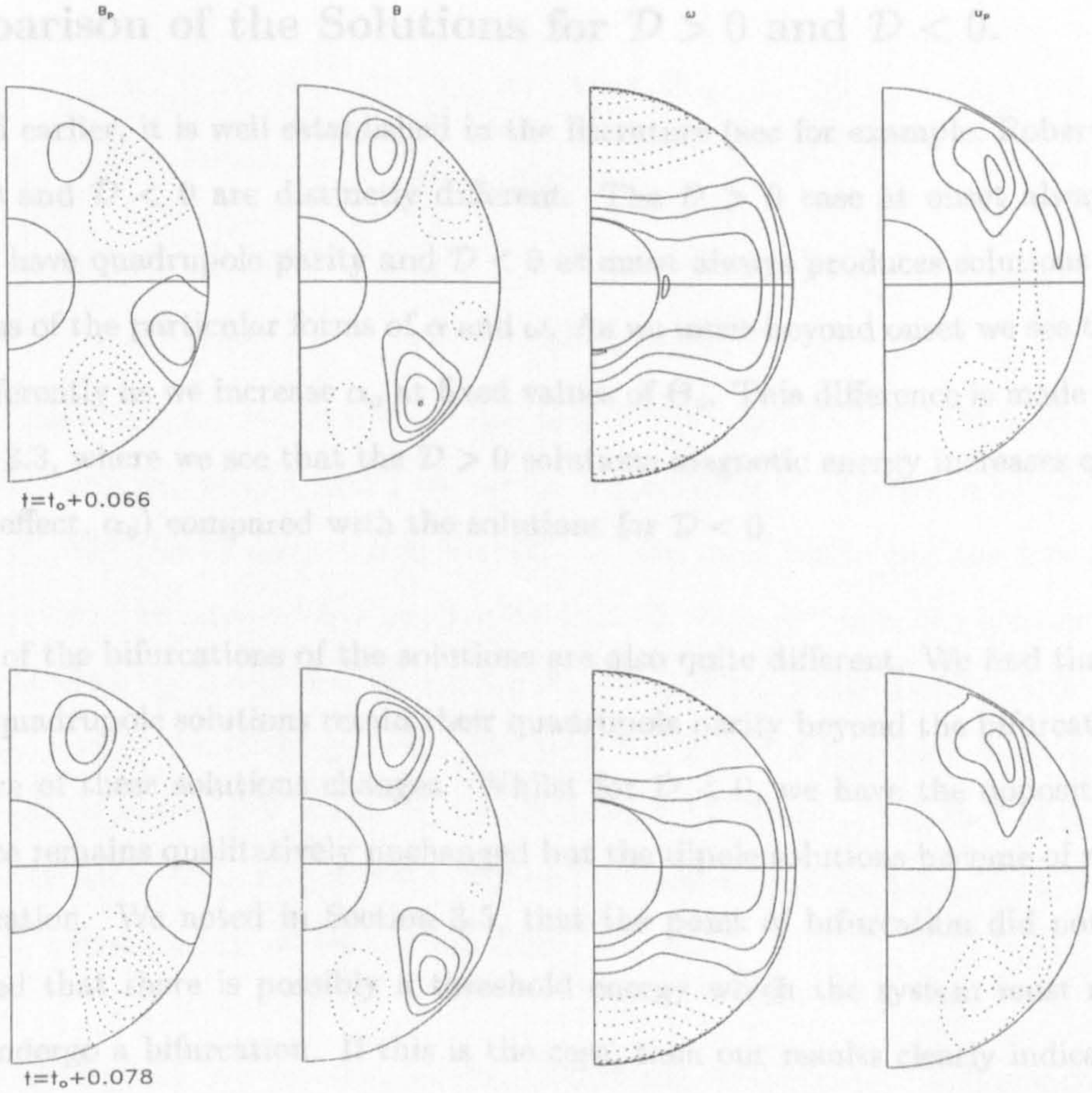

Figure 3.13 continued.

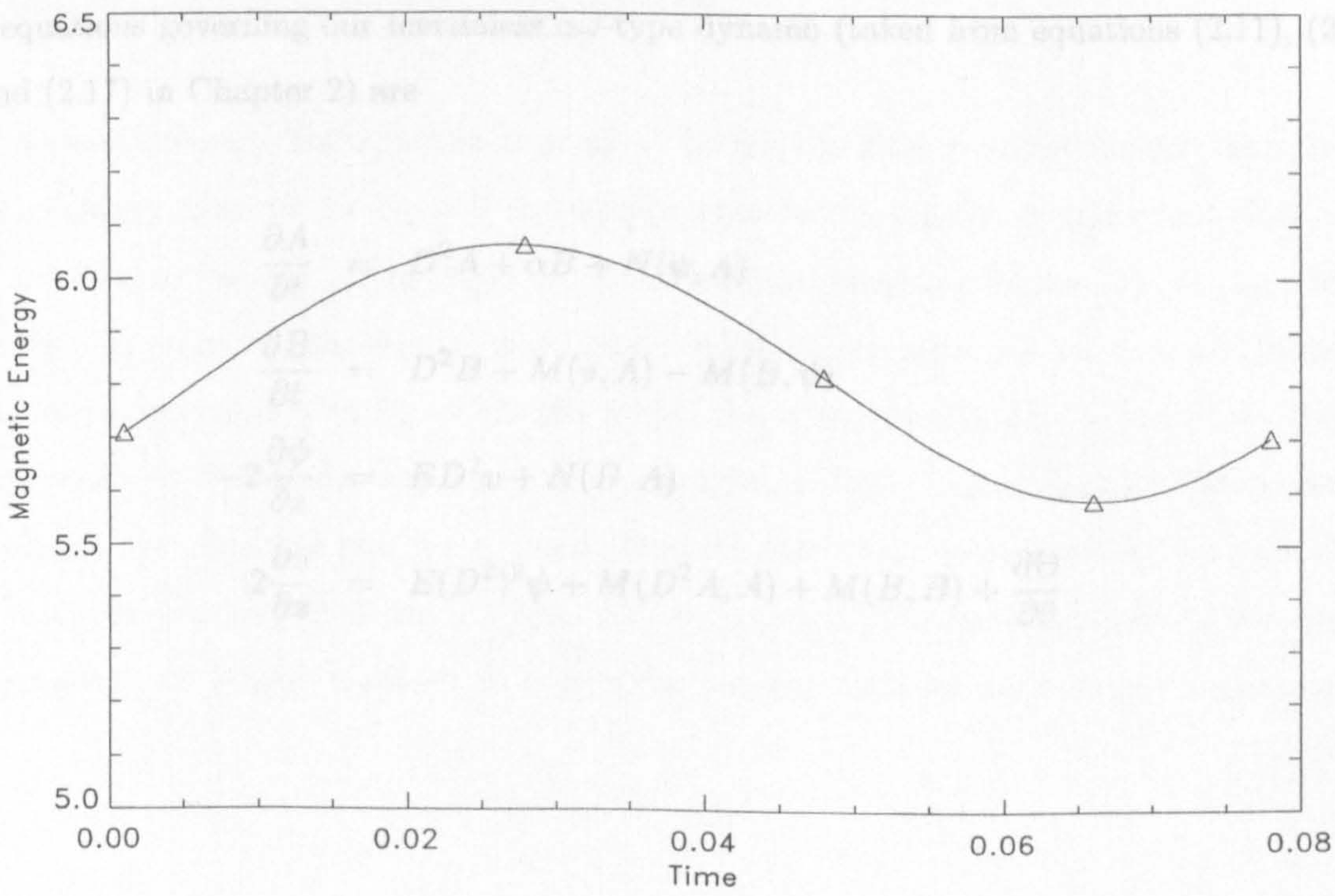

Figure 3.14: As Figure 3.5, but for $\alpha_o = 18$ and $\Theta_o = -200$.

3.7 Comparison of the Solutions for $\mathcal{D} > 0$ and $\mathcal{D} < 0$.

As discussed earlier, it is well established in the literature (see for example, Roberts 1972) the cases of $\mathcal{D} > 0$ and $\mathcal{D} < 0$ are distinctly different. The $\mathcal{D} > 0$ case at onset always produces solutions which have quadrupole parity and $\mathcal{D} < 0$ at onset always produces solutions with dipole parity, regardless of the particular forms of α and ω. As we move beyond onset we see the solutions evolve quite differently as we increase α_o at fixed values of Θ_o. This difference is made particularly clear by Figure 3.3, where we see that the $\mathcal{D} > 0$ solutions magnetic energy increases quite rapidly with $|\mathcal{D}|$ (or in effect, α_o) compared with the solutions for $\mathcal{D} < 0$.

The nature of the bifurcations of the solutions are also quite different. We find that for $\mathcal{D} > 0$ the vacillating quadrupole solutions retain their quadrupole parity beyond the bifurcation, but the time dependence of these solutions changes. Whilst for $\mathcal{D} < 0$, we have the opposite effect; the time dependence remains qualitatively unchanged but the dipole solutions become of mixed parity after the bifurcation. We noted in Section 3.5, that the point of bifurcation did not depend on $\mathcal{D}$ and suggested that there is possibly a threshold energy which the system must reach before the solutions undergo a bifurcation. If this is the case, then our results clearly indicate that this threshold energy is entirely different in the cases of $\mathcal{D} > 0$ and $\mathcal{D} < 0$.

3.8 The role of Θ in the equilibration of the dynamo.

The equations governing our inertialess $\alpha\omega$-type dynamo (taken from equations (2.11), (2.12), (2.15) and (2.17) in Chapter 2) are

$$\frac{\partial A}{\partial t} = D^2 A + \alpha B + N(\psi, A) \tag{3.1}$$

$$\frac{\partial B}{\partial t} = D^2 B + M(v, A) - M(B, \psi) \tag{3.2}$$

$$-2\frac{\partial \psi}{\partial z} = E D^2 v + N(B, A) \tag{3.3}$$

$$2\frac{\partial v}{\partial z} = E(D^2)^2 \psi + M(D^2 A, A) + M(B, B) + \frac{\partial \Theta}{\partial \theta} \tag{3.4}$$

where

$$\begin{aligned}
\frac{\partial}{\partial z} &= \cos\theta\frac{\partial}{\partial r} - \frac{\sin\theta}{r}\frac{\partial}{\partial\theta} \\
D^2 &= \nabla^2 - (r\sin\theta)^{-2} \\
N(X,Y) &= \mathbf{e}_\phi \cdot [\nabla \times (X\mathbf{e}_\phi) \times \nabla \times (Y\mathbf{e}_\phi)] \\
M(X,Y) &= \mathbf{e}_\phi \cdot \nabla \times [X\mathbf{e}_\phi \times \nabla \times (Y\mathbf{e}_\phi)]
\end{aligned}$$

Now, at the onset of dynamo action the magnitude of the magnetic field, $|\mathbf{B}|$ is small. Therefore the Lorentz force terms will be of $O(|\mathbf{B}|^2)$ and so the contribution to the overall balance of equation (3.4) will be negligible. As we discussed in Section 2.7, the main balance of the momentum equation then lies between the imposed buoyancy force and the Coriolis force; the buoyancy force then driving a thermal wind v_T. Therefore, examining the components of the Lorentz force at the onset of dynamo action enables us to compare the effects of the imposed buoyancy force at $\Theta_o = \pm 200$, whilst the strength of the field is small. Figures 3.15 and 3.16 show a snapshot of the solution at onset for $\Theta_o = 200$ and -200, respectively. Below the snapshot of the solution in each figure we plot the r, θ and ϕ components of the Lorentz force.

Examining Figure 3.15, we see that the $\Theta_o = 200$ solutions produce a Lorentz force that is largely confined within the tangent cylinder. The solutions in Figure 3.16 show the Lorentz force confined largely in the region outside the tangent cylinder and close to the equator. We examined the solutions we find at $\Theta_o = \pm 100$ (not shown) and find that the behaviour is similar; the location of the Lorentz force being dependent on the sign of Θ_o.

Now we were interested in trying to determine whether the location of the Lorentz force; largely inside the tangent cylinder for $\Theta_o > 0$ and largely outside the tangent cylinder and close to the equator for $\Theta_o < 0$, was due to the direction of the imposed buoyancy driven flow, or the parity of the solutions. In order to determine this, we imposed dipole symmetry on the code and looked for the onset of dynamo action at $\Theta_o = 200$ (for which the parity of solutions would have otherwise been quadrupolar). We found that onset occurred at $\alpha_c = 9.95$, higher than for the quadrupole parity solution, as expected (see for example, Roberts (1972) for more details). Examining the Lorentz force components, as shown in Figure 3.17 we see that this dipole solution has the contours of the Lorentz force largely confined to within the tangent cylinder also, clearly indicating that

the direction of the buoyancy driven flow is responsible for the equilibrated location of the Lorentz force. We then consider the situation as we increase α_o beyond the onset of dynamo action, to see whether this behaviour is continued.

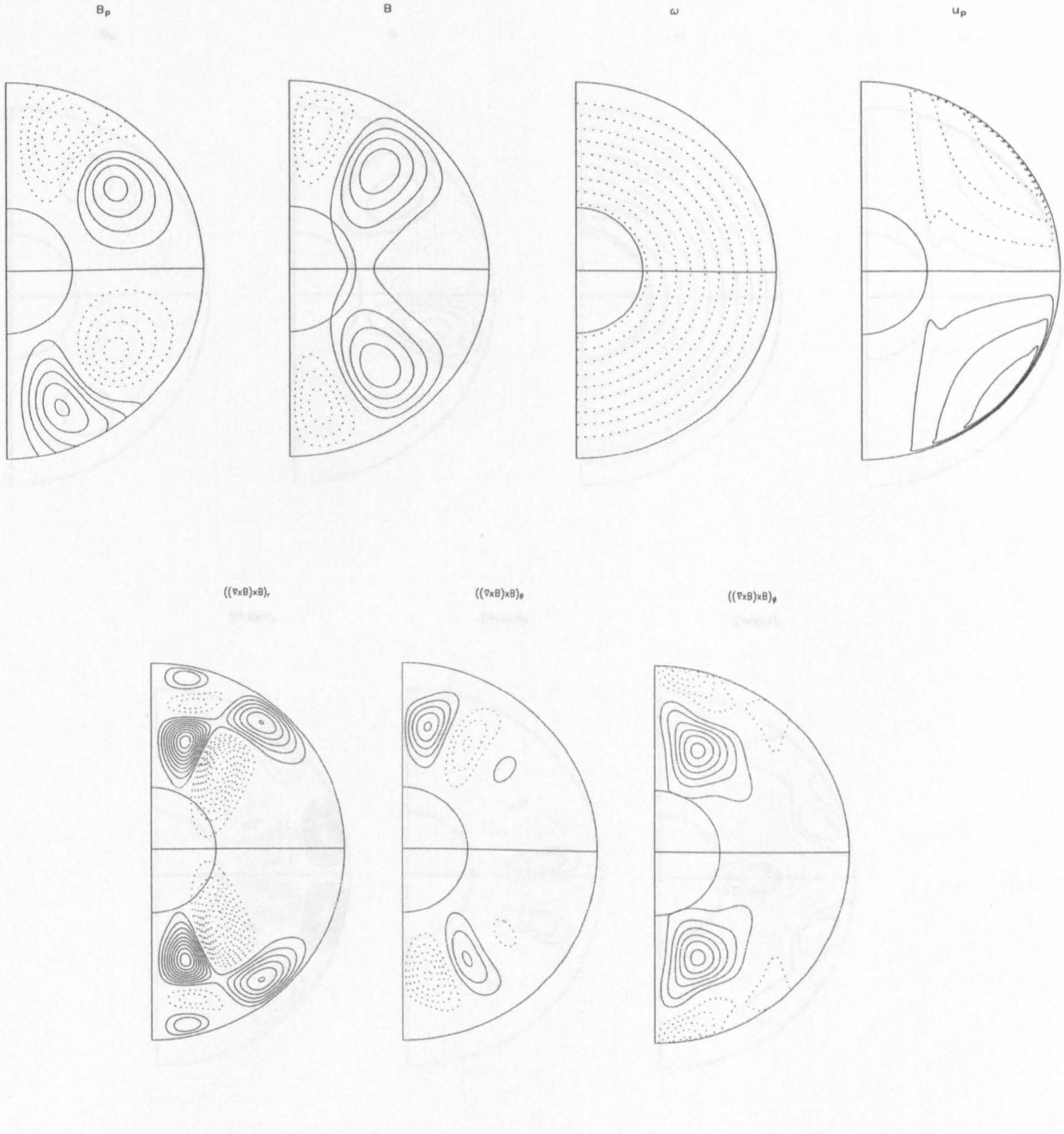

Figure 3.15: Top: A snapshot of the solution at $\alpha_c = 8.12$ and $\Theta_o = 200$. The contour intervals from left to right are; 0.001, 0.002, 20, 0.1. Bottom: Here we show the r, θ, ϕ components of the Lorentz force for the above solution. The contour intervals from left to right are; 0.002, 0.01, 0.002.

Examining the solutions shown in Figures 3.18 and 3.19 we see that the snapshots of the solutions look qualitatively similar to those we obtained at onset and we also see that the angular velocity contours between Figures 3.18 and 3.19 are a similar shape, despite the flow being driven in opposite directions. We notice that the meridional circulation contours in each case are quite

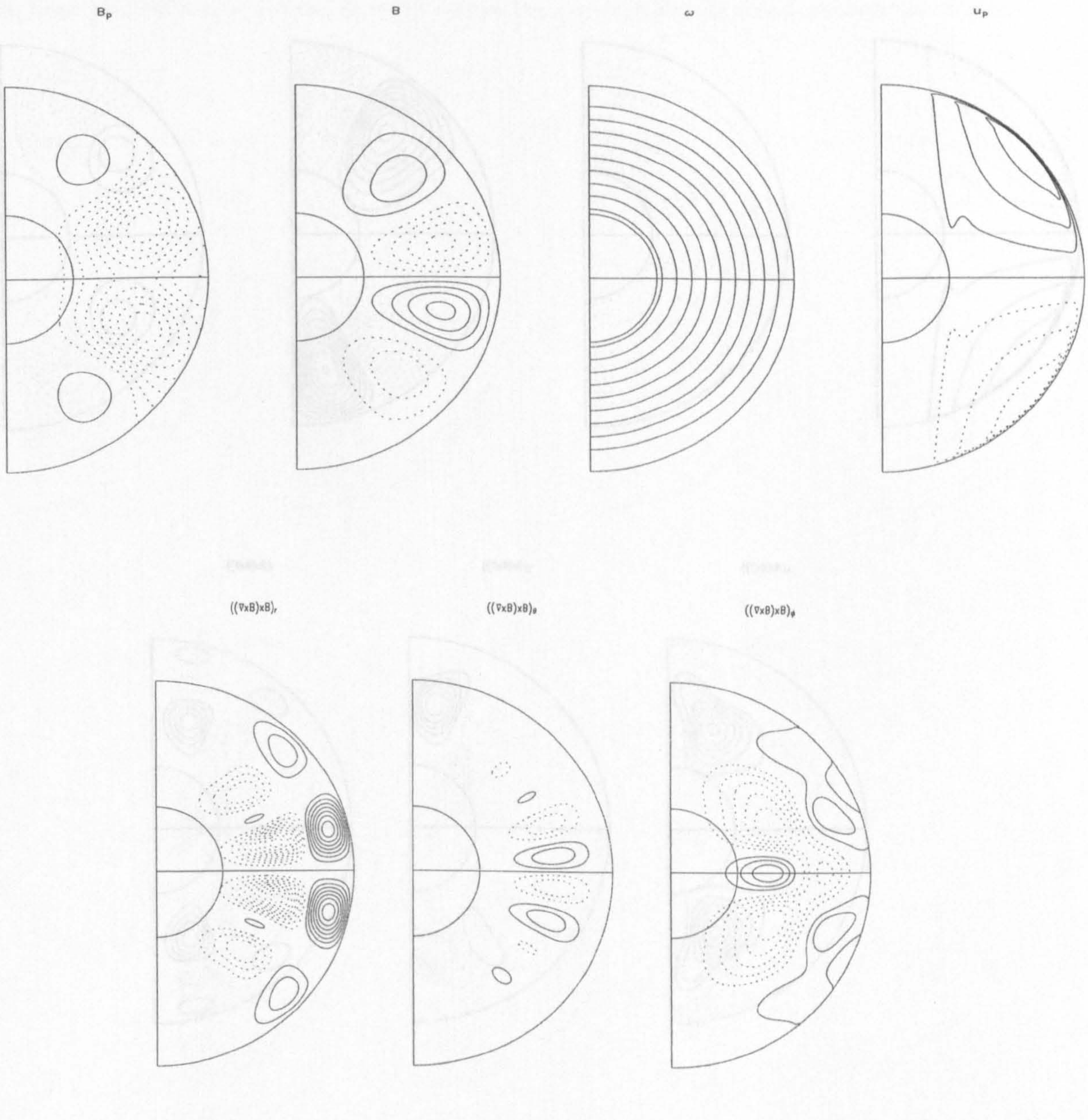

Figure 3.16: As Figure 3.15, but for $\alpha_c = 7.57$ and $\Theta_o = -200$. The contour intervals are 0.0002, 0.005, 20, 0.1 (top, left-right). 0.0001, 0.0005, 0.00005 (bottom, left-right).

different. The contours of the Lorentz force show the same preference as we found at onset. Comparing the snapshots of the solutions in Figures 3.15, 3.16, 3.18 and 3.19 we see that at fixed values of Θ_o as α_o is increased beyond the onset of dynamo action at α_c, the angular velocity

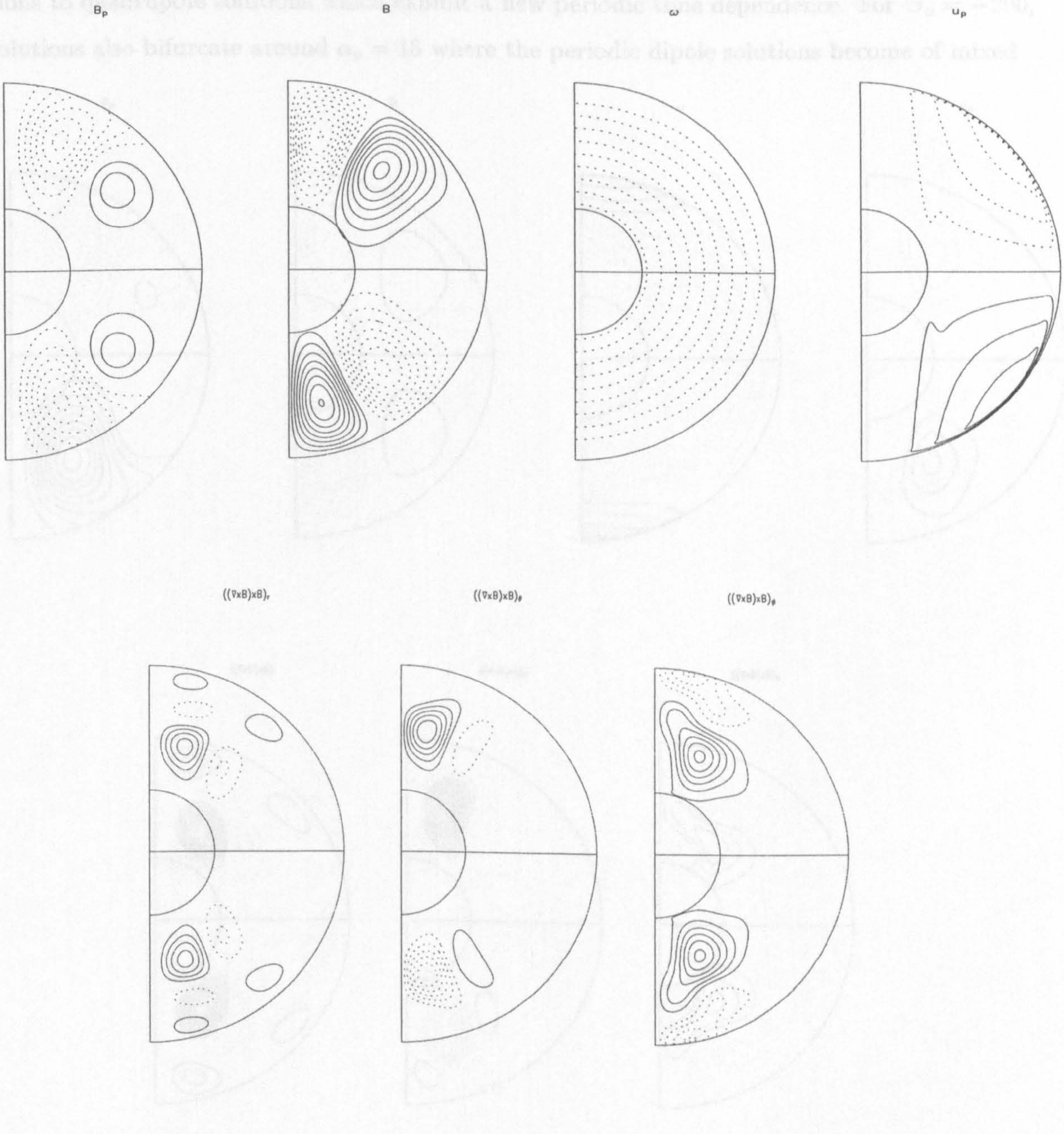

Figure 3.17: As Figure 3.15, but for a solution at onset ($\alpha_c = 9.95$) for $\Theta_o = 200$ when dipole symmetry is imposed on the problem. The contour intervals are 0.0001, 0.001, 20, 0.01 (top, left-right) and 0.00005, 0.0001, 0.00002 (bottom, left-right).

contours reveal that the flow induced by the Lorentz force partially counteracts the imposed flow. As noted earlier, as we increase α_o, the solutions undergo a bifurcation to different behaviour for all Θ_o considered. For $\Theta_o = 200$, the solutions bifurcate at $\alpha_o = 18$ from periodic quadrupole parity solutions to quadrupole solutions which exhibit a new periodic time dependence. For $\Theta_o = -200$, the solutions also bifurcate around $\alpha_o = 18$ where the periodic dipole solutions become of mixed

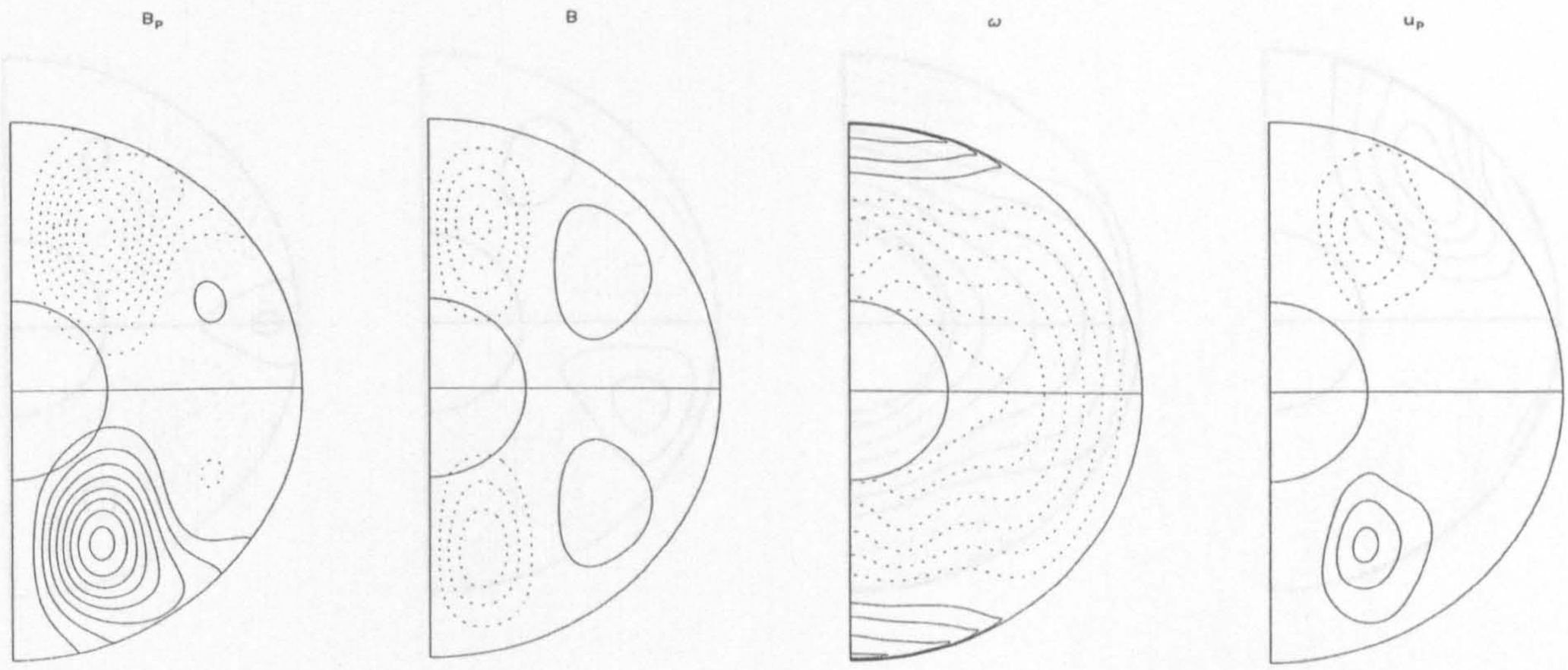

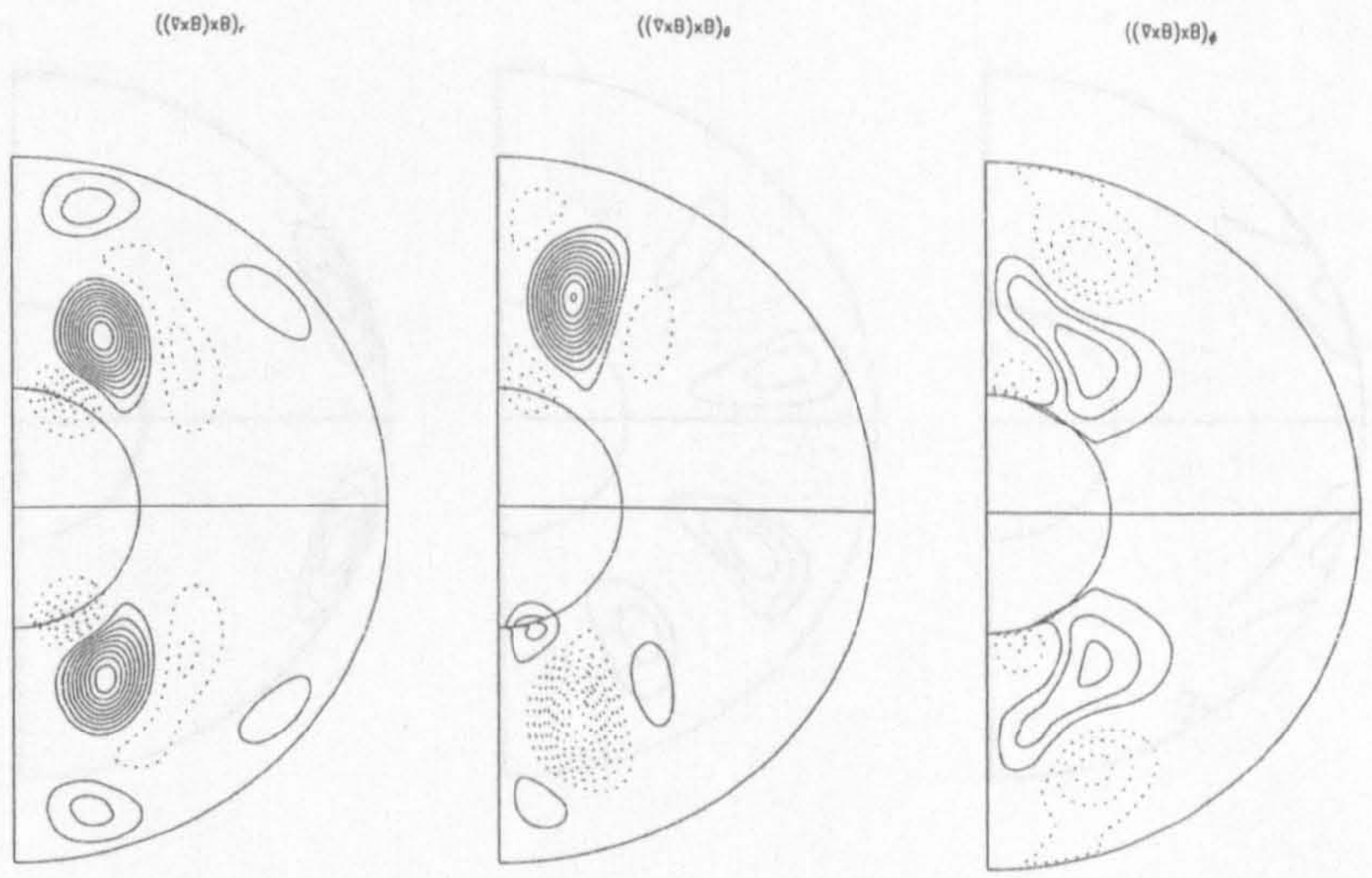

Figure 3.18: As Figure 3.15, but for $\alpha_o = 12$ and $\Theta_o = 200$. The contour intervals are 0.02, 0.5, 20, 0.1 (top, left-right) and 1, 2, 1 (bottom, left-right).

parity. Examining the snapshots of the solutions at $\alpha_o = 20$, as shown in Figures 3.20 and 3.21, for $\Theta_o = 200$ and -200, respectively, we see that the plots of angular velocity and meridional circulation now look quite different between the two solutions. The contours of the Lorentz force appears as before in the case of $\Theta_o = 200$. The Lorentz force contours at $\Theta_o = -200$, remained

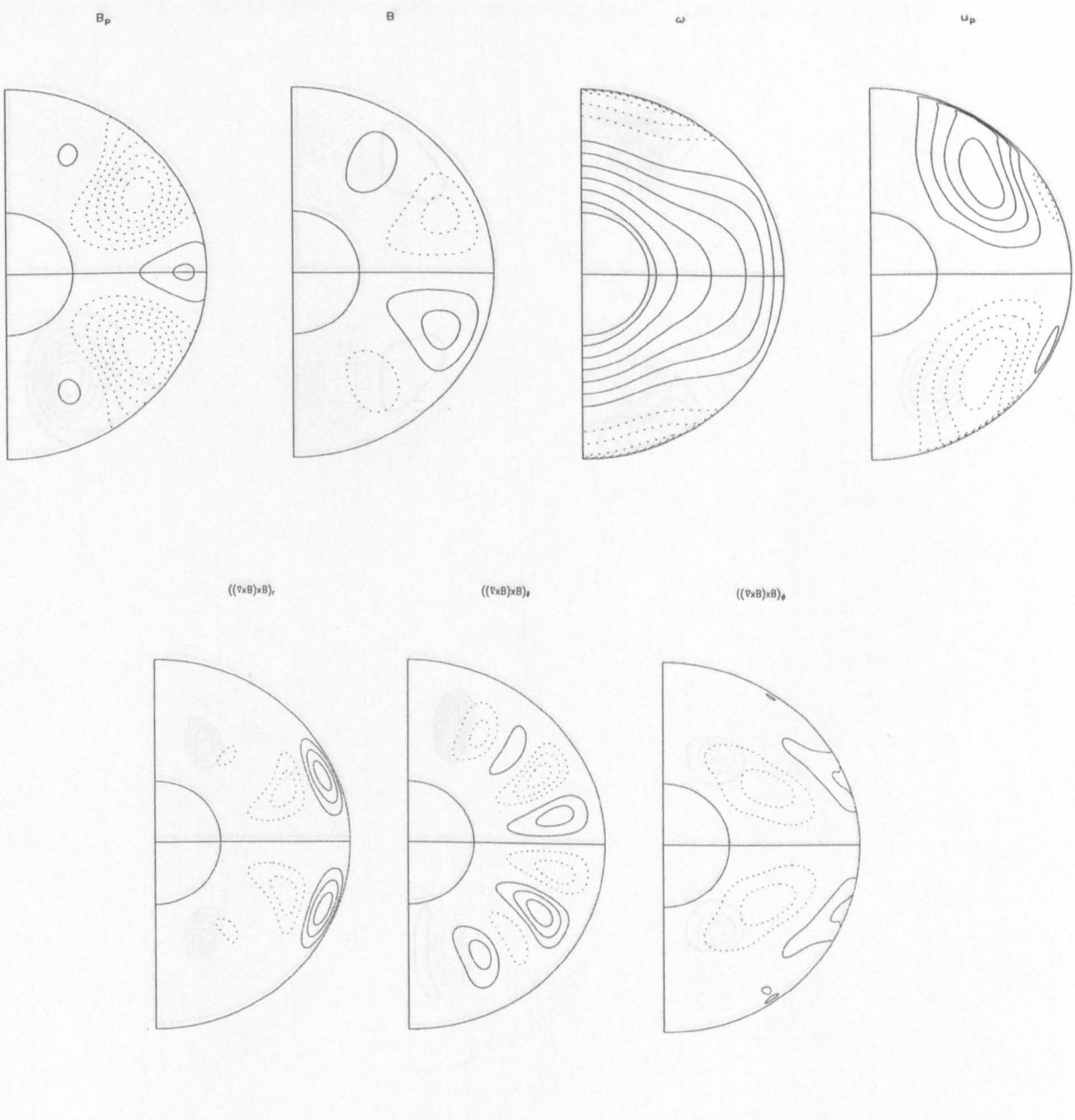

Figure 3.19: As Figure 3.15, but for $\alpha_o = 12$ and $\Theta_o = -200$. The contour intervals are 0.02, 0.5, 20, 0.05 (top, left-right) and 1, 1, 0.5 (bottom, left-right).

confined largely outwith the tangent cylinder, but now the concentration in each component is no longer close to the equator. Since we are specifically interested in how Θ_o acts to equilibrate the system, we fix $\alpha_o = 20$ and examine snapshots of the solutions at $\Theta_o = \pm 100$. The solution for $\Theta_o = 100$ is shown in Figure 3.22 and the $\Theta_o = -100$ solution is shown in Figure 3.23. For $\alpha_o = 20$

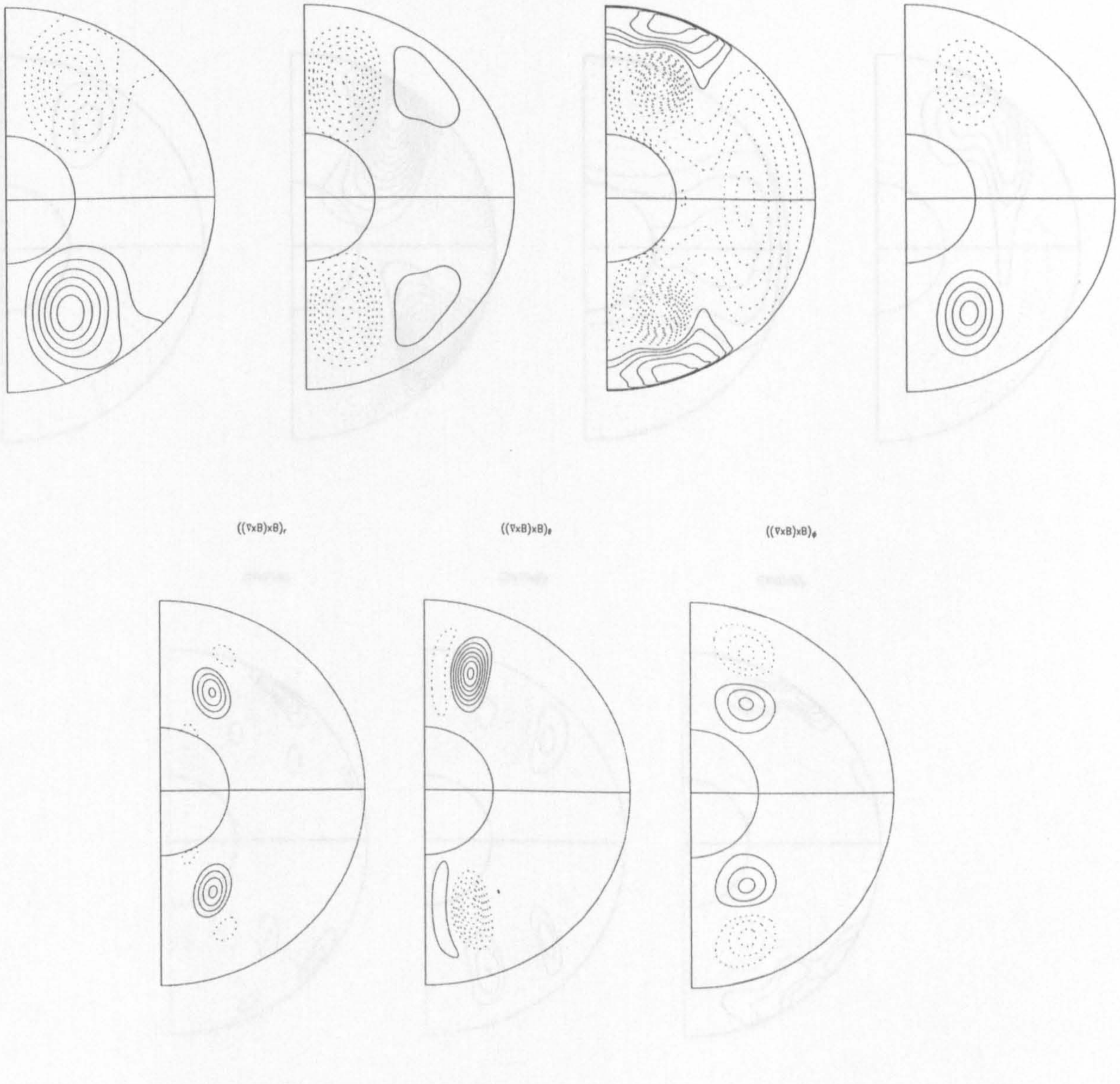

Figure 3.20: As Figure 3.15, but for $\alpha_o = 20$ and $\Theta_o = 200$. The contour intervals are 0.1, 1, 20, 1 (top, left-right) and 50, 50, 20 (bottom, left-right).

and $\Theta_o = \pm 100$, the solutions are just beyond onset ($\alpha_c \sim 16$) and so the solutions resemble those given in Figures 3.18 and 3.19, though clearly the flow is not nearly so strong. Our findings reveal that the Lorentz force components lie in the locations found before; largely within the tangent cylinder for $\Theta = 100$ and largely outside the tangent cylinder and close to the equator for $\Theta_o = -100$. Comparing these solutions with those in Figures 3.20 and 3.21, it is difficult

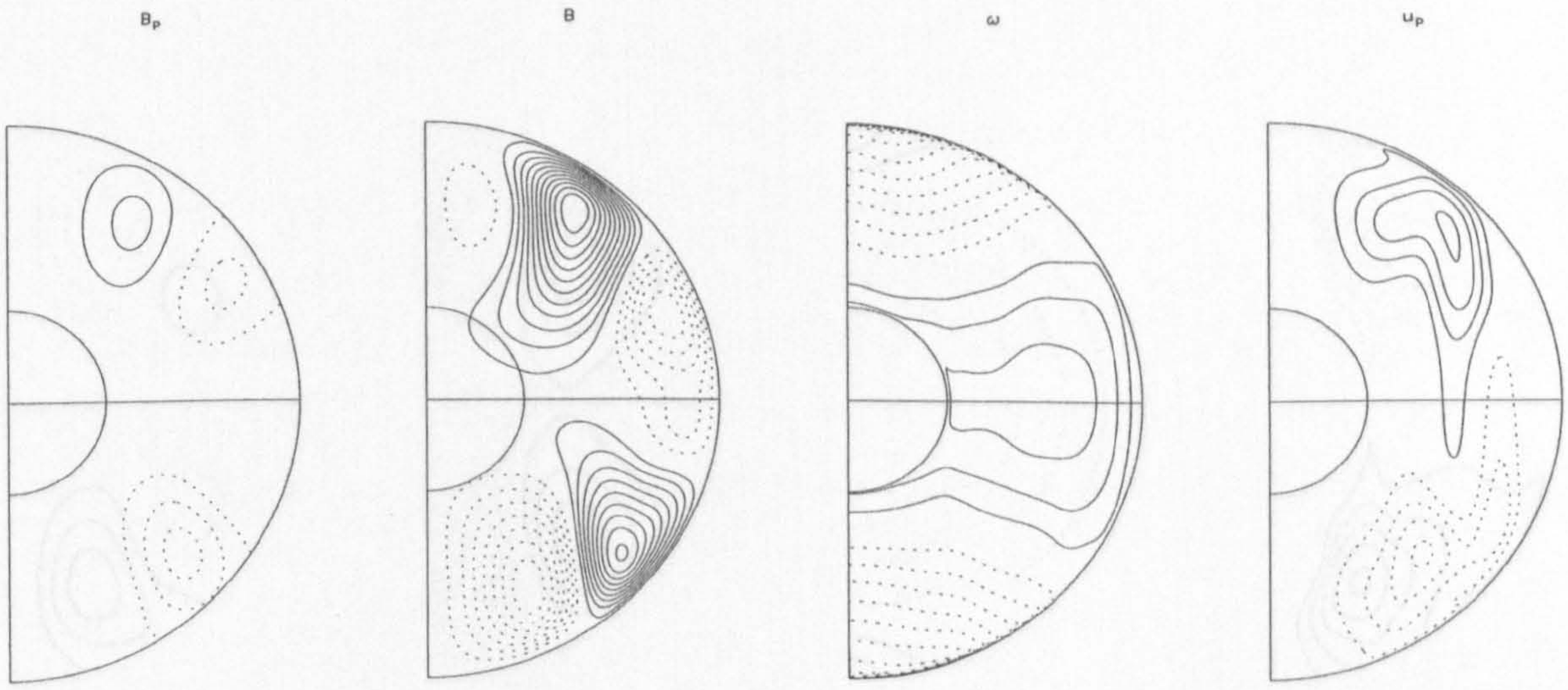

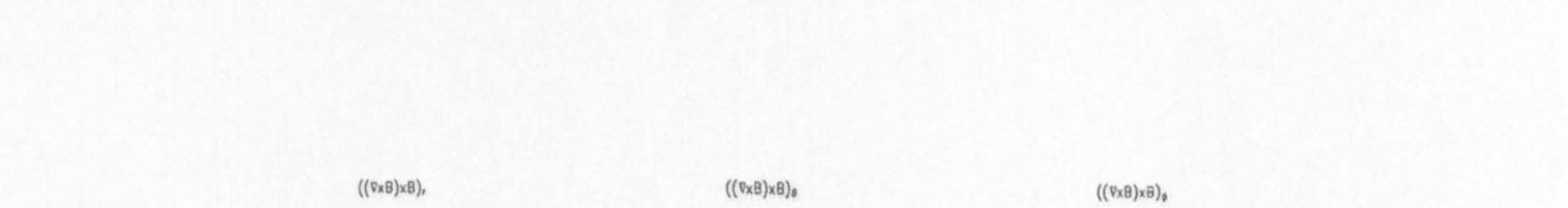

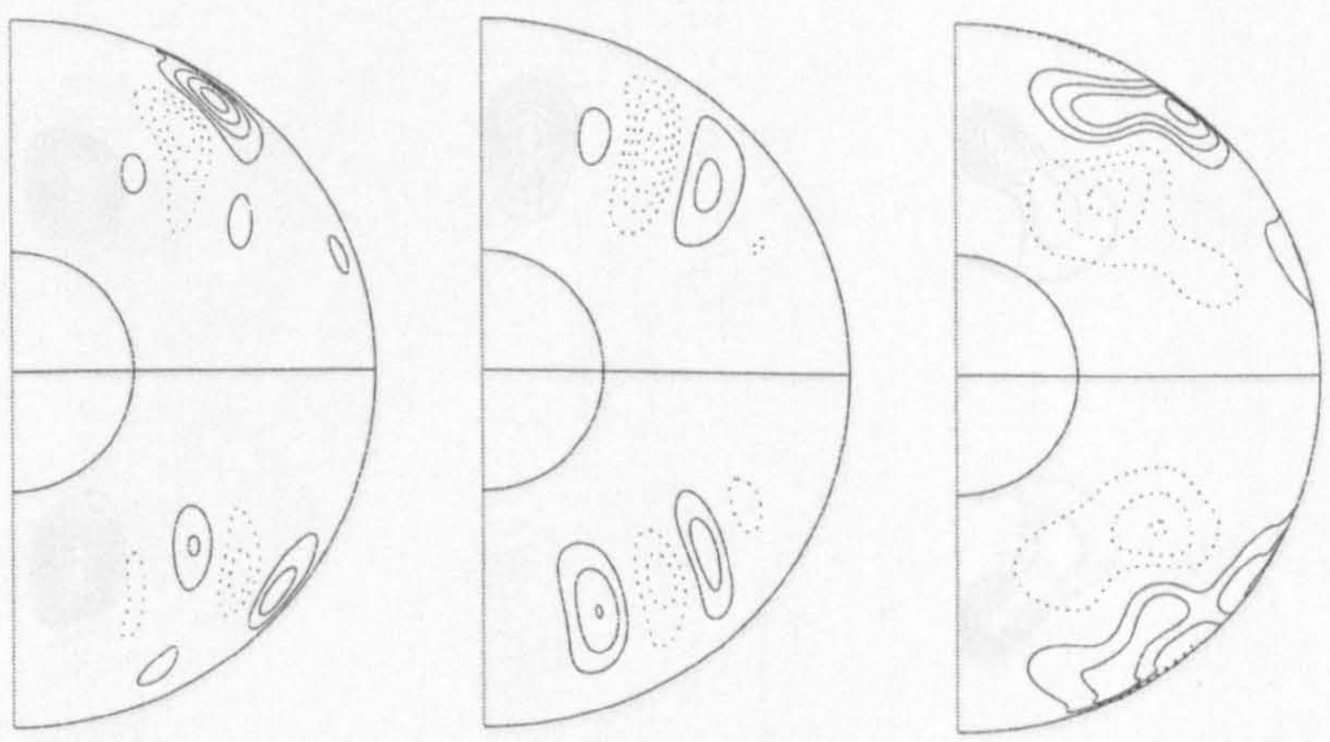

Figure 3.21: As Figure 3.15, but for $\alpha_o = 20$ and $\Theta_o = -200$. The contour intervals are 0.1, 0.2, 20, 0.2 (top, left-right) and 5, 5, 2 (bottom, left-right).

to abstract any further ideas about how the imposed buoyancy force modifies the Lorentz force to equilibrate the system. Despite fixing $\alpha_o = 20$, we see that the forcing within the system is significantly larger for $\Theta_o = \pm 200$ and so one can not deduce that the differences we are seeing are due to changing Θ_o (they could be due to simply increasing the level of forcing). To obtain any feeling for the effect of Θ_o on the solutions, an approach of taking smaller jumps in Θ_o at fixed α_o

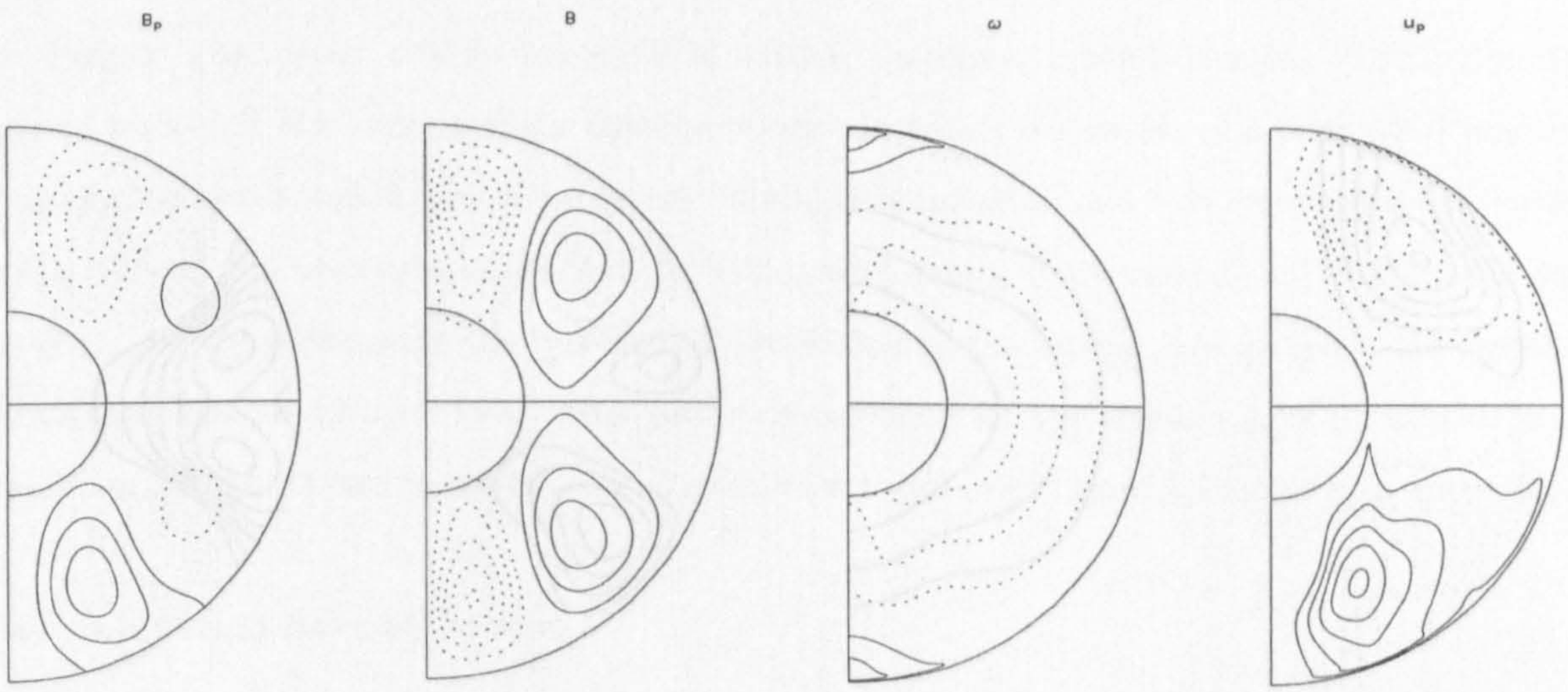

Figure 3.22: As Figure 3.15, but for $\alpha_o = 20$ and $\Theta_o = 100$. The contour intervals are 0.02, 0.1, 20, 0.01 (top, left-right) and 0.5, 2, 0.2 (bottom, left-right).

may be the way forward. We note that whilst we have only shown randomly chosen snapshots of the solution in this discussion, we have examined the behaviour of the contours of the Lorentz force over a period. We find that whilst the magnitude of the components change, the location of the concentrations of each of the Lorentz force components remain confined largely inside the tangent cylinder for $\Theta_o > 0$ and outside the tangent cylinder and close to the equator for $\Theta_o < 0$.

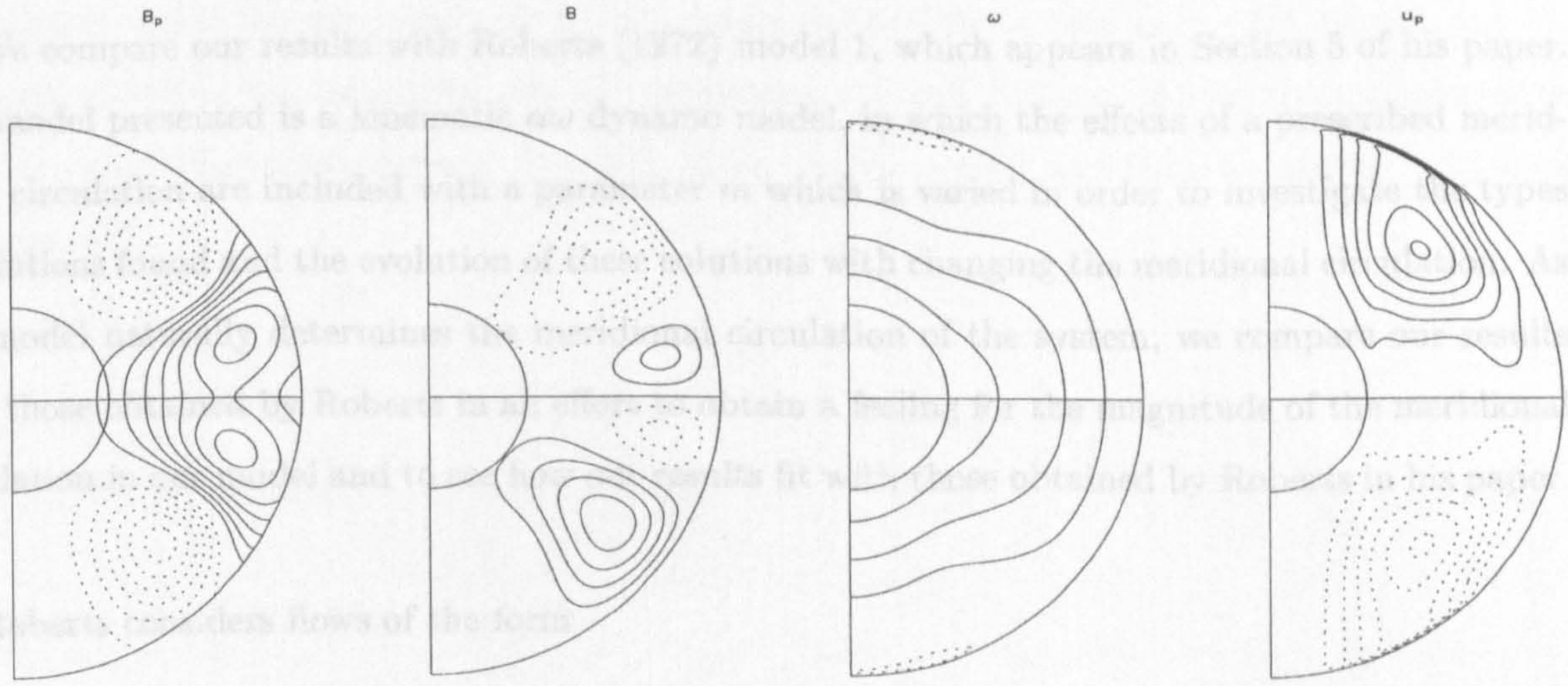

Figure 3.23: As Figure 3.15, but for $\alpha_o = 20$ and $\Theta_o = -100$. The contour intervals are 0.01, 0.1, 20, 0.01 (top, left-right) and 0.05, 0.2, 0.05 (bottom, left-right).

3.9 Comparisons with previous work.

In this section we compare our findings with those of Roberts (1972) (Section 3.9.1) and Hollerbach and Glatzmaier (1998) (Section 3.9.2).

3.9.1 Roberts Model.

We compare our results with Roberts (1972) model 1, which appears in Section 5 of his paper. The model presented is a kinematic $\alpha\omega$ dynamo model, in which the effects of a prescribed meridional circulation are included with a parameter m which is varied in order to investigate the types of solutions found and the evolution of these solutions with changing the meridional circulation. As our model naturally determines the meridional circulation of the system, we compare our results with those obtained by Roberts in an effort to obtain a feeling for the magnitude of the meridional circulation in our model and to see how our results fit with those obtained by Roberts in his paper.

Roberts considers flows of the form

$$\mathbf{U} = \nabla \times t\hat{\mathbf{r}} + \nabla \times \nabla \times s\hat{\mathbf{r}}$$

and chooses a prescribed flow

$$t(r) = \begin{cases} -\frac{3\sqrt{3}}{8} r^2(1-r^2)^2 \mathrm{P}_1(\cos\theta) & \text{for } \alpha\omega' > 0 \\ +\frac{3\sqrt{3}}{8} r^2(1-r^2)^2 \mathrm{P}_1(\cos\theta) & \text{for } \alpha\omega' < 0 \end{cases} \tag{3.5}$$

$$s(r) = \frac{7168\sqrt{2}}{729} m r^6 (1-r)^2 \mathrm{P}_2(\cos\theta), \tag{3.6}$$

$$\alpha(r) = \frac{48\sqrt{3}}{5} r^2(1-r)^2 [\mathrm{P}_1(\cos\theta) - \mathrm{P}_3(\cos\theta)]. \tag{3.7}$$

where ω' is the spatial gradient of the angular velocity, $\omega = v/r\sin\theta$ and α is the parametrisation of small-scale non-axisymmetric flows. The form of α is chosen such that it reaches its maximum value of unity at $r = 1/2$ and $\theta = \cos^{-1}(1/\sqrt{3})$. Likewise the form chosen for the prescribed flow is such that $\omega' = \frac{3\sqrt{3}}{2} r(1-r^2)$ and reaches its maximum value of unity at $r = 1/\sqrt{3}$. Therefore the angular velocity and meridional circulation of the prescribed flow, which are shown in Figure 3.24

are given as,

$$\omega = \frac{v}{r\sin\theta} = \begin{cases} -\frac{3\sqrt{3}}{8}(1-r^2)^2 & \text{for } \alpha\omega' > 0 \\ +\frac{3\sqrt{3}}{8}(1-r^2)^2 & \text{for } \alpha\omega' < 0 \end{cases} \tag{3.8}$$

$$U_p = \psi r\sin\theta = \frac{7168\sqrt{2}}{243} m r^6 (1-r)^2 \cos\theta \sin^2\theta \tag{3.9}$$

Roberts varied the magnitude of the circulation in the flow, considering $-1 \leq m \leq 1$ and established the effect the circulation had on the dynamo process. Roberts plotted the variation of m with the critical Reynolds number, $R = \sqrt{R_\alpha R_\omega} (\propto \sqrt{\alpha_o \Theta_o} = \sqrt{\mathcal{D}})$ and these are shown in Figures 3.26 and 3.27.

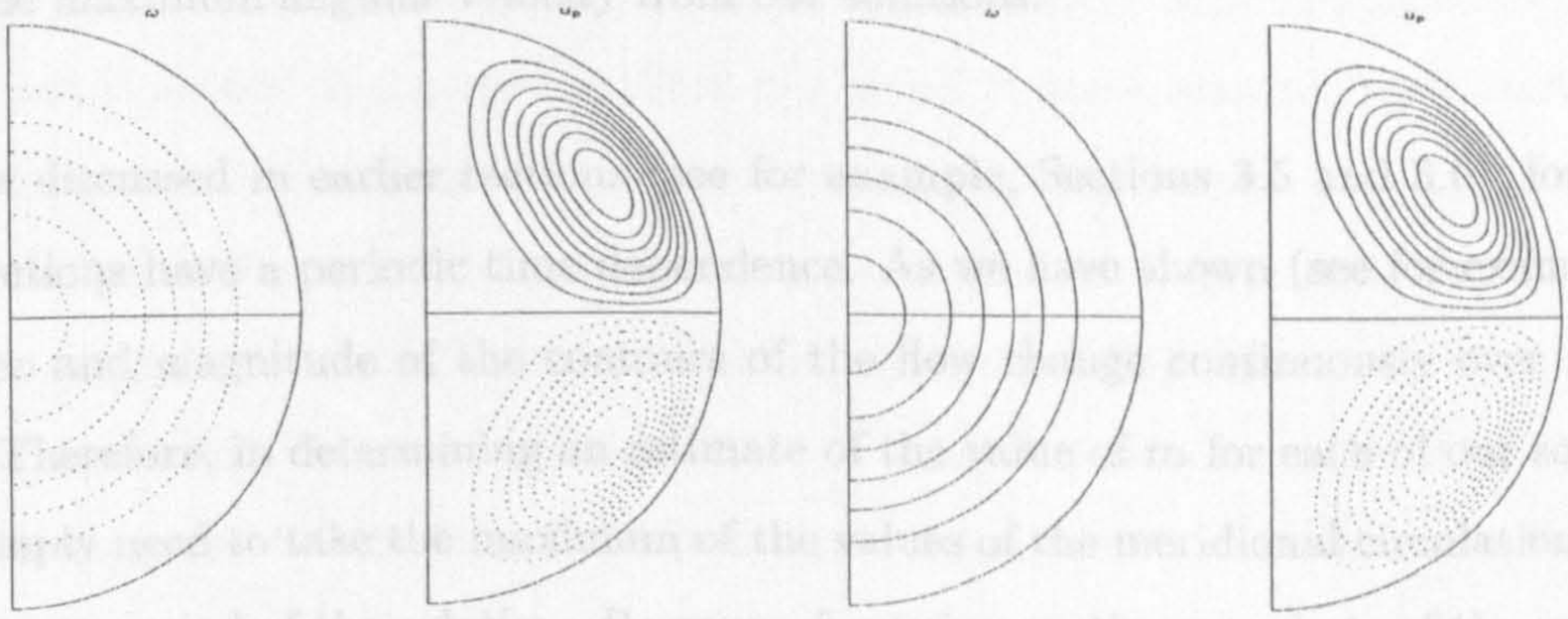

Figure 3.24: The angular velocity and meridional circulation of Roberts prescribed flow. The contour intervals are 0.1 and 0.02, respectively. On the left-hand side we show the flow in the case of $\alpha\omega' > 0$ and on the right-hand side, the case of $\alpha\omega' < 0$. In both cases we have fixed $m = 1$.

To compare Roberts' model, with our own solutions we calculate the maximum value of the meridional circulation and angular velocity for his prescribed flow given in (3.8) and (3.9). These have maximum values,

$$(\psi r\sin\theta)_{\max} = \frac{7}{16\sqrt{6}} m, \quad \text{at } r = 3/4 \text{ and } \theta = \cos^{-1}(1/\sqrt{3})$$

$$(v/r\sin\theta)_{\max} = \begin{cases} -\frac{3\sqrt{3}}{8} & \text{for } \alpha\omega' > 0 \\ +\frac{3\sqrt{3}}{8} & \text{for } \alpha\omega' < 0 \end{cases}$$

In order to estimate the parameter m for our results, we constructed the following ratio. For

the $\alpha\omega' > 0$ case

$$\begin{aligned}
\frac{(\psi r \sin\theta)_{\max}}{(v/r\sin\theta)_{\max}} &= \frac{U_{p\max}}{\omega_{\max}}, \\
-\frac{7/16\sqrt{6}}{3\sqrt{3}/8}m &= \frac{U_{p\max}}{\omega_{\max}}, \\
-\frac{7\sqrt{2}}{36}m &= \frac{U_{p\max}}{\omega_{\max}} \\
\longrightarrow m &= -\frac{18\sqrt{2}}{7}\frac{U_{p\max}}{\omega_{\max}}.
\end{aligned} \tag{3.10}$$

Similarly, in the $\alpha\omega' < 0$ case, $m = \dfrac{18\sqrt{2}}{7}\dfrac{U_{p\max}}{\omega_{\max}}$

where $U_{p\max}$ is the maximum meridional circulation in the northern hemisphere from our results, and $\omega_{\max}$ is the maximum angular velocity from our solutions.

Now as we discussed in earlier sections (see for example, Sections 3.5 and 3.6), for all values of Θ_o, our solutions have a periodic time dependence. As we have shown (see for example, Figure 3.8), the shape and magnitude of the contours of the flow change continuously over a period of the solution. Therefore, in determining an estimate of the value of m for each of our solutions, we would then simply need to take the maximum of the values of the meridional circulation and angular velocity over a period of the solution. However, focussing on the snapshots of the solution over a period, we find that the meridional circulation and angular velocity do not reach their maximum values simultaneously.

Therefore, we proceed by calculating the value of m for each snapshot of a solution over a cycle, and from this find the time variation of m, which of course shares the same period as the solution itself. Figure 3.25 shows an example of the variation of m with time, and as we can see the value of m varies between a maximum and minimum value and so for each data point in Figures 3.28, 3.29 and 3.30 we show the average value, with error bars indicating the amplitude of variation we find in m.

Examining Figure 3.28, we see that our results give an estimate of Roberts' parameter m of $-0.07 \lesssim m \lesssim 0$ for $\Theta_o > 0$ and $-0.08 \lesssim m \lesssim 0.02$ for $\Theta_o < 0$. Comparing these estimates with Roberts' results in Figures 3.26 and 3.27, we see that our results lie firmly within the oscillatory

regime identified by Roberts, with the relative strength of the meridional circulation in our solutions too small to move the solutions into the steady regime. Our solutions appear to favour a negative value of m as forcing is increased in both cases. The sign of m switches for the $\Theta_o < 0$ solutions as the forcing is increased, due to an increase in the negative contours of ω as α_o is increased. These quickly exceed the positive ω contours, thus altering $\omega_{\max}$ from being positive to negative and so changing the sign of m. In the $\Theta_o > 0$ case, as α_o is increased, the negative contours of ω increase reinforcing the existing negative angular velocity contours.

Comparing Figure 3.28 with Roberts' results in Figures 3.26 and 3.27, we see that the parity selection and time dependent nature of our solutions matches Roberts' predictions for values of m close to zero. Our solutions do not appear to lie on the oscillatory branches indicated in Figures 3.26 and 3.27, but it should be remembered that our model is non-linear, whilst Roberts' model is linear and so a precise fit is not expected as the flows are quite different. Our solutions at onset, as shown for example in Figure 2.1, give the best match of Roberts' prescribed flow, allowing us to estimate where our onset solutions lie on Roberts critical curves. The value of m at onset is shown most clearly in Figure 3.29, where we see that $\Theta_o > 0$ solutions produce a value of m which is very close to zero but negative and for $\Theta_o < 0$ solutions, m is again very close to zero and has a positive sign. Another aspect to notice which applies to both Θ_o positive and negative, is the increase in the amplitude of m as $|\mathcal{D}|$ is increased.

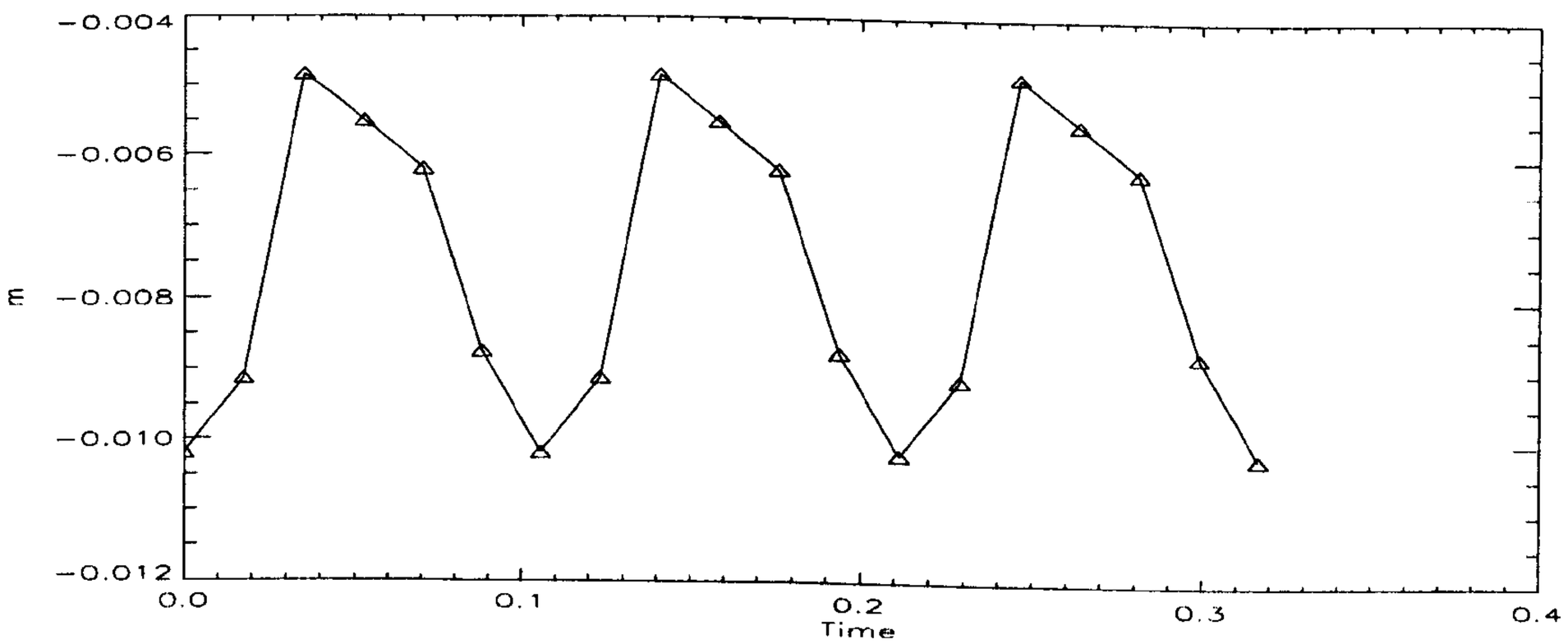

Figure 3.25: The time dependence of our estimated value of m, calculated from the snapshots of the solution over a cycle. Here we take the solution at $\alpha_o = 14$ and $\Theta_o = 200$, as pictured in Figures 3.6 and 3.8.

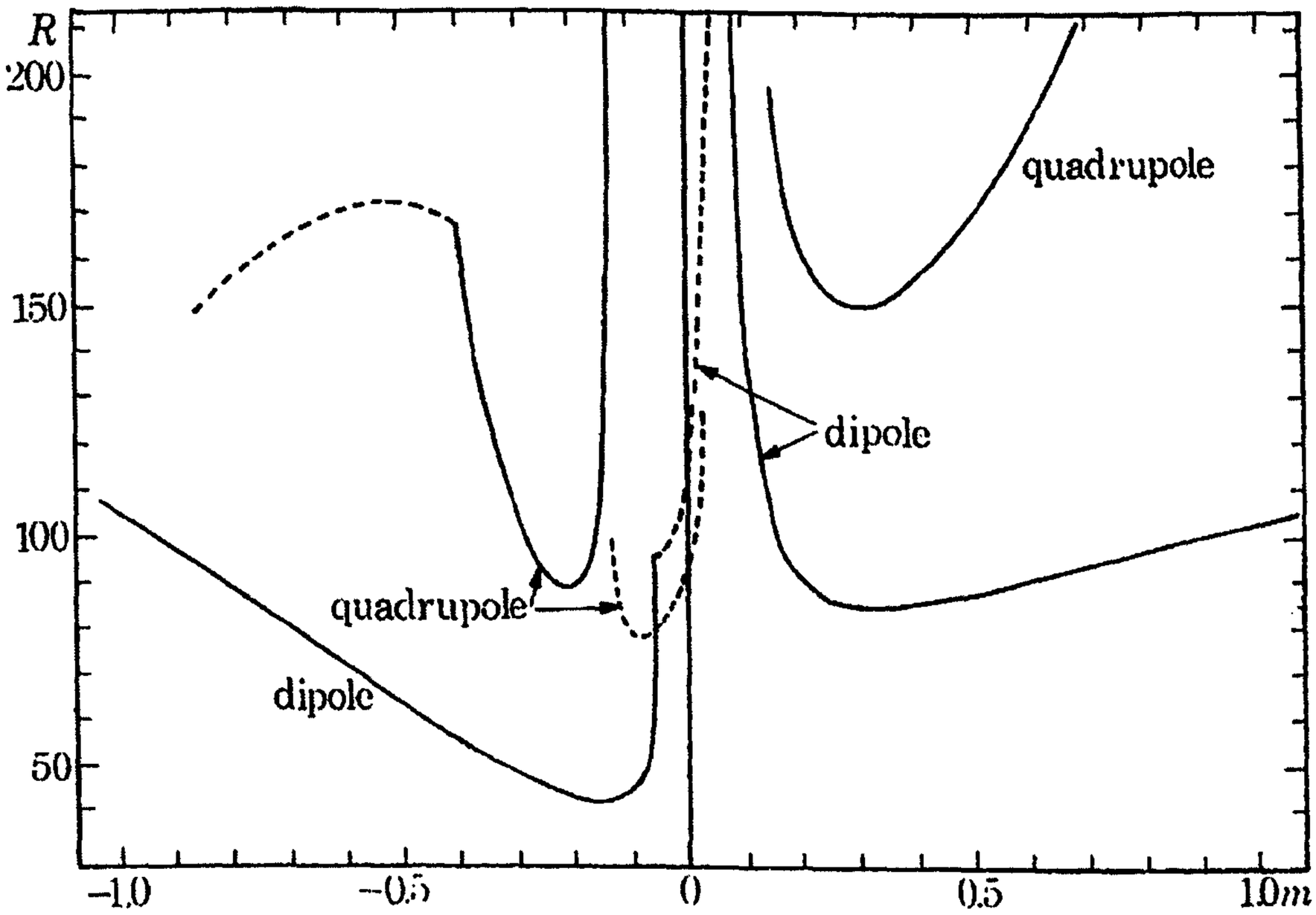

Figure 3.26: Roberts' Figure 7. Equivalent to our $\Theta_o > 0$ case. "The critical Reynolds number, R, as a function of the meridional circulation speed, m, for the Braginsky model, normalised to conform with (3.5)-(3.7). The dashed lines refer to oscillatory modes. the truncation level was 18 harmonics and 20 grid points. It was supposed that $\alpha\omega'$ was positive".

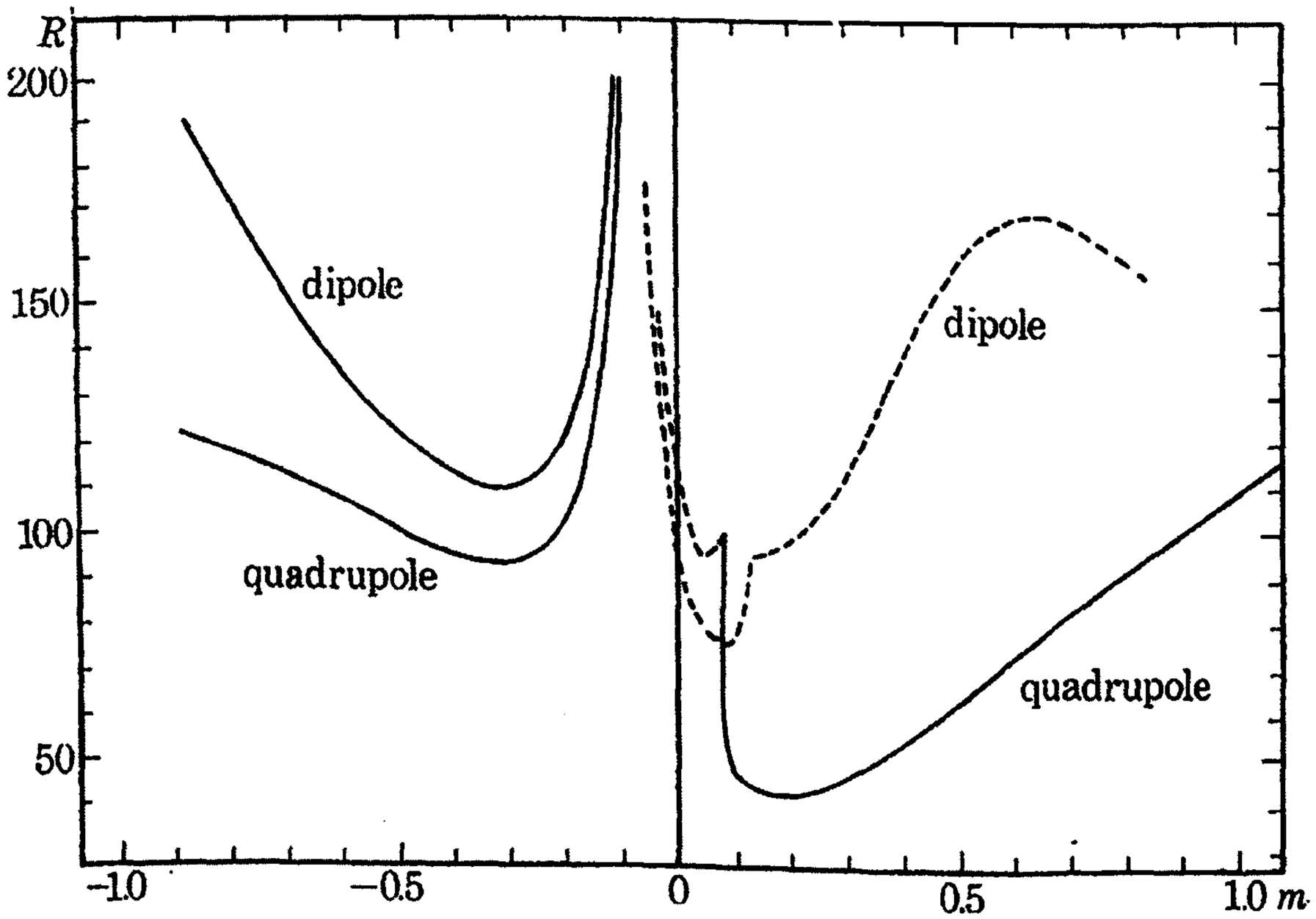

Figure 3.27: Roberts' Figure 8. Equivalent to our $\Theta_o < 0$ case. "The case described in the caption to figure 7 (Figure 3.26 above), except that $\alpha\omega'$ was assumed to be negative".

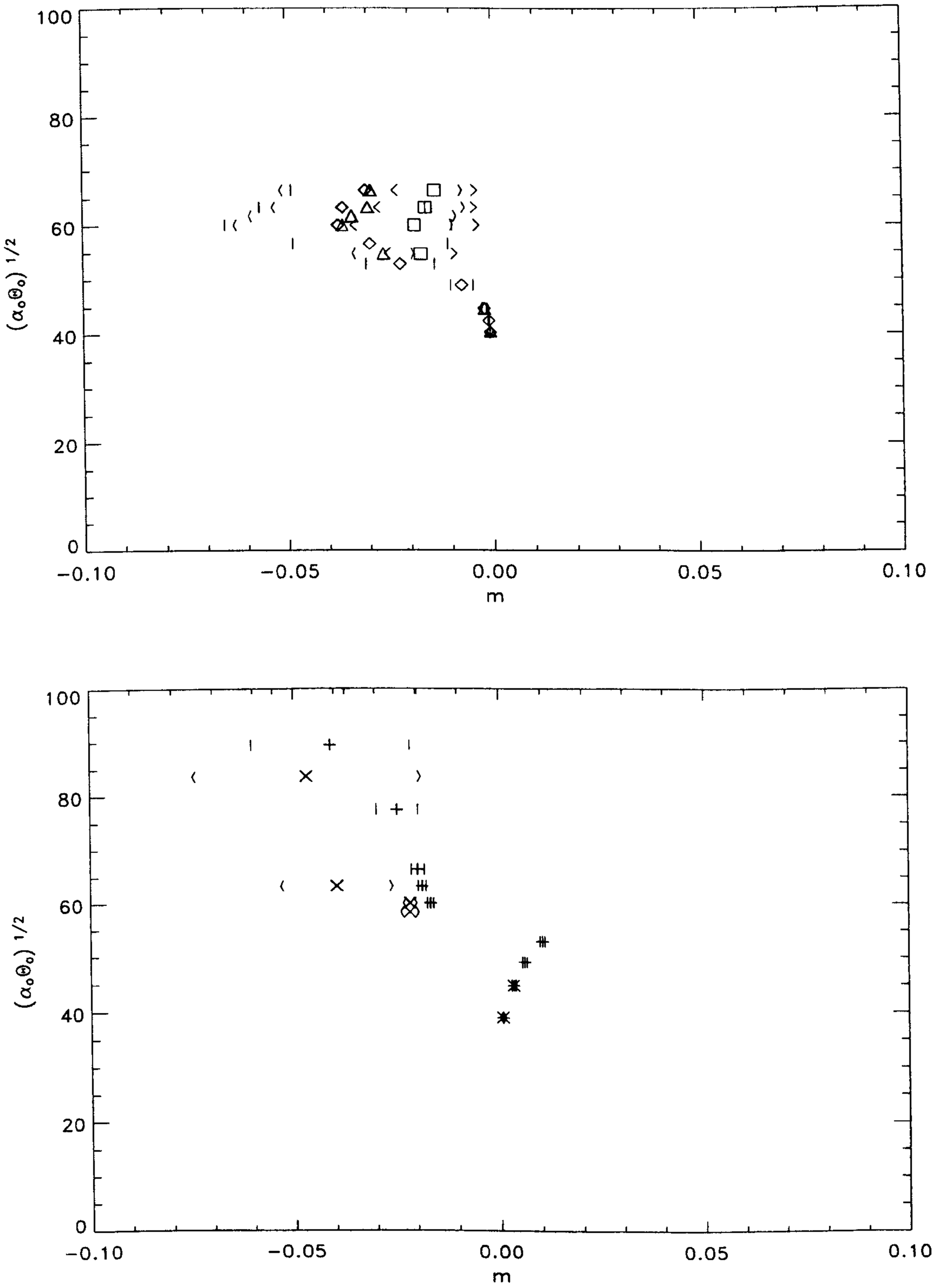

Figure 3.28: Estimates of the Roberts parameter m, for our $\Theta_o > 0$ (top) and $\Theta_o < 0$ (bottom) solutions. As in Figure 3.3, $\Theta_o = 200$: $\diamond$, $\Theta_o = 100$: $\triangle$, $\Theta_o = 50$: $\square$, $\Theta_o = -100$: $\times$ and $\Theta_o = -200$: $+$. Symbols in bold indicate solutions which have bifurcated.

We also examine how our estimates of m varies with α_o. These are shown in Figure 3.29. Focussing on the $\Theta_o > 0$ solutions first, we see that the solutions at onset ($\alpha_c = 8.12$ for $\Theta_o = 200$ and $\alpha_c = 16.4$ for $\Theta_o = 100$) produce values of m close to zero, which as we increase α_o the value of m decreases. At $\alpha_o = 18$ for $\Theta_o = 200$, the value of m reaches a minimum and then increases as α_o is further increased. A similar trend is shown for the solutions at $\Theta_o = 100$ which finds m reaching a minimum at $\alpha_o = 36$ and then increasing again. An interesting point to note is that the $\Theta_o = 200$ and $\Theta_o = 100$ solutions bifurcate at $\alpha_o = 18$ and $\alpha_o = 38$ respectively, which is close to the minimum points of these graphs. However the solutions shown at $\Theta_o = 50$ do not share this behaviour, as they decrease and then increase without reaching a minimum value of m close to the solutions at $\Theta_o = 100$ and $\Theta_o = 200$ and without undergoing a bifurcation.

Examining the behaviour of the $\Theta_o < 0$ solutions, we see that the values at onset ($\alpha_c = 7.57$ for $\Theta_o = -200$ and $\alpha_c = 15.2$ for $\Theta_o = -100$), again produce values of m close to zero. As we increase α_o we see an increase in the value of m, however as commented earlier, once the negative contribution to the angular velocity exceeds the contribution to the positive ω contours, the sign of m switches and we obtain negative values of m for all subsequent values of α_o. The point at which the system bifurcates ($\alpha_o = 18$ for $\Theta_o = -200$ and $\alpha_o = 36$ for $\Theta_o = -100$) almost coincides with the point at which solutions change from m being positive to negative. As α_o is further increased, the value of m decreases.

In Figure 3.30, we replot the data shown in Figure 3.29 where we instead plot the variation of m with $|\mathcal{D}|$. This enables us to easily compare the variation between each of the values of Θ_o. For $\Theta_o > 0$, we are able to see very clearly that the $\Theta_o = 200$ and $\Theta_o = 100$ solutions are exhibiting the same trend in the variation with m, with the solutions at $\Theta_o = 50$ producing quite different results. For $\Theta_o < 0$, we see very good agreement between the solutions at $\Theta_o = -200$ and $\Theta_o = -100$ at small values of $|\mathcal{D}|$, where the values of m coincide. At the larger values of $|\mathcal{D}|$ the agreement between the solutions is not nearly as good as we found in the case of $\Theta_o > 0$, however the solutions do exhibit the same decreasing trend in m as $|\mathcal{D}|$ is increased.

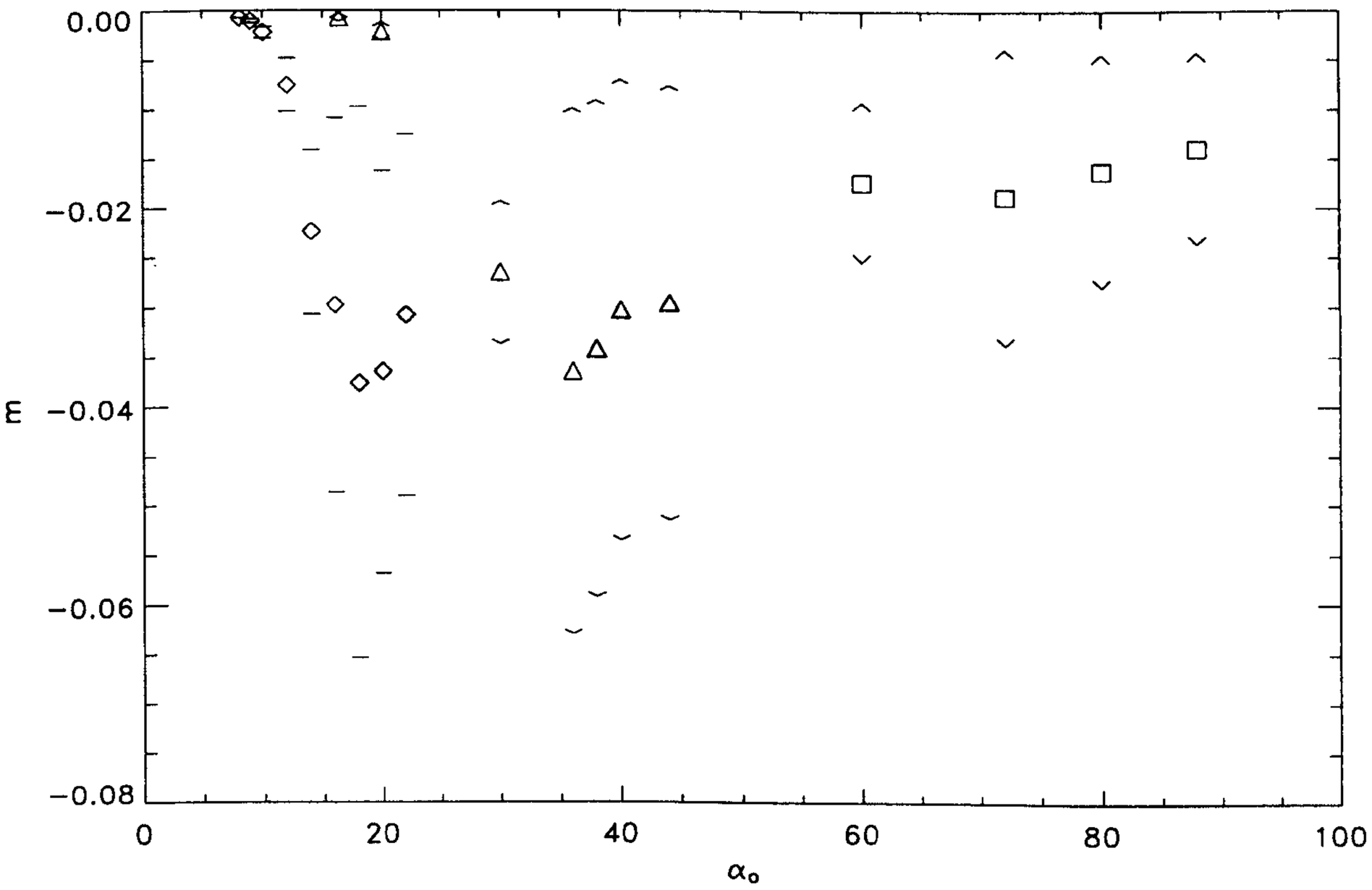

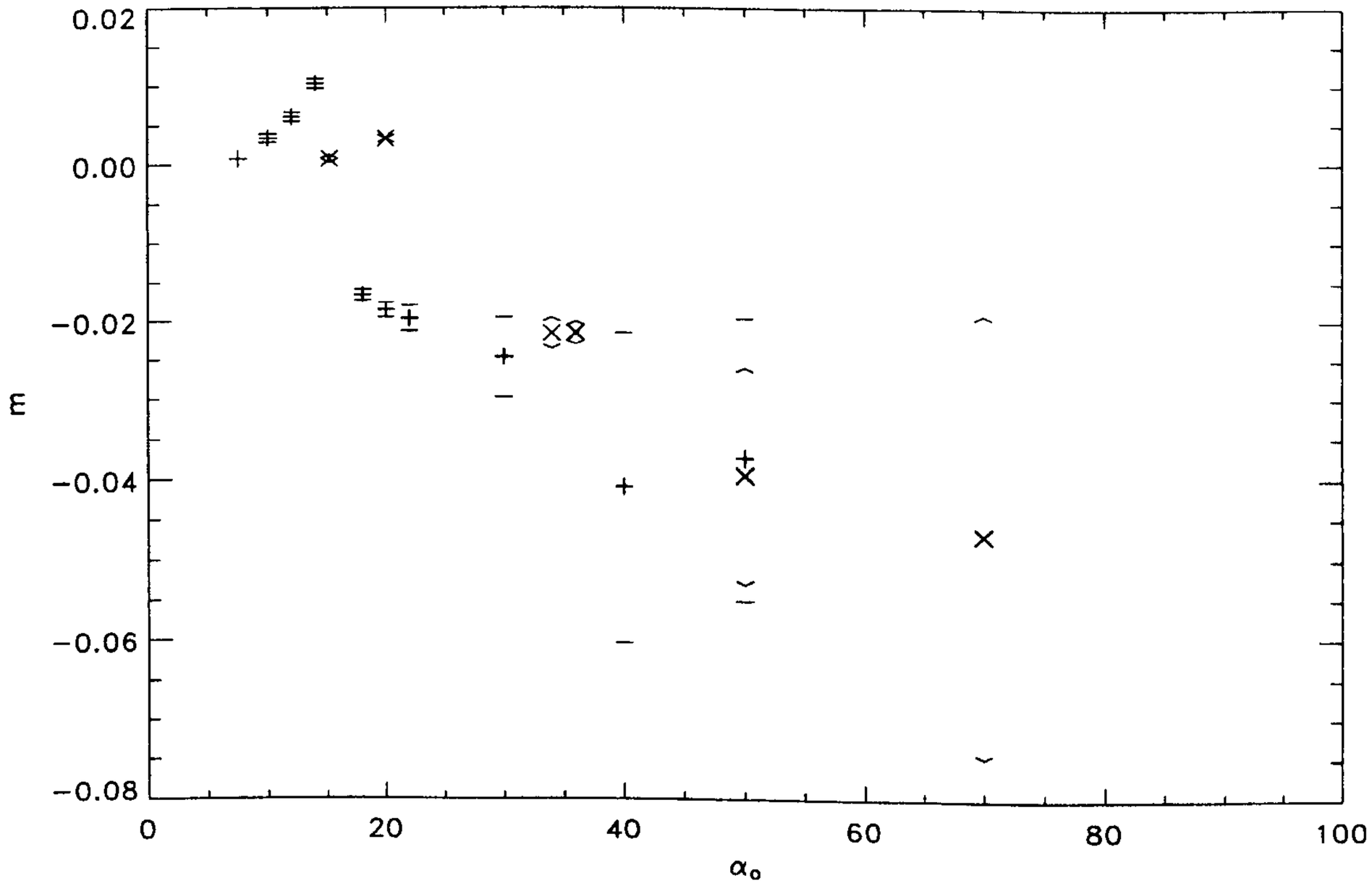

Figure 3.29: Variation of the Roberts parameter m, with α_o for our $\Theta_o > 0$ (top) and $\Theta_o < 0$ (bottom) solutions. As in Figure 3.3, $\Theta_o = 200$: $\diamond$, $\Theta_o = 100$: $\triangle$, $\Theta_o = 50$: $\square$, $\Theta_o = -100$: $\times$ and $\Theta_o = -200$: $+$. Symbols in bold indicate solutions which have bifurcated.

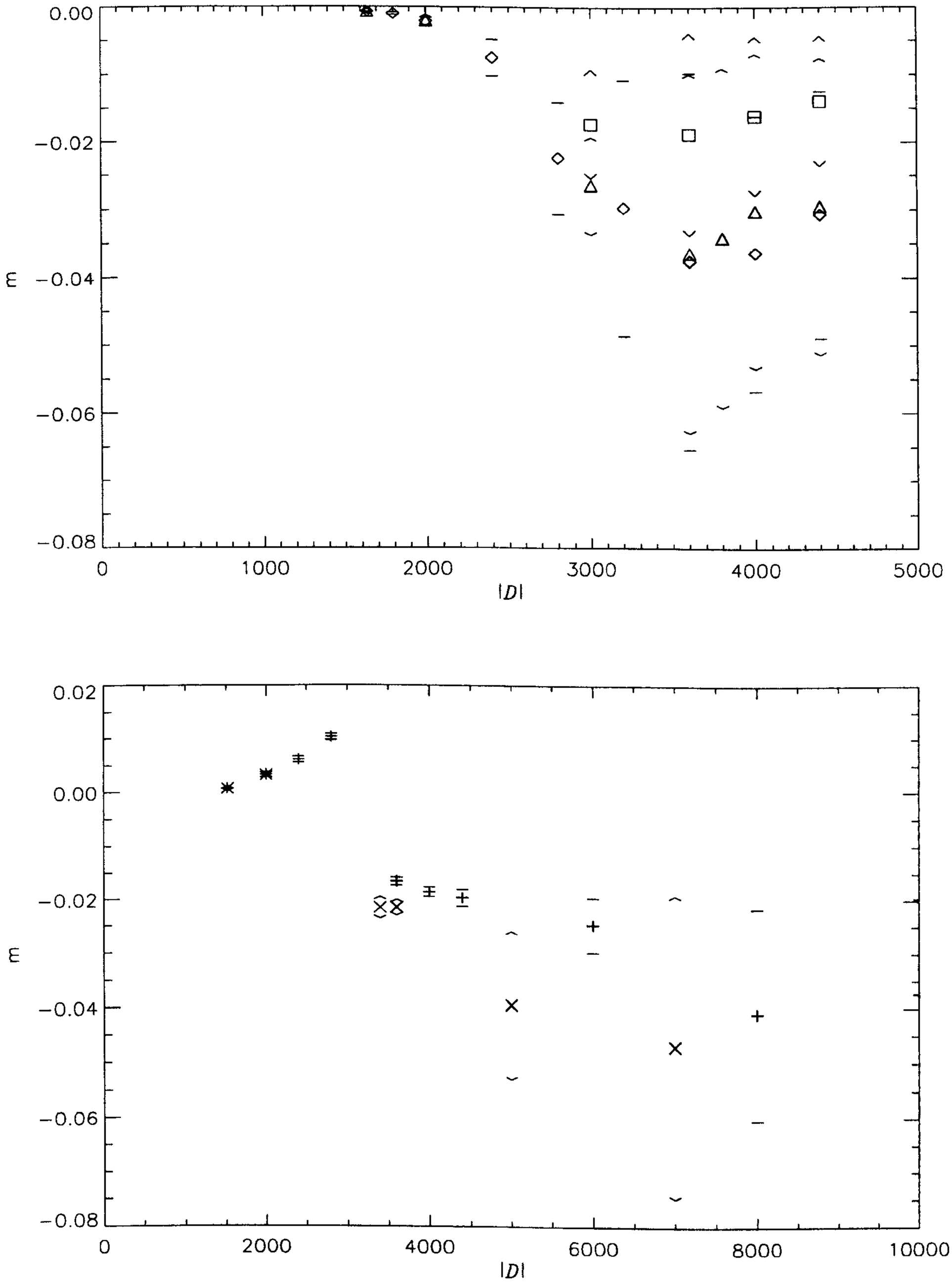

Figure 3.30: Variation of the Roberts parameter m, with $|\mathcal{D}|$ for our $\Theta_o > 0$ (top) and $\Theta_o < 0$ (bottom) solutions. As in Figure 3.3, $\Theta_o = 200$: $\diamond$, $\Theta_o = 100$: $\triangle$, $\Theta_o = 50$: $\square$, $\Theta_o = -100$: $\times$ and $\Theta_o = -200$: $+$. Symbols in bold indicate solutions which have bifurcated.

3.9.2 Hollerbach & Glatzmaier's model.

We may compare our results with those obtained in the Hollerbach and Glatzmaier (1998) paper. As noted earlier, the model we presented in Chapter 2 is the same as that used in their paper, with the difference lying in the form of the α-effect considered. We also note that the Ekman number, E, is 5×10^{-4} in their model, and for most of our calculations in this chapter our Ekman number is fixed at 1×10^{-4}. In the course of our research, we had hoped to be able to extend Hollerbach and Glatzmaier's results by lowering the value of the Ekman number, so that it was in line with our own results. Unfortunately, we ran into resolution difficulties at parameter values of $\alpha_o = 50, \Theta_o = 200, E = 1 \times 10^{-4}$, and were unable to obtain an equilibrated solution. However, as Figure 3.1 showed, the dependence of the solutions upon E is not significant and so whilst a lower Ekman number may cause slight differences in equilibrated magnetic energies, for example, and slight changes in the point at which bifurcations occur, the general behaviour of the solutions remains unchanged.

Comparing Hollerbach and Glatzmaiers' solutions with our own we see that in both cases the onset occurs as quadrupole parity dynamo waves which propagate from the equator to the poles. These (now well established) aspects of dynamo models, were discovered by Roberts (1972) as noted in Section 3.2. However, we note that the direction of propagation of the dynamo waves is independent of the parity of the solutions and is determined by the direction of the forced differential rotation, i.e. the sign of Θ_o. This is clearly shown in the solutions by Hollerbach and Jones (1993b,1995), whose dipole imposed parity solutions occur as dynamo waves which propagate from the equator to poles. This is also seen, for example, in the $\alpha\omega$ dynamo models considered by Hollerbach *et al* (1992), and Anufriev and Hejda (1998).

Comparing the onset of dynamo action in the two models, we see that at $E = 5 \times 10^{-4}$, the $\alpha = \alpha_o \cos\theta$ model onsets first at $\alpha_c \sim 6$, with onset occurring in the $\alpha = \alpha_o \cos\theta \sin(\pi(r - r_i))$ model around $\alpha_c \sim 8.3$. This difference is not unexpected as the average value of α in the $\alpha = \alpha_o \cos\theta \sin(\pi(r - r_i))$ case is lower than in the $\alpha = \alpha_o \cos\theta$ case, and so one would expect the onset to occur at a higher value of α_o in the $\alpha = \alpha_o \cos\theta \sin(\pi(r - r_i))$ case. The period of the solution at onset is similar; Hollerbach and Glatzmaier find $T = 0.22$, whilst we find $T = 0.24$.

Beyond the onset of dynamo action we compare the field structures between the two models. An exact comparison of these models is made more difficult as Hollerbach and Glatzmaier (1998) do not reveal the magnetic energy of their solutions. Therefore, in comparing their solution at $\alpha_o = 10$, we choose a value of α which produces solutions with broadly similar magnitudes, which we deduce will have a comparable magnetic energy. We find that choosing an $\alpha_o = 14$, produces a good comparison. Figures 3.6(a) and 3.8 show the appropriate solution, plotted over its period, $T = 0.21$. Comparing this solution with Figure 1 of Hollerbach and Glatzmaier (1998), we find the solutions are qualitatively the same. Solutions are, as expected, quadrupole dynamo waves which propagate from the equator to pole.

Hollerbach and Glatzmaier's model then bifurcates at $\alpha_o \approx 11$, where solutions then become of mixed parity. They show a solution at $\alpha_o = 15$ in Figure 2 of their paper. Our model bifurcates at $\alpha_o \simeq 18$, to solutions which have a slightly different periodic time behaviour, but which retain their quadrupole parity, as shown in Figures 3.6(b) and 3.9. It is here that we establish that the different α-effect is making a substantial difference to the solutions.

As we have shown, the solutions at onset and at low levels of forcing have produced qualitatively similar solutions for both forms of α. As α_o is increased and the system undergoes a bifurcation, we see the difference in the form of the α-effect results in a change in the nature of the solutions. The fact that the radial structure introduced to the α-effect does not take effect until α_o is sufficiently large seems very natural, and this is also found in the work by Fearn and Rahman (2004a). Hollerbach and Jones (1993a) presented an α^2-type model, which used $\alpha = \alpha_o \cos\theta$. This model was extended by Fearn and Rahman (2004a) who using $\alpha = \alpha_o \cos\theta \sin(\pi(r - r_i))$ found that at onset and small values of α_o, the solutions they obtained were qualitatively similar. Fearn and Rahman's model then bifurcated as α_o was further increased, and an unusual spiky periodic behaviour set in. In Hollerbach and Jones model, they considered only α_o up to 8, but their model was extended by Rahman (2003) up to $\alpha_o = 22$ who finds that no bifurcation occurs.

3.10 Conclusions.

In this chapter we investigated a number of aspects of our $\alpha\omega$-type dynamo model. This served a number of purposes; this enabled comparisons with previous linear and non-linear $\alpha\omega$ models and also provided us with a solid reference case for the work including inertia in the following chapter. To conclude this chapter, we will summarise the main findings of each section in turn and then finally place our model in the context of mean-field dynamos and its relevance to earlier work.

Unlike α^2-type dynamo models at the onset of dynamo action, which consist of solving the induction equation in the absence of a flow for α_c, the $\alpha\omega$-type model is a more complex system, since from the outset, we are driving a flow in the momentum equation via the prescribed buoyancy force. This therefore introduces the effects of viscosity into the system. In Section 3.3 we investigated the extent to which viscosity plays a role in the equilibration of the dynamo at onset. Our results show that as E is decreased towards zero (and its geophysically appropriate value $\sim O(10^{-15})$), our findings are consistent with α_c approaching a constant (non-zero) value.

We also examined the onset of dynamo action for 4 different values of Θ_o. As discussed in Chapter 2, analysis of linear $\alpha\omega$ models revealed that the behaviour of the dynamo may be characterised by a single parameter named the dynamo number, $\mathcal{D}$. The dynamo number, determined as the product of the magnitude of the prescribed forcings, α_o and Θ_o, naturally allowed the governing equations of such models to be rescaled. As we showed in Section 2.9, our governing equations made such a rescaling impossible, even at the onset of dynamo action when the system is linear and the Lorentz force is negligible. Therefore, we were interested in seeing to what extent the parameter remained a useful measure in the system. In the literature (see for example Hollerbach *et al* (1992) and Anufriev and Hejda (1998)), it has been established that the cases for positive and negative $\mathcal{D}$, are quite different, however in many cases dipole symmetry is imposed on the solutions which will affect the natural parity of the solutions and the ensuing bifurcation sequence. Our analysis in Section 3.4, in which we consider the dependence of the system on α_o and Θ_o at the onset of dynamo action, confirmed this result. In Section 2.9 we examined the governing equations and found that they did not scale exactly with $\mathcal{D}$. However focussing on the onset of dynamo action revealed that we have good agreement between the values of $\mathcal{D}_c$, which suggests that the equations

are close to scaling with $\mathcal{D}$. Therefore despite α_o and Θ_o requiring to be specified independently, $\mathcal{D}$ remains a useful measure in the system. Increasing α_o beyond onset for each value of Θ_o considered, the difference in the sign of $\mathcal{D}$, becomes much more apparent. The bifurcation sequences of the solutions for $\mathcal{D} > 0$ and $\mathcal{D} < 0$, are described in detail in Sections 3.5 and 3.6, respectively.

In examining the solutions for $\mathcal{D} > 0$ and $\mathcal{D} < 0$, we were interested in understanding the way in which the buoyancy force acts upon the system, and the influence this has on the equilibrating Lorentz force. We found that the distribution of the Lorentz force, either near the poles or close to the equator, depended on the sign of $\mathcal{D}$, and was independent of the parity of the solutions.

Finally, we focussed in on how our solutions compared with other models. Specifically we looked at Roberts (1972) study and the findings of Hollerbach and Glatzmaier (1998). Roberts presents a linear $\alpha\omega$ model, and includes a prescribed flow, which generates a meridional component of the flow, which he allows to have a variable magnitude, m. We compared our magnitudes of meridional circulation and found that we have qualitative agreement with his model and find that for all our results, our estimates of m remain very small; lying between ± 0.08, which is within the regime identified by Roberts in which the strength of meridional circulation is not large enough to make solutions steady. We also compared with the Hollerbach and Glatzmaier (1998) model, as this is exactly the same model as we use, only we include a radial distribution in the form of the prescribed α-effect. Drawing parallels with α^2 studies, which compare the same two α-effects and are in all other ways equal, we are able to deduce the differences caused by introducing a radial structure in α. We find that including this radial form into the prescription of the α-effect only changes the form of the solutions once the strength of α_o is sufficiently large.

Chapter 4

$\alpha\omega$-dynamos with inertia.

4.1 Introduction.

In this chapter we investigate the effect of inertia on the $\alpha\omega$-type model we introduced in Chapter 3. The motivation for this study stems from the work by Fearn and Rahman (2004b) who, through their investigation of the effect of inertia on their α^2-type dynamo model, found that as the strength of inertia was increased, this enabled dynamo action to occur more easily. This result conflicted with results found in 2.5D and 3D models (see for example, Fearn and Morrison (2001), Christensen *et al* (1999)) which found that increasing the strength of inertia caused the dynamo to fail. In the α^2-type model considered by Fearn and Rahman (2004b), the dynamo is driven by the prescribed α-effect which is unaffected by inertia. Therefore we consider the effect of inertia on our $\alpha\omega$-type dynamo model, where an ω-effect is driven by the prescribed buoyancy force, Θ. In our $\alpha\omega$-type model, the α-effect will be unaffected by inertia as in the α^2-case, however, inertia is now able to influence the ω-effect through the balance of the momentum equation. Our $\alpha\omega$-type model is then intermediate to the α^2-type model and the 2.5D hydrodynamic model. Since our $\alpha\omega$-type model is just 2D but contains much of the physics considered important to the dynamo mechanism, it is hoped that it is simple enough that it may enable us to better understand the physical implications of introducing inertial effects into the system, and possibly reconcile Fearn and Rahman's results with the 2.5D and 3D models.

4.2 Background

Fearn and Morrison (2001) investigated the effect caused by the introduction of inertia into a hydrodynamic geodynamo model. They include the effects of a finitely conducting inner core in a 2.5D model, which has full resolution in the radial and colatitude directions r, θ, but which is severely truncated in the azimuthal direction, ϕ. The resolution chosen in the azimuthal direction is simply the $m = 0$ mode and the $m = m_1 = 2$ mode, thus including only a single non-axisymmetric mode, which is sufficient to prevent Cowling's theorem coming into play. Fearn and Morrison, systematically increase the strength of inertia, $E_\eta = \frac{Ro}{2}$, fixing all other parameters in the system, enabling them to see how the magnetic and kinetic energy in the system vary with Ro. They found that there existed an oscillatory weak field branch for $1 \times 10^{-4} \leq Ro \leq 2 \times 10^{-4}$ and a chaotic strong field branch for $2 \times 10^{-4} \leq Ro \leq 1 \times 10^{-3}$. Beyond $Ro = 1 \times 10^{-3}$ no solutions were found and dynamo action fails. In the weak field branch they find the solutions match up well with the inertialess solution obtained using a different code and observe the trend that with increasing Ro, there is an increase in magnetic energy. Beyond $Ro \sim 2 \times 10^{-4}$, solutions switch to the chaotic strong field branch, which show a decrease in magnetic energy until around $Ro \sim 1 \times 10^{-3}$ when no further solutions are found and dynamo action stops. Their explanation of this inertia dependent behaviour is as follows; at zero or small values of Ro, the magnetic energy undergoes a rapid growth and decay pattern, by increasing the strength of inertia, this slows down the feedback between the field and flow, allowing the field to grow in strength. However, further increasing the strength of inertia, causes the inertia term in the momentum equation to have a more significant role, thus altering the force balance and making it harder to generate a magnetic field. They then investigated the effect caused by varying the magnitude of the (modified) Rayleigh number Ra. This term changes the importance of the buoyancy force in the momentum equation and therefore varying this term could help compensate for the high levels of inertia in the system. For investigating the effect of inertia, $Ra = 50$; therefore, as a test of whether the strength of the buoyancy force driving the flow, could act to prevent the system from decaying and cutting off dynamo action, they considered $Ra = 45$ and 55. At $Ra = 45$, they found similar behaviour to the case at $Ra = 50$, but of a slightly lower magnitude. Increasing Ra to 55, however results in a solution which is quite different. The solution at higher Ra has a much more steady field of a higher average amplitude. The solutions at higher Ra are no longer reversing dynamo solutions and their field structure reveals that solutions

have become more asymmetric with more field diffusing into the inner core. Despite increasing Ra, as Ro is increased dynamo action still shuts off.

Christensen *et al* (1999), present details of a parameter study of a 3D hydrodynamic dynamo model and investigate the dependence of solutions on different non-dimensional parameters. They find that through examining the boundary between stable and decaying solutions for different values of the Ekman number, E as a function of the (modified) Rayleigh number Ra (see Section 1.3 for a definition) and the magnetic Prandtl number Pm $(= \frac{E}{Ro})$, that there exists a minimum magnetic Prandtl number below which dynamo action does not occur, obtaining the approximate relation $Pm_{crit} = 450E^{3/4}$. They also found that dynamo action occurred when Ra exceeded some critical value, and that this critical value is increased at low magnetic Prandtl number. However, if Ra is too large for a given value of Pm, dynamo action dies out. This finding is in keeping with the 2.5D results of Fearn and Morrison, who find equivalently that as Ro is increased (at fixed E), dynamo action shuts off.

Fearn and Rahman (2004), consider a mean-field α^2-type dynamo model, including the full inertia term, similar to the model we describe in Chapter 2, but in the absence of the prescribed buoyancy force. They find that, through increasing the strength of inertia, Ro, from close to zero (where they obtain very good agreement with the solution at $Ro = 0$, which is found using an independent code), the solutions begin with dipole parity solutions which exhibit an unusual 'spiky' time dependence (see Section 5.2, for further details). As the strength of inertia is increased, these spiky solutions give way to steady solutions around $Ro \sim 2 \times 10^{-2}$ which retain their dipole parity. Beyond $Ro = 2 \times 10^{-2}$ solutions were steady, and as they gradually increase Ro, they observe a roughly linear increase in the magnetic and kinetic energy of the steady solutions until $Ro \sim 8 \times 10^{-2}$. For $Ro \gtrsim 8.5 \times 10^{-2}$ the solutions become chaotic. Fearn and Rahman's results in this model find that the effect of inertia actually acts to aid the production of magnetic field. This unexpected result could prove very revealing about the nature of the dynamo process and may help us to better understand the exact mechanisms present which act to inhibit dynamo action. Fearn and Rahman suggest that the failure of hydrodynamic models may be due to a more-than-compensating reduction in convective vigour or a reduction in the effectiveness of convection in

generating magnetic field as inertia is increased. Here we consider our $\alpha\omega$-type model including the effect of inertia, and investigate how the solutions vary with Ro and how they compare with Fearn and Rahman's α^2-type model and the 2.5D and 3D hydrodynamic models. As our comparatively simple model includes most of the essential physics of the dynamo problem, it may be possible to determine the reasons for the decay of the hydrodynamic models as inertia is increased and the ability of inertia to facilitate dynamo action in Fearn and Rahman's α^2-type model.

4.3 Energy variation with increasing Ro.

In Chapter 3 we investigated the behaviour of our $\alpha\omega$-type dynamo and its dependence on the parameters α_o and Θ_o. Here we investigate the effect of increasing the strength of inertia on a solution at fixed α_o, Θ_o and E. We focus on solutions at $\alpha_o = 30$, $\Theta_o = 100$ and $E = 2.5 \times 10^{-4}$.

As we gradually increase inertia from $Ro = 1 \times 10^{-5}$, we see a natural progression from the inertialess solution obtained using the model in Chapter 3. These solutions retain their quadrupole parity up to $Ro = 5 \times 10^{-3}$. The solutions then go through a transition region for $5 \times 10^{-2} < Ro < 7 \times 10^{-2}$. We examined the solutions at $Ro = 5.5 \times 10^{-2}$ and $Ro = 6 \times 10^{-2}$ and found that the solutions exhibited a more complex time dependence (different in each case) and have a mixed parity.

Increasing the strength of inertia to $Ro = 7 \times 10^{-3}$, we find the system has bifurcated onto a new branch of solutions which have dipole parity. This sequence of bifurcations is shown in Figures 4.1 and 4.2, where we plot the variation of the magnetic and kinetic energy of the solutions with increasing Ro.

As we increase the strength of inertia, we see in Figure 4.2 an almost linear variation of the kinetic energy with Ro, which is expected given the equation for the kinetic energy in (2.51). The magnetic energy variation with Ro, shown in Figure 4.1, is quite different. The magnetic energy variation of the quadrupole parity solutions found for $0 \leq Ro \leq 5 \times 10^{-2}$ initially increases quite steeply with increasing Ro and then decreases more slowly as we continue to increase Ro. The solutions then become mixed parity, as the system makes the transition from quadrupole to dipole

parity solutions. For the dipole parity solutions found for $7 \times 10^{-2} \leq Ro \leq 1.1 \times 10^{-2}$ we see a similar behaviour in the magnetic energy variation as we observed for the quadrupole solutions. Here the magnetic energy of the solutions initially increases, though not as steeply as we see in the quadrupole parity region, and then decreases sharply as Ro is increased.

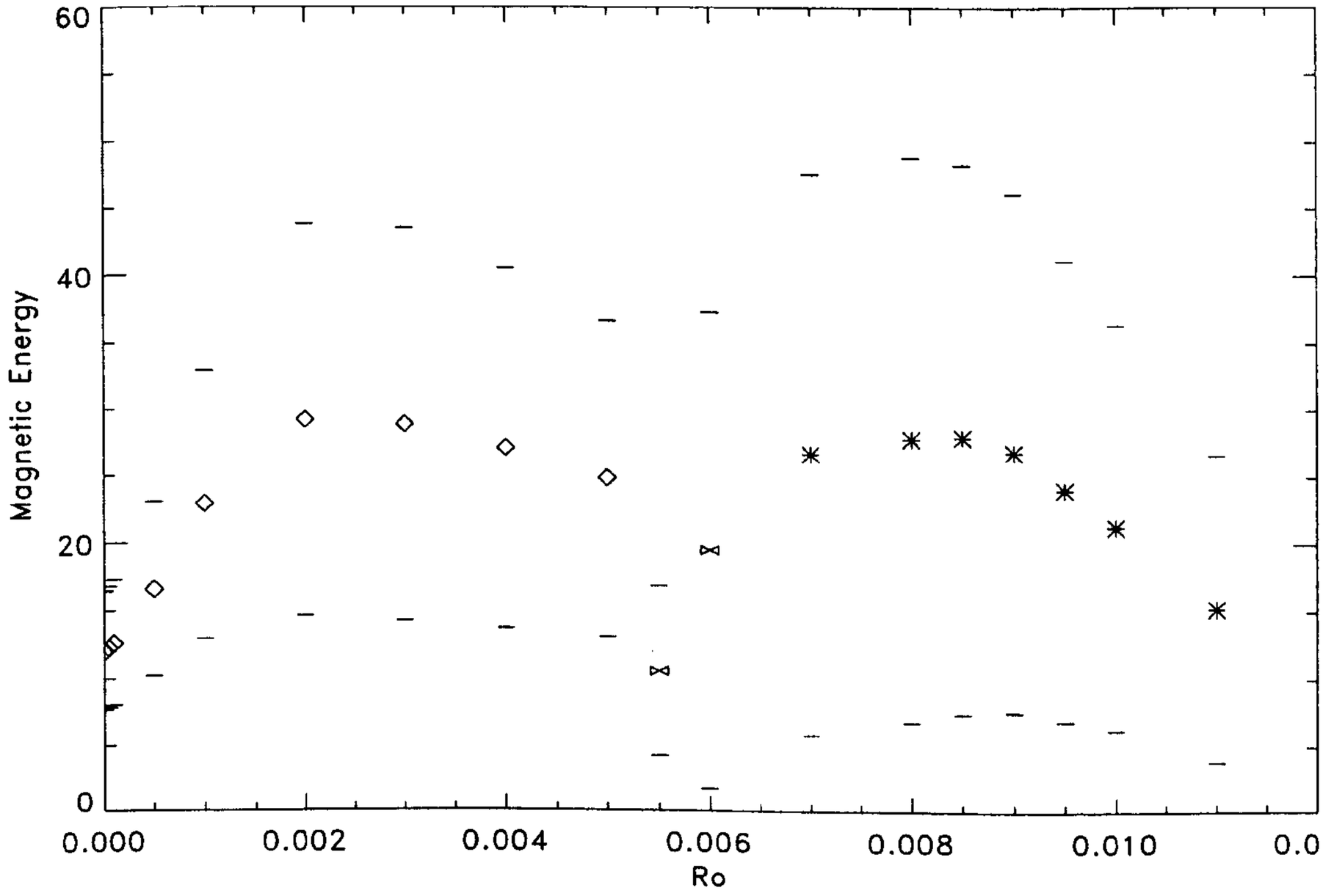

Figure 4.1: Plot of the variation of the average magnetic energy with Ro. 'Error bars' indicate the maximum and minimum amplitudes of the oscillatory solutions. The $\Diamond$ denote solutions which have a quadrupole parity, $\bowtie$ show mixed parity solutions in the transition region and $*$ denotes dipole parity solutions. For all solutions shown above, $\alpha_o = 30, \Theta_o = 100$ and $E = 2.5 \times 10^{-4}$.

Obtaining solutions as we increase Ro, proved to be quite difficult. The solutions we used as initial conditions for subsequent runs at higher inertia needed to be well resolved spatially and fully equilibrated in time. Even taking these factors into consideration, if too large a step was taken in Ro, we found that the solution would decay away to zero. We also ran into difficulties with the timestep at which the code would run. As inertia is increased, the solutions changed much more rapidly in time, developing a ragged appearance. In order to resolve this rapidly changing time behaviour, we attempted to reduce the timestep at which we ran the solutions. We found that we were unable to reduce the timestep below 4×10^{-6}, a timestep lower than this value resulted in the

solution blowing up. In the dipole region of Figure 4.1, we are unable to follow the solution beyond $Ro = 1.1 \times 10^{-2}$, as the values of Ro we considered resulted in a solution which decayed away to zero. It is of course possible that we are simply unable to find solutions beyond this point and that the strength of inertia is such that it inhibits dynamo action sufficiently to cut it off altogether, as this has been the finding of other models, for example the 2.5D hydrodynamic model of Fearn and Morrison (2001) or the 3D model of Christensen *et al* (1999). However, given the sensitivity of the model to the initial conditions and our inability to reduce the timestep below 4×10^{-6}, we believe that Figure 4.1 suggests that the dynamo mechanism is being inhibited by the increasing strength of inertia, but whether it shuts off the dynamo altogether at this point is unclear. We do note however, that the solution we obtain at $Ro = 1.1 \times 10^{-2}$ has evidence of becoming slightly mixed in parity, and it may be the generation of a non-dipole contribution in the system which leads to the decay of the solutions.

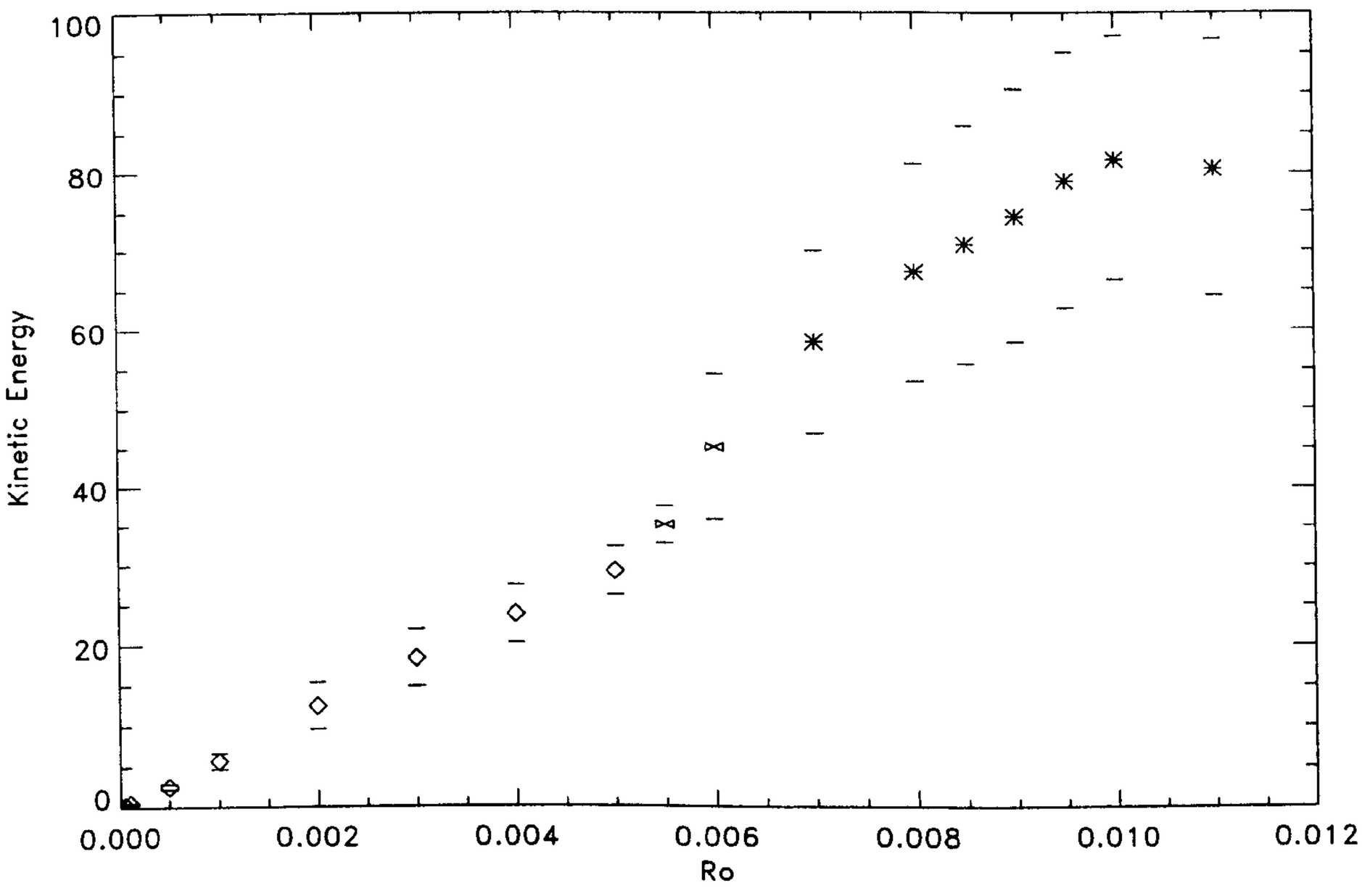

Figure 4.2: As Figure 4.1, but showing the kinetic energy variation with Ro.

In Sections 4.3.1 and 4.3.2 we focus on the nature of the solutions in the quadrupole and dipole regions respectively, and plot snapshots of their variation over a period.

4.3.1 The Quadrupole Solutions.

Here we focus on a quadrupole solution at $Ro = 2 \times 10^{-3}$. The $\triangle$'s featuring on the magnetic and kinetic energy variations shown in Figure 4.3, denote the points at which we have plotted the contours of the solution. We find that we have a reversing type solution which over a cycle of magnetic or kinetic energy, has undergone only half a period of its solution. Snapshots of the solution over the half period, $\frac{T}{2} = 0.117$ are shown in Figure 4.4.

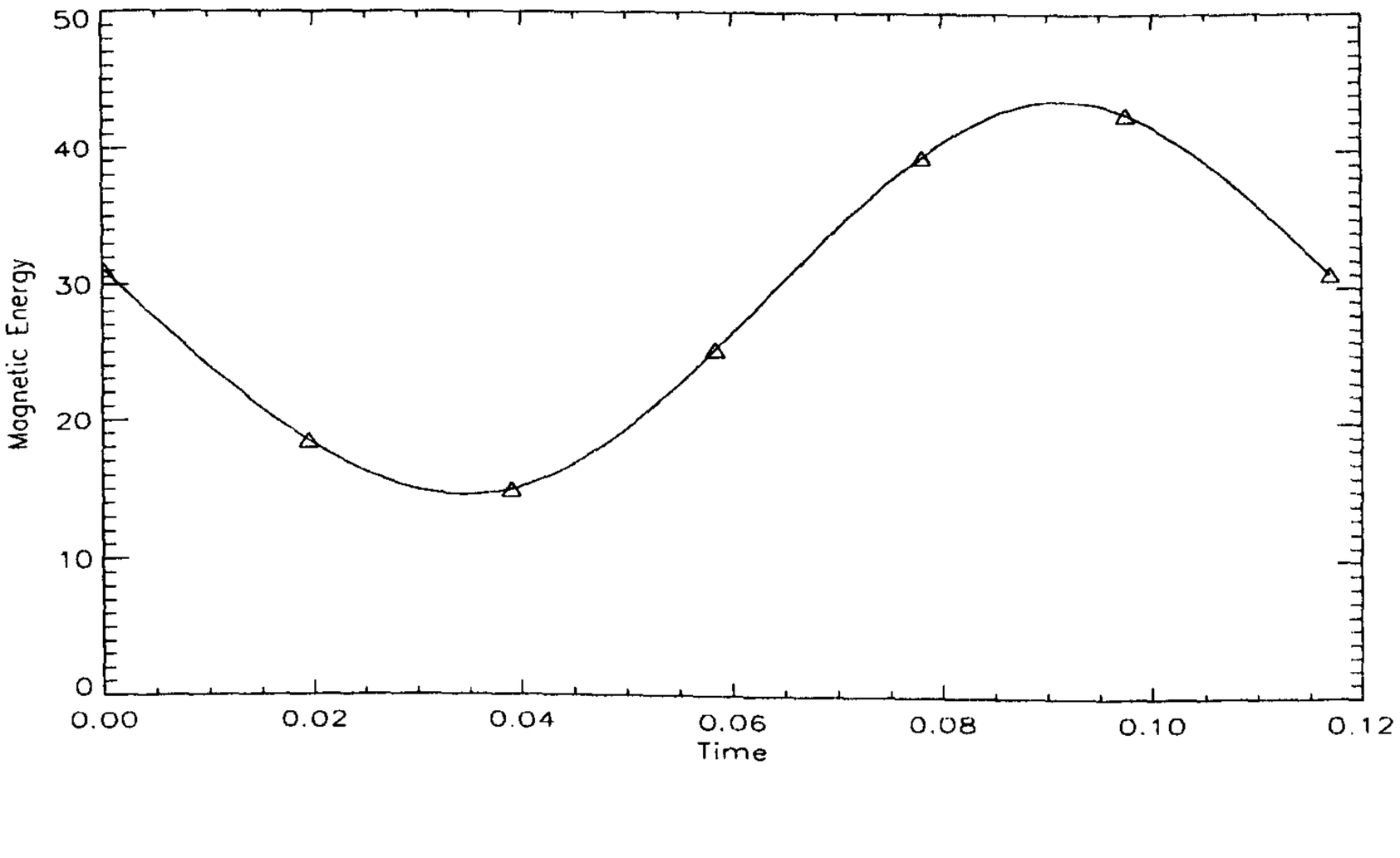

Figure 4.3: Plot of the magnetic energy (top) and kinetic energy (bottom) variation over one cycle. For $\alpha_o = 30, \Theta_o = 100, E = 2.5 \times 10^{-4}$ and $Ro = 2 \times 10^{-3}$.

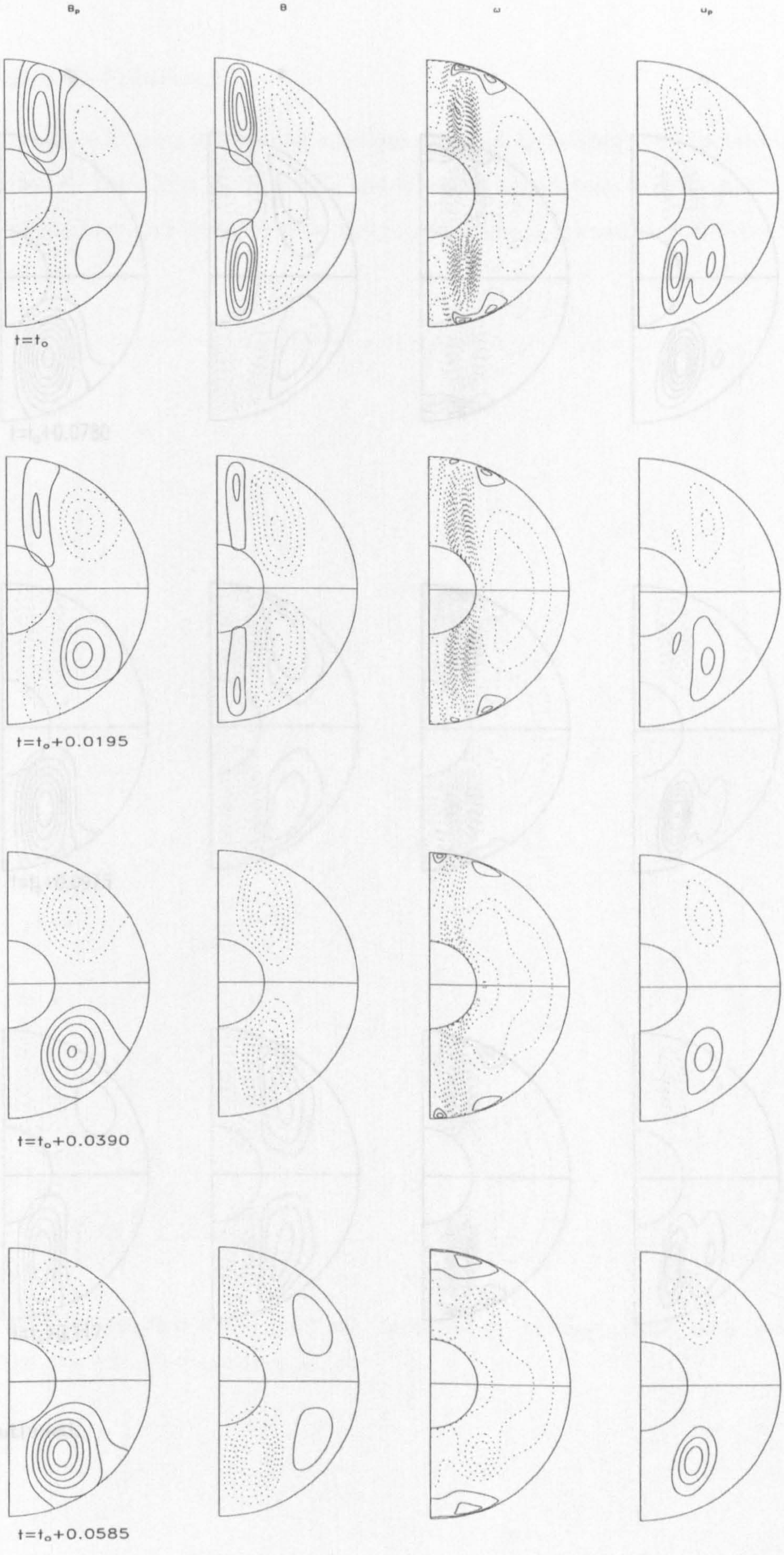

Figure 4.4: The poloidal field, toroidal field, angular velocity and meridional circulation (from left to right) contours of the solution at 6 equally spaced snapshots over the half period, $\frac{T}{2} = 0.117$. For $\alpha_o = 30, \Theta_o = 100, E = 2.5 \times 10^{-4}$ and $Ro = 2 \times 10^{-3}$, with contour intervals of 0.1, 0.5 , 20 , 0.5, respectively.

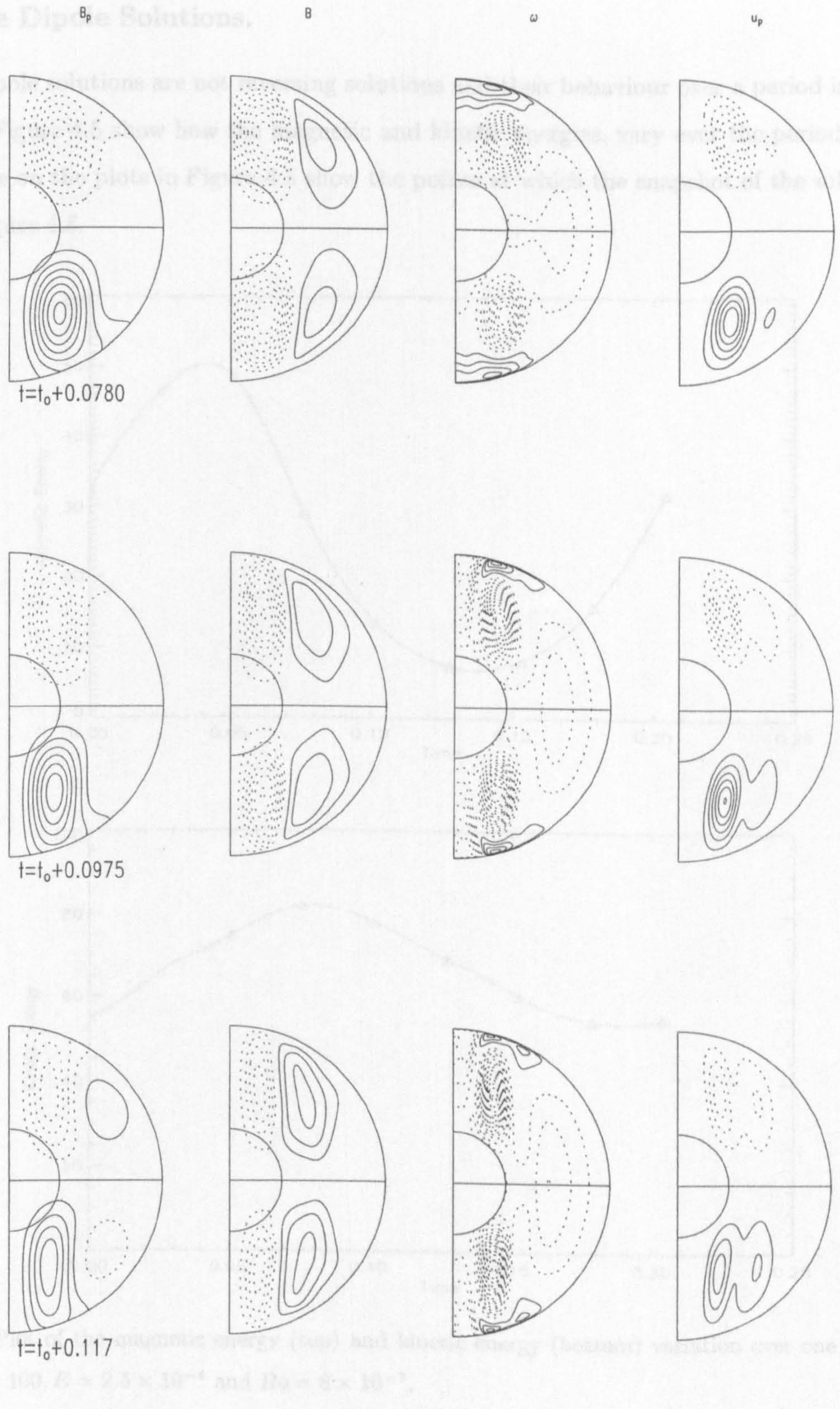

Figure 4.4 continued.

4.3.2 The Dipole Solutions.

These dipole solutions are not reversing solutions and their behaviour over a period is shown in Figure 4.6. Figure 4.5 show how the magnetic and kinetic energies, vary over the period. The $\triangle$'s which feature on the plots in Figure 4.5 show the points at which the snapshot of the solutions are shown in Figure 4.6.

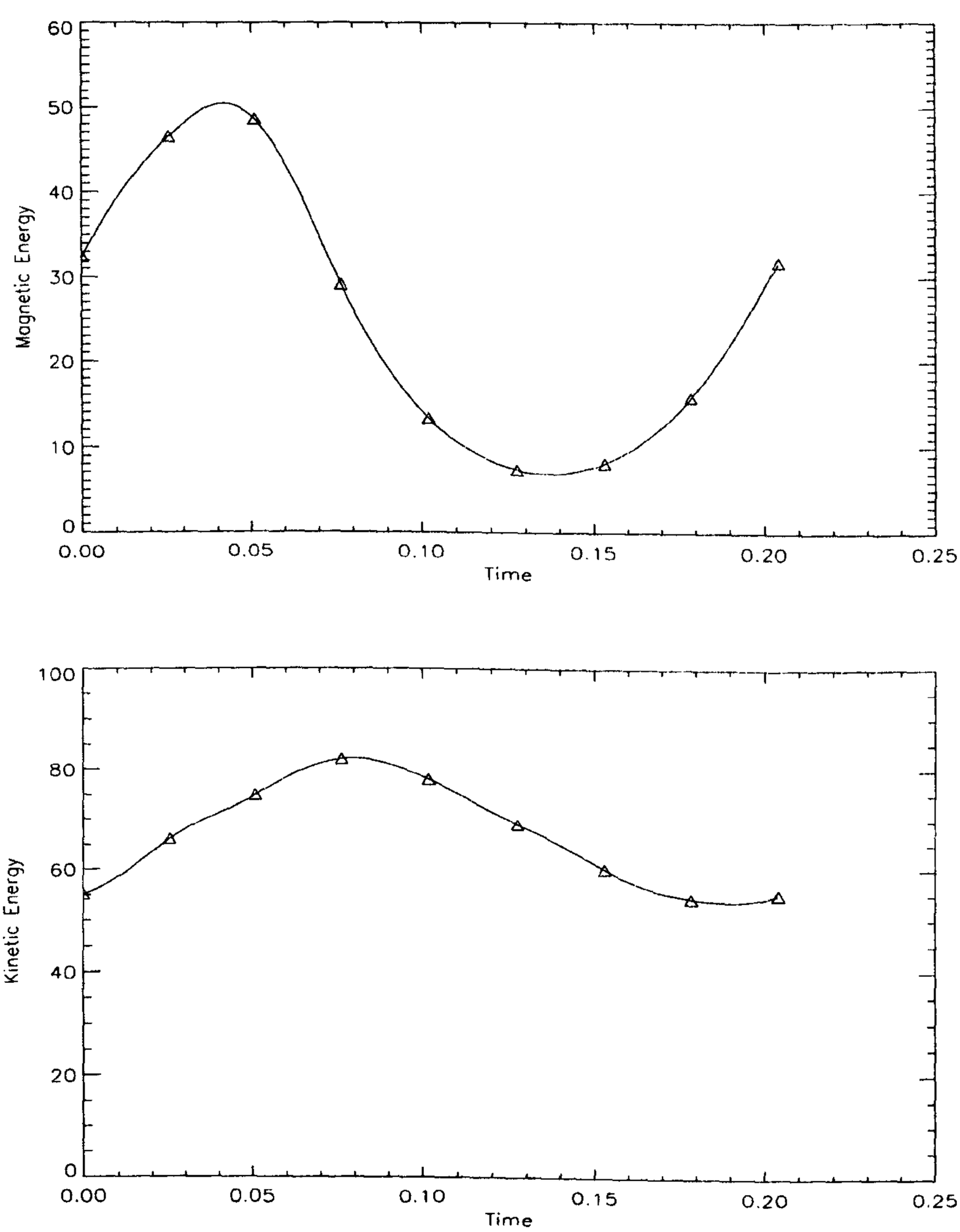

Figure 4.5: Plot of the magnetic energy (top) and kinetic energy (bottom) variation over one cycle. For $\alpha_o = 30, \Theta_o = 100, E = 2.5 \times 10^{-4}$ and $Ro = 8 \times 10^{-3}$.

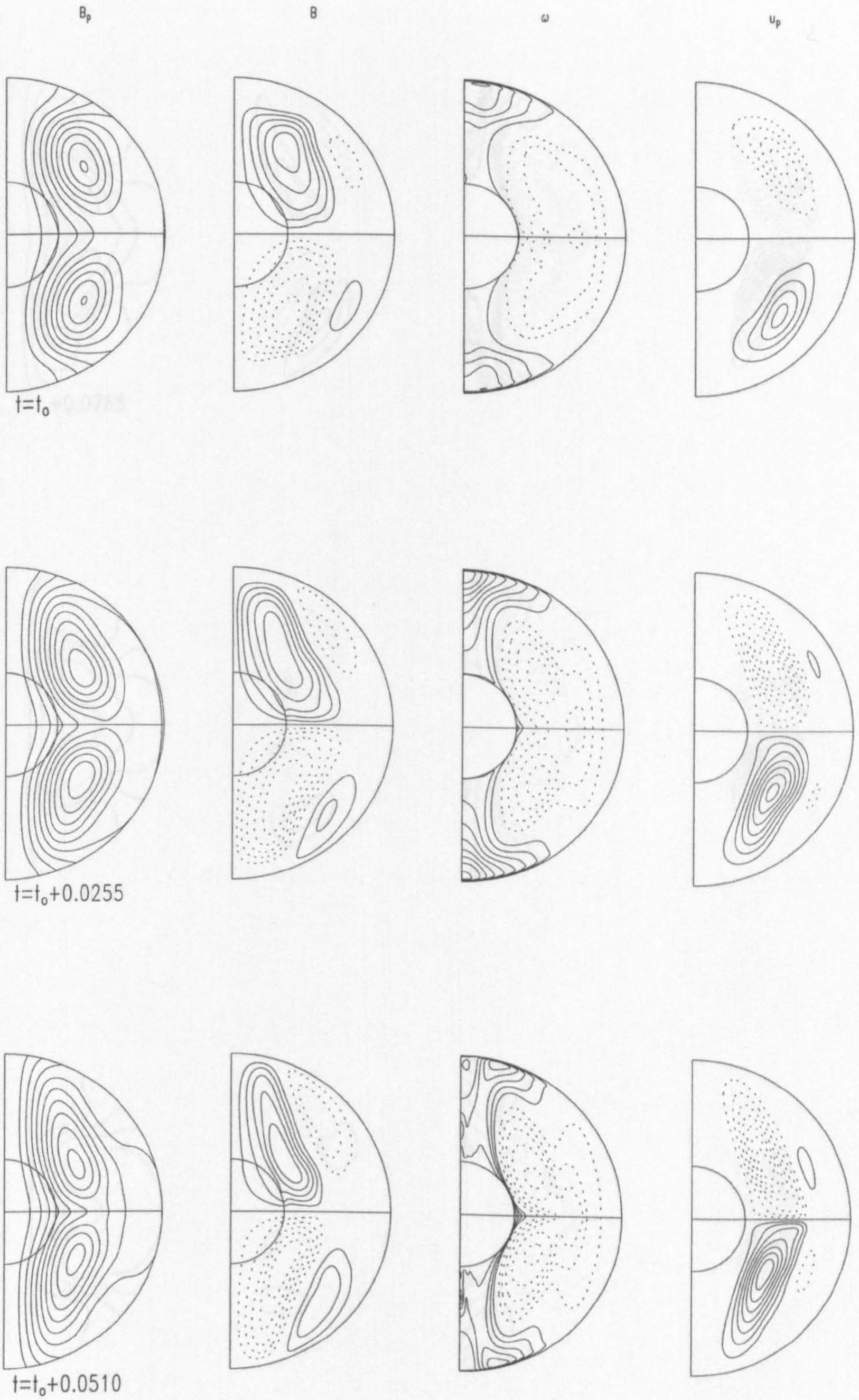

Figure 4.6: As Figure 4.4, but for $\alpha_o = 30, \Theta_o = 100, E = 2.5 \times 10^{-4}$ and $Ro = 8 \times 10^{-3}$. We show snapshots of the solution at 8 equally spaced points over the period, $T = 0.204$.

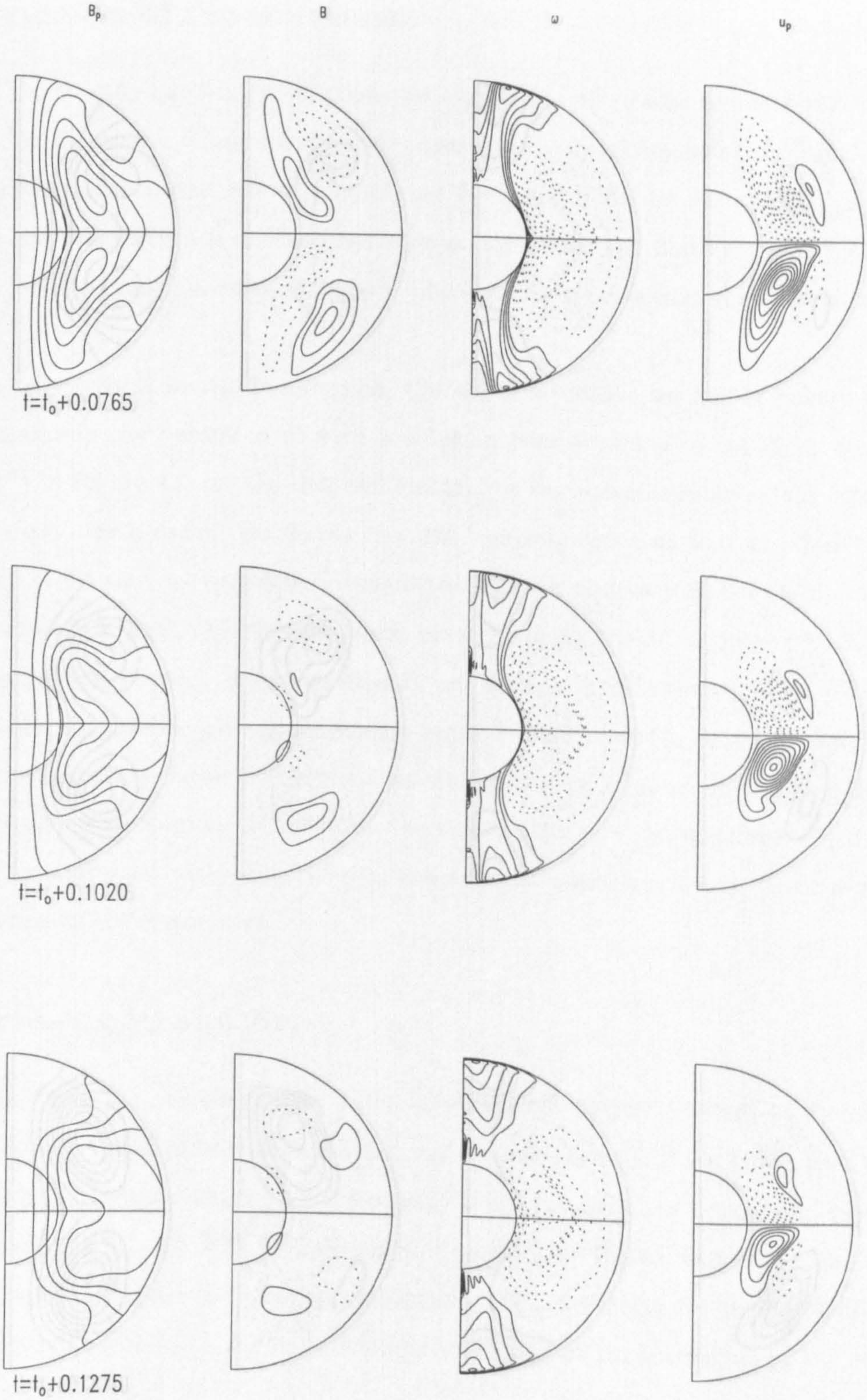

Figure 4.6 continued.

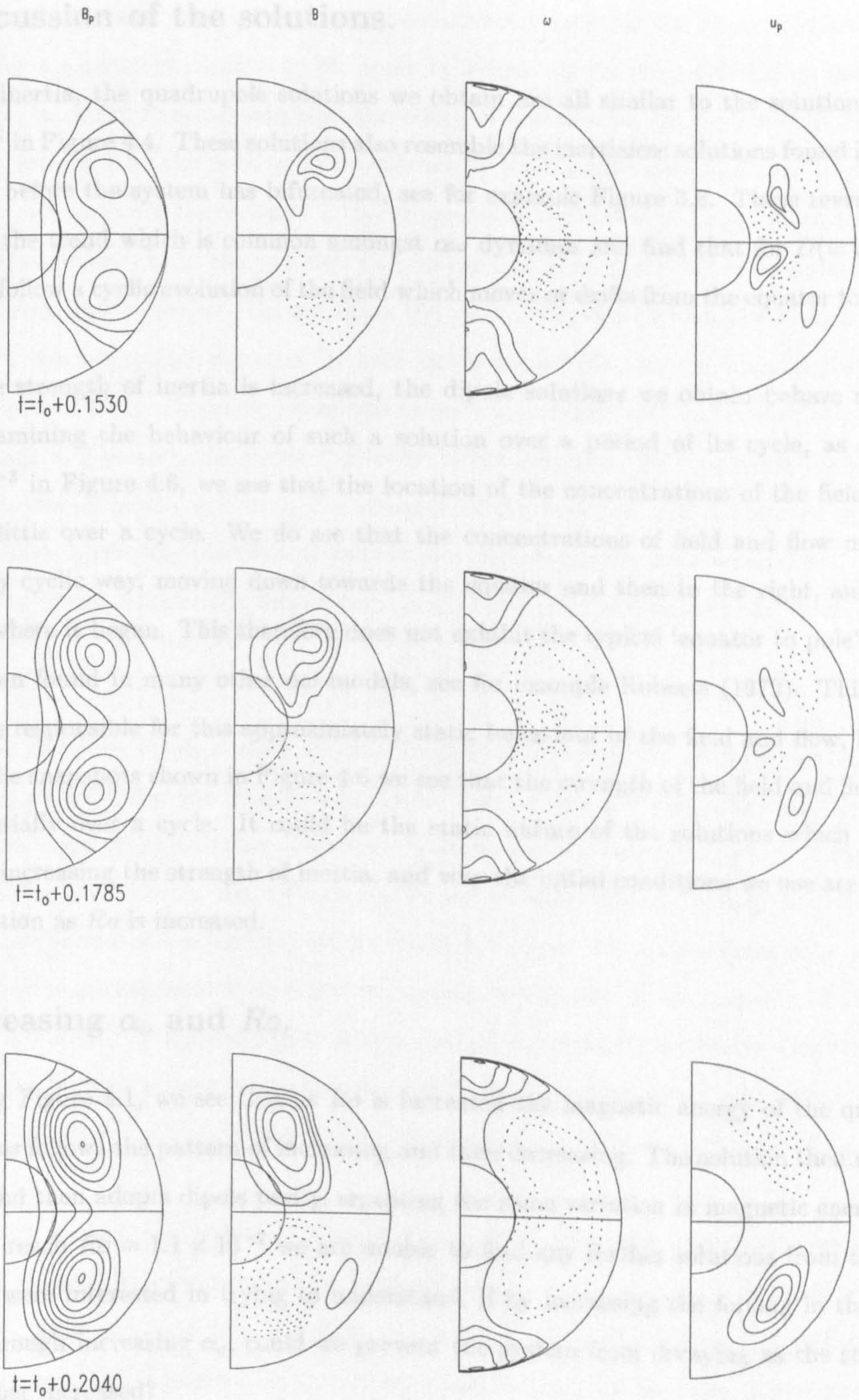

Figure 4.6 continued.

4.4 Discussion of the solutions.

At small inertia, the quadrupole solutions we obtain are all similar to the solution shown at $Ro = 2\times10^{-3}$ in Figure 4.4. These solutions also resemble the inertialess solutions found in Chapter 3, for $\mathcal{D} > 0$ before the system has bifurcated, see for example Figure 3.8. These reversing solutions exhibit the trend which is common amongst $\alpha\omega$ dynamos and find that for $\mathcal{D}(= \alpha_o\Theta_o) > 0$ the solutions follow a cyclic evolution of the field which moves or drifts from the equator to the poles.

When the strength of inertia is increased, the dipole solutions we obtain behave rather differently. Examining the behaviour of such a solution over a period of its cycle, as shown for $Ro = 8 \times 10^{-3}$ in Figure 4.6, we see that the location of the concentrations of the field and flow change very little over a cycle. We do see that the concentrations of field and flow move in an approximately cyclic way, moving down towards the equator and then to the right, and then up and back to where it began. This therefore does not exhibit the typical 'equator to pole' evolution which has been found in many other $\alpha\omega$ models, see for example Roberts (1972). This suggests that inertia is responsible for this approximately static behaviour of the field and flow, however if we examine the snapshots shown in Figure 4.6 we see that the strength of the field and flow change quite substantially over a cycle. It could be the static nature of the solutions which cause the difficulties in increasing the strength of inertia, and why the initial conditions we use are crucial in finding a solution as Ro is increased.

4.5 Increasing α_o and Ro.

Examining Figure 4.1, we see that as Ro is increased the magnetic energy of the quadrupole parity solutions follows the pattern of increasing and then decreasing. The solution then undergoes a transition and then adopts dipole parity, repeating the same variation in magnetic energy. However, once we reach $Ro = 1.1 \times 10^{-2}$ we are unable to find any further solutions from this point. Therefore we were interested in trying to understand, if by increasing the forcing in the system, specifically through increasing α_o, could we prevent the system from decaying as the strength of inertia is further increased?

We specifically focus on increasing α_o as a mechanism to prevent the decay of solutions as Ro is increased, for a number of reasons. In the work by Fearn and Rahman (2004b) on their α^2-type dynamo model in which they investigated the effect of introducing inertia into the system, the direct forcing provided by the α-effect is unaffected by inertia and they find that increasing the strength of inertia increases the strength of the magnetic field generated; thus inertia actually acts to facilitate dynamo action. In their model, they found that the Lorentz force balances the inertia term in the momentum equation. Focussing on the $\alpha\omega$-type model we consider here, a zonal flow is generated in the momentum equation by both the Lorentz force and the buoyancy force, as we discussed in Section 2.8.1. Therefore, these two forces will compete with each other to produce the zonal flow which will balance the remaining terms in the equation. By increasing the strength of the α-effect in the induction equation, the strength of the field will increase and so the Lorentz force will increase. Increasing the Lorentz force in the momentum equation balance may enable the Lorentz force to better balance the inertia term and so prevent the failure of the dynamo as Ro is increased.

Also, if we compare Fearn and Morrison's 2.5D hydrodynamic model with our 2D $\alpha\omega$-type model, we can identify that the buoyancy forces in both models are comparable as they play the same role in the momentum equation. Therefore in some sense, increasing Θ_o in our model is equivalent to increasing Ra in theirs. Since Fearn and Morrison found that increasing Ra did not enable them to prevent dynamo action shutting off, we might well expect the same behaviour as we increase Θ_o. We note however, that these models are not directly comparable as the buoyancy force in Fearn and Morrison's model is dynamically determined through the equation for thermal convection, and in our model the buoyancy force is prescribed. Had time allowed we would also have investigated this aspect of this model, to see whether we find the dynamo mechanism shuts off as Θ_o is increased.

In Figure 4.7 we see the result of increasing α_o on the magnetic and kinetic energy of the system. These chaotically varying solutions show that as α_o is increased from 30 to 40 we are able to increase Ro, while previous attempts to increase Ro at $\alpha_o = 30$ resulted in a solutions which decayed away to zero. This increase in Ro and α_o yields an expected increase in kinetic energy. In Figure 4.7(b) we see an approximately linear dependence of the kinetic energy with Ro, with the

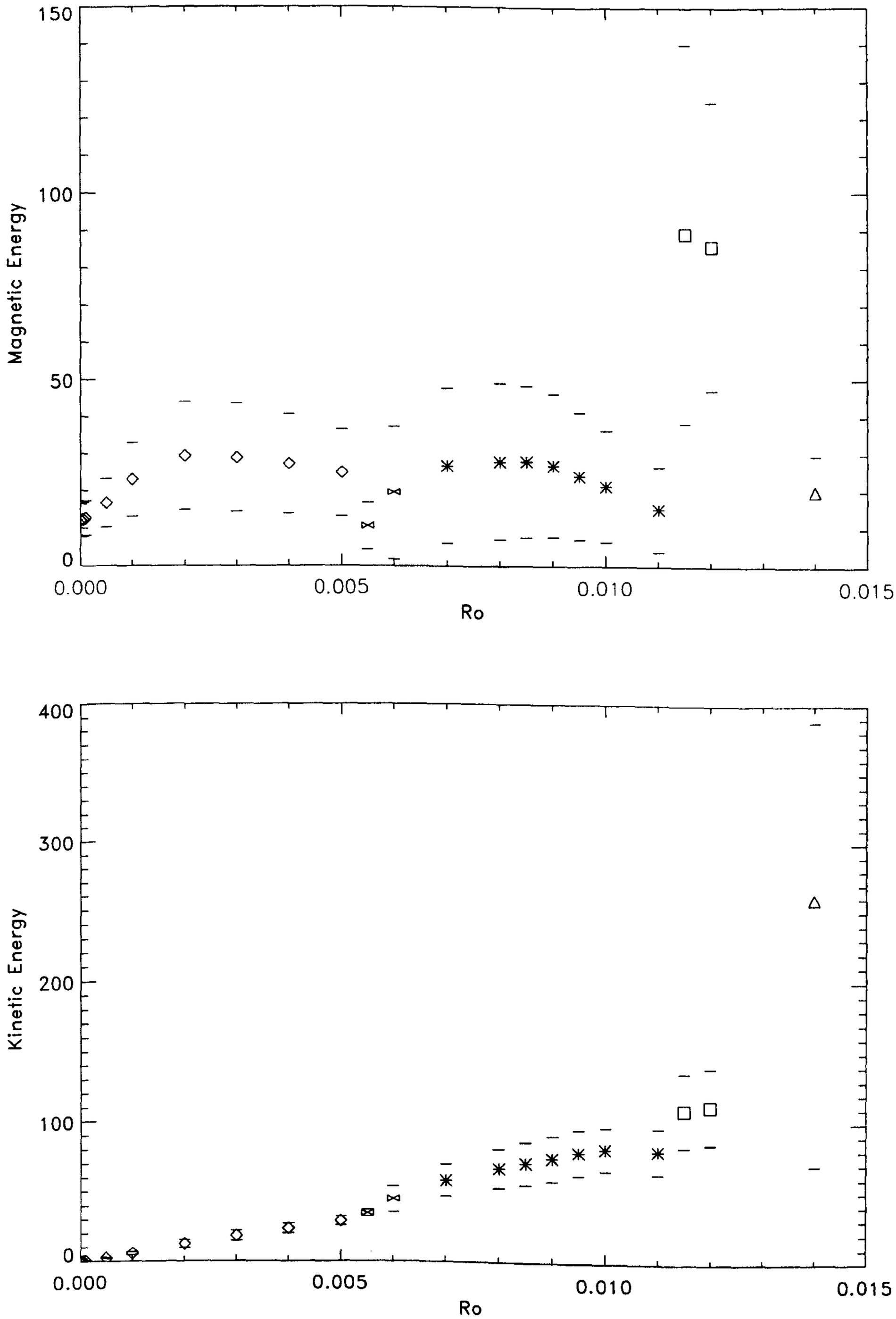

Figure 4.7: As Figures 4.1 and 4.2, but extended to higher values of α_o and *Ro*. The top graph shows the variation of the magnetic energy with *Ro* and the bottom graph shows the variation of the kinetic energy with *Ro*. The $\Diamond$ denote quadrupolar solutions and $*$ dipolar solutions. $\bowtie$ denote mixed parity solutions in the transition region. These are calculated at $\alpha_o = 30$. $\Box$ denotes mixed solutions at $\alpha_o = 40$ and Δ denotes mixed solutions at $\alpha_o = 50$.

solutions at $\alpha_o = 40$ still higher than the solutions we obtained at $\alpha_o = 30$. The α-effect which acts on the field, will not directly cause an increase in the kinetic energy of the system, but due to the feedback of the field on the flow, a modest increase in α_o increases the net forcing in the system, so leads to a small increase in kinetic energy. As α_o and Ro are increased this leads to a fairly substantial increase in the magnetic energy of the system. Increasing Ro further at $\alpha_o = 40$, the magnetic energy falls suggesting that having increased the strength of α_o is not sufficient to prevent the dynamo from decaying as the strength of inertia is increased. Increasing α_o to 50 and Ro to 1.4×10^{-2}, we find the solution which is shown in Figure 4.8, exhibits an erratic, rapidly varying time dependence, which has a low average magnetic energy, but which does not appear to be decaying. The kinetic energy by comparison, shows large variations with time, chaotically varying between ~ 70 and ~ 390.

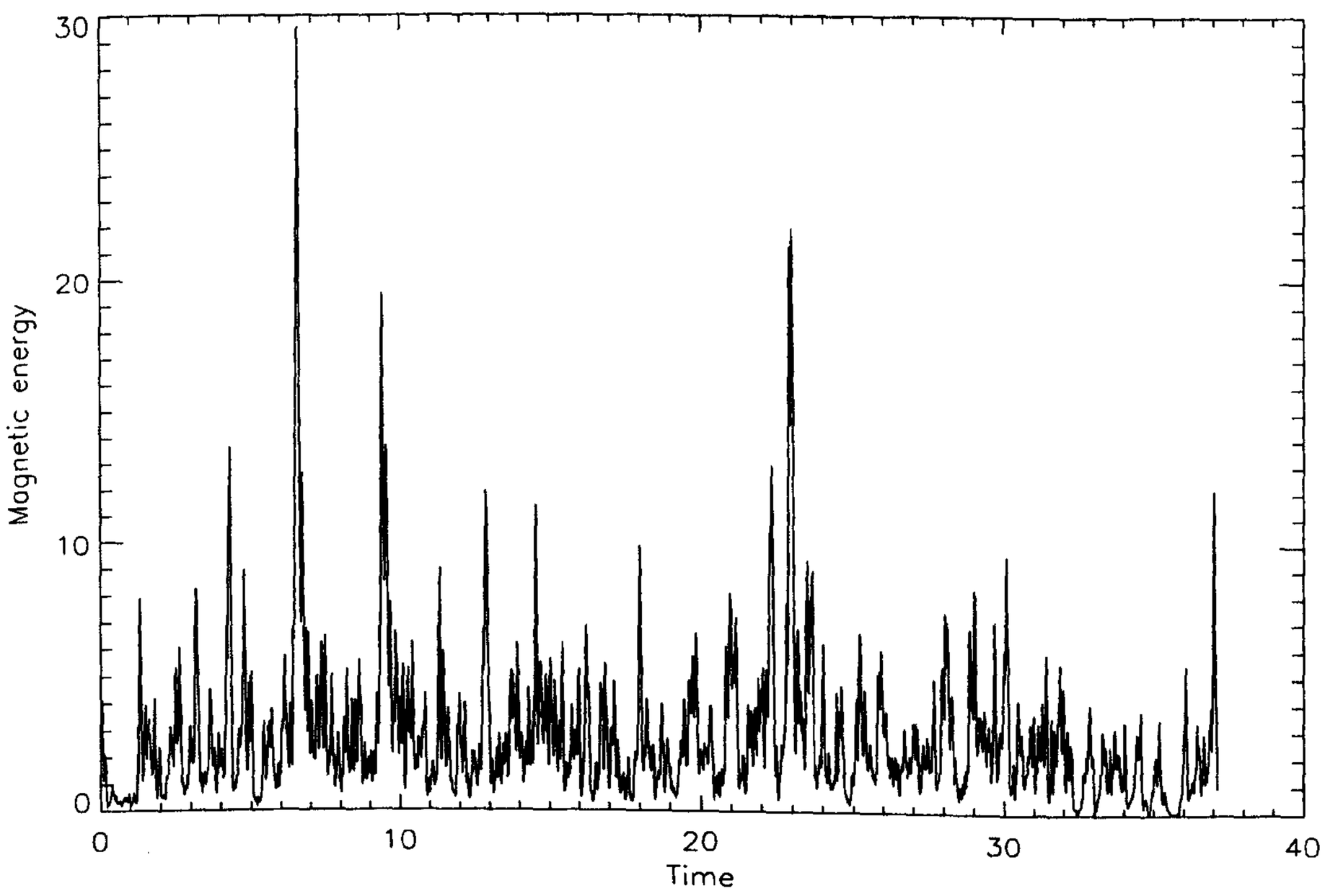

Figure 4.8: The time variation of the magnetic energy of the solution at $\alpha_o = 50$, $\Theta_o = 100$, $E = 2.5 \times 10^{-4}$ and $Ro = 1.4 \times 10^{-2}$. Here we show the variation of the solution for nearly 40 diffusion times; the solution previously having run for over 25 diffusion times, allowing any transient behaviour to die away.

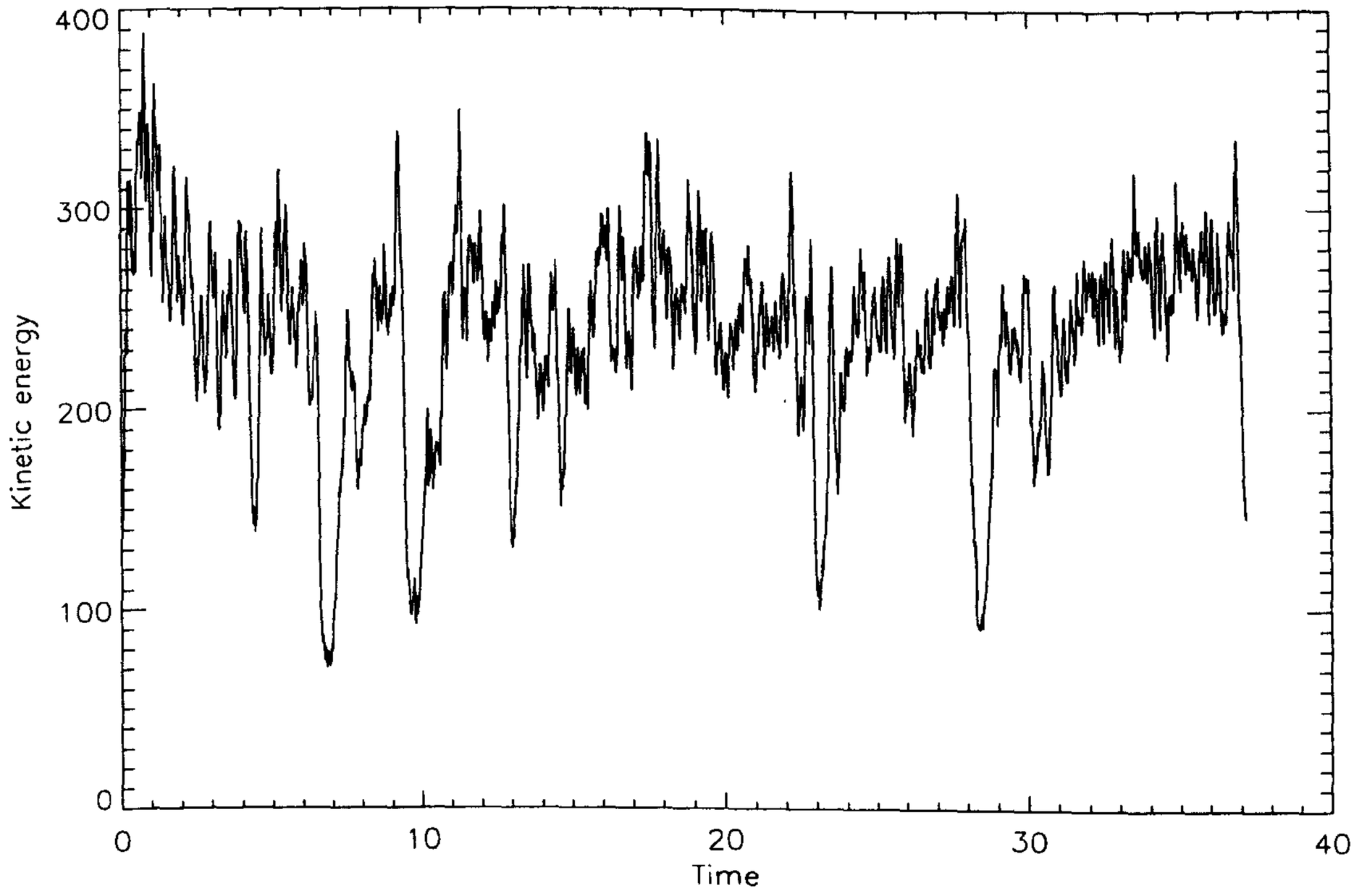

Figure 4.9: As Figure 4.8 but showing the time variation of the kinetic energy of the solution at $\alpha_o = 50$, $\Theta_o = 100$, $E = 2.5 \times 10^{-4}$ and $Ro = 1.4 \times 10^{-2}$.

4.6 More Dipole Solutions.

As we commented in Section 4.3, we have to be very careful of the solutions we choose as our initial conditions.

We found previously, that if the solutions we chose as initial conditions had not fully equilibrated, then the next run at higher values of Ro decayed to zero. Using a solution obtained from the $\alpha^2\omega$ with inertia model which we consider in Chapter 6 as an initial condition, we found that the equilibrated solution we obtained has dipole parity. As we reduced Ro towards zero, we found that the dipole parity of the solutions was maintained. We took these dipole parity solutions and used it in the code for the $\alpha\omega$-type model without inertia and again found that the nature of the solution remained dipolar, however the magnetic energy of this dipole solution was lower than the quadrupole parity solution found at these same parameter values. It is of course perfectly feasible that a lower energy dipole solution may exist, as the systems preferred state will always be one of

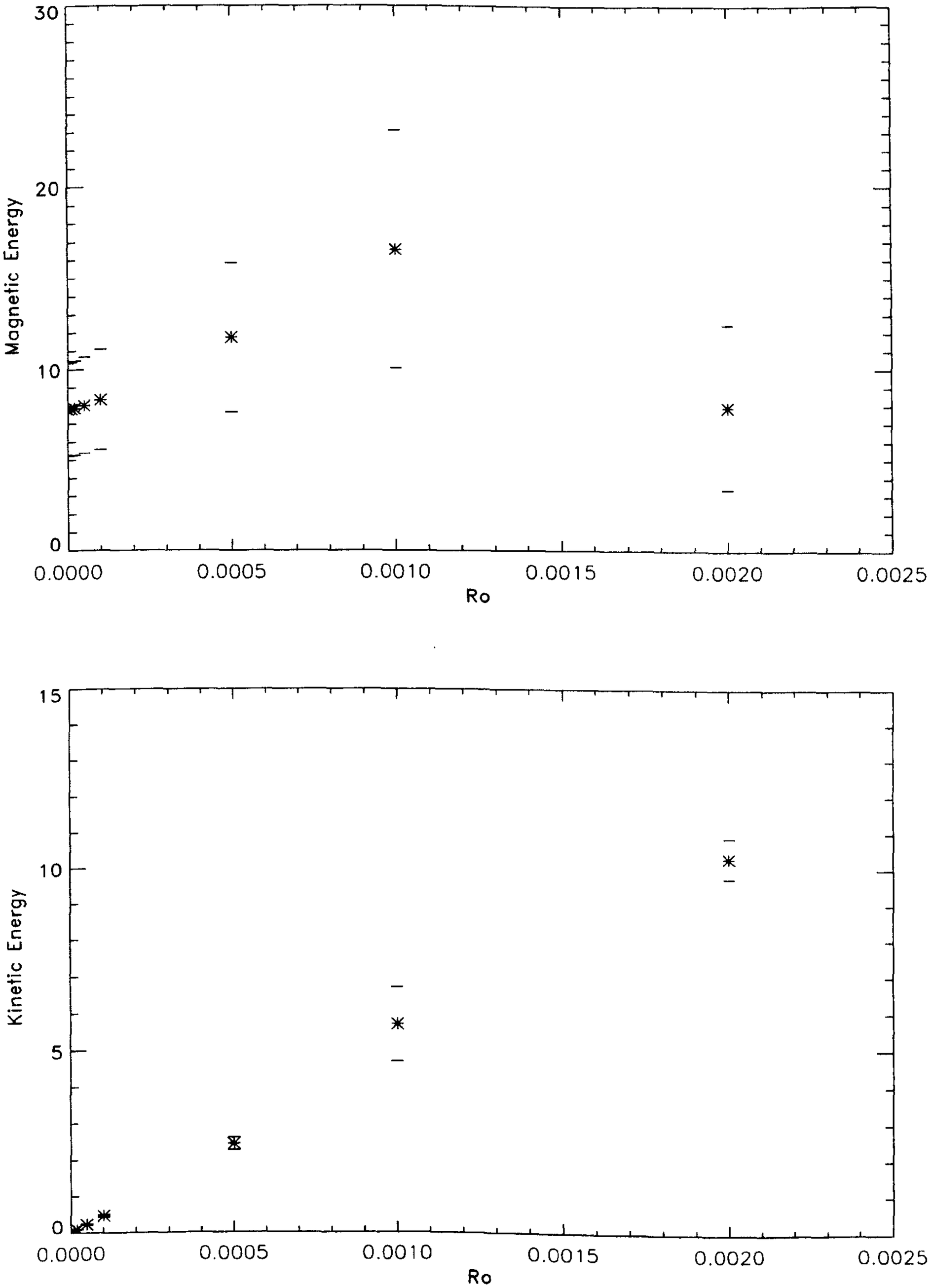

Figure 4.10: The top plot (a) shows the variation of the average magnetic energy with Ro and the bottom plot (b) shows the variation of the average kinetic energy with Ro. 'Error bars' indicate the maximum and minimum amplitudes of the oscillatory solutions. The $*$ denotes dipole parity solutions. For all solutions shown above, $\alpha_o = 30, \Theta_o = 100$ and $E = 2.5 \times 10^{-4}$.

higher energy.

As a test of this, we took one of the dipole solutions we obtained at small inertia and gave it a small quadrupole perturbation to test how stable these dipole solutions were and how sensitive they were to the initial conditions used. We found that the solution quickly evolved to a quadrupole parity solution as expected. However, this shows that the model is fairly sensitive to the initial conditions used, that if a solution exists which is close to the solution used as an initial condition, then the system may not evolve to the correct state of the system, or we may have to wait a long time for such a transition to occur.

As a point of interest, we decided to follow this dipole branch of the solution as we increased the strength of inertia in the system. We were only able to follow the solution as far as $Ro = 2 \times 10^{-3}$, with solutions remaining fairly similar along this branch. As the strength of inertia is increased we naturally see an increase in kinetic energy, as shown in Figure 4.10(b). The magnetic energy, shown in Figure 4.10(a), also increases as we increase Ro, however once we reach $Ro = 2 \times 10^{-3}$, we see the magnetic energy of the system has dropped sharply. The solution we obtain at $Ro = 2 \times 10^{-3}$ was well resolved in both r and θ directions, however in attempting to increase the strength of inertia further, we were unable to obtain an equilibrated solution. At this time we have no conclusive ideas about why we are unable to follow this solution further (despite reducing the timestep to 1×10^{-7}), but believe that there must be a substantial change in the solution at this point, making it difficult to follow the solution beyond this point. This growing and decaying of the solutions with increasing Ro was observed in Section 4.3 for the natural branch of solutions.

We consider in more detail the time evolution of these dipole solutions. We focus on the behaviour of the solution we obtain at $Ro = 1 \times 10^{-3}$, as the other solutions we find on this branch are likely to be similar. The magnetic and kinetic variation over a cycle is shown in Figure 4.11. We plot the snapshots of the solution over the cycle, in Figure 4.12 where we see that we have a reversing solution, which after 1 cycle of the magnetic or kinetic energy has completed only half a period of its solution. Examining the dipole solution shown in Figure 4.12, we see that the solution exhibits the same cyclic evolution of the field, which drifts from the equator to the pole, as we

found for the quadrupole parity solutions at small inertia.

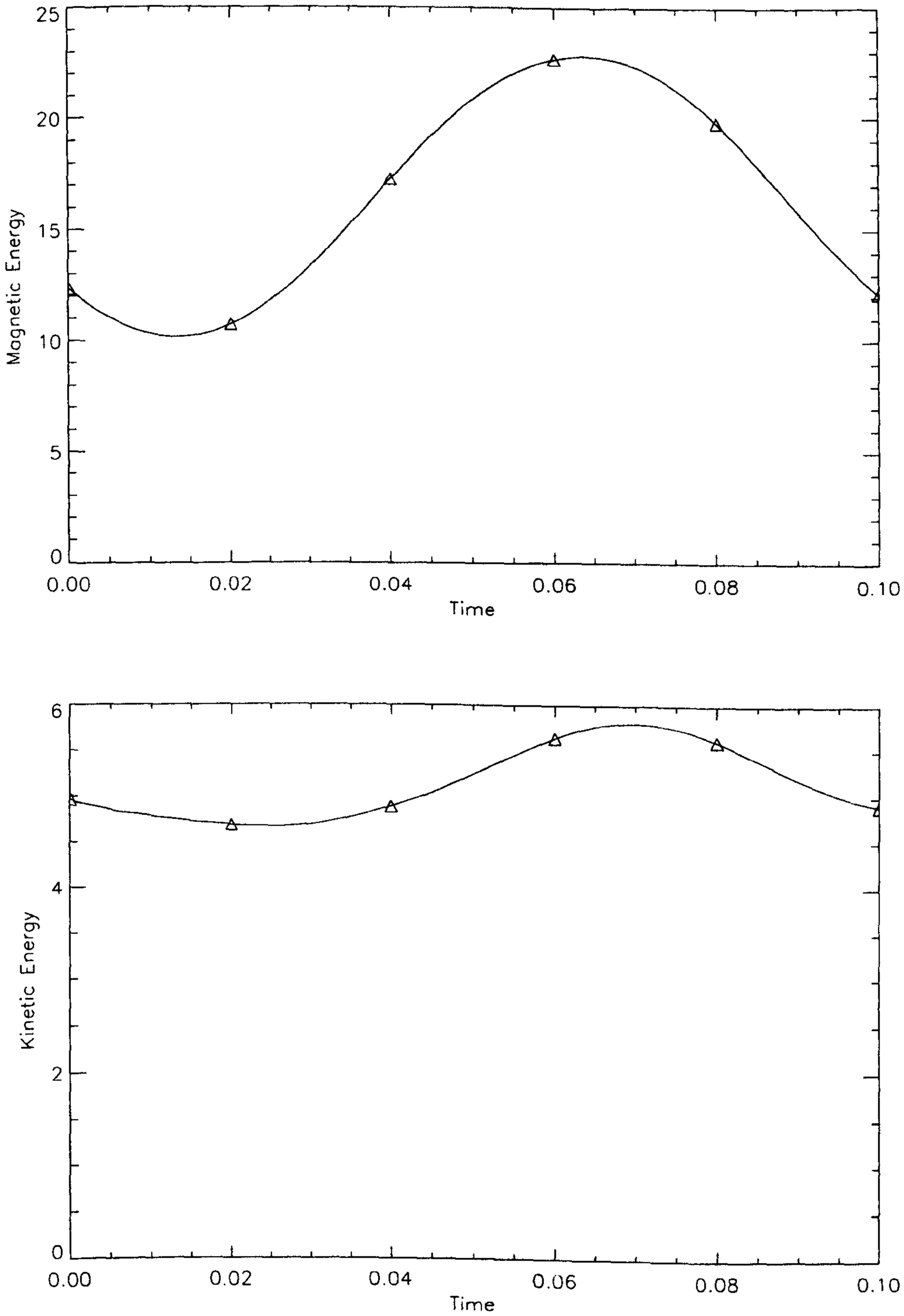

Figure 4.11: The magnetic (top) and kinetic (bottom) energy variation with time for the dipole solution at $Ro = 1 \times 10^{-3}$, $\alpha_o = 30$, $\Theta_o = 100$ and $E = 2.5 \times 10^{-4}$.

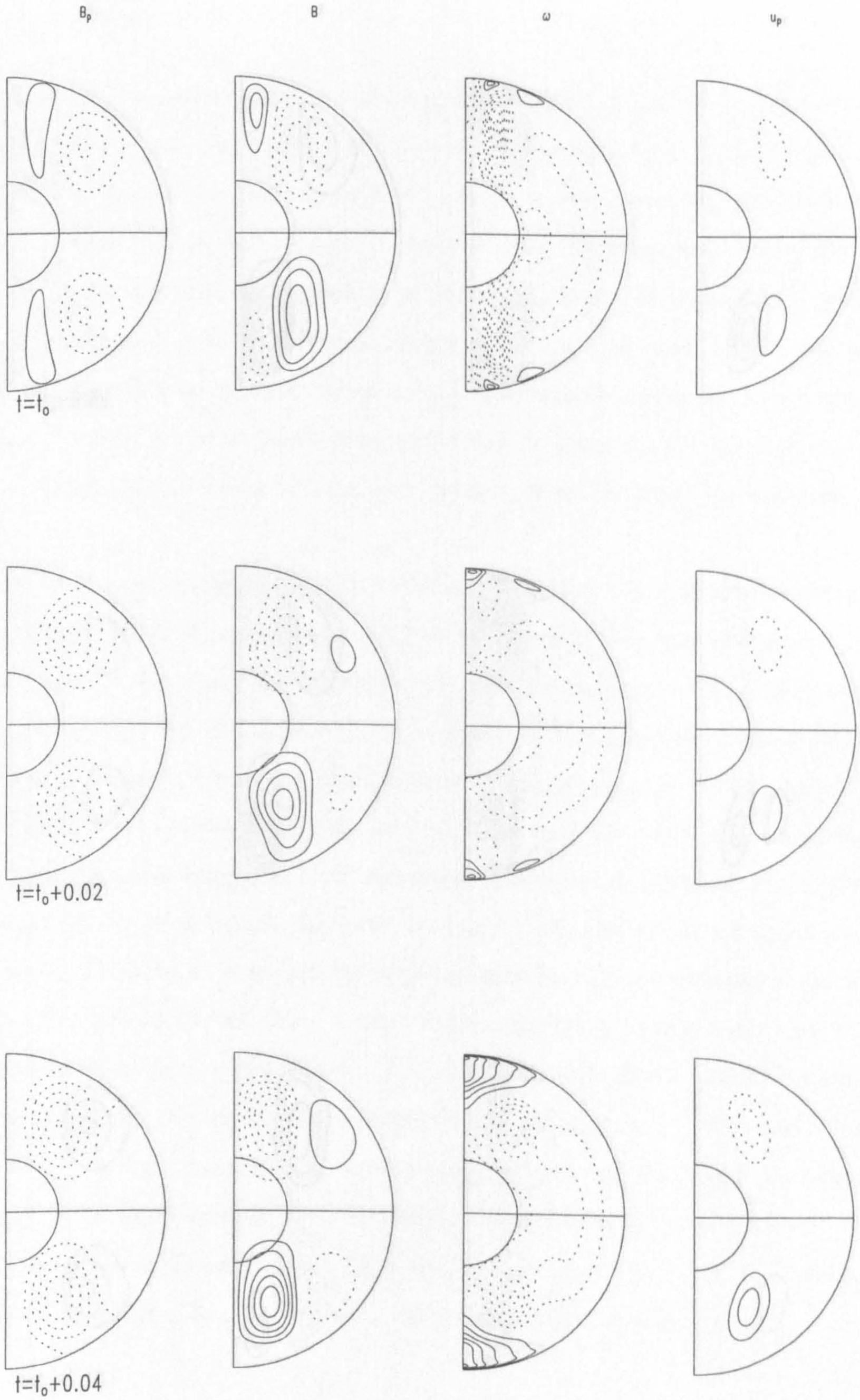

Figure 4.12: As Figure 4.4, but for $\alpha_o = 30, \Theta_o = 100, E = 2.5 \times 10^{-4}$ and $Ro = 1 \times 10^{-3}$. We show snapshots of the solution at 5 equally spaced points over the half period, $\frac{T}{2} = 0.1$.

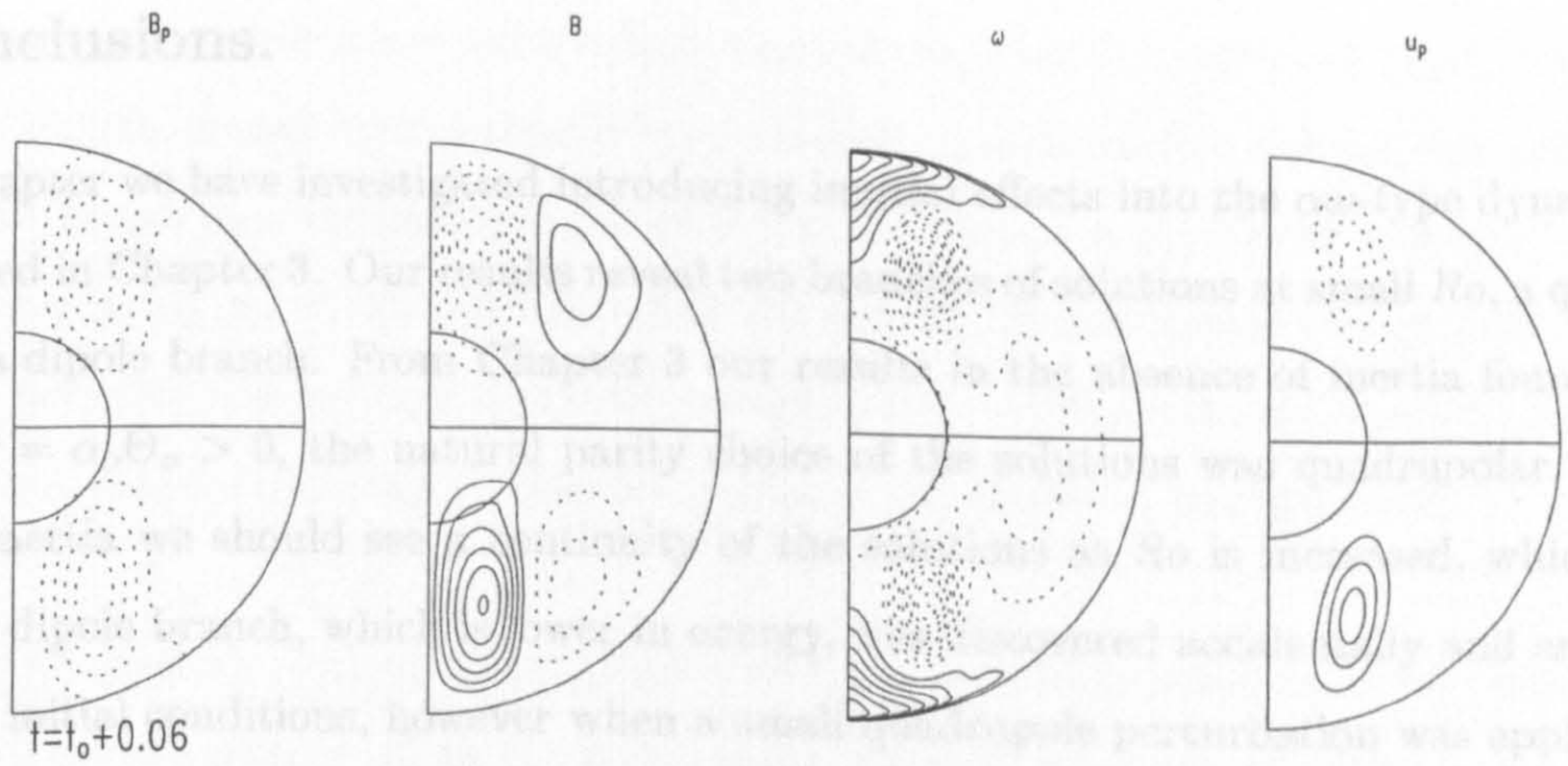

Figure 4.12 continued.

4.7 Conclusions.

In this chapter we have investigated introducing inertial effects into the $\alpha\omega$-type dynamo model we investigated in Chapter 3. Our results reveal two branches of solutions at small Ro, a quadrupole branch and a dipole branch. From Chapter 3 our results in the absence of inertia found that solutions for $\mathcal{D} = \alpha_o\Theta_o > 0$, the natural parity choice of the solutions was quadrupolar, and so as we increase inertia we should see a continuity of the solutions as Ro is increased, which is what we find. The dipole branch, which is lower in energy, was discovered accidentally and arose out of our choice of initial conditions, however when a small quadrupole perturbation was applied to the solution the solution evolved onto the quadrupole branch, confirming that the quadrupole branch was indeed the correct one to follow and the energetically favoured state of the system.

We focussed on the quadrupole branch of solutions in Section 4.3. The kinetic energy variation of the solutions with Ro is shown in Figure 4.2, where we see that the kinetic energy increases approximately linearly with Ro. The variation of the magnetic energy with Ro is shown in Figure 4.1. The magnetic energy initially increases quite steeply with Ro and then slowly decreases. The solutions then goes through a transition phase in which the solutions are mixed and have a unusual time dependence. These transition solutions then give way to dipole solutions, which then follow a similar variation in magnetic energy as Ro is increased, as we saw for the quadrupole solutions. The low energy dipole branch of solutions, discussed in Section 4.6, also exhibited this same behaviour with increased Ro. The magnetic energy initially increases and then decreases as Ro is increased. This time instead of finding the solutions undergoing a bifurcation to new behaviour, the solutions appear to decay away to zero as we increase Ro. This shutting off of dynamo action, had been found in studies by many others, see for example Fearn and Morrison (2001) and Christensen *et al* (1999). However we have succeeded in reaching higher values of Ro (lower Pm) than either of these studies, as Fearn and Morrison were only able to reach Ro as high as 1×10^{-3}. Christensen *et al* (1999) found dynamo action died out for a range of values of Pm $(= E/Ro)$, which depended on Ra, but did not achieve a Rossby number as large as we have obtained here.

We were then interested in whether it would be possible to prevent this shutting off of dynamo action as Ro is increased through increasing the forcing within our model. We chose to do this

through increasing the strength of our α-effect, since the α-effect is unaffected by inertia and Fearn and Rahman (2004b) found that in their α^2-type model, dynamo action did not shut off as Ro was increased. We found that increasing α_o from 30 to 40, caused a significant increase in magnetic energy, however fixing α_o at 40 and increasing Ro slightly, the magnetic energy falls. Increasing α_o to 50, we find that the average magnetic energy falls to ~ 20 occasionally exhibiting energetic peaks where the magnetic energy reaches as high as ~ 30, as shown in Figure 4.8.

Fearn and Morrison's work on their 2.5D hydrodynamic model, found that they were unable to prevent the dynamo shutting off as Ro is increased, despite increasing the forcing in the system. From this study it certainly seems possible to reach higher values of Ro through increasing α_o, however it as yet remains unclear whether one can completely override the shutting off mechanism of the dynamo through this process.

Chapter 5

$\alpha^2\omega$-dynamos without inertia.

5.1 Introduction.

In this chapter, we investigate an $\alpha^2\omega$-type model. This dynamo model is a more general, intermediate model between the $\alpha\omega$-type model we considered in Chapter 3 and the α^2-type model considered by Fearn and Rahman (2004a). The α^2-type model and $\alpha\omega$-type model are very different problems as we see through comparing our results in Chapters 3 and 4 with Fearn and Rahman's studies. Through considering the $\alpha^2\omega$-type model, we hope to be able to reconcile these two models. Therefore, we begin with the α^2 solution at fixed α_o and we investigate the effect of introducing our buoyancy driven ω-effect. This study will also provide us with a reference case for the work we present in Chapter 6, where we then include the effects of inertia.

5.2 Background

Recent work by Fearn and Rahman (2004a) focussed on an axisymmetric non-linear α^2-type model in a spherical shell geometry retaining a finitely conducting inner core. Solutions have a dipole parity imposed upon them, as integration times are long and expensive, though a test solution found without the parity restriction was dipolar. Here the parametrised α-effect is now allowed to act on both toroidal and poloidal parts of the field in order to generate poloidal and toroidal field in turn. In their investigation, the chosen α variation is $\alpha = \alpha_o \cos\theta \sin(\pi(r - r_i))$. Using this model, they investigate a range of values of the Ekman number, $5\times10^{-5} \leq E \leq 2.5\times10^{-3}$, and find that an interesting type of solution develops in a region of parameter space. They find

that for $E \geq 4 \times 10^{-4}$ solutions remain steady, for all values of α_o. For $1 \times 10^{-4} \leq E \leq 3 \times 10^{-4}$, where the lower bound on E is limited by the numerics, they find an unusual periodic disturbance develops when α_o exceeds some critical value. They find that the solutions grow rapidly until their maximum value is reached, where the solutions then undergo a rapid decay. The solutions then follow a slow decay for most of the period, where during this slow decay phase the solutions resemble the solutions found in the steady regime. Once the solutions reach their minimum magnetic energy they then begin to grow rapidly and the cycle begins again. The periodic nature of these solutions was found to depend on the Ekman number and the value of α_o. The trend that evolved was that as the Ekman number decreased, the period of the disturbance decreased for a fixed value of α_o. In addition, examining the solution at increased values of α_o yielded the result that the period decreased, eventually tending to a fixed value as $\alpha_o \to \infty$.

5.3 Variation of magnetic energy with Θ_o.

Figure 5.1, shows the magnetic energy variation with Θ_o. In Figure 5.1 we chose to represent the periodic solutions in a different way to the spiky solutions, as it did not naturally make sense to take the average of the spiky solutions, since in reality the average would be close to the minimum of each solution. We have chosen to represent the spiky solutions in the same way as presented by Fearn and Rahman (2004a), plotting the maximum and minimum amplitudes of the magnetic energy variation. The representations we have used here for the periodic solutions, is the same as we used in Chapter 3 for the $\alpha\omega$-type dynamos, where we plot the average magnetic energy and use 'error bars' to indicate the maximum and minimum amplitudes of the magnetic energy. This helps to reinforce the similarity between these solutions.

From Figure 5.1 we see very clearly the distinction between the steady, periodic, and spiky solutions, with the transition from steady to spiky solutions occurring around $\Theta_p \simeq -7$ and a transition between the steady solutions to periodic behaviour beyond $\Theta_o = -30$ as Θ_o is decreased. The time dependence of the spiky periodic solutions is shown in Figures 5.10, 5.11 and 5.12 for various values of Θ_o. The time dependence of the periodic solutions can be found in Figures 5.3 and 5.4.

Let us examine the magnetic energy variation for $\Theta_o \geq -4$. We see that the maximum and

minimum energies achieved for the spiky periodic behaviour remains approximately constant for Θ_o up to 50. For $\Theta_o \geq 50$ the solutions maximum magnetic energy begins to increase sharply, and the minimum magnetic energy decreases quickly to close to zero. This suggests that for $\Theta_o > 50$ the differential rotation driven by the imposed buoyancy force is beginning to have a more significant effect on the system. The steady solutions we find for $-30 \leq \Theta_o \leq -10$, shows a fairly linear increasing variation in magnetic energy as we decrease Θ_o. As we further decrease Θ_o, we find that periodic behaviour has set in. We see that the average magnetic energy of the solution at $\Theta_o = -50$ is close to the energy of the steady solution, showing a continuous change in the energy of the solutions. As Θ_o is decreased further, the magnetic energy falls reaching a minimum around $\Theta_o = -100$. Decreasing Θ_o to -120, we find that the solution has changed slightly, the magnetic energy variation with time becoming more smooth and the average energy has increased slightly.

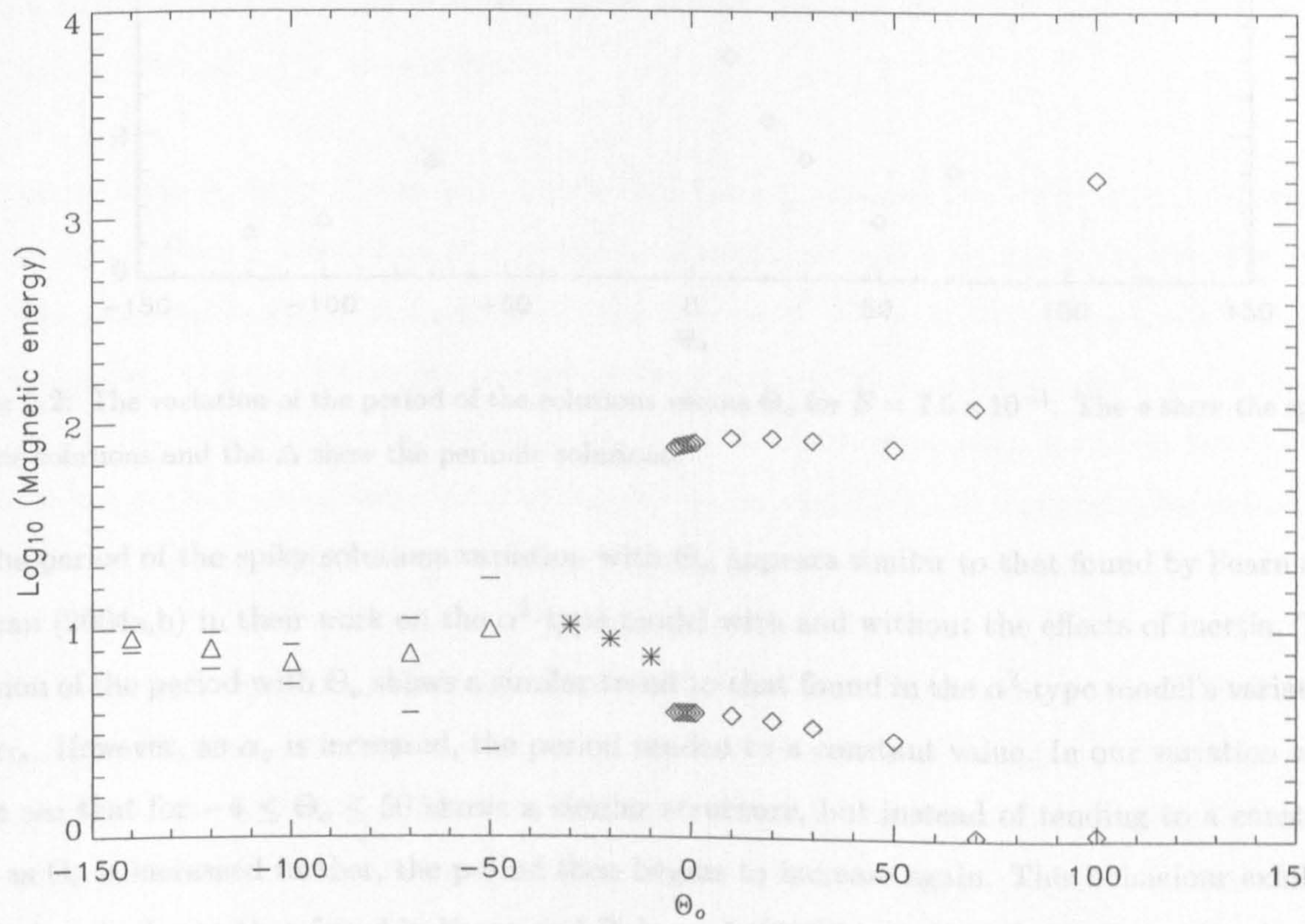

Figure 5.1: Variation of magnetic energy with Θ_o for $E = 2.5 \times 10^{-4}$. $\diamond$ indicate the maximum and minimum amplitudes of the spiky type solutions, see for example Figure 5.10. $\divideontimes$ show the magnetic energies of the steady solutions and $\triangle$ show the average magnetic energy of periodic solutions, see for example Figure 5.3. The 'error bars' indicate the maximum and minimum amplitudes of the periodic solutions.

5.4 Variation of the period with Θ_o.

The graph in Figure 5.2 shows the variation of the period, T of the solutions with Θ_o. This graph shows the behaviour of respective periods of the spiky solutions and the periodic solutions.

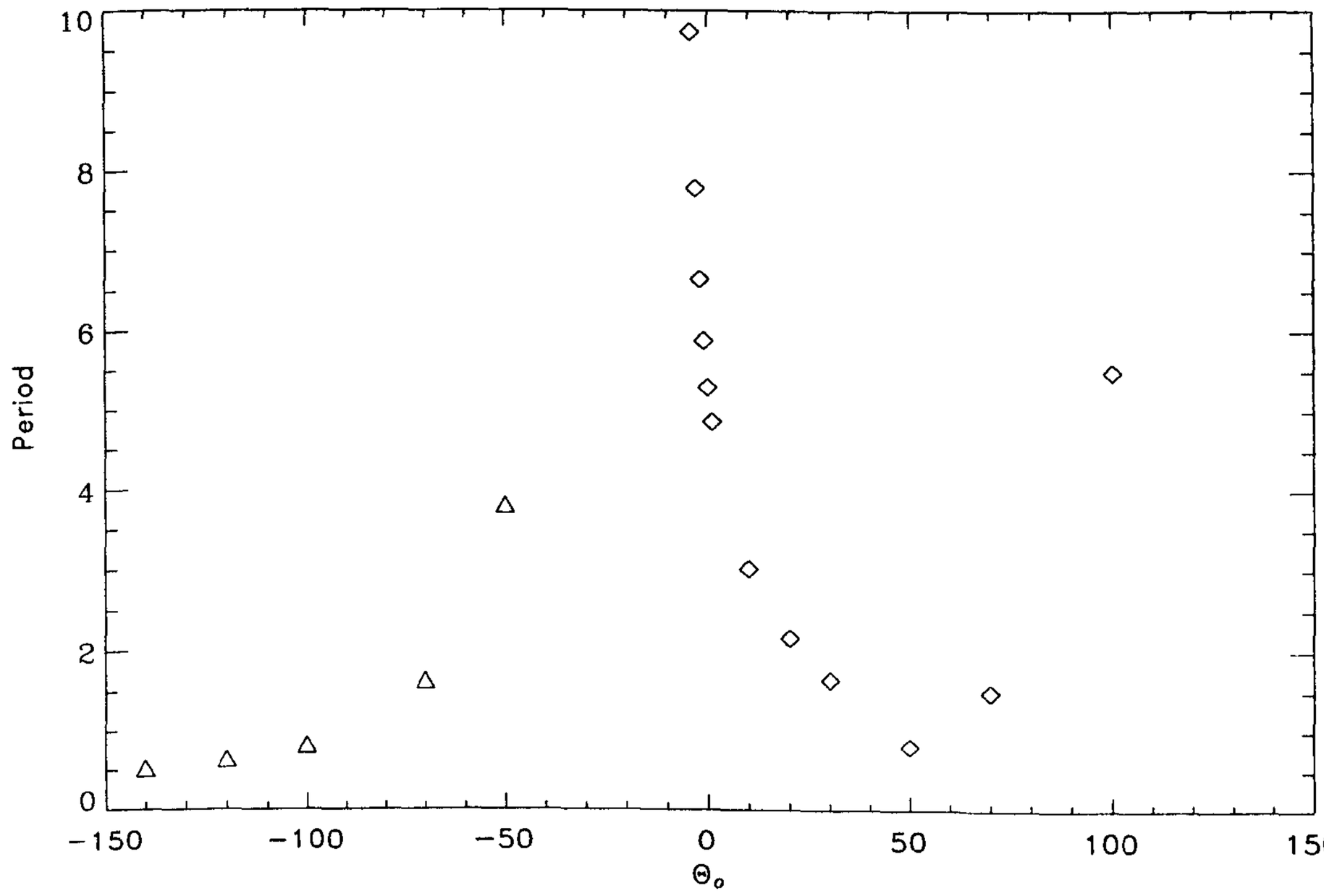

Figure 5.2: The variation of the period of the solutions versus Θ_o for $E = 2.5 \times 10^{-4}$. The $\diamond$ show the spiky periodic solutions and the $\triangle$ show the periodic solutions.

The period of the spiky solutions variation with Θ_o appears similar to that found by Fearn and Rahman (2004a,b) in their work on the α^2-type model with and without the effects of inertia. The variation of the period with Θ_o shows a similar trend to that found in the α^2-type model's variation with α_o. However, as α_o is increased, the period tended to a constant value. In our variation with Θ_o we see that for $-4 \leq \Theta_o \leq 50$ shows a similar structure, but instead of tending to a constant value as Θ_o is increased further, the period then begins to increase again. This behaviour exhibits a variation similar to that found in Fearn and Rahman's (2004b) studies of the effect of inertia on their α^2-type model. There they find, as they increase the strength of inertia Ro, the period of the spiky solutions decreases and then increases again, in a manner similar to that shown in Figure 5.2, as we increase Θ_o. Their variation with increasing Ro eventually results in a bifurcation to steady

behaviour, a transition we do not observe here with increasing Θ_o. We discuss these solutions further in Section 5.7.

In Figure 5.2 we see how the period of the periodic type solutions changes with decreasing Θ_o. We see that as we decrease Θ_o, the period of the solutions decrease from the vertical asymptote generated by (the infinite period of) the steady solutions. As Θ_o is decreased, the period of the solutions decreases, appearing to tend towards a constant value. We discuss these solutions in more detail in Section 5.5.

5.5 Periodic solutions.

As we decreased Θ_o from the -30, which produced a steady solution, we see that the solutions bifurcate to give the periodic behaviour as shown in Figure 5.3 at $\Theta_o = -50$ and -70 and Figure 5.4 at $\Theta_o = -100$ and -120, respectively.

As we decrease Θ_o from -50 to -70, we see that having increased the strength of the imposed buoyancy driving, has resulted in a shorter period of evolution, and a smoothing of the time variation. The magnetic energy of the system has also decreased. As Θ_o is further decreased to -100, there is a continued reduction in the magnetic energy and period of evolution as Θ_o is decreased. Reducing Θ_o to -120 we see from Figure 5.4(b), that the magnetic energy variation has become smoothed, the average energy has increased slightly and the period of the vacillation has continued to fall, though Figure 5.2 suggests that this will level off as Θ_o is decreased further.

Examining the snapshots of the solution over a cycle of the magnetic energy shown in Figures 5.5, 5.6, 5.7 and 5.8 we are able to see how the solutions evolve with time and gain some understanding of how decreasing Θ_o affects the solutions. We see that these are reversing solutions, which undergo half a period of their solution over a cycle of the magnetic energy. We notice that these solutions over their half period evolution show some similar features to those found for the steady and spiky periodic solutions shown in Figures 5.9, 5.13 and 5.14. We see that snapshots at $t = t_o + 0.2375 \rightarrow t_o + 0.95$ in Figure 5.5 and $t = t_o + 0.328$ in Figure 5.6 look very much like the steady solutions in Figure 5.9.

An aspect which is also found in the slow decay phase of the spiky periodic solutions. A feature which is reminiscent of the spiky periodic solutions is the presence of a nearly geostrophic component of the flow in $t = t_o + 1.6625$ of Figure 5.5 and $t = t_o + 0.492$ of Figure 5.6. This kind of geostrophic behaviour in the flow was found in the spiky periodic case (see Fearn and Rahman (2004a,b) for more details) when the magnetic energy of the solution was in the rapid growth phase

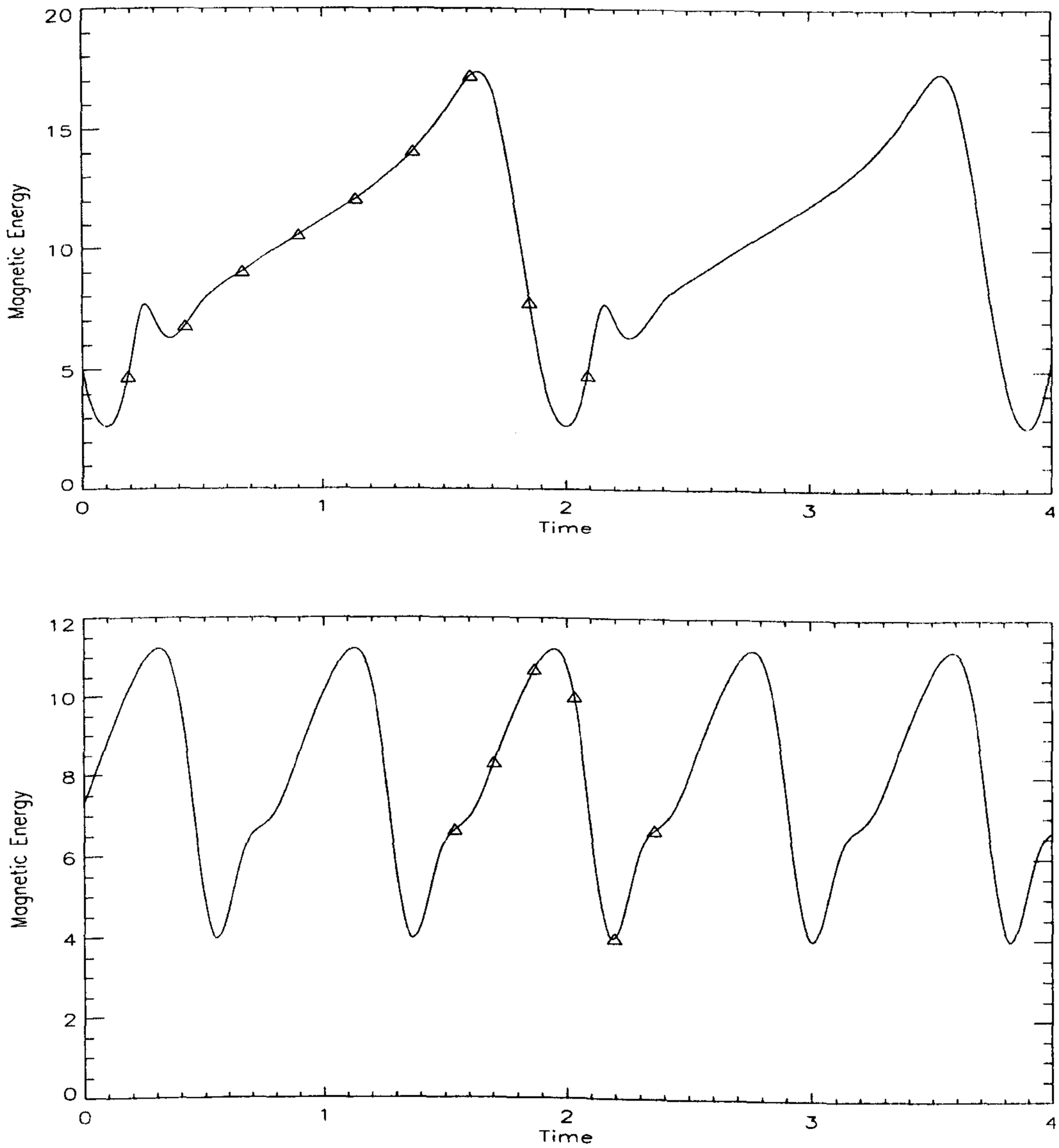

Figure 5.3: The magnetic energy variation of the solution at $\alpha_o = 11$, $E = 2.5 \times 10^{-4}$ and (a) $\Theta_o = -50$ (top) and (b) $\Theta_o = -70$ (bottom). The triangles indicate the points over a cycle at which the solutions is plotted. Snapshots of the solutions over a cycle may be found in Figures 5.5 and 5.6, respectively.

of its time evolution. If we examine our time dependent magnetic energy variation as shown in Figures 5.3 and 5.4, we also see a rapid decrease in the energy. We see that as we reduce Θ_o to -100 and -120, the solutions do not share the resemblance of the steady and spiky solutions to the same extent. We also do not see the same concentration of the geostrophic flow-like contours next to the rotation axis. This is likely due to the smoothed magnetic energy variation.

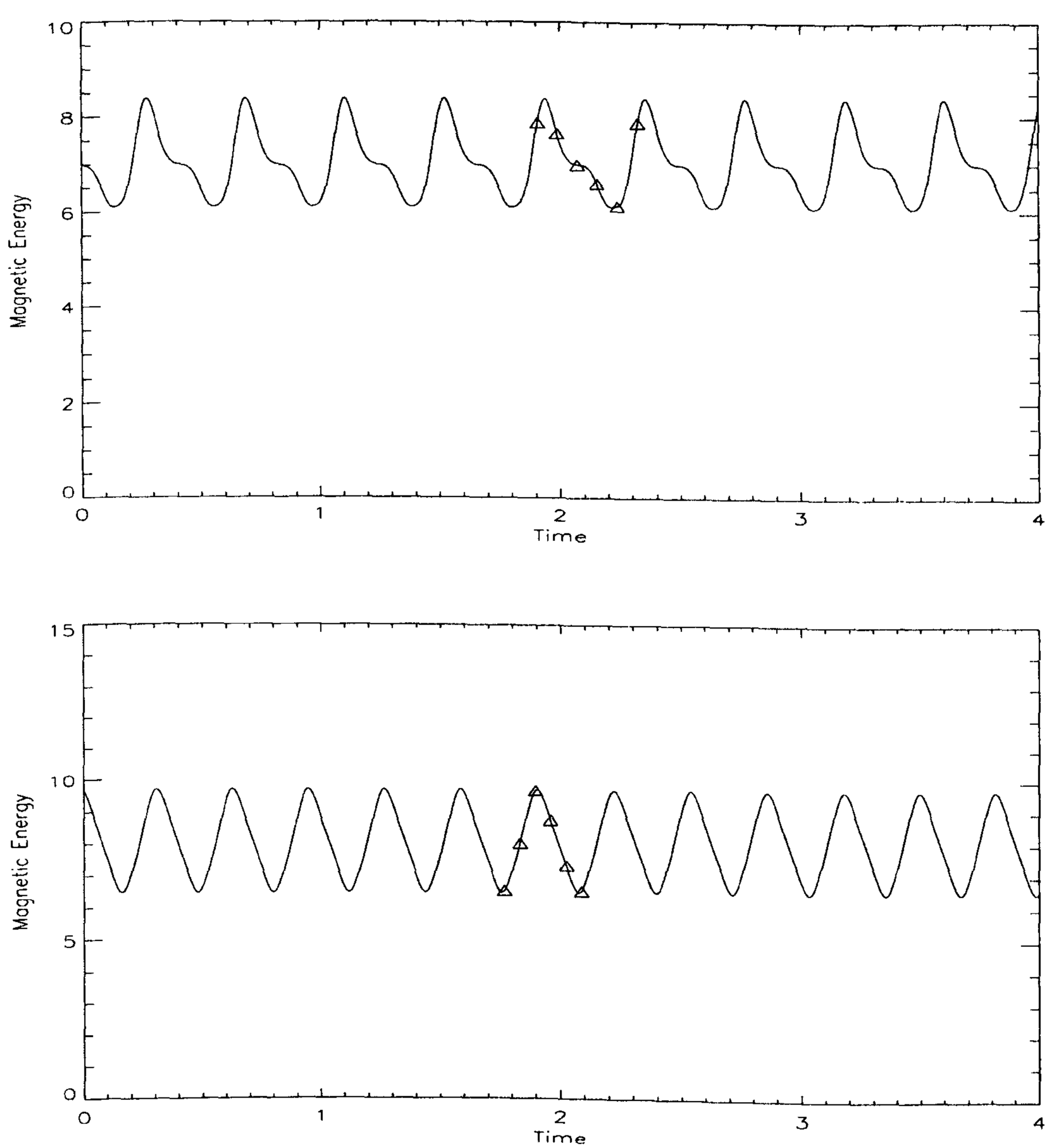

Figure 5.4: As Figure 5.3, but for (a) $\Theta_o = -100$ (top) and (b) $\Theta_o = -120$ (bottom). Snapshots of the solutions over a cycle may be found in Figure 5.7 and 5.8, respectively.

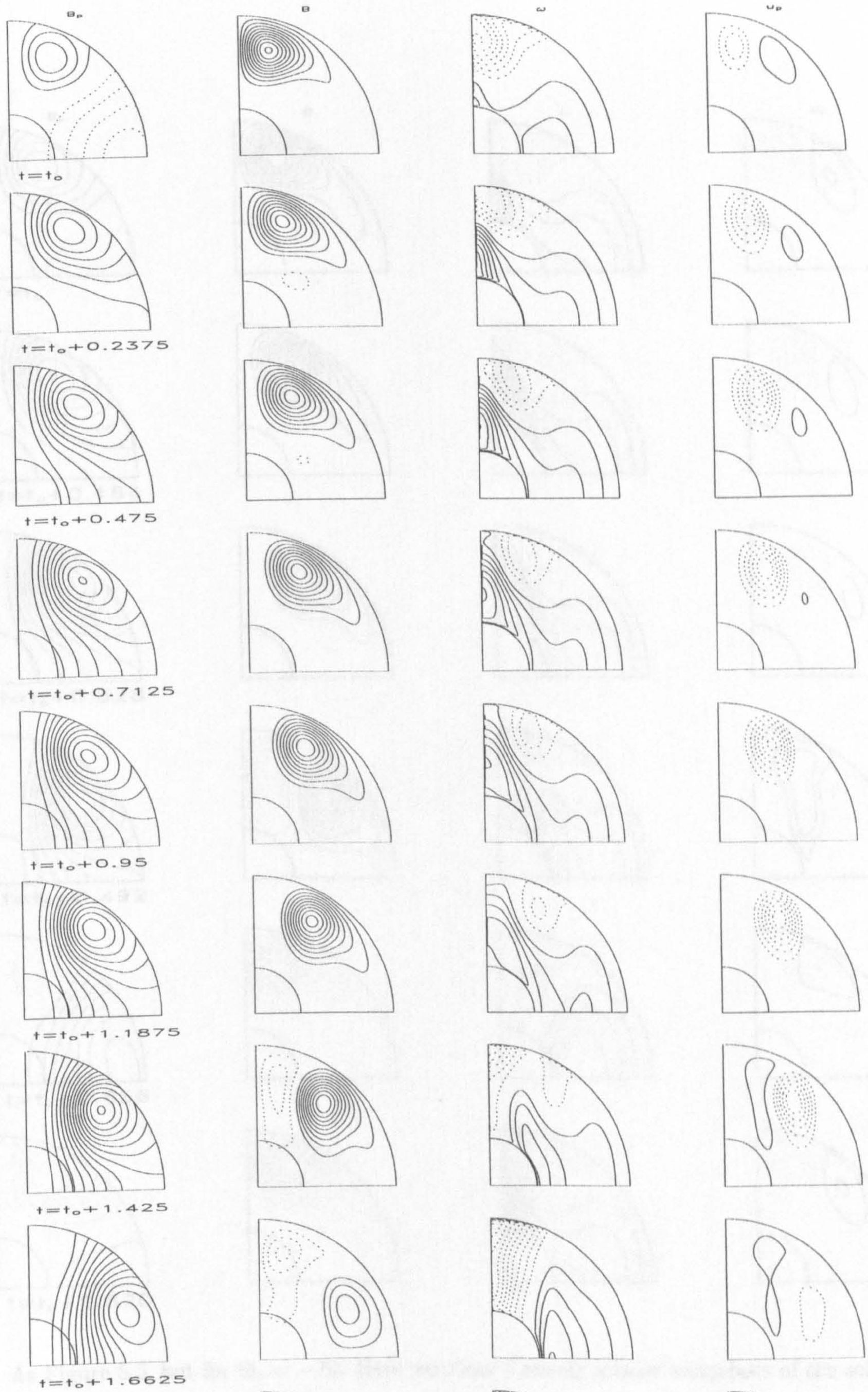

Figure 5.5: (From left to right) The poloidal field, toroidal field, angular velocity and meridional circulation components at contour intervals of 0.05, 0.3, 10, 0.1, respectively. For $\alpha_o = 11$, $\Theta_o = -50$ and $E = 2.5\times10^{-4}$, we show 8 evenly spaced snapshots of the solution over a half period, $\frac{T}{2} = 1.9$.

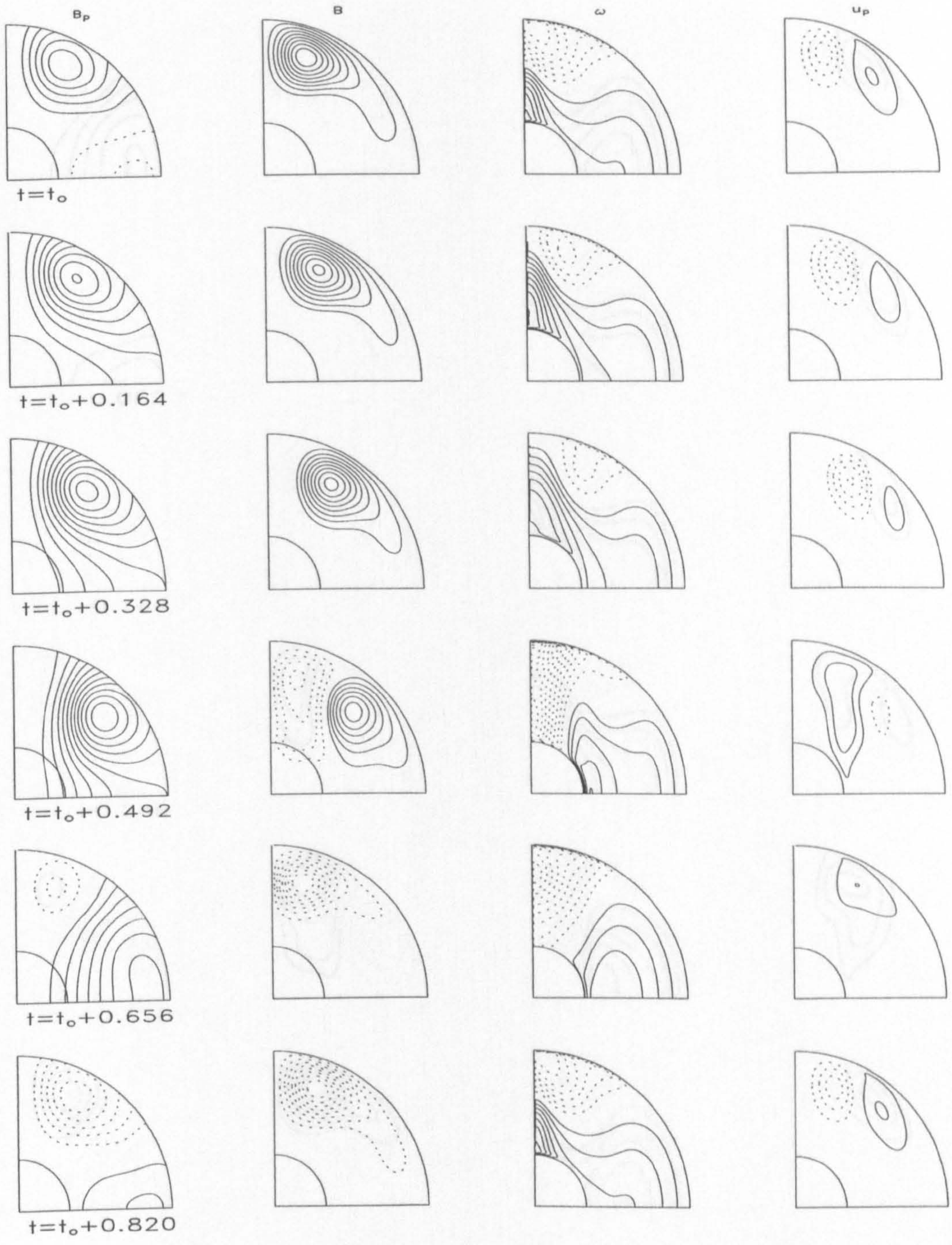

Figure 5.6: As Figure 5.5, but for $\Theta_o = -70$. Here we show 5 evenly spaced snapshots of the solution over a half period, $\frac{T}{2} = 0.82$.

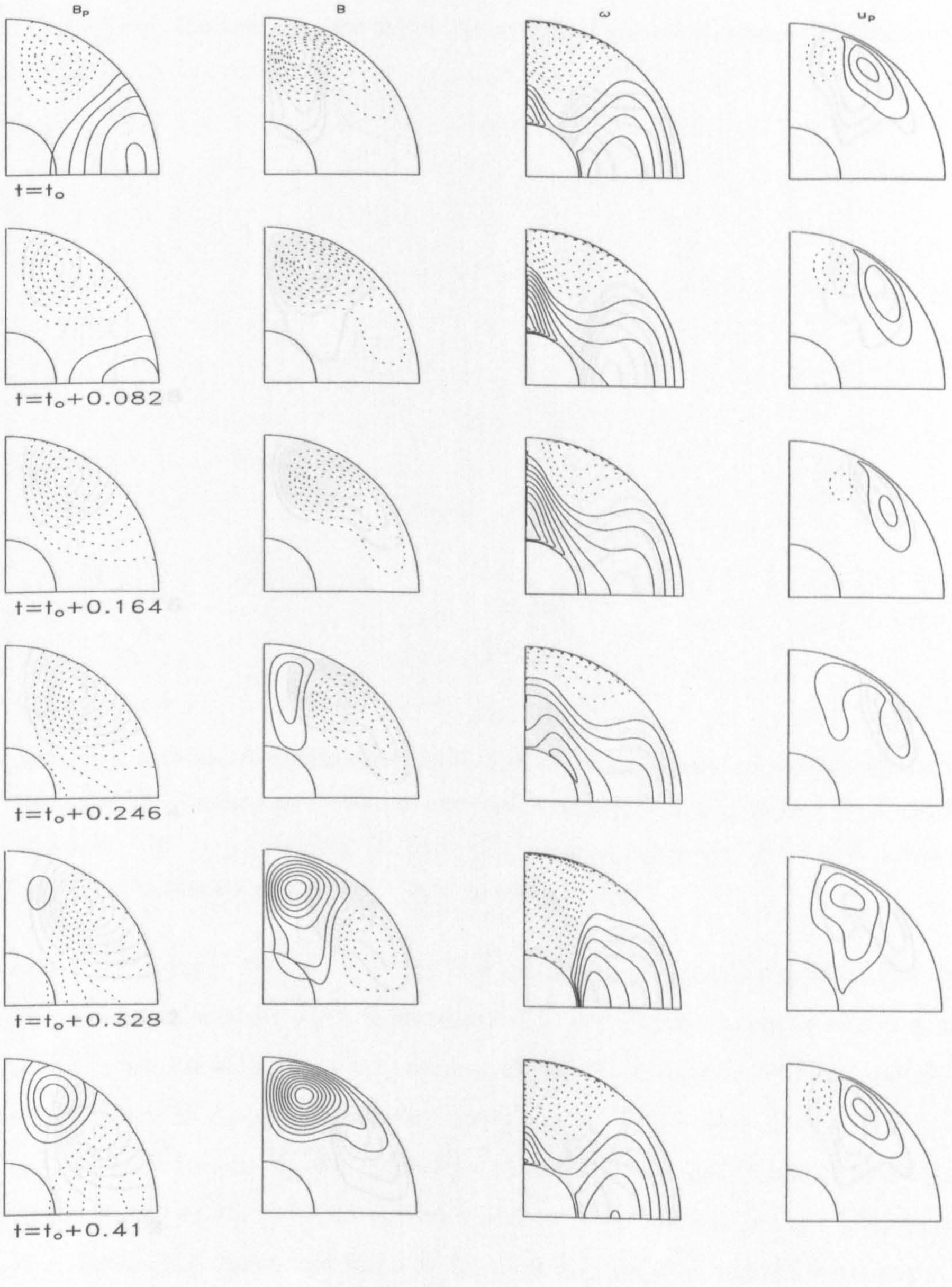

Figure 5.7: As Figure 5.5, but for $\Theta_o = -100$. Here we show 5 evenly spaced snapshots of the solution over a half period, $\frac{T}{2} = 0.41$.

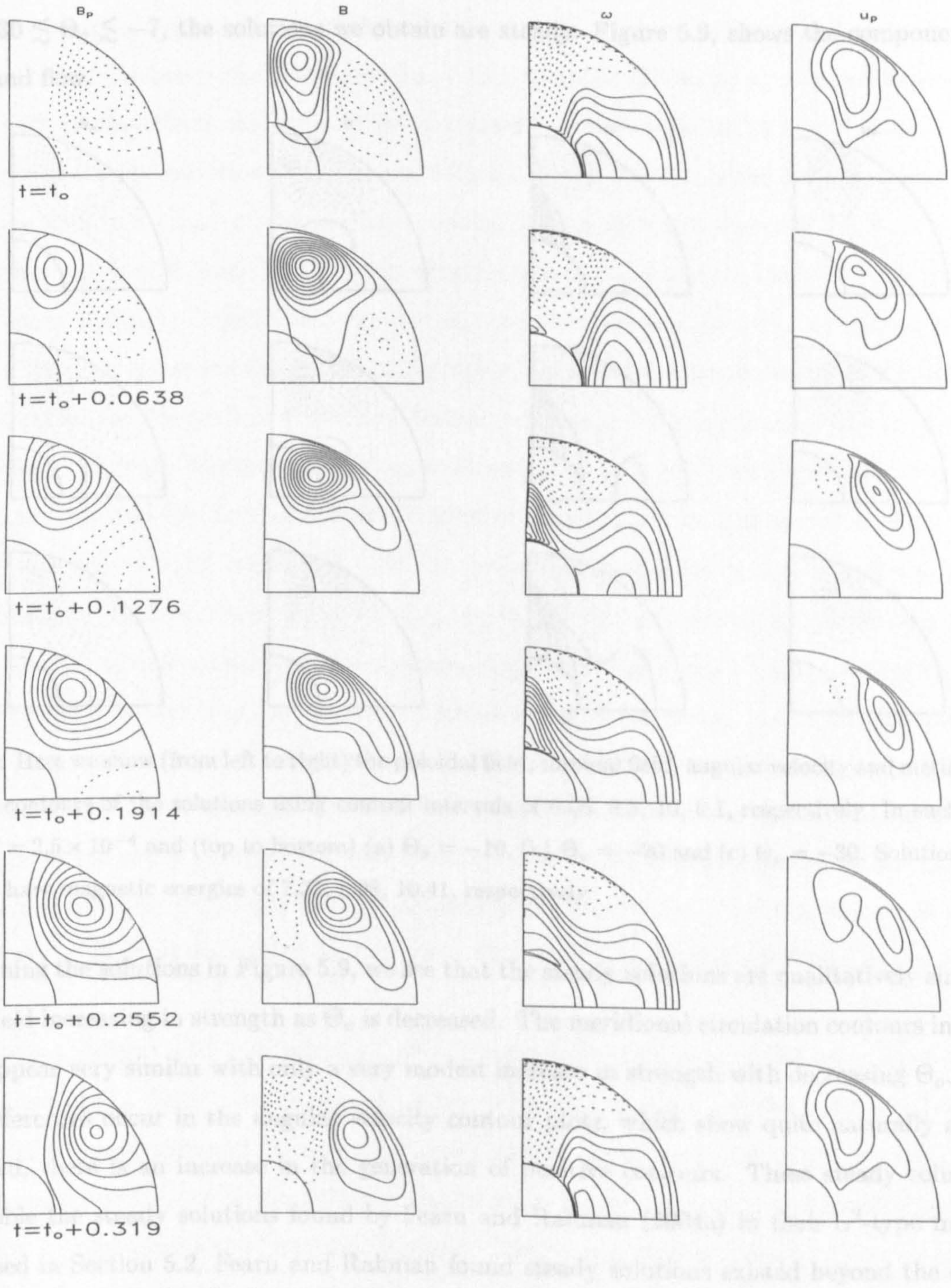

Figure 5.8: As Figure 5.5, but for $\Theta_o = -120$. Here we show 5 evenly spaced snapshots of the solution over a half period, $\frac{T}{2} = 0.319$.

5.6 Steady solutions.

For $-30 \lesssim \Theta_o \lesssim -7$, the solutions we obtain are steady. Figure 5.9, shows the components of the field and flow.

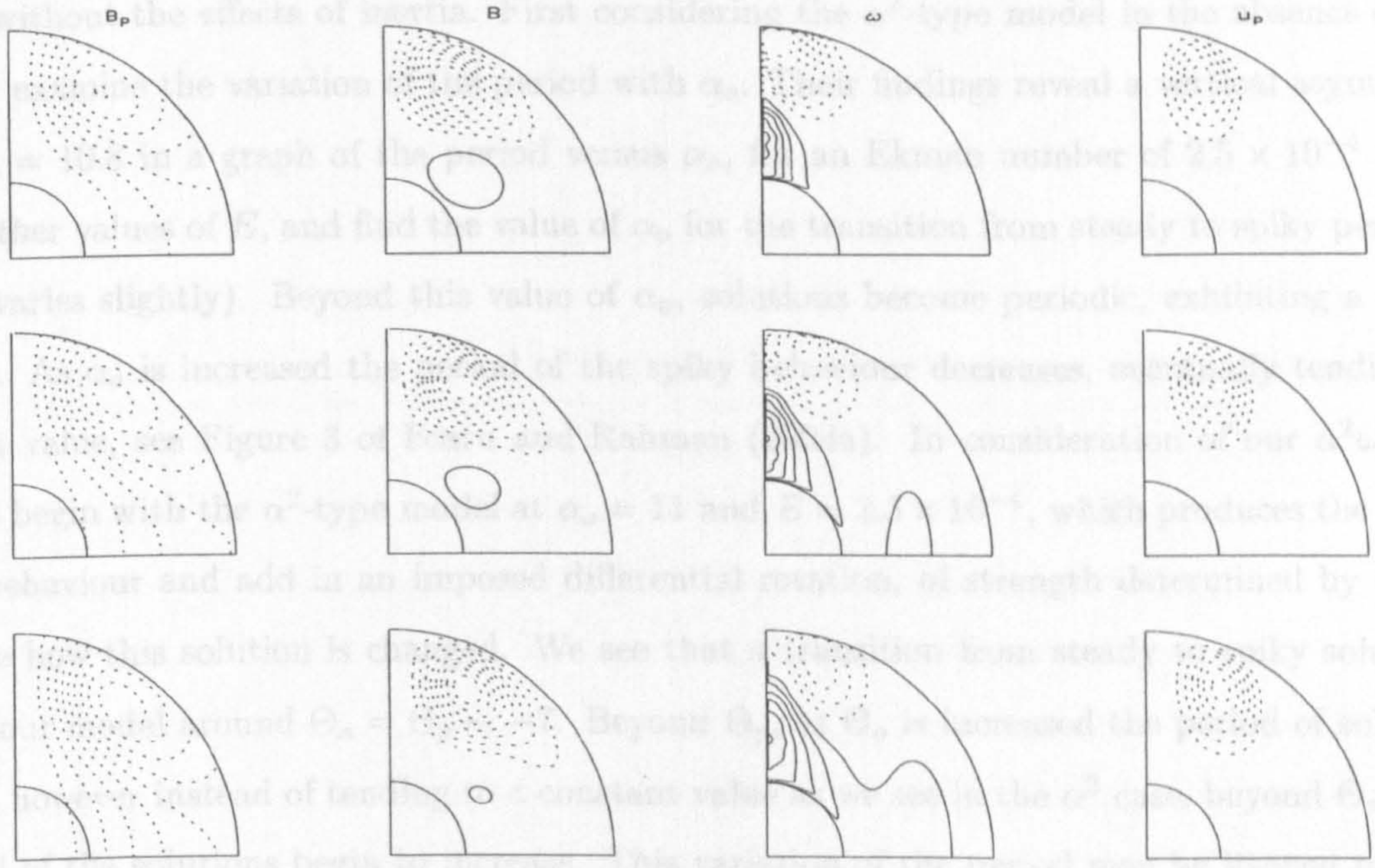

Figure 5.9: Here we show (from left to right) the poloidal field, toroidal field, angular velocity and meridional circulation contours of the solutions using contour intervals of 0.05, 0.3, 10, 0.1, respectively. In each case $\alpha_o = 11$, $E = 2.5 \times 10^{-4}$ and (top to bottom) (a) $\Theta_o = -10$, (b) $\Theta_o = -20$ and (c) $\Theta_o = -30$. Solutions are steady and have magnetic energies of 7.32, 8.98, 10.41, respectively.

Examining the solutions in Figure 5.9, we see that the steady solutions are qualitatively similar, with the field increasing in strength as Θ_o is decreased. The meridional circulation contours in each solution appear very similar with only a very modest increase in strength with decreasing Θ_o. The biggest differences occur in the angular velocity contour plots, which show quite naturally as Θ_o is decreased, there is an increase in the generation of positive contours. These steady solutions also resemble the steady solutions found by Fearn and Rahman (2004a) in their α^2-type model. As discussed in Section 5.2, Fearn and Rahman found steady solutions existed beyond the onset of dynamo action until α exceeded α_p ($\simeq 10.8$ for $E = 2.5 \times 10^{-4}$), at which point the solutions then became time dependent with the solutions exhibiting a spiky periodic behaviour. Figure 1 of Fearn and Rahman (2004a), shows a steady solution at $\alpha_o = 10$ and $E = 2.5 \times 10^{-4}$.

5.7 Spiky solutions.

From the variation of the period of the solution with Θ_o, shown in Figure 5.2, we may draw comparisons with the behaviour found by Fearn and Rahman (2004a,b) in their α^2-type model with and without the effects of inertia. First considering the α^2-type model in the absence of inertia, they examine the variation of the period with α_o. Their findings reveal a vertical asymptote around $\alpha_o = 10.8$ in a graph of the period versus α_o, for an Ekman number of 2.5×10^{-4} (they consider other values of E, and find the value of α_o for the transition from steady to spiky periodic solutions varies slightly). Beyond this value of α_o, solutions become periodic, exhibiting a spiky behaviour. As α_o is increased the period of the spiky behaviour decreases, eventually tending to a constant value, see Figure 3 of Fearn and Rahman (2004a). In consideration of our $\alpha^2\omega$-type model, we begin with the α^2-type model at $\alpha_o = 11$ and $E = 2.5 \times 10^{-4}$, which produces the spiky periodic behaviour and add in an imposed differential rotation, of strength determined by Θ_o to investigate how this solution is changed. We see that a transition from steady to spiky solutions occurs in our model around $\Theta_o = \Theta_p \sim -7$. Beyond Θ_p, as Θ_o is increased the period of solution decreases, however instead of tending to a constant value as we see in the α^2 case, beyond $\Theta_o \sim 50$ the period of the solutions begin to increase. This variation of the period may be likened to that found by Fearn and Rahman (2004b), in their investigation. In this model, they begin with an $Ro = 0$ solution at $\alpha_o = 11$ and $E = 2.5 \times 10^{-4}$ and gradually increase the strength of the inertia, Ro. They find that as Ro is increased, the period of these spiky solutions decreases and then increases again, eventually tending to the vertical asymptote around $Ro = 0.012$ in the graph of the period versus Ro. Beyond the vertical asymptote as Ro is further increased, the solutions are steady.

The plots in Figures 5.10, 5.11 and 5.12, show the periodic behaviour of the spiky solutions at different values of Θ_o, (N.B. The timescales on the horizontal axes are not the same in all plots). The solutions at small values of Θ_o very much resemble the solutions found in the α^2-type model in the absence of inertia. At higher values of Θ_o, at $\Theta_o = 50$ for example, the solution exhibits a slight change to this established behaviour pattern. Closer inspection of Figure 5.12(a) reveals an alternating peak height. For the period of this cycle, we take the time between the two large peaks (or two small peaks), as one naturally would to calculate the period of oscillation of a disturbance. We notice that it is not simply the case that the solution requires a longer run time, as the smaller

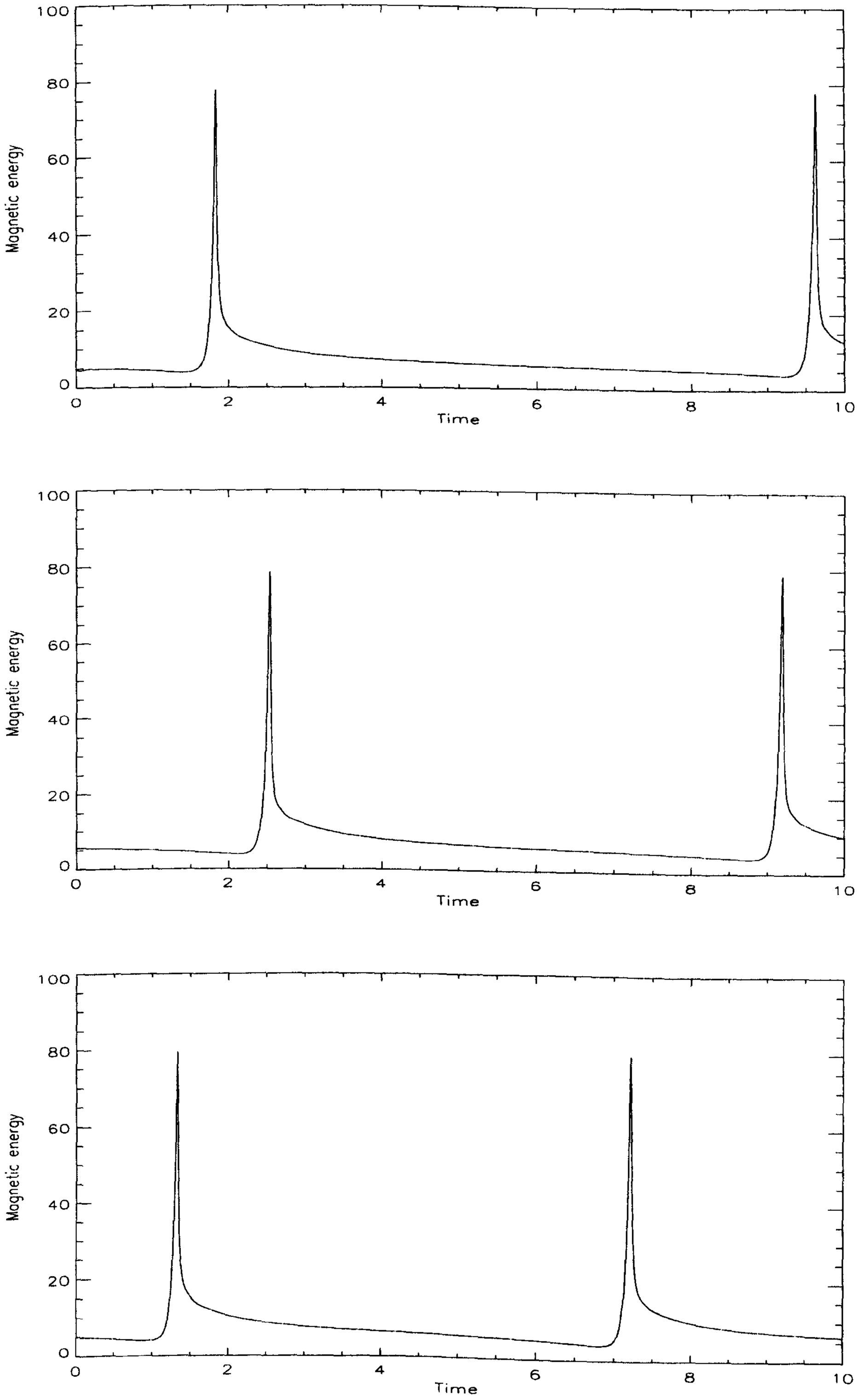

Figure 5.10: Time variation of magnetic energy for $\alpha_o = 11$, $E = 2.5 \times 10^{-4}$ and (top to bottom) (a) $\Theta_o = -3$, (b) $\Theta_o = -2$ and (c) $\Theta_o = -1$. The period in each case is 7.81, 6.64, 5.86, respectively.

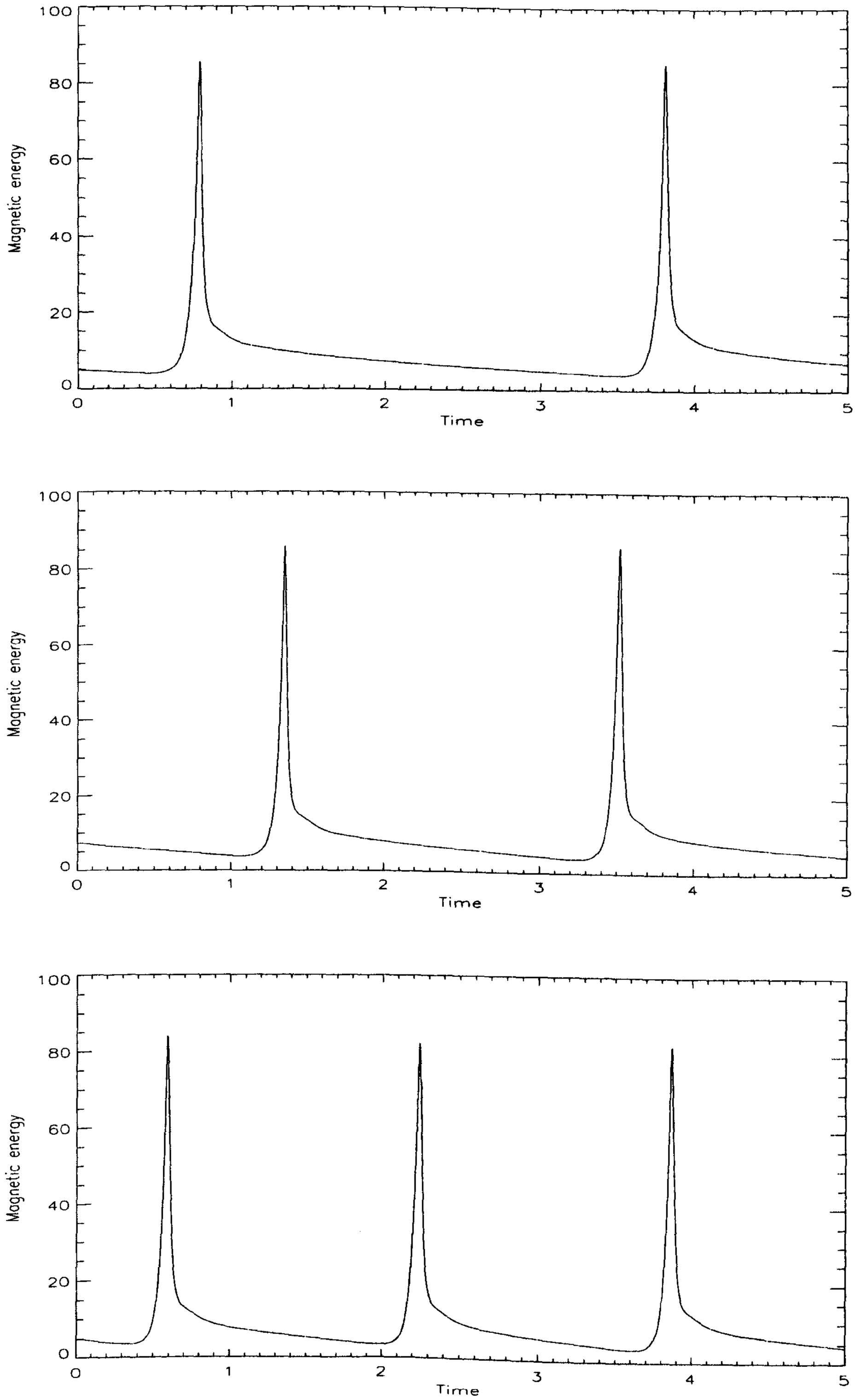

Figure 5.11: As Figure 5.10, but for top-bottom, (a) $\Theta_o = 10$, (b) $\Theta_o = 20$ and (c) $\Theta_o = 30$. The period in each case is 2.81, 2.15, 1.64, respectively.

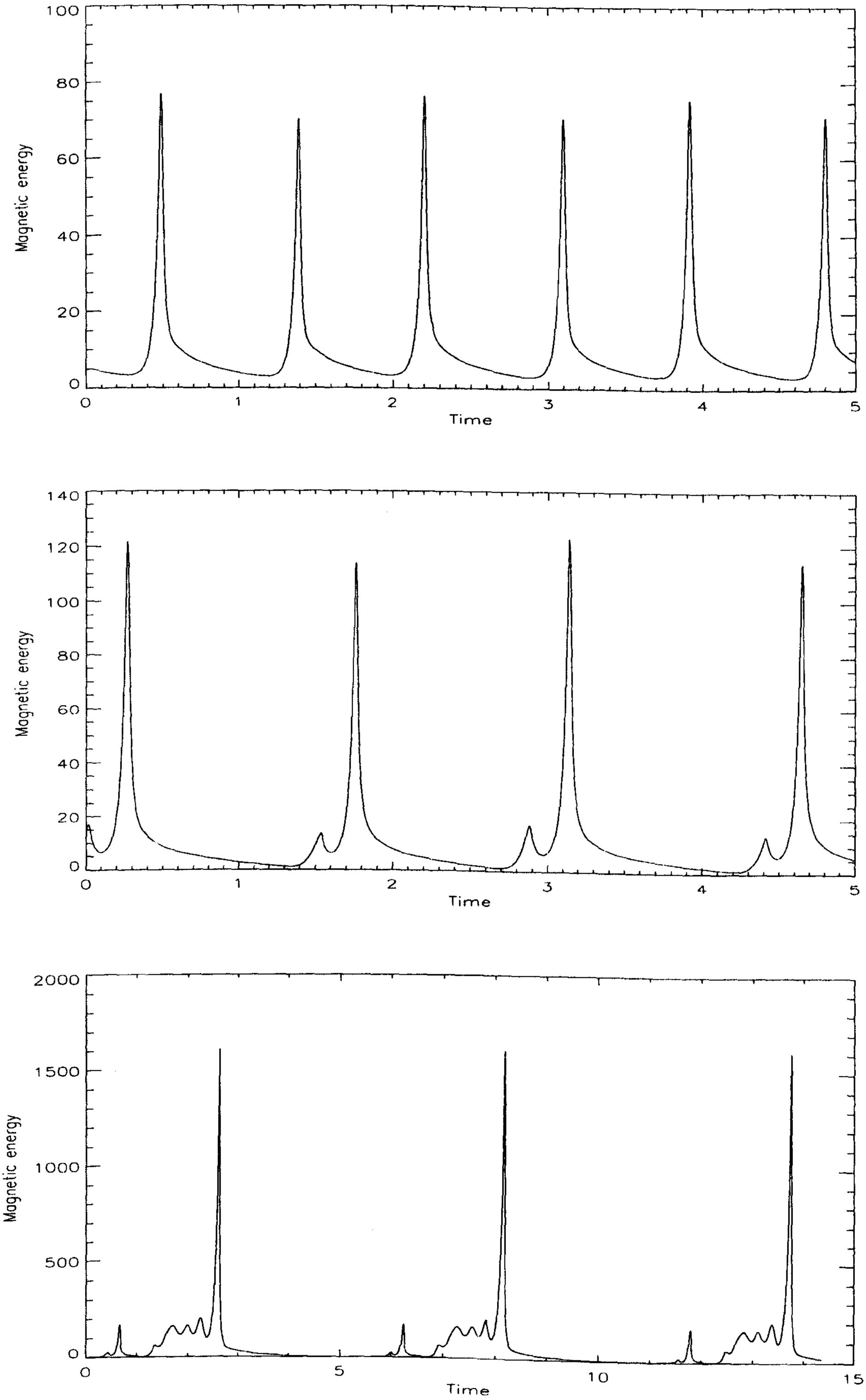

Figure 5.12: As Figure 5.10, but for top-bottom, (a) $\Theta_o = 50$, (b) $\Theta_o = 70$ and (c) $\Theta_o = 100$. The period in each case is 1.72, 2.85, 4.92, respectively.

height peak does not fall directly in between the two large peaks on either side, lying 0.9 diffusion times to the right of a large peak and 0.82 diffusion times to the left. Examining the periodic behaviour of $\Theta_o = 70$, we see the same trend as in $\Theta_o = 50$, with the period occurring as 2.84 diffusion times, and the lower peak sitting off centre again, lying 1.48 diffusion times to the right of a large peak and 1.38 diffusion times to the left. In the magnetic energy variation in Figure 5.12(b), we also see the emergence of low amplitude peaks or kinks to the left of the large peaks, with the exponential decay phase of the solutions unaffected. The solution at $\Theta_o = 100$, exhibits a similar periodic behaviour, but now includes much more (comparatively) low amplitude time dependent behaviour. The solutions are clearly much more complex here and the equilibration mechanism less clear cut. We also tried increasing Θ_o to 150 (solutions not shown). The time variation here is substantially more complicated, but initial results suggested that the periodic behaviour would be continued. Given Figure 5.2, the period of this solution is anticipated to be quite large and computationally such a calculation would take a substantial length of time to run. We note that whilst Figure 5.2 appears qualitatively similar to the observed variation of the period with Rossby number in Fearn and Rahman's (2004b) model, we do not find a transition to steady behaviour as Θ_o is increased.

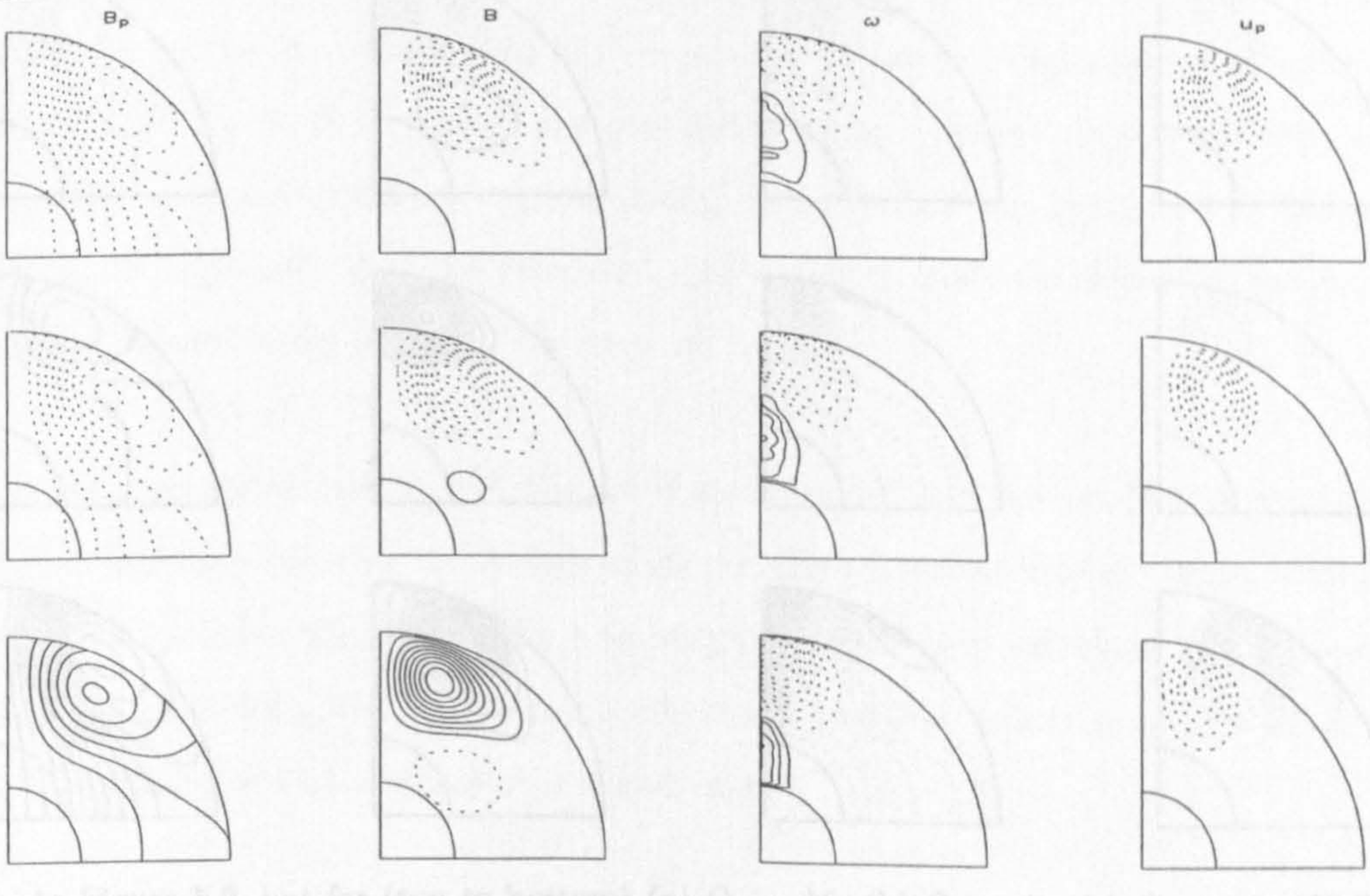

Figure 5.13: As Figure 5.9, but for (top to bottom) (a) $\Theta_o = -3$, (b) $\Theta_o = -2$ and (c) $\Theta_o = -1$. Here we show snapshots of these periodic solutions in the slow decay phase, which resemble the steady solutions in Figure 5.9

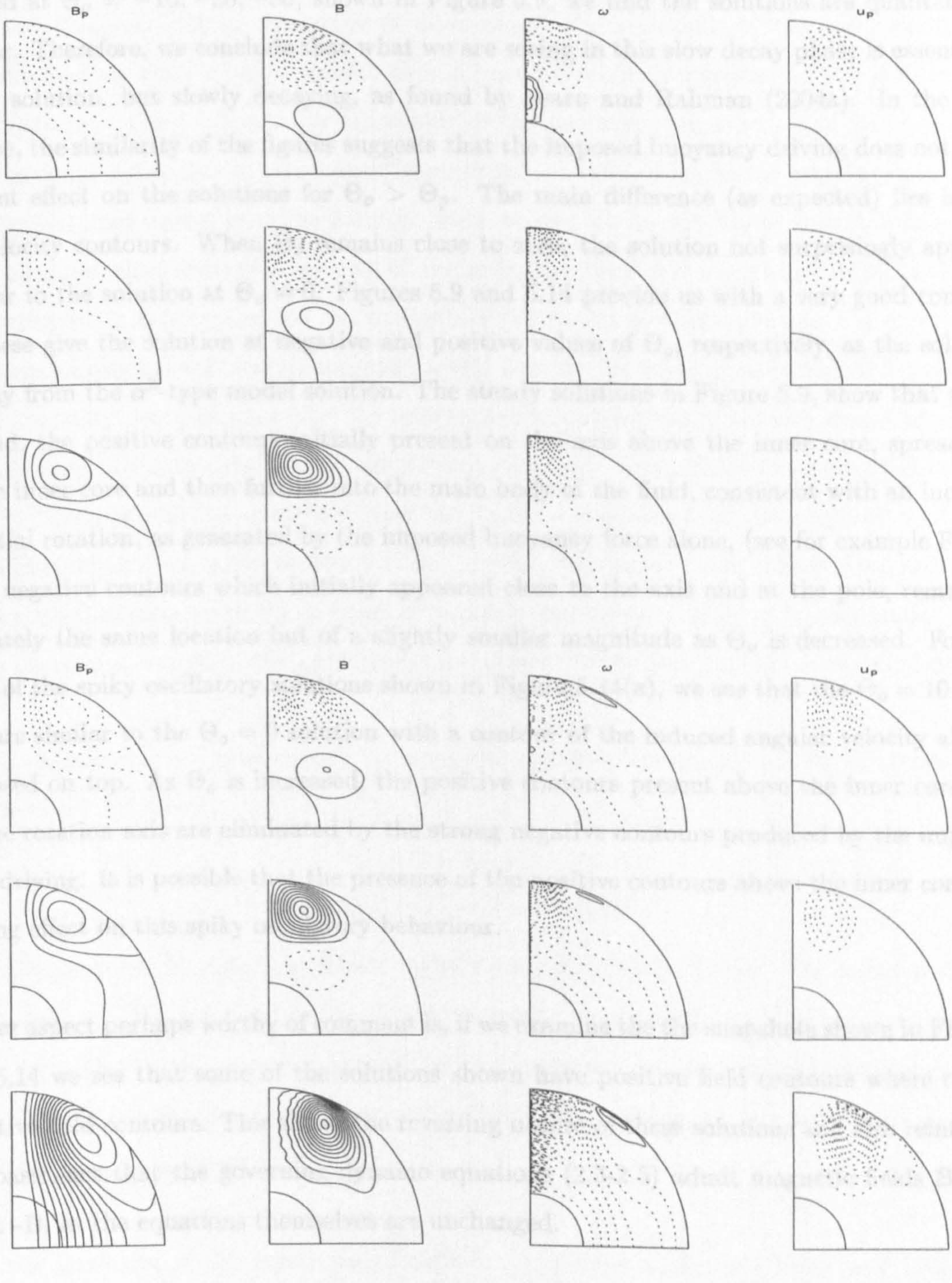

Figure 5.14: As Figure 5.9, but for (top to bottom) (a) $\Theta_o = 10$, (b) $\Theta_o = 20$, (c) $\Theta_o = 30$, (d) $\Theta_o = 50$, (e) $\Theta_o = 70$ and (f) $\Theta_o = 100$. Here we show snapshots of these periodic solutions in the slow decay phase.

If we compare the snapshots of the solutions in Figures 5.13 and 5.14, with the steady solutions we obtained at $\Theta_o = -10, -20, -30$, shown in Figure 5.9, we find the solutions are qualitatively very similar. Therefore, we conclude that what we are seeing in this slow decay phase is essentially the steady solution, but slowly decaying, as found by Fearn and Rahman (2004a). In the slow decay phase, the similarity of the figures suggests that the imposed buoyancy driving does not have a significant effect on the solutions for $\Theta_o > \Theta_p$. The main difference (as expected) lies in the angular velocity contours. When Θ_o remains close to zero, the solution not surprisingly appears very similar to the solution at $\Theta_o = 0$. Figures 5.9 and 5.14 provide us with a very good comparison, as these give the solution at negative and positive values of Θ_o, respectively, as the solution moves away from the α^2-type model solution. The steady solutions in Figure 5.9, show that as Θ_o is decreased, the positive contours initially present on the axis above the inner core, spread out around the inner core and then further into the main body of the fluid, consistent with an increase in differential rotation, as generated by the imposed buoyancy force alone, (see for example Figure 2.1). The negative contours which initially appeared close to the axis and at the pole, remain in approximately the same location but of a slightly smaller magnitude as Θ_o is decreased. For the snapshots of the spiky oscillatory solutions shown in Figure 5.14(a), we see that the $\Theta_o = 10$ solution appears similar to the $\Theta_o = 0$ solution with a contour of the induced angular velocity almost superimposed on top. As Θ_o is increased, the positive contours present above the inner core and close to the rotation axis are eliminated by the strong negative contours produced by the imposed buoyancy driving. It is possible that the presence of the positive contours above the inner core has a stabilising effect on this spiky oscillatory behaviour.

Another aspect perhaps worthy of comment is, if we examine the the snapshots shown in Figures 5.13 and 5.14 we see that some of the solutions shown have positive field contours where others have negative field contours. This shows the reversing nature of these solutions and also reinforces the very basic fact that the governing dynamo equations (2.3-2.5) admit magnetic fields **B**, but also admit -**B**, as the equations themselves are unchanged.

5.8 Taylor's constraint.

Fearn and Rahman (2004a) examined in close detail the behaviour of the spiky oscillatory solutions obtained by their α^2-type model, and in particular the dependence of the solutions on Taylor's constraint. They followed the behaviour of the solution over a period of its oscillation, focussing particular attention on the change in solutions over the spike. In the rapid growth phase of its oscillation, they found that the solution grew at essentially the linear growth rate in this phase. In addition, they observe a reversal of the field, and find that the evolution of the flow is almost geostrophic in this region. As the strength of the magnetic field increases, the geostrophic flow decreases leaving behind a weak magnetic wind. Beyond the rapid growth phase, the solution moves into the rapid decay phase where the system, having reached its maximum magnetic energy, sees a rapid decay in the toroidal component of magnetic field. The poloidal magnetic field decays more slowly. The poloidal flow closely mirrors the toroidal component of the magnetic field. The greatest differences appear in the contours of the angular velocity as these change drastically over a very short space of time, with the differential rotation increasing quickly as the magnetic energy reaches its maximum, and then the geostrophic component of the flow evolves as the field decays.

To help explain this behaviour, they focus on the systems dependence on Taylor's constraint (see also Section 1.5). Using,

$$T(s) = \frac{\int_{C(s)} [(\nabla \times \mathbf{B}) \times \mathbf{B}]_\phi dS}{\max \int_{C(s)} |[(\nabla \times \mathbf{B}) \times \mathbf{B}]_\phi| dS} \tag{5.1}$$

to obtain a measure of the extent to which Taylor's constraint (1.21) holds. The steady solutions and the snapshots of the solutions in the slowly decaying phase, satisfy Taylor's constraint. They investigate the ability of the system to satisfy Taylor's constraint in the spiky region of its periodic evolution. Taylor's constraint is reasonably well satisfied over a cycle, though the extent to which it is satisfied over a cycle varies.

Given the similarity of the behaviour of both our $\alpha^2\omega$-type model and Fearn and Rahman's (2004b) α^2-type model with inertia to the original inertialess α^2-type model considered by Fearn and Rahman (2004a), leads us to believe that the particular details over a cycle of the solution are likely to be very similar, and therefore not worthy of an indepth and time-consuming analysis at

this time.

5.9 Comparison of solutions as we vary Θ_o.

Fearn and Rahman (2004a) investigated in detail the mechanism responsible for the spiky periodic behaviour of their α^2-type model, for $\alpha_o > \alpha_p$. The spiky periodic behaviour sees a rapid increase in magnetic energy, followed by a much slower decay. In the slow decay phase, the solutions resemble the steady solutions which were found at values of $\alpha_o < \alpha_p$.

In this chapter, we considered an $\alpha^2\omega$-type dynamo model, by incorporating the imposed buoyancy force, $\Theta\mathbf{r}$ in order to generate an ω-effect, as discussed in Section 2.7, and investigate the effect of varying the magnitude of this force, Θ_o. In Section 1.6.4, we discussed the general $\alpha^2\omega$ model and its two limiting cases; the α^2 model and the $\alpha\omega$ model.

Let us examine the governing equations presented in Chapter 2. Equations (2.11), (2.12), (2.15) and (2.17) in the absence of inertia are

$$\frac{\partial A}{\partial t} = D^2 A + \alpha B + N(\psi, A) \tag{5.2}$$

$$\frac{\partial B}{\partial t} = D^2 B + \mathbf{e}_\phi \cdot \nabla[\alpha \nabla \times (A\mathbf{e}_\phi)] + M(v, A) - M(B, \psi) \tag{5.3}$$

$$-2\frac{\partial \psi}{\partial z} = ED^2 v + N(B, A) \tag{5.4}$$

$$2\frac{\partial v}{\partial z} = E(D^2)^2\psi + M(D^2 A, A) + M(B, B) + \frac{\partial \Theta}{\partial \theta} \tag{5.5}$$

where

$$\frac{\partial}{\partial z} = \cos\theta \frac{\partial}{\partial r} - \frac{\sin\theta}{r}\frac{\partial}{\partial \theta}$$

$$D^2 = \nabla^2 - (r\sin\theta)^{-2}$$

$$N(X, Y) = \mathbf{e}_\phi \cdot [\nabla \times (X\mathbf{e}_\phi) \times \nabla \times (Y\mathbf{e}_\phi)]$$

$$M(X, Y) = \mathbf{e}_\phi \cdot \nabla \times [X\mathbf{e}_\phi \times \nabla \times (Y\mathbf{e}_\phi)]$$

Now we see that in (5.2) the α-effect acts on the toroidal field to generate poloidal field. In (5.3) the α-effect acts on the poloidal field to generate toroidal field. The imposed buoyancy force

appearing in equation (5.5), generates a thermal wind v which feeds into the term $M(v, A)$ in equation (5.3) to act on the poloidal field to generate toroidal field. These two terms in (5.3) both then act to generate the toroidal component of the field. In the limit that $\mathbf{e}_\phi \cdot \nabla[\alpha\nabla \times (A\mathbf{e}_\phi)] > M(v, A)$, the balance of the equations is α^2 whereas $\mathbf{e}_\phi \cdot \nabla[\alpha\nabla \times (A\mathbf{e}_\phi)] < M(v, A)$, results in the balance of the equations being $\alpha\omega$.

The solutions we find for $-50 \lesssim \Theta_o \lesssim 50$ resemble those found in the α^2-type model investigated by Fearn and Rahman (2004a), which saw a change from steady solutions to spiky periodic behaviour as α_o was increased. The period of the spiky periodic behaviour decreased as α_o is increased eventually tending to a constant value. We see this same trend as Θ_o is increased from -30 up to 50, changing from steady solutions to spiky periodic behaviour. This is in keeping with the dynamo equations being in the α^2-type model limit.

For $\Theta_o < -50$ we see that the steady solutions have given way to periodic solutions, which are reminscent of the $\alpha\omega$ solutions we obtained in Chapter 3. This type of behaviour as Θ_o is decreased is not unexpected. As we discussed above in our examination of the limits of the equations, when the strength of the imposed buoyancy force is sufficiently strong, $M(v, A)$ will exceed $\mathbf{e}_\phi \cdot \nabla[\alpha\nabla \times (A\mathbf{e}_\phi)]$ and the character of equations becomes more like the $\alpha\omega$-type model. The solutions we find here exhibit a periodic variation with magnetic energy, which examining the graphs in Figures 5.3 and 5.4, we see an initial decrease in the average magnetic energy which then increases slightly appearing to level off as Θ_o is decreased. We also see a decrease in the period of the solutions eventually appearing to tend to a constant value as we lower Θ_o. If we compare this behaviour with the $\alpha\omega$ solutions we find in Chapter 3 we see the decreasing trend in the period is quite common, but did not find a decrease in the average magnetic energy of the solutions at all, and therefore deduce that this must be a feature of the $\alpha^2\omega$-type model, presumably arising from the presence of the α-term in (5.3).

For $\Theta_o > 50$, the spiky periodic solutions continue, but instead of the period tending to a constant value, as was observed in the α^2-type model with increasing α_o, with increasing Θ_o we see the period of the solution increases as Θ_o is increased beyond 50. The behaviour we find here

is not like the characteristic $\alpha\omega$ solutions we found in Chapter 3, but shares similarities with the work by Fearn and Rahman (2004b) on their α^2-type dynamo including the effect of inertia. The influence of inertia on the α^2-type model is a quite different problem to the one of the effect of Θ_o on our $\alpha^2\omega$-type model. The equilibrating mechanism in each case is different, and we see that as we increase Θ_o, despite the similarities in the variation of the period the solutions become more complex in their time behaviour, unlike in the α^2 case where, as Ro is increased the time variation of the solutions remains qualitatively the same and only the period changes. Whilst the contours of the magnetic field and meridional circulation are very similar, we also see differences in the angular velocity contours of the solutions in the slow decay phase, between the α^2-type model with inertia and the $\alpha^2\omega$-type model. The $\alpha^2\omega$ solutions naturally see a greater contribution to the angular velocity, as the buoyancy force drives an angular velocity in the flow. The angular velocity contours in the α^2-type model with inertia change very little with an increase in Ro, whilst in the slow decay phase. We examine the combination of these two effects more closely in the Chapter 6, where we include the full inertia term in the $\alpha^2\omega$-type model we presented here.

5.10 Conclusions.

The results of Fearn and Rahman's (2004a) α^2-type model, which introduced a radial structure to the α-effect, produced solutions whose variation with magnetic energy exhibited an unusual spiky periodic time behaviour. Hollerbach and Ierley (1991) were the first to observe time dependent solutions using an α^2 model. They considered an α^2 dynamo model in a rotating spherical shell, neglecting inertial effects, focussing on the behaviour of solutions as they chose different forms for their prescribed α-effect. Some of their choices revealed steady solutions, whilst other choices led to unsteady periodic behaviour. In Fearn and Rahman (2004b), they included inertial effects into the system and investigated how the behaviour of the system changes as inertia is increased. In this Chapter we investigated an $\alpha^2\omega$-type model, in which we take Fearn and Rahman's (2004a) α^2-type model and included the prescribed buoyancy driven ω-effect. The main aim of our investigation here, was to see how our imposed buoyancy force modified the behaviour of their solutions.

Fixing $\alpha_o = 11$ (which revealed spiky solutions in the α^2-model), we then varied the strength of Θ_o. Our studies revealed a bifurcation from steady solutions to spiky solutions around $\Theta_o \sim -7$,

similar to the behaviour in the α^2 case, which saw a transition from steady solutions to the spiky solutions as α_o was increased beyond the onset of dynamo action. In the spiky behaviour regime, we increased Θ_o and found that instead of the period of the solutions tending towards a constant value, as had been found in the α^2-type model, the period decreased to a minimum and then increased again. This behaviour at large Θ_o was reminiscent of the periodic behaviour of the spiky solutions in Fearn and Rahman's (2004b) α^2-type model which included inertial effects. In this model as the strength of inertia is increased, the period of the solutions initially decreases and then increases again eventually tending to infinity, as the solutions then become steady. Our variation with period also resembles this behaviour as shown in Figure 5.2, but increasing Θ_o as high as 100 we found no evidence of steady behaviour setting in or of a bifurcation to different behaviour.

As we decreased Θ_o away from the steady solutions at $\Theta_o = -30$, we found the solutions became periodic, as shown in Figures 5.3 and 5.4. We see that as Θ_o is decreased, the time variation of the magnetic energy becomes smoothed out by the increasing influence of Θ_o. The period of these solutions decreases as Θ_o is decreased, eventually tending to a constant value as shown in Figure 5.2. The evolution of the solutions over a cycle of the magnetic energy revealed that the solutions themselves appeared very similar as Θ_o is decreased, which also shared elements of the steady and spiky solutions. The magnetic field contours completed half a period in a cycle of the magnetic energy, with the flow completing a full period in this time. These solutions were reminiscent of the $\alpha\omega$ solutions found in Chapter 3, which is not altogether unexpected as the $\alpha\omega$-type dynamo is a natural limiting case of the $\alpha^2\omega$-type model when Θ_o is large, as we discussed in Section 5.9. For $-50 < \Theta_o < 50$, the solutions resemble the α^2-type solutions of Fearn and Rahman (2004a) suggesting that the $\alpha^2\omega$-type dynamo is in the α^2 regime and the ω-effect is dominated by the α-effect term in the governing equations.

It should be noted that the code has a dipole imposed parity in order to enable faster integration times, an especially important consideration given the length of the period for some of the values of Θ_o. However, as has been commented by Hollerbach and Glatzmaier (1998) and Sarson *et al* (1998), it is possible that we may obtain solutions which are radically different from a general mixed-parity model, especially at high values of Θ_o.

Chapter 6

$\alpha^2\omega$-dynamos with inertia.

6.1 Introduction.

In this chapter we include the effect of inertia in the $\alpha^2\omega$-type model that we introduced in the previous chapter. In addition, we investigate how the solutions at a fixed value of Ro change as we vary the strength of the imposed buoyancy driving. Through varying both these parameters, we are able to obtain a map of $Ro - \Theta_o$ space. Examining these solutions may help to reveal the mechanisms within the system which are responsible for the enhanced generation of dynamo action in the α^2-type model and the apparent failure of the dynamo in the $\alpha\omega$-type model investigated in Chapter 4.

6.2 Background

In the same way as we approached the $\alpha\omega$-type model we considered in Chapters 3 and 4, we extend the work on the $\alpha^2\omega$-type model discussed in Chapter 5 by including the effect of inertia, and investigating the behaviour of the solutions as Ro is increased. We summarised the findings of Fearn and Rahman (2004b) in Chapter 4, see Section 4.2 for further details. Also relevant here is the work we presented in Chapter 5, as this gives us the $\alpha^2\omega$ solutions in the inertialess case, which the solutions we obtain in this chapter should tend towards as Ro is reduced to zero.

6.3 The effect of the imposed buoyancy force.

In this section we investigate the effect the imposed buoyancy force has on the α^2-type dynamo with inertia solutions found by Fearn and Rahman (2004b), described in Section 4.2. We begin with their solution at $\alpha_o = 11$, $Ro = 2 \times 10^{-2}$ and $E = 2.5 \times 10^{-4}$. Our of choice of parameters here, is simply due to the fact that, at this particular value of the Rossby number, the effect of inertia had been sufficient to change the character of the solutions from the spiky periodic type found in the absence of the inertia and at low values of inertia, to steady solutions. It therefore seemed an obvious place to begin the investigation of the effect of the buoyancy force, as we were already aware that this magnitude of the Rossby number should be sufficient to alter the balance of the system of equations and produce some interesting results; hopefully illuminating how these effects influence the equilibration mechanism.

We then consider higher values of Ro. Fixing $\alpha_o = 11$ and $E = 2.5 \times 10^{-4}$ we then take Fearn and Rahman's solution at $Ro = 5 \times 10^{-2}$, as this lies firmly in the middle of the range of values which yielded steady solutions. The next values we choose for the strength of inertia are 7×10^{-2} and 8×10^{-2}, which lay toward the limit of resolution of Fearn and Rahman's solutions. Through considering this range of values of Ro we are able to vary Θ_o in each case and see if there is a general trend in the variation of the magnetic and kinetic energy, as Ro is increased.

In Figures 6.1 and 6.2 we show the variation of the magnetic and kinetic energies with Θ_o at fixed values of $\alpha_o = 11$ and $E = 2.5 \times 10^{-4}$. Figure 6.1(a) shows this variation at $Ro = 2 \times 10^{-2}$. In Figure 6.1(b) the Rossby number has been increased to 5×10^{-2}, and the process of studying the solutions produced at varying values of Θ_o is repeated. Comparing Figures 6.1(a) and 6.1(b), we see that they exhibit the same trend as Θ_o is increased. The shape of these two graphs appears similar between the two values of Ro. The results we obtained at $Ro = 7 \times 10^{-2}$ and 8×10^{-2} are shown in Figure 6.2. We encountered numerical difficulties in reducing Θ_o below -20 and so have no results in this region. However for $\Theta_o \geq -20$, the energy variation with Θ_o appears similar to that found at $Ro = 2 \times 10^{-2}$ and $Ro = 5 \times 10^{-2}$. The behaviour of the solutions in Figure 6.1 for $\Theta_o < -20$ as Θ_o is decreased is erratic and does not show the same evolution as for Θ_o positive, which sees a natural progression from steady solutions to oscillatory ones. The erratic solutions

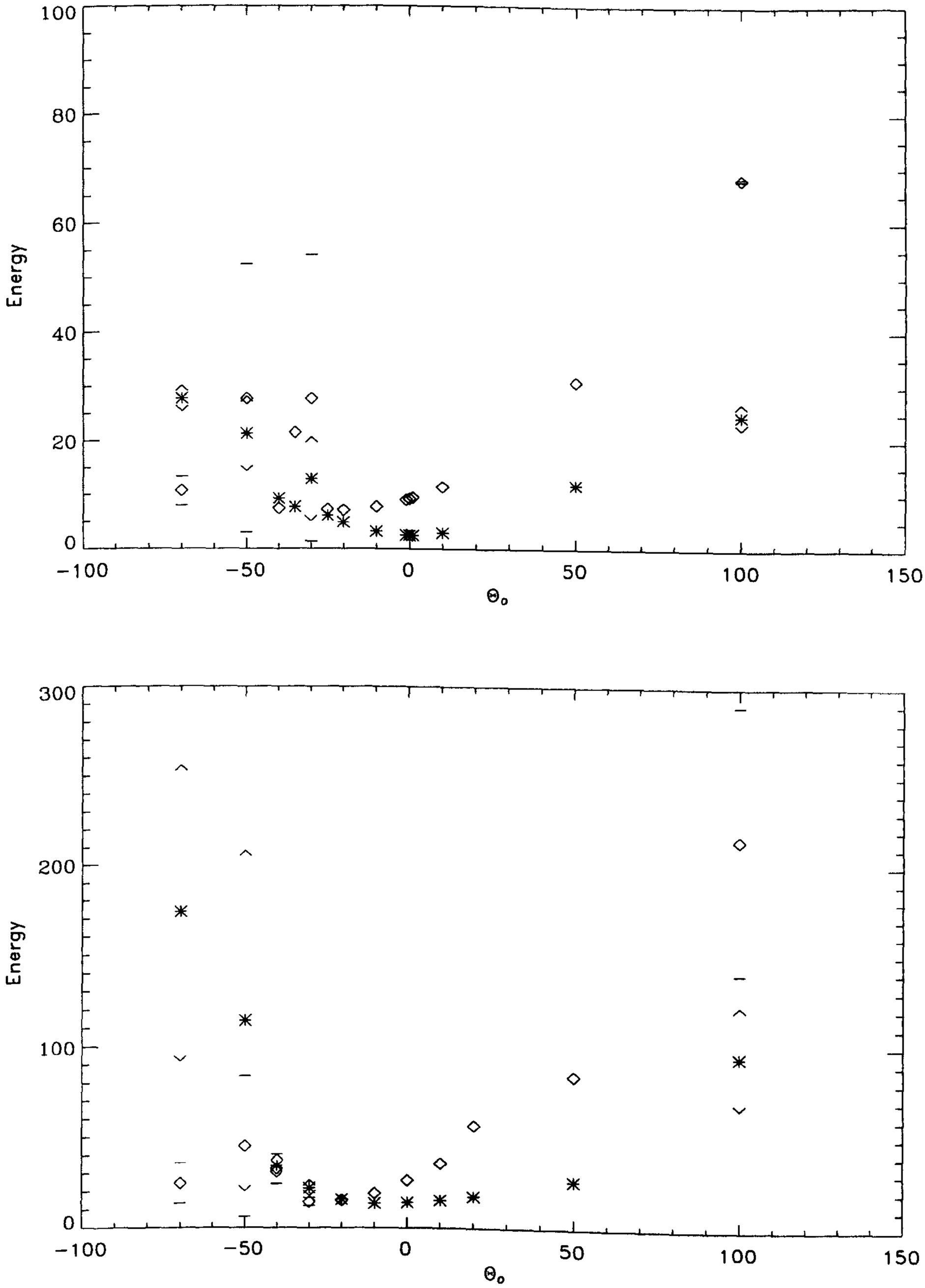

Figure 6.1: Energy versus Θ_o for $E = 2.5 \times 10^{-4}$ and $\alpha_o = 11$. From top to bottom we have, (a) $Ro = 2 \times 10^{-2}$ and (b) $Ro = 5 \times 10^{-2}$. $\divideontimes$ represents the average kinetic energies and $\diamond$ represents the average magnetic energies. $\hat{}$ shows the max/min values of the kinetic energy and $-$ shows the max/min values of the magnetic energy.

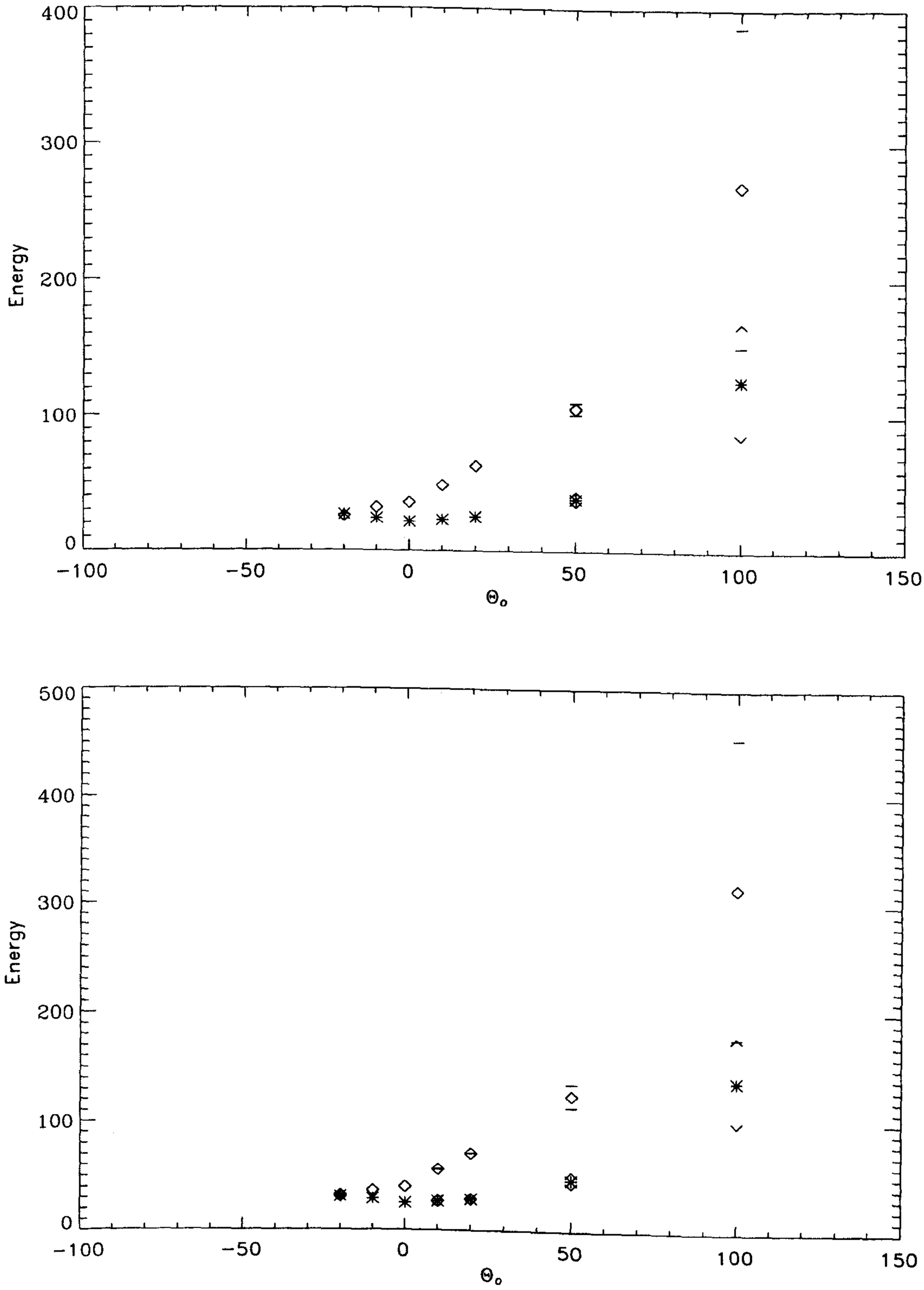

Figure 6.2: As Figure 6.1, but from top to bottom, (a) $Ro = 7 \times 10^{-2}$ and (b) $Ro = 8 \times 10^{-2}$.

obtained for $\Theta_o < -20$ also appear to be a trend occurring in both Figures 6.1(a) and 6.1(b). However, further evidence of this erratic behaviour of the solutions at higher values of *Ro* proves more difficult due to their unpredictable time-dependent behaviour, and hence the absence of solutions on the left-hand side of Figure 6.2(a) and 6.2(b).

The variation in the magnetic and kinetic energy we see with increasing Θ_o in Figures 6.1 and 6.2, arises from the fact that this is an $\alpha^2\omega$-type dynamo model and the behaviour may be explained as follows. When $\Theta_o = 0$, our dynamo is then simply the α^2-type model of Fearn and Rahman (2004b) and the dynamo is maintained by the α-effect alone, see Section 2.8.1 for a discussion on the equilibration of this type of dynamo model. As we increase Θ_o from zero, the buoyancy force drives a zonal flow in the momentum equation. As discussed in Section 2.8.1, the α-effect in the induction equation (2.35) acts on both components of the magnetic field to generate field, which then feeds into the Lorentz force appearing in the momentum equation (2.36). The Lorentz force then drives a zonal flow in the momentum equation which competes with the zonal flow driven by the buoyancy force. For $\Theta_o > 0$, the graphs in Figures 6.1 and 6.2, suggest that these two flows are acting in the same direction and so producing a stronger net zonal flow. This then balances the remaining terms in the momentum equation, ultimately obtaining a flow, $\mathbf{U}$, which feeds into the advection term in the induction equation, producing a large magnetic field $\mathbf{B}$ which feeds into the Lorentz force equilibrating the dynamo.

Examining Figures 6.1 and 6.2, we see that the magnetic and kinetic energy both increase as Θ_o is increased beyond zero, which is consistent with this explanation. In Figure 6.1(a), we notice that as we increase Θ_o the solutions change from steady solutions to oscillatory solutions – consistent with the solutions moving from the α^2 regime to the $\alpha\omega$ regime. As we increase the strength of *Ro* the solutions follow this same pattern, but as Θ_o is increased the time-dependence of the solutions is now chaotic. This is likely due to the magnitude of the inertia term. Through comparing Figures 6.1 and 6.2 we see that the field is able to grow much stronger and more quickly as *Ro* is increased, supporting the α^2 result of Fearn and Rahman who found that inertia acted to facilitate dynamo action.

We also notice that as the strength of inertia is increased, the solutions have evolved to a more chaotic time dependent state. This is especially evident in the low Θ_o solutions which at $Ro = 2 \times 10^{-2}, 5 \times 10^{-2}, 7 \times 10^{-2}$ are steady, but which, once Ro is increased to 8×10^{-2}, are unsteady but do not exhibit any periodicity in their low amplitude behaviour. Focussing on the results in Figure 6.2(b) reveals that the only steady solutions we obtain at $Ro = 8 \times 10^{-2}$ appear at $\Theta_o = -10$ and 0. All other solutions obtained are unsteady and chaotically varying in time.

For $\Theta_o < 0$, the zonal flow driven by the buoyancy force now acts in the opposite direction to the flow driven by the Lorentz force. When $|\Theta_o|$ is small, the zonal flow driven by the Lorentz force dominates the buoyancy driven flow but the net zonal flow generated is weaker than in the $\Theta_o > 0$ case described above but acts in the same direction. The equilibration of the dynamo then proceeds in the manner described above, but generates a smaller magnetic field, and hence the decrease in the magnetic energy curve in Figures 6.1 and 6.2. As we decrease Θ_o further, the zonal flow driven by the buoyancy force exceeds that driven by the Lorentz force term, and the net zonal flow now acts in the opposite direction causing the balance of the equations to be quite different. Examining Figure 6.1 the graphs suggest that this switch in the direction of the net zonal flow occurs around $\Theta_o = -30$, as at this point the character of the solutions change from being steady to being time dependent and there is a suggestion from the graphs that the kinetic energy exceeds the magnetic energy in this region. In Figure 6.2 we are unable to reduce Θ_o below -20, which is likely to be as a result of the switch in the direction of the net zonal flow, with the magnitude of Ro now too large to allow us to follow the solutions any further.

6.4 The effect of inertia.

In this section we regraph the solutions shown in Section 6.3 so that we may examine more easily the behaviour of the magnetic and kinetic energies of the solutions with Ro at fixed values of Θ_o. These results are shown in Figures 6.3, 6.4, 6.5, 6.6 and 6.7.

Examining each of these graphs in turn, we see that for all but Figure 6.6(a), the kinetic and magnetic energies increase with increasing Ro. As Ro is increased from zero, the spiky solutions we find for $\Theta_o \gtrsim -7$ (see Chapter 5 and also Figures 6.3 and 6.4) become steady showing the

same variation with Ro as found by Fearn and Rahman (2004b) in their α^2 studies. The difference caused by the introduction of Θ_o is simply to increase the magnitude of the magnetic and kinetic energies and change the nature of the solutions from being steady to time dependent, as shown in Figure 6.3(a) for $\Theta_o = 100$. We also see that even at low values of Θ_o (see for example Figure 6.4), increasing the strength of inertia is sufficient to change the solutions from being steady to having a time dependence. From the inertialess study we presented in Chapter 5, we found for $\Theta_o \lesssim -7$, the solutions we obtained were steady but became periodic as Θ_o is decreased. As we increase Ro, the solutions in Figure 6.5 exhibit the same energy variation with Ro as found in Figures 6.3 and 6.4 once $Ro \geq 2\times10^{-2}$ as the solutions are no longer in the viscously controlled regime.

The solution at $\Theta_o = -30$ shown in Figure 6.6(a) shows an increase and then a decrease in the magnetic energy, with the expected increase in kinetic energy with Ro. As we decrease Θ_o to -40 we find that the values of the magnetic and kinetic energies lie fairly close together and increase as Ro is increased, with the kinetic energy slightly exceeding the magnetic energy. Decreasing Θ_o to -50 and -70 as shown in Figure 6.7, we see that the kinetic and magnetic energies occur close together at $Ro = 2\times10^{-2}$, but then once Ro is increased to 5×10^{-2} the difference in the values is quite significant, with the kinetic energy exceeding the magnetic energy. Given that we only have 2 or 3 datapoints in Figures 6.6 and 6.7 it is difficult to discern the behaviour of the system at large Ro and whether the solutions beyond $Ro = 2\times10^{-2}$ exhibit the roughly linear behaviour found for $-20 \leq \Theta_o \leq 100$. It is likely the reason the variation with Ro for $\Theta_o = -30$ is different to the increasing trend in energy found for all other values of Θ_o considered, is due to the change in direction of the net driven zonal flow, as discussed in Section 6.3.

Graphs in Figures 6.3, 6.4 and 6.5 show for $Ro \geqslant 2\times10^{-2}$ a fairly linear variation of their magnetic and kinetic energies with Ro. This linear trend was found in Fearn and Rahman's (2004b) work on the effects of inertia on their α^2-type dynamo. Fearn and Rahman noted that inertial effects do not appear to have a controlling influence on the solutions until beyond $Ro \gtrsim 1.2\times10^{-2}$. Therefore in Section 6.5 we consider only solutions beyond $Ro = 2\times10^{-2}$. We also limit our attention to values of Θ_o between 100 and -20, as the energy variation appears linear. As we see from Figures 6.6 and 6.7 we are unable to obtain sufficient points to determine whether this linear

behaviour is continued below $\Theta_o = -20$ due to numerical difficulties as the strength of inertia is increased.

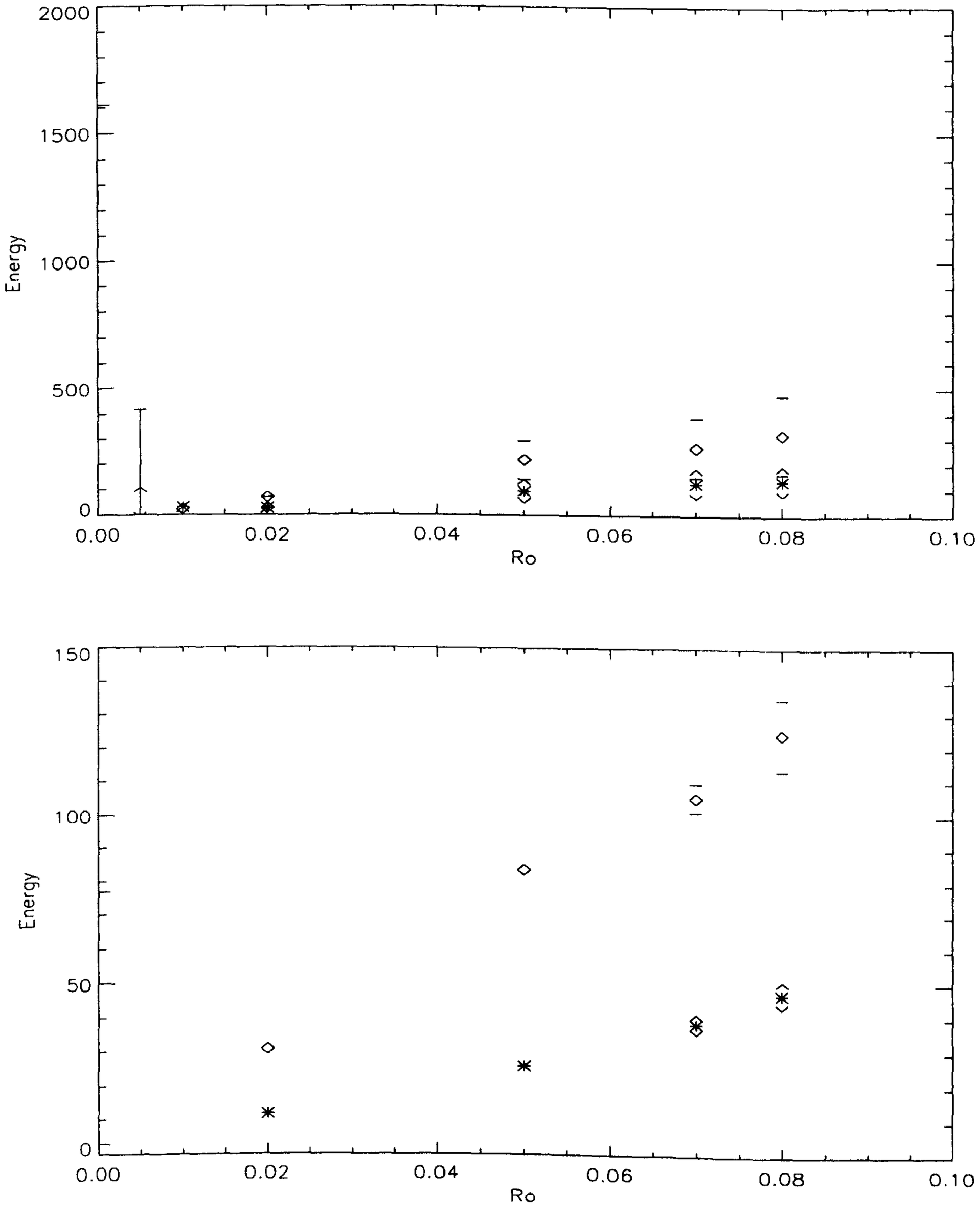

Figure 6.3: Energy versus Ro for $E = 2.5 \times 10^{-4}$, $\alpha_o = 11$ and from top to bottom (a) $\Theta_o = 100$ and (b) $\Theta_o = 50$. $\diamond$ represent average magnetic energy, with error bars used to indicate the maximum and minimum amplitudes of unsteady solutions. $*$ represent the average kinetic energy, with the$\hat{}$indicating the maximum and minimum amplitudes of the unsteady solutions.

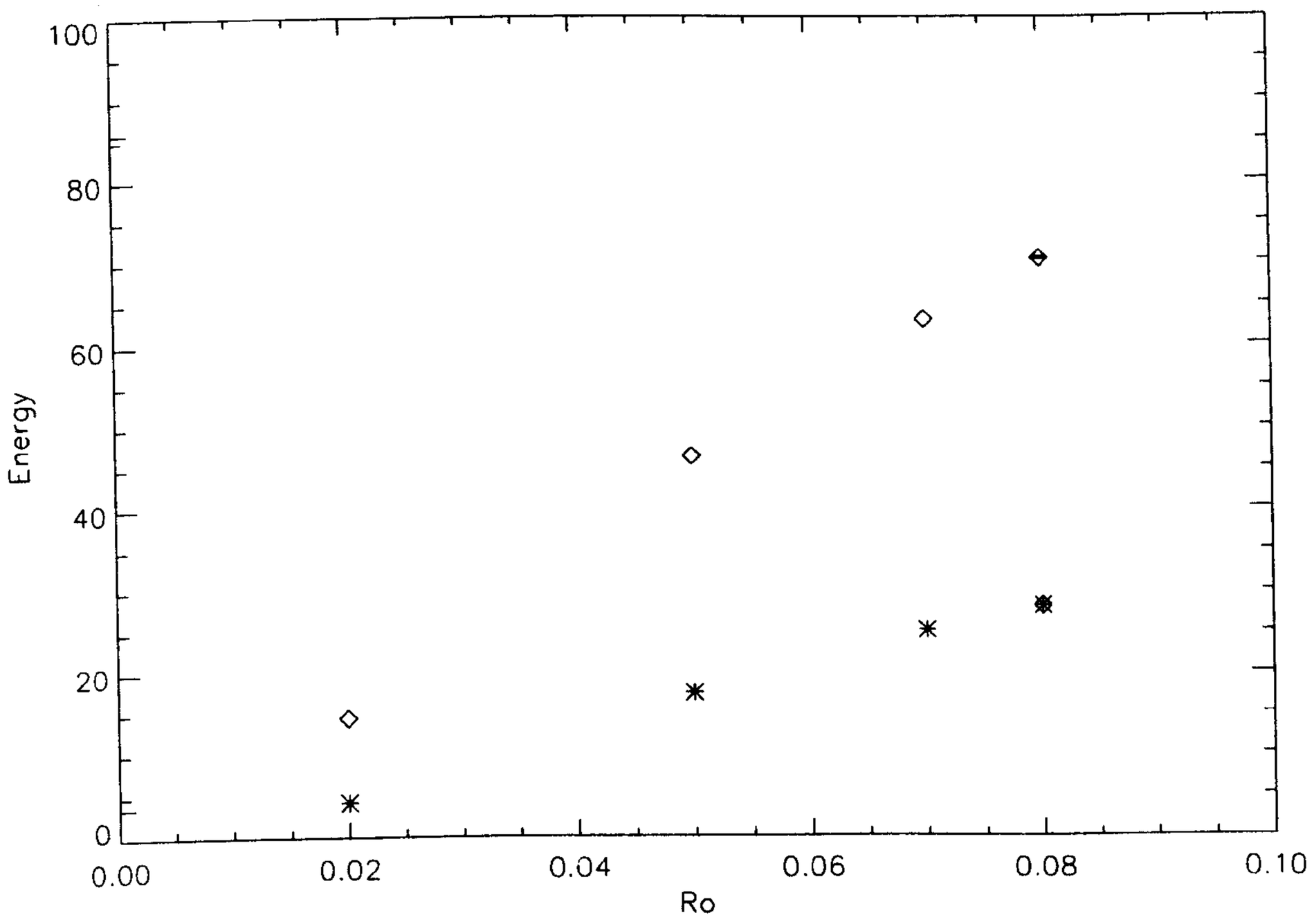

Figure 6.4: As Figure 6.3, but from top to bottom (a) $\Theta_o = 20$ and (b) $\Theta_o = 10$.

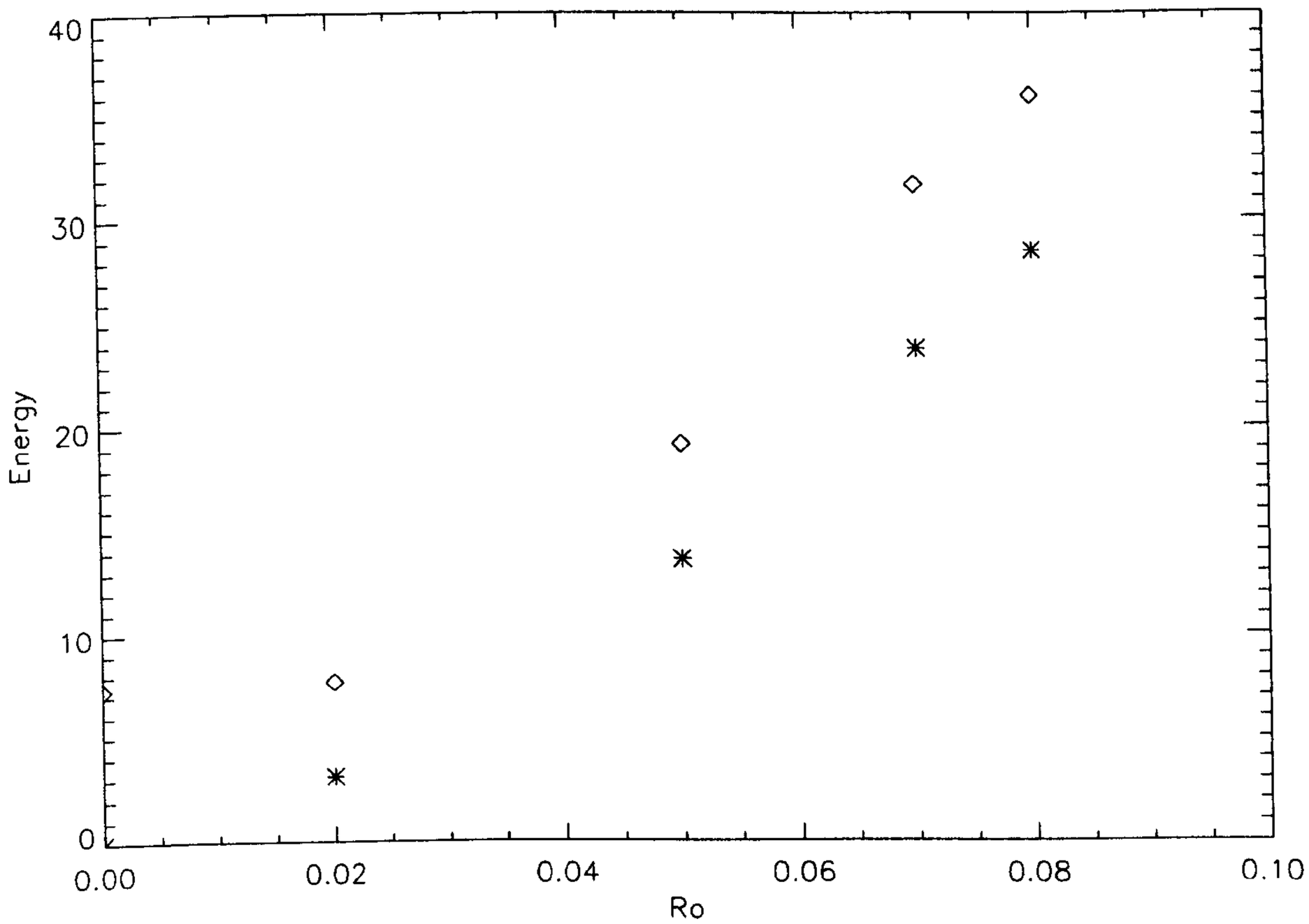

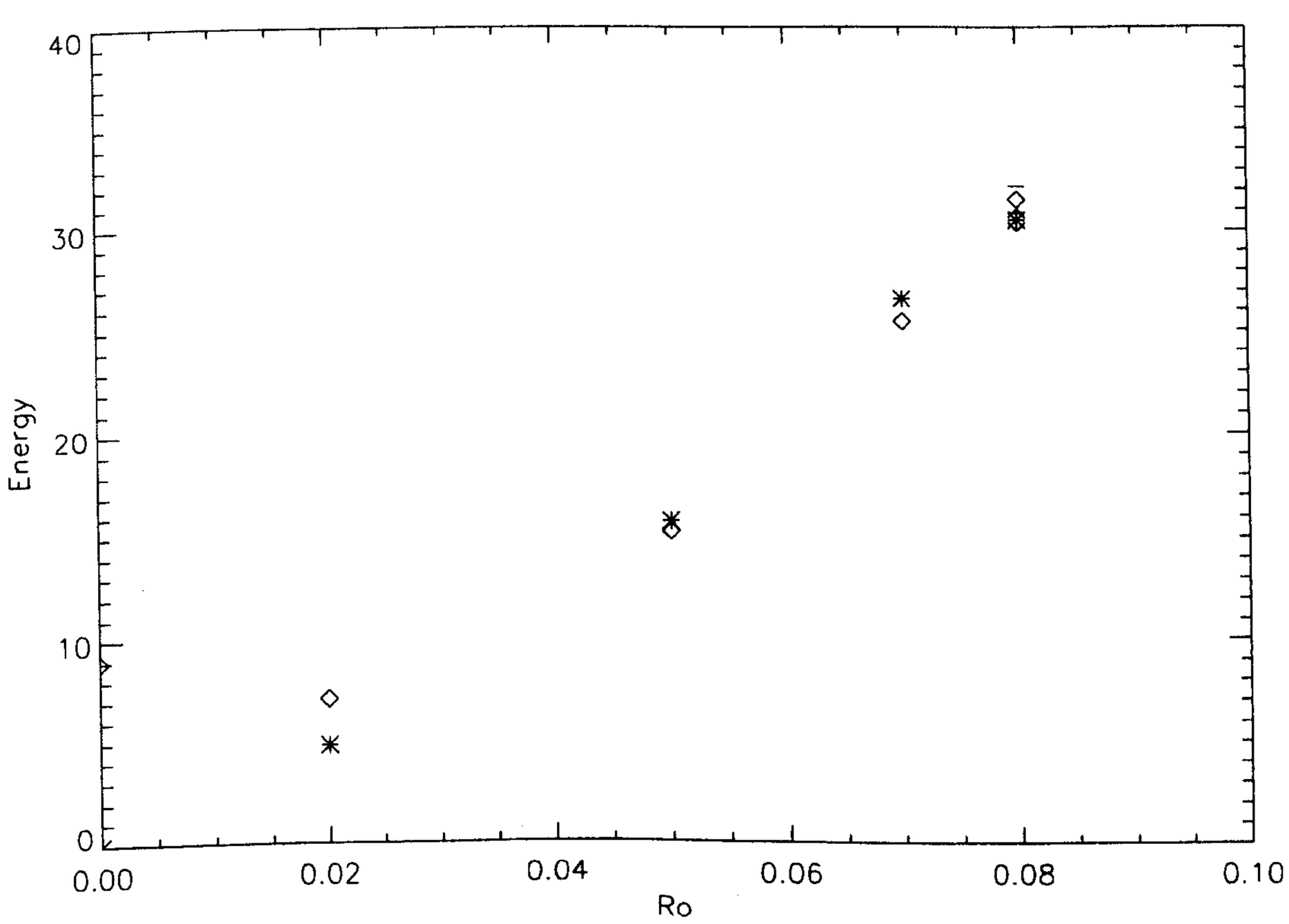

Figure 6.5: As Figure 6.3, but from top to bottom (a) $\Theta_o = -10$ and (b) $\Theta_o = -20$.

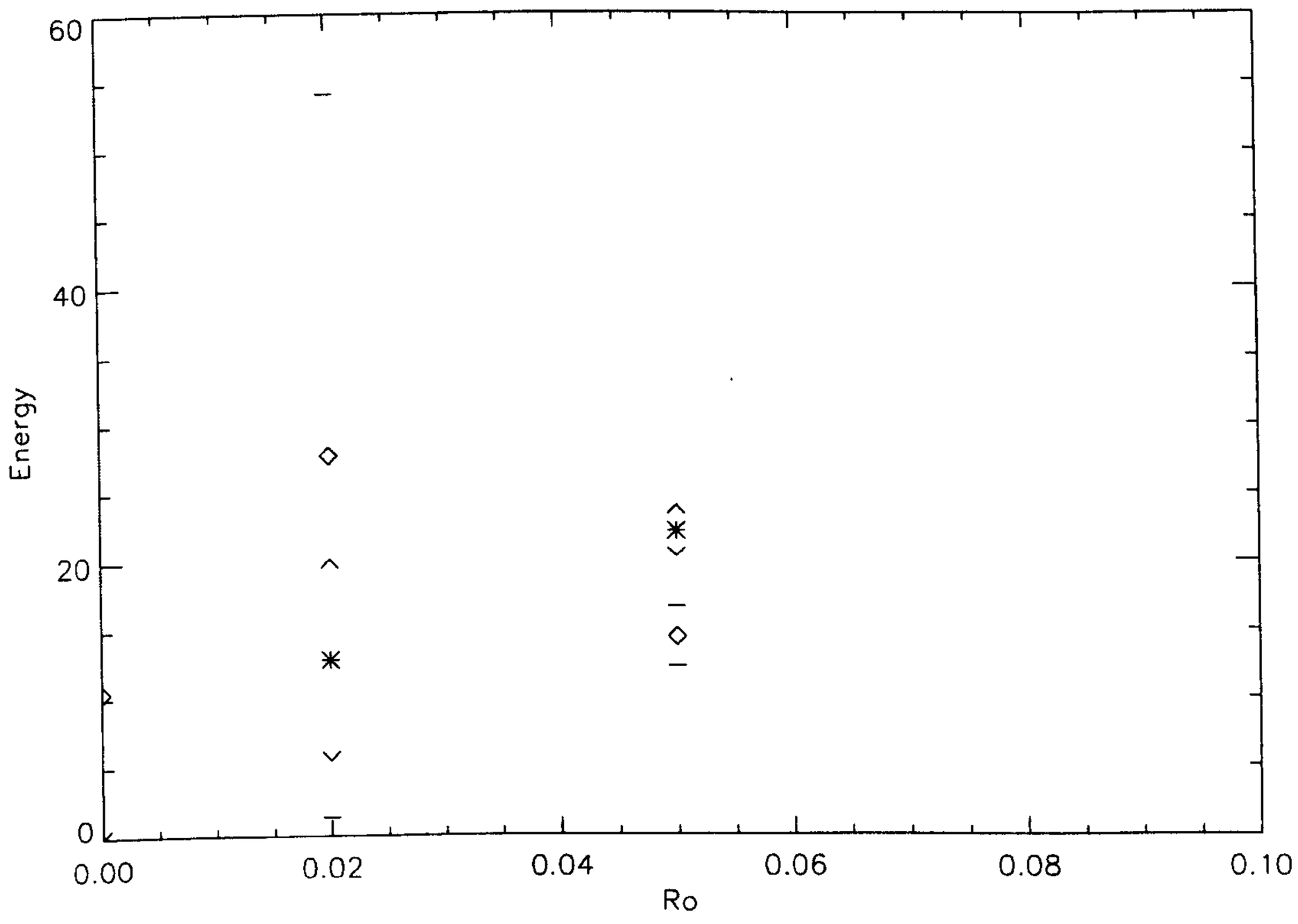

Figure 6.6: As Figure 6.3 but for but from top to bottom (a) $\Theta_o = -30$ and (b) $\Theta_o = -40$.

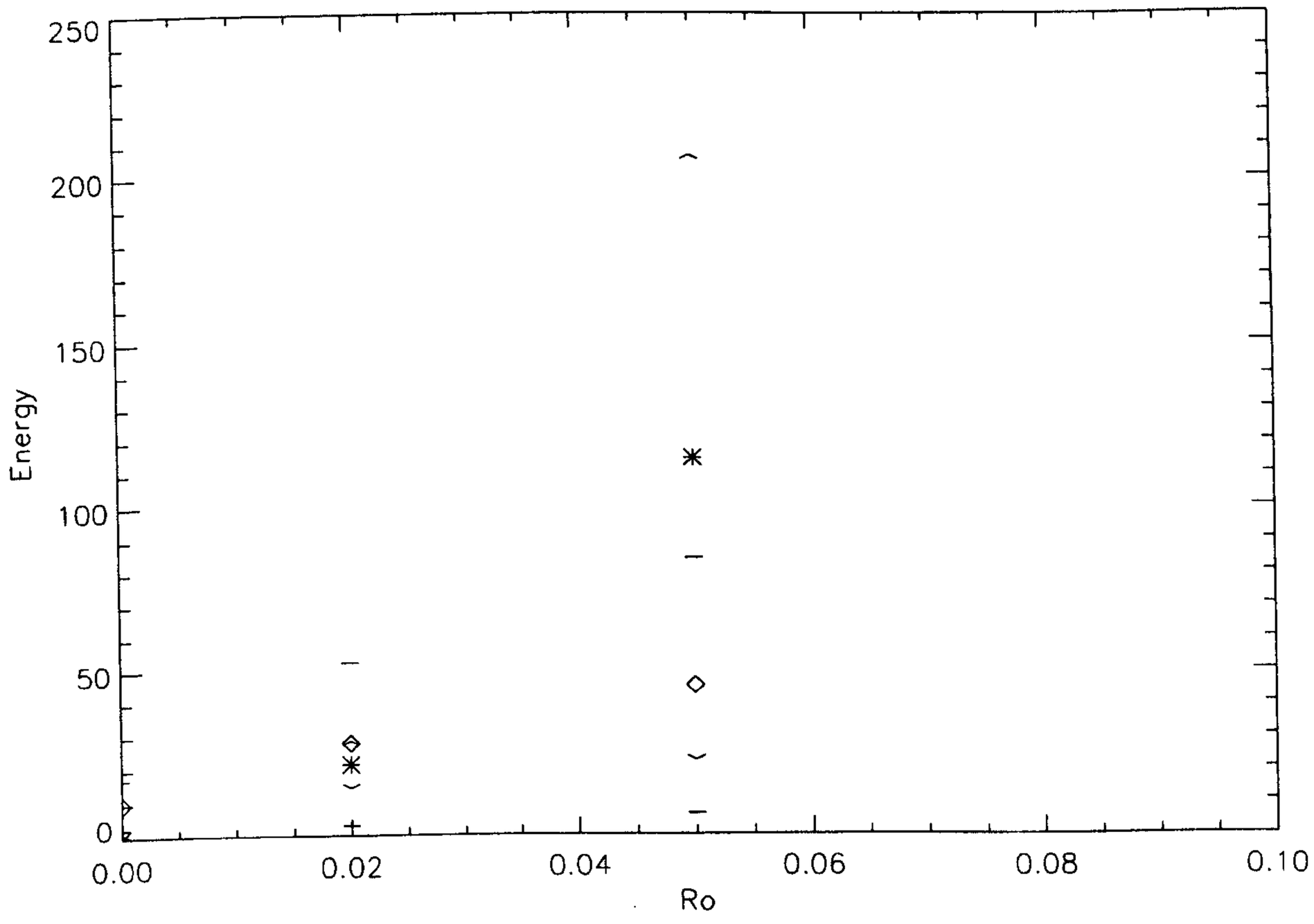

Figure 6.7: As Figure 6.3, but from top to bottom (a) $\Theta_o = -50$ and (b) $\Theta_o = -70$.

6.5 Linear variation of Energy with *Ro*.

In this section we investigate more closely the linear relationship we identified between the energy and the Rossby number at different values of Θ_o. This linearity between the energy and *Ro* was identified in the α^2-type dynamo of Fearn and Rahman, whose solutions are shown by $*$ in Figures 6.8 and 6.9.

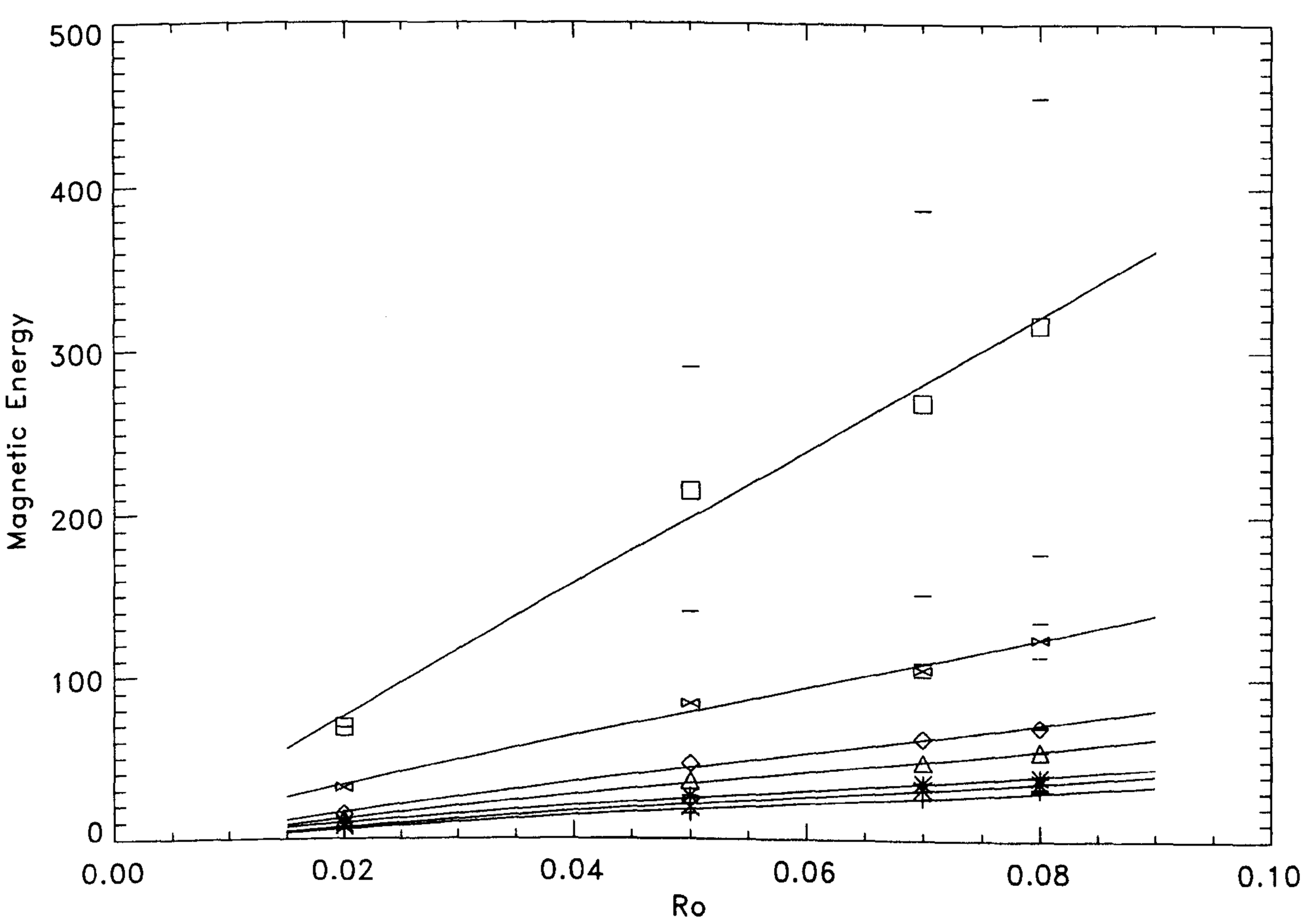

Figure 6.8: Magnetic energy versus *Ro* for $E = 2.5 \times 10^{-4}$ and $\alpha_o = 11$. We considered a range of values of Θ_o and noticed the linear trend in each. The following symbols are used to represent average magnetic energies, with error bars used to indicate the maximum and minimum amplitudes of unsteady solutions; $\Theta_o = 100 : \square$, $\Theta_o = 50 : \bowtie$, $\Theta_o = 20 : \diamond$, $\Theta_o = 10 : \Delta$, $\Theta_o = 0 : *$, $\Theta_o = -10 : \times$ and $\Theta_0 = -20 : +$.

In Fearn and Rahman (2004b), they observe a linear dependence between the magnetic/kinetic energy and the Rossby number, when $Ro \gtrsim 1.2 \times 10^{-2}$. For $Ro \lesssim 1.2 \times 10^{-2}$, solutions are spiky and

viscosity has a controlling influence. We then investigate whether the same dependence applies in our $\alpha^2\omega$-type model. Examining the graphs in Figures 6.8 and 6.9, we see that both the magnetic and kinetic energy vary in a roughly linear way with Ro, where E_m and E_k are the magnetic and kinetic energies respectively ($E_m \propto Ro$ and $E_k \propto Ro$). We see from the definitions for the magnetic and kinetic energy given in Section 2.10, that

$$E_m = \frac{1}{2}\int_V |\mathbf{B}|^2 dV \propto Ro \quad \text{and} \quad E_k = \frac{1}{2} Ro \int_{V_o} |\mathbf{U}|^2 dV \propto Ro.$$

This then suggests that $|\mathbf{B}| \sim Ro^{1/2}$ and $|\mathbf{U}| \sim Ro^0$. If we examine the induction equation as given in (2.4) we see that the leading order term balance is then independent of Ro.

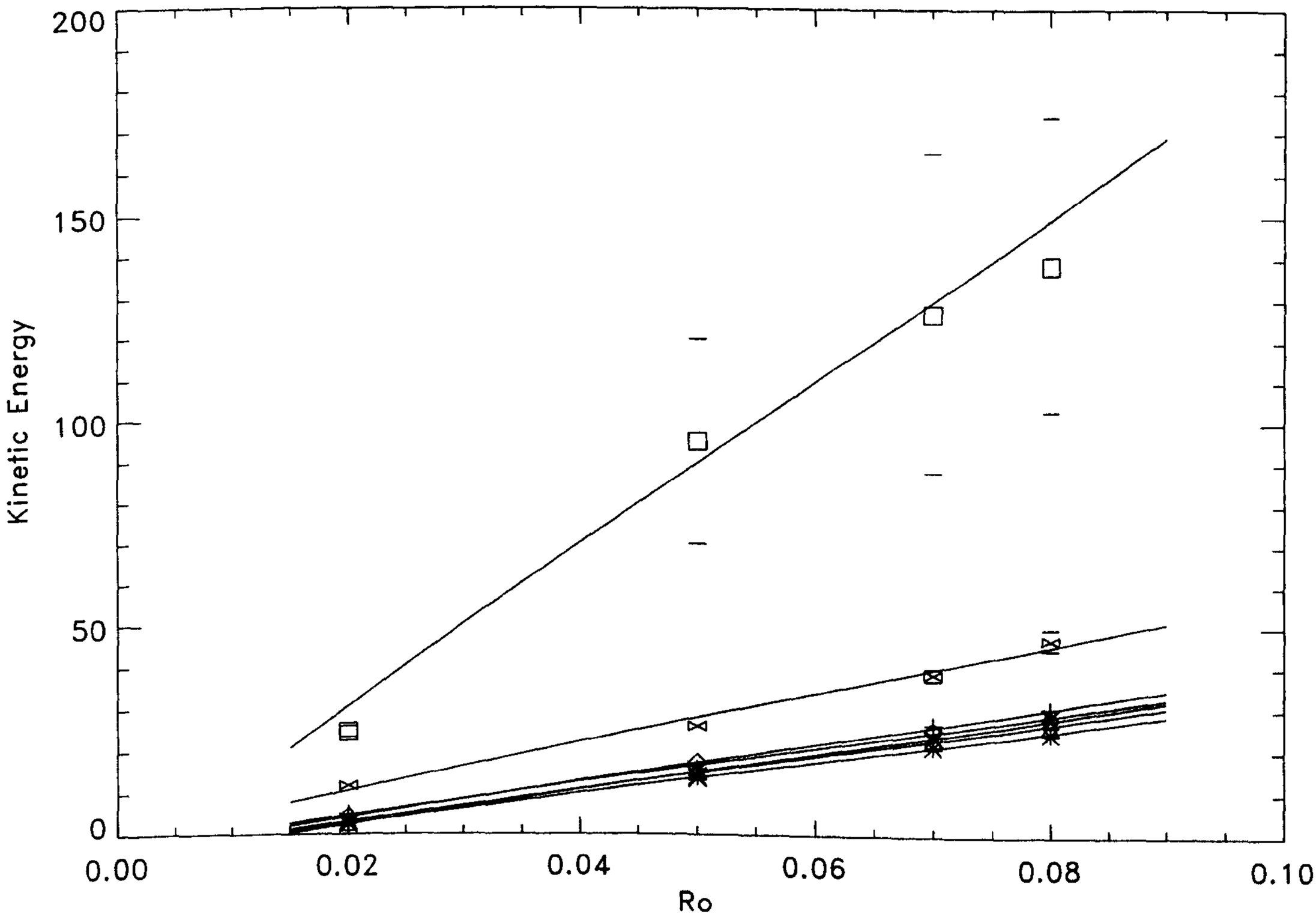

Figure 6.9: As Figure 6.8 but for the kinetic energy.

Examining the momentum equation, (2.5), we see that the Lorentz force and the inertial terms are both of order Ro, whilst the viscous term remains of order E. For values of Ro close to zero,

viscosity has a controlling influence, however as Ro is gradually increased from zero, beyond some critical value, the effect of inertia becomes more important and a balance is struck between the Lorentz force and the inertial terms which results in an increase in $|\mathbf{B}|$ with $Ro^{1/2}$.

In Figure 6.8 we plot the magnetic energy against Ro and apply a least squares fit to the data points to obtain the best fit straight line through the points (we use Microsoft Excel to do this). Similarly, in Figure 6.9 we show the kinetic energy variation with Ro and again apply a least squares fit to the datapoints. We investigated whether there is any correlation between the gradient of these lines and Θ_o. The equations of these straight lines are given in Table 6.1 below.

$$
\begin{aligned}
E_m &= 4091.6Ro - 6.3193 \quad \text{and} \quad E_k = 1887.5Ro - 7.4316, \quad \text{for } \Theta_o = 100 \\
E_m &= 1524.1Ro + 2.3471 \quad \text{and} \quad E_k = 578.86Ro - 0.9171, \quad \text{for } \Theta_o = 50 \\
E_m &= 933.45Ro - 2.8674 \quad \text{and} \quad E_k = 400.90Ro - 3.3608, \quad \text{for } \Theta_o = 20 \\
E_m &= 733.98Ro - 2.6662 \quad \text{and} \quad E_k = 392.45Ro - 4.7324, \quad \text{for } \Theta_o = 10 \\
E_m &= 507.98Ro - 0.6062 \quad \text{and} \quad E_k = 370.93Ro - 4.8436, \quad \text{for } \Theta_o = 0 \\
E_m &= 479.50Ro - 2.8000 \quad \text{and} \quad E_k = 422.64Ro - 6.0529, \quad \text{for } \Theta_o = -10 \\
E_m &= 401.24Ro - 2.2631 \quad \text{and} \quad E_k = 436.31Ro - 4.5345, \quad \text{for } \Theta_o = -20.
\end{aligned}
$$

Table 6.1: The equations of the lines of best fit for the magnetic and kinetic energy variation with Ro for each value of Θ_o considered.

Therefore, using the gradient of the lines, taken from the best fit equations in Table 6.1 we plot the gradient against Θ_o. The plot of the gradient versus Θ_o in the magnetic energy case is shown in Figure 6.10. As Figure 6.10 shows, there is a definite trend in the data points, to which we chose to fit a third order polynomial. The cubic curve we obtain (again using Microsoft Excel) is,

$$\text{gradient} = 0.0016\Theta_o^3 + 0.0722\Theta_o^2 + 11.547\Theta_o + 591.79.$$

Similarly in the kinetic energy case we plot the gradient of these lines against Θ_o, which is shown in Figure 6.11. Fitting a third order polynomial to the datapoints, we obtain the cubic curve,

$$\text{gradient} = 0.0012\Theta_o^3 + 0.0485\Theta_o^2 - 1.5627\Theta_o + 394.23.$$

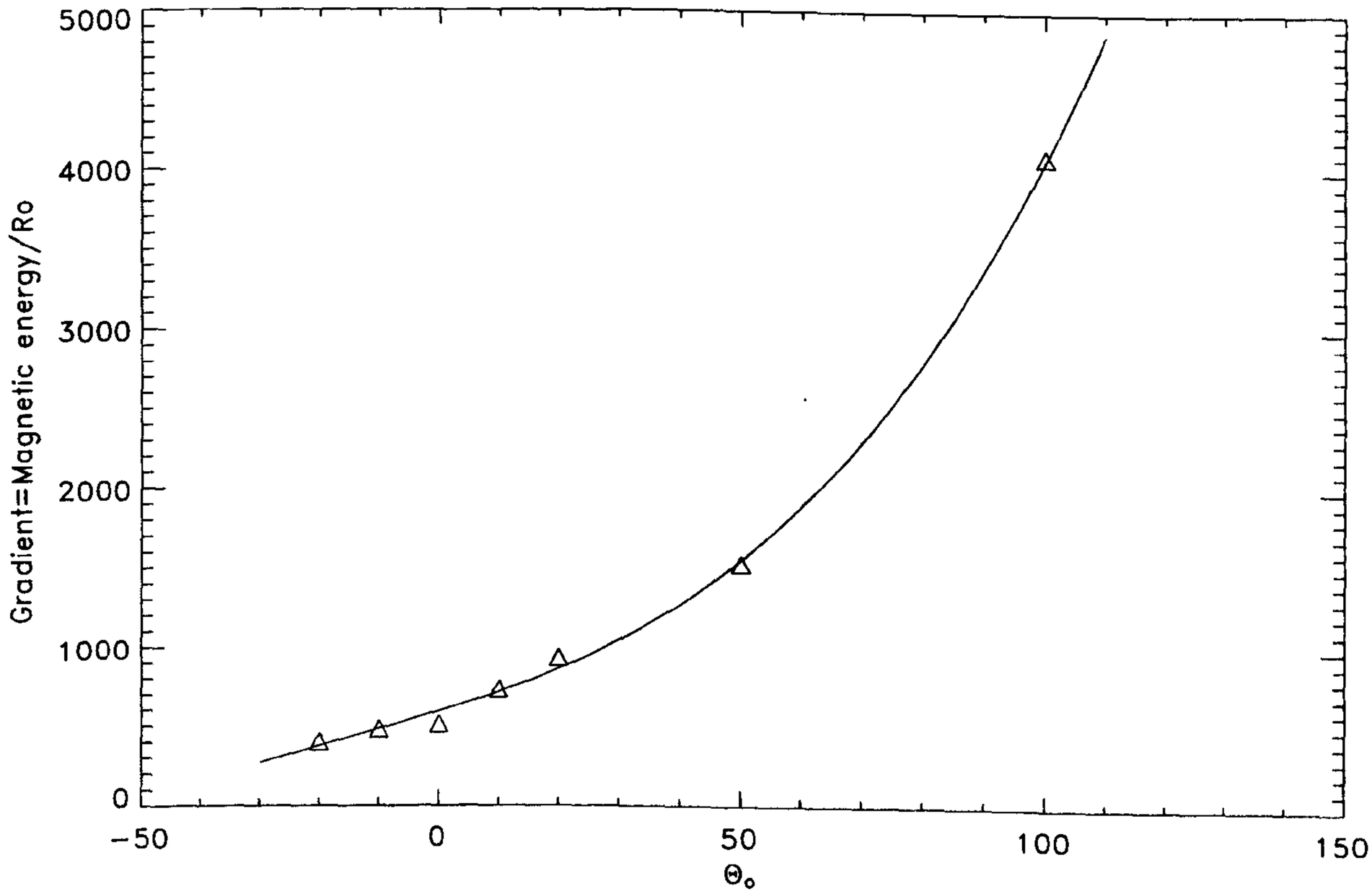

Figure 6.10: The gradient of the best fit straight lines from Figure 6.8 plotted against Θ_o. The fitted curve has equation, gradient $= 0.0016\Theta_o^3 + 0.0722\Theta_o^2 + 11.547\Theta_o + 591.79$.

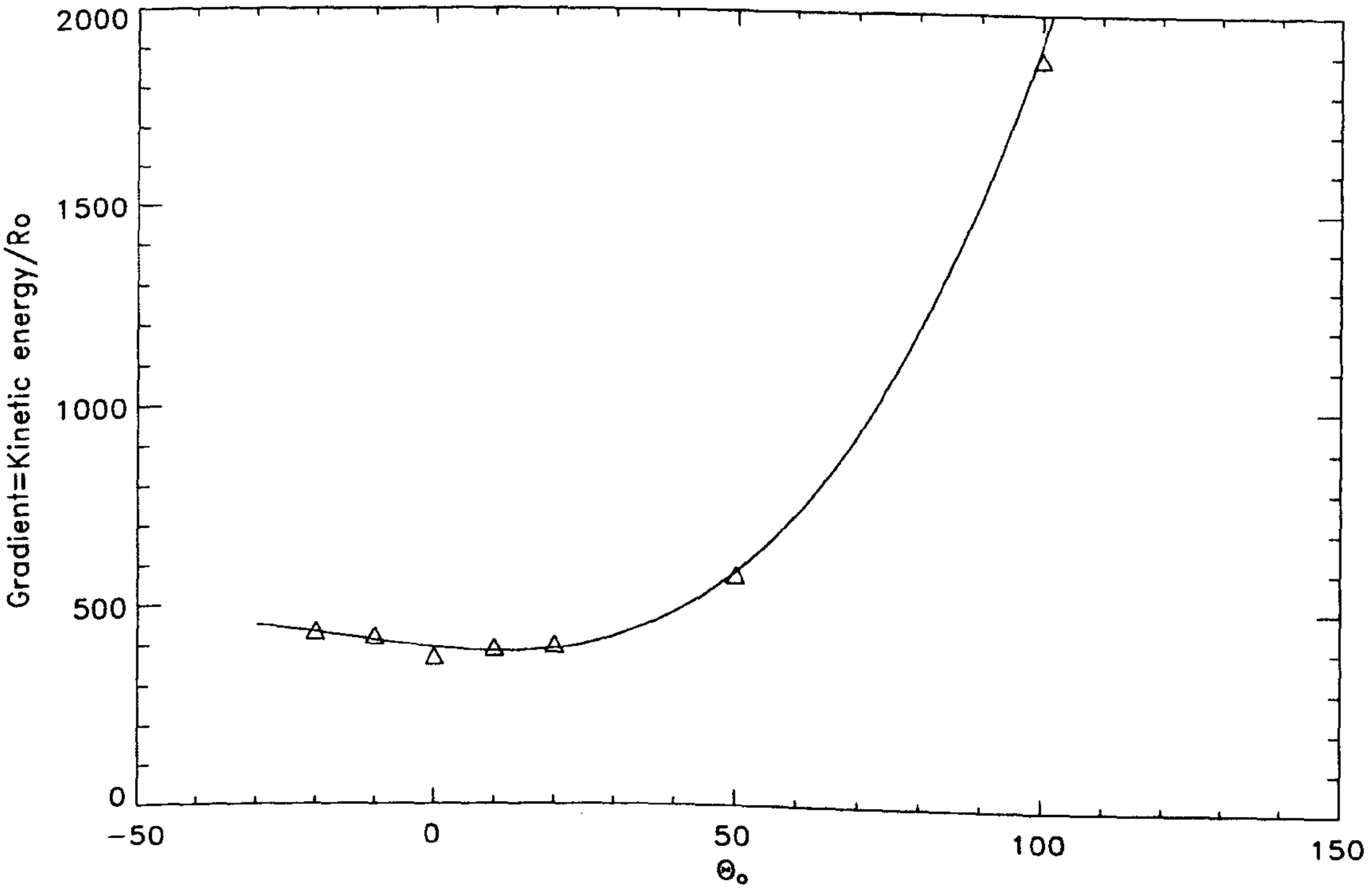

Figure 6.11: The gradient of the best fit straight lines from Figure 6.9 plotted against Θ_o. The fitted curve has equation, gradient $= 0.0012\Theta_o^3 + 0.0485\Theta_o^2 - 1.5627\Theta_o + 394.23$.

The plots in Figures 6.10 and 6.11 capture in a slightly different way the information which is presented in Section 6.3. If we consider the case in which Ro is fixed, then we see that these figures are simply a more general representation of the variation of the magnetic and kinetic energy with Θ_o as shown in Figures 6.1 and 6.2.

6.6 The effects of inertia and differential rotation.

The graph shown in Figure 6.12, shows the types of solutions found as both Θ_o and Ro are varied. The data along the $\Theta_o = 0$ axis is taken from the results obtained by Fearn and Rahman (2004b) on their work on the α^2-type dynamo model, which was extended as discussed earlier to include an ω-effect and thus produce an $\alpha^2\omega$-type dynamo model. From this graph we can easily see how the inertialess $\alpha^2\omega$-type model discussed in Chapter 5, fits with the α^2-type model investigated by Fearn and Rahman (2004b) and the more general inertia $\alpha^2\omega$-type model we have discussed in this chapter.

We see how these solutions evolve from spiky type solutions into steady solutions, which then become periodic and eventually chaotic type solutions as the Rossby number is increased. There is also the suggestion of a similar trend as $|\Theta_o|$ is increased away from 0. Combining the variation of both of the factors, we see that there exist regimes in which certain types of solution can be expected to occur.

The contour plots in Figures 6.13, 6.14, 6.15 and 6.16, show the components of magnetic field and flow at $\Theta_o = 100, 50, 20, -20$ respectively. Within each of these figures, we show the solution at increasing values of inertia; $Ro = 2 \times 10^{-2}$, 5×10^{-2}, 7×10^{-2}, 8×10^{-2}. This then enables a comparison with the α^2 results (at $\Theta_o = 0$) obtained by Fearn and Rahman (2004b) (see their Figure 6). (Note that our choice of contour interval here differs from Fearn and Rahman's, as it was necessary to increase the contour intervals of B_p, B, U_p in order to accomodate the strong field and flow shown in Figure 6.13, but decrease the contour interval from 20 to 10 for ω. The angular velocity contour interval at 20 gave very good agreement between the plots at different values of Θ_o, however this did not help us to understand how the imposed buoyancy driving was affecting the flow).

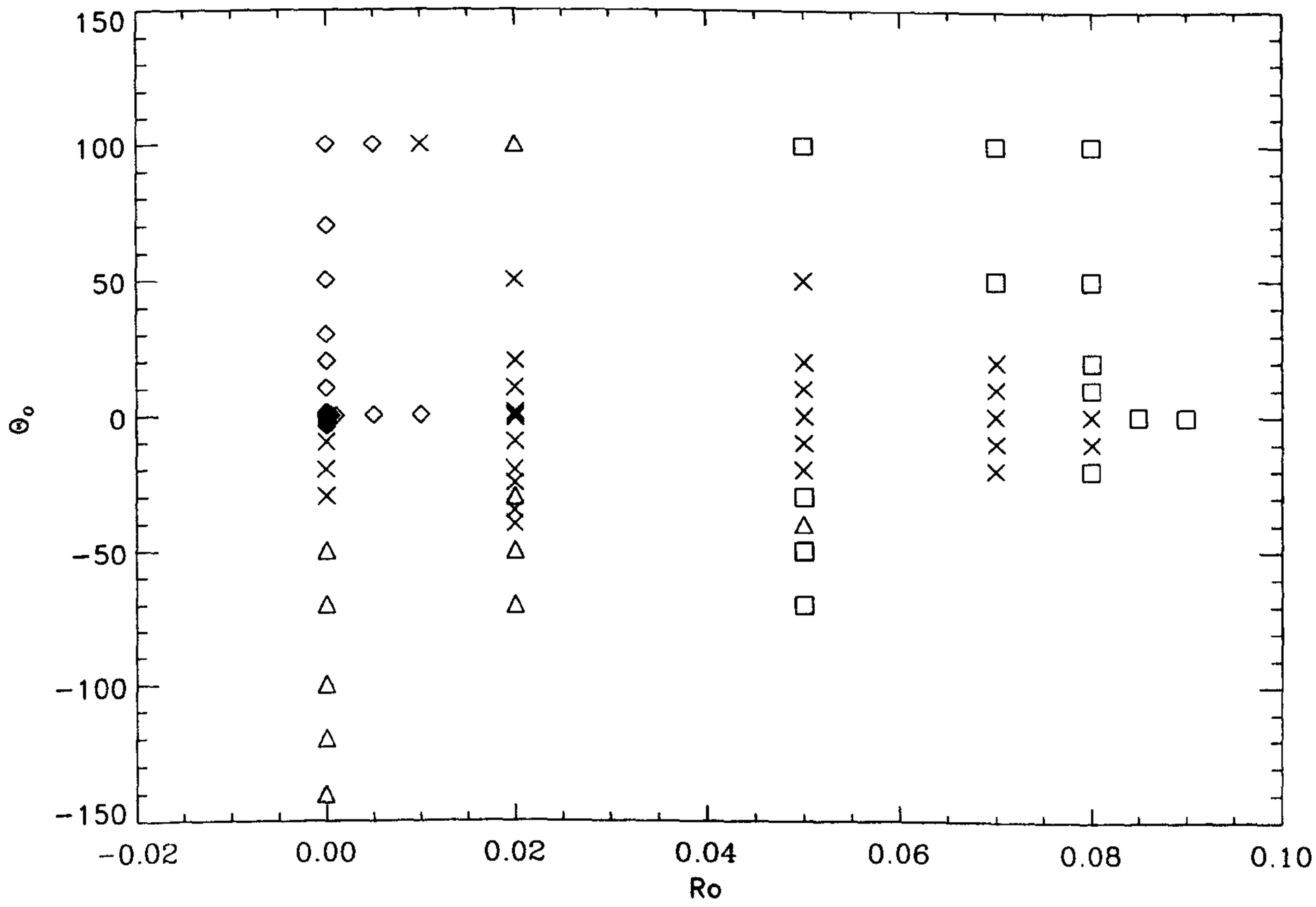

Figure 6.12: Θ_o versus Ro for $E = 2.5 \times 10^{-4}$ and $\alpha_o = 11$. $\diamond$ represent spiky solutions, $\times$ represents steady solutions, $\triangle$ represents periodic solutions and $\square$ represent chaotic solutions.

6.6.1 The effect of inertia

Examining the solutions in Figures 6.13, 6.14, 6.15 and 6.16 at fixed values of Θ_o, as we increase the value of Ro, we see that in increasing the strength of inertia there is a movement of the B and U_p contours away from the CMB and towards the equator. The contours also become confined to outside of the tangent cylinder. The poloidal field (B_p) increases in strength as Ro is increased and we also see a shift in the concentration of poloidal field components in a similar manner as found for the B and U_p contours as the influence of inertia is increased. The behaviour shown in Figure 6.13 appears slightly different, though it should be noted that at this value of Θ_o, all of the solutions shown are time dependent, and so the pictures shown are just snapshots. However we see the same general trend that the contours gradually move towards the equator filling the whole space.

We now focus on the ω contours and the effect caused by increasing the strength of inertia. We

see that, as Ro is increased in each of Figures 6.13, 6.14, 6.15 and 6.16, there do not appear to be any substantial changes in the form of the flow. For $\Theta_o > 0$, we see that the contours essentially provided by the buoyancy force alone form parallel contours to the inner core. As Ro is increased, these negative contours become slightly suppressed and become concentrated around the tangent cylinder. Further increasing inertia introduces a positive contour symmetric about the equator, which grows in strength as Ro is increased. In the case of $\Theta < 0$, we see slightly different behaviour here, since the imposed buoyancy driving is now acting in the opposite direction. We see few significant differences between the solutions as Ro is increased, though the positive contours that develop as Ro is increased in the case of $\Theta_o > 0$, are also present here but now link up with the positive contours produced by the imposed buoyancy driving, and hence the solutions for $\Theta_o < 0$ appear slightly different. We will of course discuss the development of the solutions with changing Θ_o in more detail in Section 6.6.2.

6.6.2 The effect of the imposed differential rotation.

In this Section we examine more closely the variation of the solutions with Θ_o at fixed Rossby number.

Considering the case $Ro = 0.02$.

We begin by considering the solutions at $Ro = 0.02$ as solutions for $\Theta_o = 50, 20, -20$ are steady and may enable us to establish some ideas about the general trends in the evolution of the solutions with Θ_o, before we examine the solutions at higher values Ro.

The form of the solution for $\Theta_o = 100, 50, 20, -20$ (shown in Row 1 of Figures 6.13, 6.14, 6.15 and 6.16, respectively) appears very similiar in each case. We see, as Θ_o is increased, the field and flow increase in strength, which is quite natural as we are increasing the amount of imposed forcing in the system. We note that the solution at $\Theta_o = -20$ appears slightly weaker than its counterpart at $\Theta_o = 20$, however, as we have observed earlier, the system is sensitive to the direction of the imposed buoyancy driven flow, and we expect to find different solutions for $\pm\Theta_o$. More generally we see that with increasing Θ_o, contours appear to become more elongated, moving down towards the equator.

Comparing the solutions at $\Theta_o = 20$ and -20, we see the contours of B and U_p are a slightly different shape, the solutions at $\Theta = 20$ appearing more round, with the solutions at $\Theta_o = -20$ appearing more oval shaped. The biggest differences, as one would expect, lie in the contours of the angular velocity. The α^2 solution at $Ro = 0.02$ has a small positive contribution to the angular velocity aligned with the vertical z-axis, and a concentration of negative contours near the pole. If we now examine the solution at $\Theta_o = -20$, we see a stronger concentration of positive contours close to the vertical z-axis and a weaker negative concentration near the pole. These aspects are reversed when we examine the solutions at $\Theta_o = 20$. These differences are likely caused by the direction of the imposed buoyancy driven flow, as $\Theta_o < 0$ generates positive angular velocity contours parallel to the inner core with $\Theta_o > 0$ conversely producing negative angular velocity contours parallel to the inner core. This we believe is the main mechanism behind the distribution of the angular velocity contours.

Increasing the strength of Inertia to $Ro = 0.05$.

Examining the solutions in (Row 2 of) Figures 6.13, 6.14, 6.15 and 6.16 at $Ro = 0.05$, we investigate whether the trends we observed in the case of $Ro = 0.02$ still hold. The solutions remain steady at $\Theta_o = 50, 20, -20$, but the solution shown at $\Theta_o = 100$ is now a snapshot of a chaotic time dependent solution.

We see that the trends we identified in the case of $Ro = 0.02$, seem to borne out by the solutions at $Ro = 0.05$. We see that, as Θ_o is increased, there is an increase in the strength of the field and flow and we again see an elongation and movement of the contours of B and U_p towards the equator. At $\Theta_o = 100$ the solution, having become chaotically time dependent, has also become of mixed parity. At this level of forcing it is difficult to identify any discernable traits associated with the increase in Θ_o, though the solution is now very strong and fills most of the space.

Further increasing the strength of Inertia to $Ro = 0.07, 0.08$.

Examining the solutions for each value of Θ_o at both $Ro = 0.07$ and $Ro = 0.08$, we see that there is very little difference between the solutions. The strength and form of the field and flow

appears essentially the same in both cases. We again see that, as Θ_o is increased, the trend of the contours of B and U_p becoming stretched towards the equator appears to hold, except at $\Theta_o = 100$ where the solution is already chaotic and of mixed parity.

6.6.3 Comparing the effects of inertia and buoyancy.

If we compare the effects of inertia and buoyancy, we see that these very different terms have a similar behaviour on the solutions. We see that increasing Ro or increasing Θ_o causes B and U_p to increase in strength and also become elongated in the direction of the equator. The B_p also grows in strength and the concentration of the field is also observed to move round and down towards the equator. Since these two effects have a similar influence on the magnetic field and poloidal flow, we are then interested in how changing either one of these parameters alters the angular velocity component of the flow.

Examining Figures 6.13, 6.14, 6.15 and 6.16, we see that inertia introduces a small amplitude positive angular velocity component to the flow, which acts to suppress the radial extent of negative contours close to the inner core. Increasing the strength of inertia appears to cause the angular velocity contours to cluster close to the z-axis and poles and near the inner core tangent cylinder. The angular velocity components also exhibit only a very small variation with z as Ro is increased.

If we now examine the top row of Figures 6.13, 6.14, 6.15 and 6.16, and see how changing Θ_o alters the angular velocity contours of the flow. We see that the solutions at $\Theta_o > 0$ and $\Theta_o < 0$ are quite different, as has been found previously. For comparison purposes we will therefore simply focus on the $\Theta_o > 0$ solutions. As we naturally expect, increasing Θ_o generates more thermal wind, of the form given in Section 2.7, as one would find in the absence of a magnetic field and no inertia or viscosity in the system. Including these other forcing terms, the resulting equilibrated systems angular velocity is modified as shown. This angular velocity is then responsible for stretching out lines of toroidal field to generate poloidal field. At the higher (fixed) values of Ro, the angular velocity contours appear dominated by the effect of inertia, though the increased number of angular velocity contours concentric to the inner core are evident.

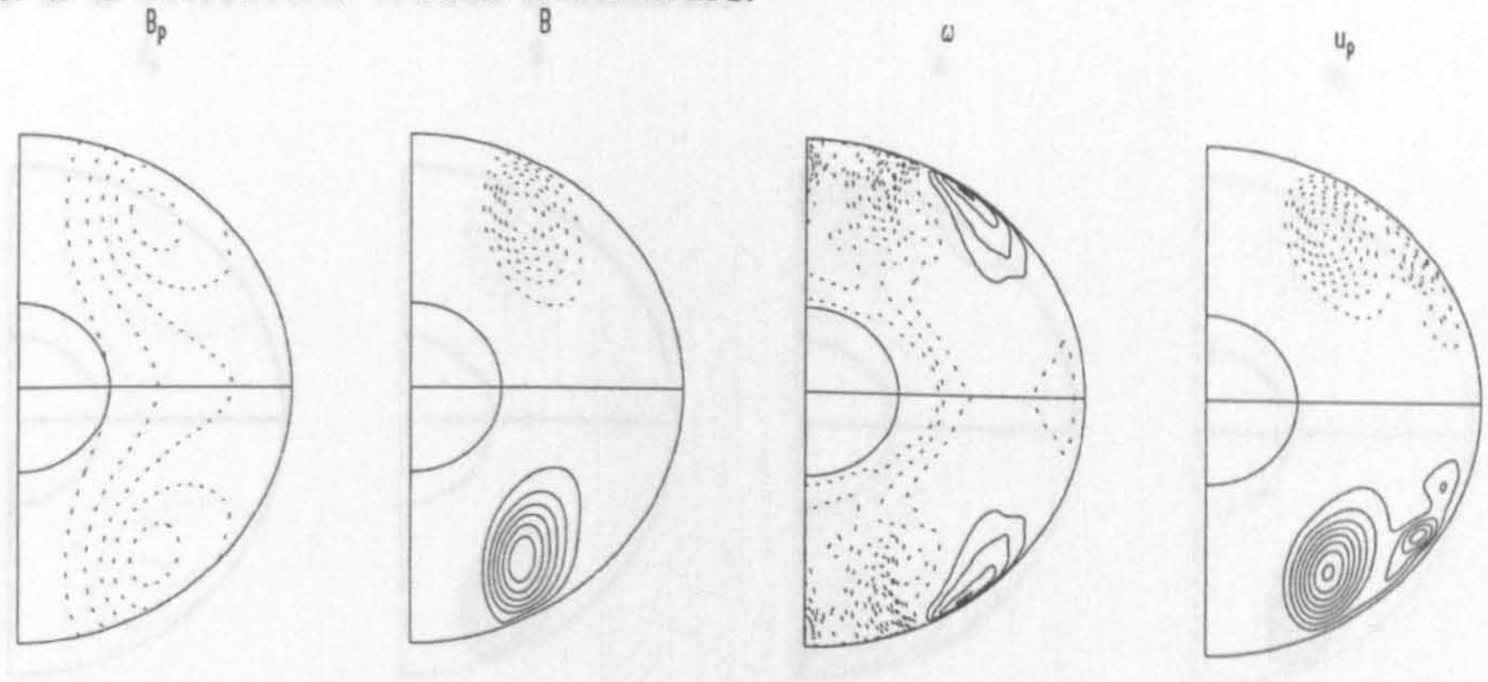

Figure 6.13: The following 4 rows show the solution at $\alpha_o = 11$, $\Theta_o = 100$, $E = 2.5 \times 10^{-4}$. The top row shows the solution at $Ro = 2 \times 10^{-2}$. Row 2 $Ro = 5 \times 10^{-2}$, row 3 $Ro = 7 \times 10^{-2}$, and row 4 $Ro = 8 \times 10^{-2}$. The plots going from left to right show the poloidal field, toroidal field, angular velocity and meridional circulation at contour intervals of 0.25, 1, 10, 0.25, respectively.

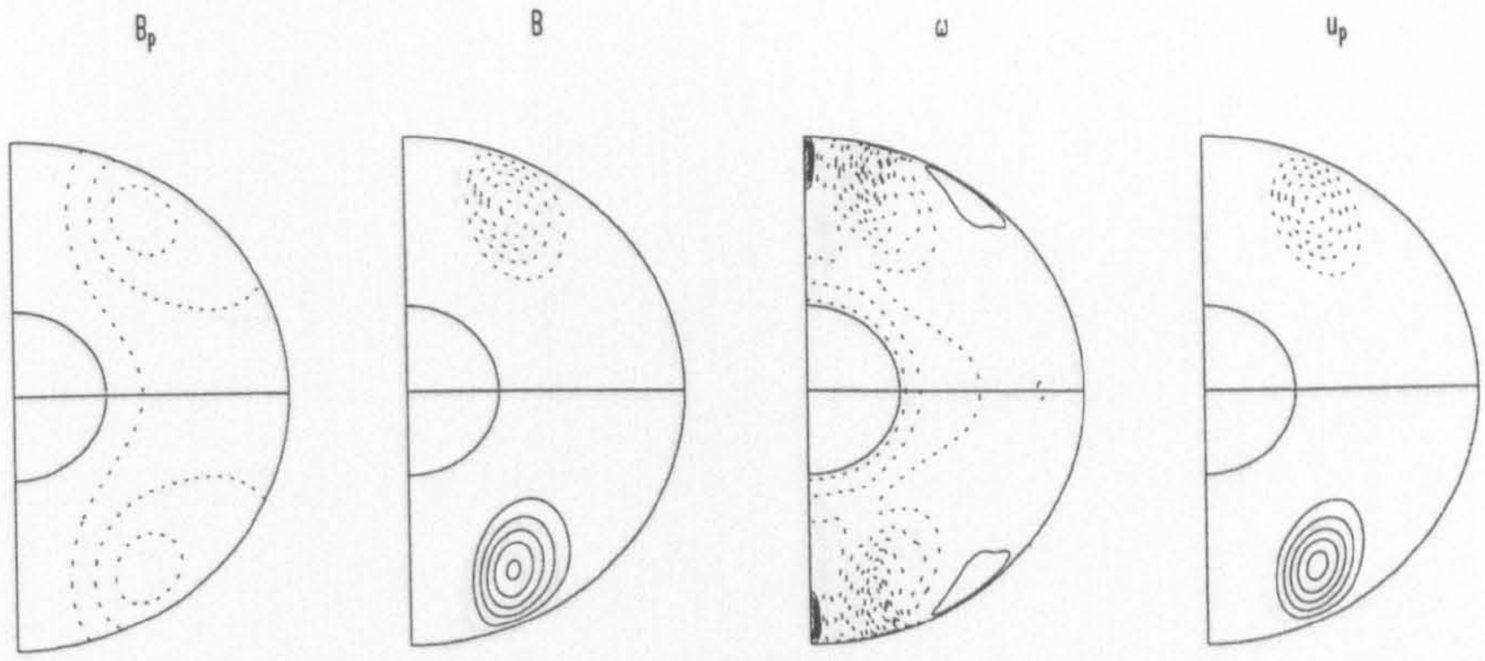

Figure 6.14: As Figure 6.13, but for $\Theta_o = 50$.

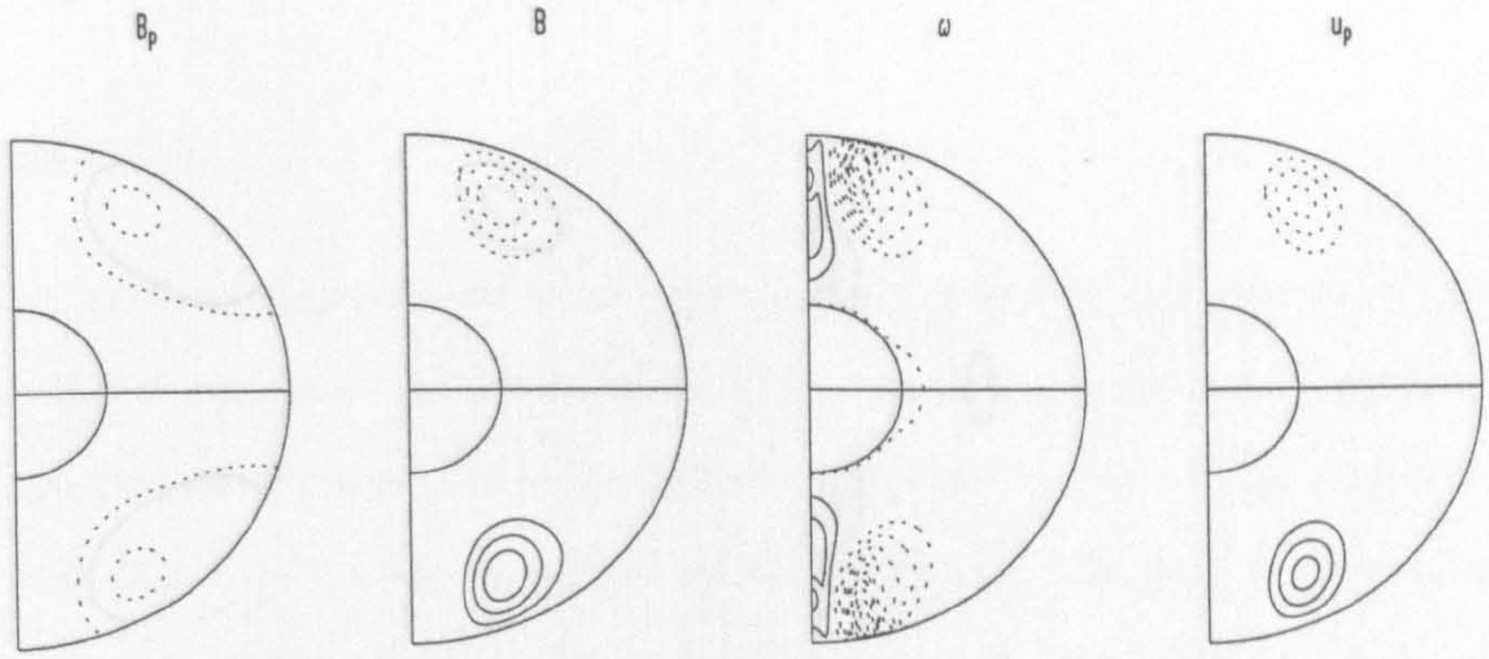

Figure 6.15: As Figure 6.13, but for $\Theta_o = 20$.

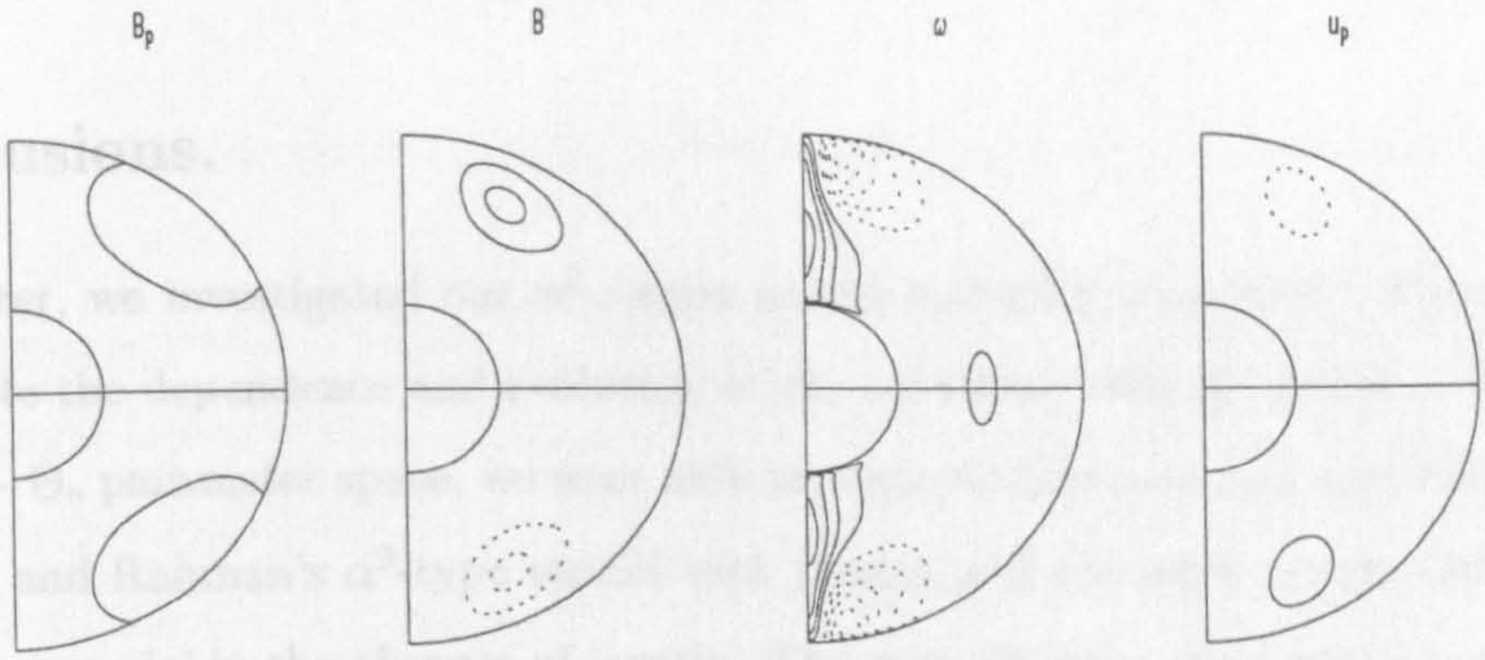

Figure 6.16: As Figure 6.13, but for $\Theta_o = -20$.

6.7 Conclusions.

In this chapter, we investigated our $\alpha^2\omega$-type model including the effects of inertia. Our aim was to investigate the dependence and evolution of the solutions with Ro and Θ_o. Through an exploration of $Ro-\Theta_o$ parameter space, we were able to map out this area and also bring together the results of Fearn and Rahman's α^2-type model with inertia and the work we presented in Chapter 5 on the $\alpha^2\omega$-type model in the absence of inertia. The map showing the regions in which different types of solutions exist within the $Ro-\Theta_o$ parameter space, is shown in Figure 6.12. In this we see the evolution of solutions from the spiky periodic type discussed in Chapter 5, to steady solutions, which then become time dependent as Ro and Θ_o are varied.

In Section 6.3 we discussed the likely way in which the dynamo equilibrates. We suggested for $\Theta_o \gtrsim -30$, the zonal flow driven by the imposed buoyancy force, reinforced the zonal flow driven by the Lorentz force in the momentum equation. This flow is then balanced by the other terms in the momentum equation, with the viscous term playing a role in damping the flow. The flow is also modified by the effect of the inertia term and this term replaces the viscous term at leading order in the momentum balance as Ro is increased. The resulting flow obtained from the balance of the momentum equation then feeds into the advection term in the induction equation, equilibrating the dynamo. We investigated the way in which the energy of the solutions evolve with Θ_o at fixed Ro, in Section 6.3 and as shown in Figures 6.1 and 6.2 we see that we obtain a stronger field and flow as Θ_o ($\gtrsim -30$) and Ro are increased. In Section 6.4, we fixed Θ_o and varied the strength of inertia. We found that, as had been found in the α^2-type model with inertia considered by Fearn and Rahman (2004b), the magnetic and kinetic energy vary linearly with Ro, as shown in Figures 6.10 and 6.11.

For $\Theta_o \lesssim -30$, we suggested that the zonal flow driven by the imposed buoyancy force exceeds the zonal flow driven by the Lorentz force. The net driven zonal flow is then acting in the opposite direction and the resulting balance of the momentum equation is quite different. The equilibrated flow then increases as Θ_o is decreased or Ro is increased, but the magnetic field as shown in Figures 6.1 and 6.2, is inhibited by these effects and is much less capable of growing as Θ_o is decreased or Ro is increased. As discussed in Section 6.4, we encountered numerical difficulties as we

increased Ro and reduced Θ_o, and we unable to obtain solutions below $\Theta_o = -30$ for $Ro > 5\times10^{-2}$.

The linear dependence we observed in Section 6.4 between the energy of the system and the strength of inertia for certain values of Θ_o, is examined more closely in Section 6.5. This particular variation had also been observed in the work by Fearn and Rahman (2004b) on their α^2-type dynamo model with inertia. Examining the solutions between $2 \times 10^{-2} \leq Ro \leq 8 \times 10^{-2}$ and $-20 \leq \Theta_o \leq 100$ and drawing a line of best fit through each set of points, we see that for each Θ_o, the solutions lines form a fan shape in both the magnetic energy-Ro space and kinetic energy-Ro space. Given this observed fan shaped behaviour with Θ_o, we plotted the gradient of the best fit lines against Θ_o. Fixing Ro, the gradient plotted on the y-axis of Figures 6.10 and 6.11 is then simply the magnetic and kinetic energies respectively. These curves then approximate the energy variation with Θ_o shown in Figures 6.1 and 6.2.

Chapter 7

Conclusions.

The aim of this thesis is to understand more about the role of inertia in the Earth's dynamo. In order to do this, we consider non-linear mean-field $\alpha\omega$ and $\alpha^2\omega$-type models which capture much of the essential physics of the problem, enabling us to investigate the influence of inertia on the solutions.

In Chapter 3, we investigated the $\alpha\omega$-type dynamo model in the absence of inertia. The reasons for this are two-fold. Firstly, this provided us a reference case for the work presented in Chapter 4 which included inertia and secondly this enabled comparisons with other $\alpha\omega$ models. As discussed in Section 2.9, we were unable to rescale our governing equations with the dynamo number, $\mathcal{D} = \alpha_o\Theta_o$, as had been found in linear, kinematic $\alpha\omega$ models. However as our results in Section 3.4 showed, we had good agreement between the values of $\mathcal{D}_c$ at the onset of dynamo action, suggesting that our equations are close to scaling with $\mathcal{D}$. In our discussion in Section 2.9 we suggested that the reason our equations were unable to rescale with $\mathcal{D}$, was due to the presence of the meridional circulation in the equations. Given the good agreement we find in our results suggests that the effect of meridional circulation is small. This finding is also emphasized by the comparison of our solutions with the work of Roberts (1972) presented in Section 3.9.1, where we found that our estimates of Roberts' parameter m (a measure of the strength of the prescribed meridional circulation) remained very small and was not large enough to lie in the steady regime identified by Roberts.

We also compared our solutions with the $\alpha\omega$-type model presented by Hollerbach and Glatzmaier

(1998). This model was the same as the model we use, only differing in the choice of their α-effect. They chose $\alpha = \alpha_o \cos\theta$, whilst our model used $\alpha = \alpha_o \cos\theta \sin(\pi(r - r_i))$. We found that the inclusion of a radial structure in the form of the α-effect only became important once the strength of the α-effect is sufficiently large. This finding is also found by Fearn and Rahman (2004a) in their studies on α^2-type dynamo models.

In Chapter 4 we investigated the effect of inertia on our $\alpha\omega$-type dynamo model. Fixing all parameters in the system and varying only the strength of inertia, Ro, we found a continuous evolution of the solution from the $Ro = 0$ case (explored using a different numerical code) investigated in Chapter 3, to solutions at higher values of Ro. We were able to follow the solutions as high as $Ro = 1.1 \times 10^{-2}$, at which point we were unable to find any further non-decaying solutions as Ro is increased. This suggested that the dynamo was shutting down – behaviour which had also been found in the 2.5D hydrodynamic model of Fearn and Morrison (2001) and the 3D hydrodynamic model of Christensen *et al* (1999) as Ro was increased (or equivalently, as $Pm = E/Ro$ was decreased).

We then investigated the possibility of preventing the failure of the dynamo as Ro is increased, through increasing the forcing in the system. We were motivated to investigate this possibility, as, in Fearn and Morrison's study they attempted to prevent the failure of dynamo action by increasing the strength of buoyancy driving in their model. Unfortunately this did not prevent the dynamo shutting off as Ro was increased. We chose to increase the strength of the α-effect, as this is unaffected by inertia, and Fearn and Rahman's (2004b) α^2-type dynamo studies found that inertia actually acted to facilitate dynamo action. Our studies here show that it possible to reach higher values of Ro through increasing the strength of the α-effect, however it is unclear whether we can prevent the dynamo shutting off.

In Chapter 5, we investigate an $\alpha^2\omega$-type model which allows us to reconcile the α^2-type model considered by Fearn and Rahman (2004a) and the $\alpha\omega$-type model considered in Chapter 3. Fearn and Rahman's α^2 solutions produced an unusual spiky periodic time dependence once the strength of α_o was sufficiently large. Beginning with a spiky periodic solution at $\alpha_o = 11$ as an initial con-

dition, we began varying the strength of the imposed buoyancy force. As we discussed in Section 2.8, the $\alpha^2\omega$-type dynamo model has two limiting cases; the α^2-type model and the $\alpha\omega$-type model. We found that the solutions we obtained for $-50 < \Theta_o < 50$ resembled the solutions found in the α^2-type model, and for $\Theta_o \lesssim -50$, the solutions were periodic and similar to the solutions found in Chapter 3. The solutions we found for $\Theta_o \gtrsim 50$ maintained their spiky periodic behaviour and shared similarities with Fearn and Rahman's (2004b) α^2-type model solutions which included the effect of inertia. We believe that increasing the strength of the buoyancy driving acts to reinforce the zonal flow driven by the Lorentz force, and so the character of the behaviour found remains qualitatively the same.

The work we presented in Chapter 5 then forms a base for the investigation of the effect of inertia considered in Chapter 6. Including inertial effects in the $\alpha^2\omega$-type model allowed us to reconcile the results of Chapter 4 and the work of Fearn and Rahman (2004b) which included the effect of inertia in their α^2-type model. The roughly linear behaviour of the magnetic and kinetic energy with Ro found in Fearn and Rahman's α^2 model, also held for fixed values of Θ_o for $\Theta_o \geqslant -20$. We encountered numerical difficulties for $\Theta_o \lesssim -30$ for $Ro > 5 \times 10^{-2}$ so have been unable to determine whether this behaviour is continued for $\Theta_o < -20$. Through varying Ro and Θ_o we were able to explore the $Ro - \Theta_o$ parameter space and found regions of parameter space in which different types of solutions existed, see Figure 6.12. We found that as Ro is increased solutions became more chaotically time dependent, and it became more difficult to decrease Θ_o.

In conclusion, from our studies of $\alpha\omega$ and $\alpha^2\omega$-type dynamo models, inertia seems to have an inhibiting effect on the solutions as its strength is increased, as shown by our results in Chapter 4. The dynamo mechanism is also fairly sensitive to the direction of the driven zonal flow, as shown in Chapters 3 and 5. Introducing inertia to this problem then makes obtaining solutions more difficult for $\Theta_o < 0$ as Ro is increased, as shown in Chapter 6.

References

[1] Abdel-Aziz M. M. and Jones C. A. $\alpha\omega$-dynamos and Taylor's constraint *Geophys. Astrophys. Fluid Dynamics*, **44**, 117-139, (1988)

[2] Abramowitz M. and Stegun I. A. *Handbook of Mathematical Functions.* Dover, New York, (1965)

[3] Anufriev A. P. and Hejda P. Effect of the magnetic field at the inner core boundary on the flow in the Earth's core *Phys. Earth Planet. Inter.*, **106**, 19-30, (1998)

[4] Barenghi C. F. Nonlinear planetary dynamos in a rotating spherical shell. II. The post Taylor equilibration for α^2-dynamos *Geophys. Astrophys. Fluid Dynam.*, **67**, 27-36, (1992)

[5] Barenghi C. F. Nonlinear planetary dynamos in a rotating spherical shell. III. $\alpha^2\omega$ models and the geodynamo. *Geophys. Astrophys. Fluid Dynam.*, **71**, 163-185, (1993)

[6] Bergman M. I. and Fearn D. R. Chimneys on the Earth's Inner-Outer Core Boundary? *Geophys. Research Letters*, **21**, 477-480, (1994)

[7] Braginsky S. I. Self-excitation of a magnetic field during the motion of a highly conducting fluid. *Zh. Exp. Teor. Fiz. SSSR*, **47**, 1084-1098 (1964a). (English transl.: Sov. Phys. JETP **20**, 726-735, (1965))

[8] Braginsky S. I. Kinematic models of the Earth's hydrodynamic dynamo. *Geomag. Aeron.*, **4**, 732-747 (1964b). (English transl.: **64**, 572-583, (1964))

[9] Braginsky S. I. Nearly axially symmetric model of the hydromagnetic dynamo of the Earth. I *Geomag. Aeron.*, **15**, 122-128, (1975)

[10] Childress S. A class of solutions of the magnetohydrodnamic dynamo problem. In *The Application of Modern Physics to the Earth and Planetary interiors* (ed. S. K. Runcorn) Wiley, 629-648, (1969)

[11] Christensen U., Olson P. and Glatmaier G. A. Numerical modelling of the geodynamo: a systematic parameter study *Geophys. J. Int.*, **138**, 393-409, (1999)

[12] Cowling T. G. The magnetic field of sunspots *Mon. Not. R. Astron. Soc.*, **94**, 39-48, (1934)

[13] de Wijs G. A., Kresse G., Vočadlo L., Dobson D., Alfè D., Gillan M. J. and Price G. D. The viscosity of liquid iron at the physical conditions of the Earth's core *Nature*, **392**, 805-807, (1998)

[14] Fearn D. R. Nonlinear Planetary Dynamos, in *Lectures on Solar and Planetary Dynamos* (eds. M. R. E. Proctor and A. D. Gilbert) Cambridge University Press, 219-244, (1994)

[15] Fearn D. R. Hydromagnetic flow in planetary cores *Rep. Prog. Phys.*, **61**, 175-235, (1998)

[16] Fearn D. R. The Geodynamo, in *Mathematical Aspects of Natural Dynamos* (ed. E. Dormy), (2004)

[17] Fearn D. R. and Morrison G. The role of inertia in hydrodynamic models of the geodynamo *Phys. Earth Planet. Int.*, **128**, 75-92, (2001)

[18] Fearn D. R. and Proctor M. R. E. Dynamically consistent magnetic fields produced by differential rotation *J. Fluid Mech.*, **178**, 521-534, (1987)

[19] Fearn D. R. and Rahman M. M. Evolution of Nonlinear α^2-dynamos and Taylor's constraint *Geophys. Astro. Fluid Dynam.*, **98**, 385-406, (2004a)

[20] Fearn D. R. and Rahman M. M. The role of inertia in models of the geodynamo *Geophys. J. Int*, **158**, 515-528, (2004b)

[21] Fearn D. R. and Rahman M. M. Instability of non-linear α^2-dynamos *Phys. Earth Planet. Inter.*, **142**, 101-112, (2004c)

[22] Glatzmaier G. A. and Roberts P. H. A three-dimensional convectivedriven dynamo solution with rotating and finitely conducting inner core and mantle *Phys. Earth Planet. Inter.*, **91**, 63-75, (1995a)

[23] Glatzmaier G. A. and Roberts P. H. A three-dimensional self consistent computer simulation of a geomagnetic field reversal *Nature*, **91**, 63-75, (1995b)

[24] Hagee V. L. and Olson P. Dynamo models with permanent dipole fields and secular variation *J. Geophys. Research*, **96**, 11673-11687, (1991)

[25] Hollerbach R. A spectral solution of the magnetoconvection equations in spherical geometry *I. J. Numerical Methods in Fluids*, **32**, 773-797, (2000)

[26] Hollerbach R., Barenghi C. F. and Jones C. A. Taylor's constraint in a spherical $\alpha\omega$ dynamo *Geophys. Astrophys. Fluid Dynam.*, **67**, 3-25, (1992)

[27] Hollerbach R. and Glatzmaier G. A. Mixed parity solutions in a mean-field dynamo model *Studia Geoph*, **42**, 239-246, (1998)

[28] Hollerbach R. and Ierley G. R. A modal α^2-dynamo in the limit of asymptotically small viscosity *Geophys. Astrophys. Fluid Dynam.*, **60**, 133-158, (1991)

[29] Hollerbach R. and Jones C. A. A geodynamo model incorporating a finitely conducting inner core *Phys. Earth Planet. Inter.*, **75**, 317-327, (1993a)

[30] Hollerbach R. and Jones C. A. Influence of the Earth's inner core on geomagnetic fluctuations and reversals *Nature*, **365**, 541-543, (1993b)

[31] Hollerbach R. and Jones C. A. The role of inertia in models of the geodynamo *Phys. Earth Planet. Inter.*, **87**, 171-181, (1995)

[32] Jacobs J. A. *Deep Interior of the Earth* Chapman & Hall, (1993)

[33] Jones C. A. Dynamo models and Taylor's constraint, in *Advances in Solar System Magneto-hydrodynamics* (ed. E. R. Priest and A. W. Hood) Cambridge University Press, 25-50, (1991)

[34] Jones C. A. Convection-driven geodynamo models *Phil. Trans. R. Soc. Lond. A*, **358**, 873-897, (2000)

[35] Jones C. A., Longbottom A. W. and Hollerbach R. A self-consistent convection driven geodynamo model, using a mean field approximation *Phys. Earth Planet. Inter.*, **92**, 119-141, (1995)

[36] Jones C. A. and Wallace S. G. Periodic, Chaotic and Steady Solutions in $\alpha\omega$-dynamos *Geophys. Astrophys. Fluid Dynam.*, **67**, 37-64, (1992)

[37] Kerswell R. R., and Davey A. On the linear instability of elliptic pipe flow *J. Fluid Mech.*, **316**, 307-324, (1996)

[38] Larmor J. How could a rotating body such as the Sun become a magnet? *Rep. Brit. Assoc. Adv. Sci.*, 159-160, (1919)

[39] Loper D. E. and Roberts P. H. A study of conditions at the inner core boundary of the earth *Phys. Earth Planet. Int.*, **24**, 302-307, (1981)

[40] Loper D. E. and Roberts P. H. *Compositional convection and the gravitationally powered dynamo, in Stellar and Planetary Magnetism* (ed. A. M. Soward) Gordon and Breach, New York, 297-327, (1983)

[41] Macouin M. Valet J-P and Besse J. Long-term evolution of the geomagnetic dipole moment *Phys. Earth Planet. Inter.*, **147**, 239-246, (2004)

[42] Malkus W. V. R. and Proctor M. R. E. The macrodynamics of α-effect dynamos in rotating fluids *J. Fluid Mech.*, **67**, 417-443, (1975)

[43] Merrill R. T., McElhinney M. W. and McFadden P. L. *The Magnetic Field of the Earth: Paleomagnetism, the Core, and the Deep Mantle* Academic Press, (1996)

[44] Poirier J-P. Light elements in the Earth's outer core: A critical review *Phys. Earth Planet. Inter.*, **85**, 319-337, (1994)

[45] Proctor M. R. E. Numerical solutions of the nonlinear α-effect dynamo equations *J. Fluid Mech.*, **80**, 769-784, (1977)

[46] Rahman M. M. Evolution and Stability of Nonlinear Mean field Dynamos *PhD Thesis*, University of Glasgow, (2003)

[47] Roberts P. H. *An introduction to Magnetohydrodynamics*, Longmans London, (1967)

[48] Roberts P. H. On the thermal instabilities of a fluid sphere containing heat sources. *Phil. Trans. R. Soc. Lond. A*, **263**, 93-117,(1968)

[49] Roberts P. H. Kinematic Dynamo Models *Proceedings of the Royal society*, **272**, 663-698, (1972)

[50] Roberts P. H. Fundamentals of Dynamo theory, in *Lectures on Solar and Planetary Dynamos* (eds. M. R. E. Proctor and A. D. Gilbert) Cambridge University Press, 1-58, (1994)

[51] Sarson G. R., Jones C. A. and Longbottom A. W. Convection driven geodynamo models of varying Ekman number. *Geophys. Astrophys. Fluid Dynam.*, **88**, 225-252, (1998)

[52] Soward A. M. and Jones C. A. α^2-dynamos and Taylor's constraint *Geophys. Astrophys. Fluid Dynam.*, **27**, 87-122, (1983)

[53] Steenbeck M. and Krause F. The generation of stellar and planetary magnetic fields by turbulent dynamo action *Z. Naturforsch*, **21a**, 1285-1296, (1966)

[54] Steenbeck M. and Krause F. Zur Dynamotheorie stellarer und planetarer Magnetfelder I. Berechnung sonnenähnlicher Wechselfeldgeneratoren *Astron. Nachr.*, **291**, 49-84, (1969)

[55] Taylor J. B. The magnetohydrodynamics of a rotating fluid and the Earth's dynamo problem *Proc. R. Soc. Lond. A*, **274**, 274-283, (1963)

[56] Zhang K. and Busse F. H. Convection driven magnetohydrodynamic dynamos in rotating spherical shells *Geophys. Astrophys. Fluid Dynam.*, **49**, 97-116, (1989)

[57] Zhang K. and Busse F. H. Generation of magnetic fields by convection in a rotating spherical fluid shell of infinite Prandtl number *Phys. Earth Planet. Inter.*, **59**, 208-222, (1990)

Appendix A

Proofs of Theorems.

For the proofs presented here, we assume a spherical shell geometry with length scaled with the outer core radius $r_o(=1)$.

A.1 Cowling's Theorem.

Theorem 1 (Cowling) *A two-dimensional or axisymmetric magnetic field can not be maintained by fluid motions.*

Sketch Proof.

We begin by separating the field and flow into the axisymmetric and non-axisymmetric parts,

$$\begin{aligned} \mathbf{B} &= \overline{\mathbf{B}}(r,\theta,t) + \mathbf{B}'(r,\theta,\phi,t) \\ \mathbf{U} &= \overline{\mathbf{U}}(r,\theta,t) + \mathbf{U}'(r,\theta,\phi,t) \end{aligned}$$

where the axisymmetric components are defined as, e.g.

$$\overline{B}_s(r,\theta,t) = \frac{1}{2\pi}\int_0^{2\pi} B_s(r,\theta,\phi,t)d\phi$$

and we define the non-axisymmetric component, $\mathbf{B}'$ by subtraction as $\mathbf{B}' = \mathbf{B} - \overline{\mathbf{B}}$. We therefore have,

$$\mathbf{B} = \overline{\mathbf{B}} + \mathbf{B}' \quad \text{and} \quad \mathbf{U} = \overline{\mathbf{U}} + \mathbf{U}'$$

The axisymmetric component may be further decomposed into zonal and meridional parts,

$$\begin{aligned}\overline{\mathbf{B}} &= \overline{\mathbf{B}}_p + \overline{\mathbf{B}}_\phi \\ \overline{\mathbf{B}} &= \nabla \times (A(r,\theta,t)\mathbf{e}_\phi) + B\mathbf{e}_\phi \end{aligned} \tag{A.1}$$

and

$$\begin{aligned}\overline{\mathbf{U}} &= \overline{\mathbf{U}}_p + \overline{\mathbf{U}}_\phi \\ \overline{\mathbf{U}} &= \nabla \times (\psi(r,\theta,t)\mathbf{e}_\phi) + v\mathbf{e}_\phi. \end{aligned} \tag{A.2}$$

Applying these decompositions to (1.3), allows the Induction equation to be divided into axisymmetic and non-axisymmetric parts, respectively

$$\frac{\partial \overline{\mathbf{B}}}{\partial t} = \nabla \times (\overline{\mathbf{U}} \times \overline{\mathbf{B}} + \overline{\boldsymbol{\mathcal{E}}}) + \nabla^2 \overline{\mathbf{B}}, \tag{A.3}$$

$$\frac{\partial \mathbf{B}'}{\partial t} = \nabla \times (\overline{\mathbf{U}} \times \mathbf{B}' + \mathbf{U}' \times \overline{\mathbf{B}} + \boldsymbol{\mathcal{E}}') + \nabla^2 \mathbf{B}' \tag{A.4}$$

where $\boldsymbol{\mathcal{E}} = \mathbf{U}' \times \mathbf{B}'$. The axisymmetric equation (A.3) may be further broken down into meridional and zonal parts,

$$\frac{\partial A}{\partial t} + \frac{1}{s}\overline{\mathbf{U}}_p \cdot \nabla(sA) = D^2 A + \overline{\mathcal{E}}_\phi \tag{A.5}$$

$$\frac{\partial B}{\partial t} + s\overline{\mathbf{U}}_p \cdot \nabla\left(\frac{B}{s}\right) = D^2 B + s\overline{\mathbf{B}}_p \cdot \nabla\left(\frac{v}{s}\right) + (\nabla \times \overline{\boldsymbol{\mathcal{E}}})_\phi \tag{A.6}$$

where $D^2 = \nabla^2 - s^{-2}$.

We will now illustrate the truth of Cowling's theorem.

For an axisymmetric magnetic field, $\mathbf{B}' = 0$ and so $\boldsymbol{\mathcal{E}} = 0$. Therefore equation (A.5) is simply

$$\frac{\partial A}{\partial t} + \frac{1}{r\sin\theta}\overline{\mathbf{U}}_p \cdot \nabla(sA) = D^2 A. \tag{A.7}$$

Multiplying through (A.7) by $s^2 A$, and integrating over all space V we have

$$\frac{d}{dt}\int_V \frac{1}{2}s^2 A^2 dV = -\int_V sA\overline{\mathbf{U}}_p \cdot \nabla(sA) dV + \int_V s^2 A\left(\nabla^2 - \frac{1}{s^2}\right) A dV \tag{A.8}$$

The LHS of equation (A.8) is a measure of the rate of change of the meridional magnetic field, which clearly is non-negative. Now considering the two terms on the RHS of equation (A.8) in turn. The first term can be written as,

$$-\int_V sA\overline{\mathbf{U}}_p \cdot \nabla(sA) dV = -\int_V \nabla \cdot \left(\frac{1}{2}(sA)^2 \overline{\mathbf{U}}_p\right) dV = -\int_S \frac{1}{2}(sA)^2 \overline{\mathbf{U}}_p \cdot \mathbf{e}_r dS$$

by applying the divergence theorem and using $\nabla \cdot \overline{\mathbf{U}}_p = 0$, (where here S is the surface (at infinity) bounding V). Outside $r = 1$, $\overline{\mathbf{U}}_p = 0$, and so this first term in equation (A.8) vanishes.

If we now consider the second term on the RHS of (A.8), we notice we can also write

$$s^2 A \nabla^2 A = \nabla \cdot (s^2 A \nabla A) - |\nabla(sA)|^2 + A^2$$

which allows us to apply the divergence theorem to the second term appearing in equation (A.8), to give

$$\int_V s^2 A \left(\nabla^2 - \frac{1}{s^2} \right) A dV = \int_S (s^2 A \nabla A) \cdot \mathbf{e}_r dS - \int_V |\nabla(sA)|^2 dV \tag{A.9}$$

The only source of A is currents flowing inside $r = 1$, so (since $|\mathbf{B}|$ must fall off at least as quickly as r^{-3} as $r \to \infty$), $|A|$ must fall off at least as quickly as r^{-2}. Since we are assuming an infinite volume of fluid with $U \sim 1/r$ as $r \to \infty$, the surface integral in equation (A.9) must therefore fall off at least as quickly as r^{-1} so vanishes in the limit $r \to \infty$. Therefore we are simply left with

$$\int_V s^2 A \left(\nabla^2 - \frac{1}{s^2} \right) A dV = - \int_V |\nabla(sA)|^2 dV$$

which shows that the meridional field energy is strictly decreasing. The more realistic case considered by Braginsky (1964a) of a finite volume of fluid, bounded by an insulator at $r = 1$, is similar.

Again given $\mathcal{E} = 0$ for an axisymmetric field and applying our newly found result that the meridional magnetic field will inevitably decay (so we may consider $A = 0$), the zonal magnetic field equation (A.6) is simply

$$\frac{\partial B}{\partial t} = -s \overline{\mathbf{U}}_p \cdot \nabla \left(\frac{B}{s} \right) + (\nabla^2 - s^{-2}) B$$

Applying a similar analysis to the zonal component of magnetic field, as we used to prove that the meridional component of the field must inevitably decay, yields the same result for the zonal component. Therefore since both the meridional and zonal components of the field must decay when $\mathcal{E} = 0$, we see that the axisymmetric field can not be maintained in the absence of a contribution from the non-axisymmetric field and flow.

A.2 Axisymmetric dynamos - energetics.

The axisymmetric induction equations presented in Section 1.6.4 are

$$\frac{\partial A}{\partial t} + \frac{1}{s}\overline{\mathbf{U}}_p \cdot \nabla(sA) = \left(\nabla^2 - \frac{1}{(r\sin\theta)^2}\right) A + \overline{\mathcal{E}}_\phi \tag{A.10}$$

$$\frac{\partial B}{\partial t} + s\overline{\mathbf{U}}_p \cdot \nabla\left(\frac{B}{s}\right) = \left(\nabla^2 - \frac{1}{(r\sin\theta)^2}\right) B + s\overline{\mathbf{B}}_p \cdot \nabla\left(\frac{v}{s}\right) + (\nabla \times \overline{\mathcal{E}})_\phi \tag{A.11}$$

where we have decoupled the axisymmetric field and flow in zonal and meridional parts as given in (A.1) and (A.2).

Now as discussed in Section 1.6.4 we can replace the 'source' non-axisymmetric contribution to the axisymmetric problem with a parametrisation of the effects of a non-axisymmetric flow through the so-called α effect.

$$\overline{\mathcal{E}} = \overline{\mathbf{U}' \times \mathbf{B}'} = \alpha\overline{\mathbf{B}} \tag{A.12}$$

The source for the poloidal component of the field is a prescribed α effect. In an α^2 dynamo model, the toroidal component of the field is generated by an α effect and in an $\alpha\omega$ dynamo model the toroidal field is generated by the prescribed ω effect. In the more general case of an $\alpha^2\omega$ dynamo model, the toroidal field is generated by both α and ω effects.

The differential rotation, v appearing in (A.11) is the $\overline{U}_\phi$ appearing in (1.22). In kinematic problems the thermal wind U_T is prescribed rather than being determined as in Equation (1.24). As first shown by Childress (1969) and as we will show below, the thermal wind is the only component of v which can lead to an increase in the toroidal field energy. As we will see, the magnetic wind (1.23) has no effect on the toroidal field energy and the effect of the geostrophic flow is dependent on the role of Ekman suction.

If we assume that we have a spherical shell model which is bounded by an insulating mantle, and assume that the Taylor cylinder in Figure 1.1 does not intersect the inner core, we have $z_B = -z_T$. Therefore to obtain the energetics of the toroidal component of the field we multiply equation (A.11) by B and integrate over the whole volume of the core. Therefore we obtain,

$$\int_V B\frac{\partial B}{\partial t}dV + \int_V Bs\overline{\mathbf{U}}_p\cdot\nabla\left(\frac{B}{s}\right)dV = \int_V B\left(\nabla^2 - \frac{1}{(r\sin\theta)^2}\right)BdV + \int_V Bs\overline{\mathbf{B}}_p\cdot\nabla\left(\frac{v}{s}\right)dV + \int_V B(\nabla\times\overline{\boldsymbol{\mathcal{E}}})_\phi dV \tag{A.13}$$

The first term on the LHS of (A.13) can be written as

$$\int_V B\frac{\partial B}{\partial t}dV = \frac{\partial}{\partial t}\int_V\left(\frac{B^2}{2}\right)dV \tag{A.14}$$

which is simply the rate of change of the toroidal field energy. The next term we consider is the second term on the RHS of (A.13).

$$\int_V Bs\overline{\mathbf{B}}_p\cdot\nabla\left(\frac{v}{s}\right)dV = \int_V Bs\overline{\mathbf{B}}_p\cdot\nabla\left(\frac{U_M}{s}\right)dV + \int_V Bs\overline{\mathbf{B}}_p\cdot\nabla\left(\frac{U_T}{s}\right)dV + \int_V Bs\overline{\mathbf{B}}_p\cdot\nabla\left(\frac{U_G}{s}\right)dV \tag{A.15}$$

since the zonal flow is simply the sum of the magnetic wind, the thermal wind and the geostrophic flow, as given by equation (1.22). Therefore if we consider the contribution by the geostrophic flow, we know that $U_G = U_G(s) = \omega_G s$, and therefore we have,

$$\begin{aligned} E_G \equiv \int_V Bs\overline{\mathbf{B}}_p\cdot\nabla\left(\frac{U_G}{s}\right)dV &= \int_V BsB_s\frac{d\omega_G}{ds}dV \\ &= \int_0^{2\pi}\int_0^1\int_{z_B}^{z_T} sBB_s\frac{d\omega_G}{ds}dzdsd\phi \\ &= 2\pi\int_0^1 s^2\frac{d\omega_G}{ds}\mathcal{T}ds \end{aligned} \tag{A.16}$$

where $\mathcal{T}$ is an alternative form of Taylor's constraint given by

$$\mathcal{T} \equiv \int_{z_B}^{z_T} B_\phi B_s dz = 0 \tag{A.17}$$

see e.g. Fearn (1994) for further details. When Taylor's constraint is satisfied, this term vanishes, and so the geostrophic flow has no net effect on the toroidal field energy. However, if Taylor's constraint is not satisfied and $\mathcal{T} \neq 0$, we may proceed by integrating equation (A.16) by parts,

$$E_G = 2\pi\int_0^1 s^2\frac{d\omega_G}{ds}\mathcal{T}ds = 2\pi[\omega_G s^2\mathcal{T}]_0^1 - 2\pi\int_0^1\omega_G\frac{d}{ds}(s^2\mathcal{T})ds \tag{A.18}$$

$$= -2\pi E^{-1/2}\int_0^1\left(\frac{\cos\theta}{2}\right)^{1/2}\frac{1}{s^3}\left(\frac{d}{ds}(s^2\mathcal{T})\right)^2 ds \tag{A.19}$$

we see that the first term on the RHS of equation (A.18) goes to zero, since applying the boundary conditions requires that $\mathcal{T} = 0$ on $r = 1$. This leaves us with equation (A.19) which is negative definite. This shows that the geostrophic flow will not lead to an increase in toroidal field energy and in fact acts to reduce it when the effects of Ekman suction are important. When viscous effects are important, equilibration in the system occurs when $B^2 = O(E_G) = O(E^{-1/2}B^4)$, i.e. when $B = O(E^{1/4})$. At this amplitude, other non-linear effects are unimportant.

Now for axisymmetric fields with $|B| \gg |\mathbf{B}_M|$ we may show that $U_M = B^2/s$, so from equation (A.13) the advection term combines with the magnetic wind term from equation (A.15) to give,

$$\begin{aligned}
\int_V Bs\overline{\mathbf{U}}_p \cdot \nabla\left(\frac{B}{s}\right) dV &- \int_V Bs\overline{\mathbf{B}}_p \cdot \nabla\left(\frac{U_M}{s}\right) dV \\
&= \int_V Bs\left[\left(\overline{\mathbf{U}}_p \cdot \nabla\left(\frac{B}{s}\right)\right) - \left(\overline{\mathbf{B}}_p \cdot \nabla\left(\frac{U_M}{s}\right)\right)\right] dV \\
&= \int_V Bs\left[\nabla\cdot\left(\frac{B}{s}\overline{\mathbf{U}}_p\right) - \nabla\cdot\left(\frac{U_M}{s}\overline{\mathbf{B}}_p\right)\right] dV \\
&= \int_V Bs\left[\nabla\cdot\left(\frac{B}{s}\overline{\mathbf{U}}_p\right) - \nabla\cdot\left(\frac{B^2}{s^2}\overline{\mathbf{B}}_p\right)\right] dV \\
&= \int_V \left[\nabla\cdot\left(\frac{B^2}{2}\overline{\mathbf{U}}_p\right) - \nabla\cdot\left(\frac{B^3}{s}\overline{\mathbf{B}}_p\right)\right] dV \qquad \text{(A.20)}
\end{aligned}$$

Applying the divergence theorem, this vanishes as $B = 0$ on the insulating boundary (see Braginsky 1975). In a similar way considering the diffusive term in equation (A.13), we have

$$\begin{aligned}
\int_V B\left(\nabla^2 - \frac{1}{(r\sin\theta)^2}\right) B dV &= \int_V B\nabla^2 B - \frac{B^2}{(r\sin\theta)^2} dV \\
&= \int_V \nabla\cdot(B\nabla B) - (\nabla B)^2 - \frac{B^2}{(r\sin\theta)^2} dV \\
&= \int_S (B\nabla B)\cdot dS - \int_V \left[(\nabla B)^2 + \frac{B^2}{(r\sin\theta)^2}\right] dV \qquad \text{(A.21)}
\end{aligned}$$

where the surface integral goes to zero, as $B = 0$ on the boundary and this condition also enables the remaining volume integral to be rewritten as

$$\int_V B\left(\nabla^2 - \frac{1}{(r\sin\theta)^2}\right) B dV = -\int_V \left(\frac{\nabla(sB)}{s}\right)^2 dV \qquad \text{(A.22)}$$

which is negative definite.

Thus the magnetic diffusion and the ω-effect associated with the geostrophic flow are sinks of toroidal field energy. As both the advective and magnetic wind terms have no net effect on the

toroidal field energy, the only possible sources are the thermal wind and the α-effect term. Applying a similar analysis to the poloidal field equation yields a similar result; the α-effect term on the RHS of equation (A.10) is the only possible source of poloidal field. In the absence of these terms we have the familiar Cowlings theorem from Section 1.2.3 and Appendix A.1.

Appendix B

Numerical Method.

In this appendix we will attempt to describe briefly the numerical method which is used to adapt our mathematical model presented in Chapter 2, to the numerical code which we use in our simulations. The original 3D code was developed by Dr. R. Hollerbach, and a more thorough description of the implementation of the numerical scheme may be found in Hollerbach (2000). This code was modified by Dr. M. M. Rahman as part of his PhD research, to cut the code down to 2D. Further details may be found in Rahman (2003).

B.1 The Modelling Equations.

From Chapter 2, the modelling equations governing our $\alpha\omega$ or $\alpha^2\omega$-type models are

$$\frac{\partial \hat{\mathbf{B}}}{\partial t} = \nabla^2 \hat{\mathbf{B}} + \nabla \times (\mathbf{u}_i \times \hat{\mathbf{B}}) \tag{B.1}$$

in the inner core, and

$$\frac{\partial \mathbf{B}}{\partial t} = \nabla^2 \mathbf{B} + \nabla \times (\alpha \mathbf{B}) + \nabla \times (\mathbf{U} \times \mathbf{B}) \tag{B.2}$$

in the outer core, where $\mathbf{B}$ is the large-scale axisymmetric magnetic field, $\mathbf{U}$ is the large-scale axisymmetric fluid flow and $\mathbf{u}_i = \Omega_i r \sin\theta \mathbf{e}_\phi$ where Ω_i denotes the inner core angular velocity. In our model we choose the axis of rotation of the inner and outer cores to be the same. Here the superscript $\hat{}$ is used to denote inner core quantities. In the outer core, our induction equation (B.2) is coupled to the momentum equation,

$$Ro\left(\frac{\partial \mathbf{U}}{\partial t} + (\mathbf{U}\cdot\nabla)\mathbf{U}\right) + 2\mathbf{k}\times\mathbf{U} = -\nabla p + E\nabla^2\mathbf{U} + (\nabla\times\mathbf{B})\times\mathbf{B} + \Theta\mathbf{r}. \tag{B.3}$$

We defined our parametrised α-effect as

$$\alpha = \alpha_o \cos\theta \sin(\pi(r - r_i)) \tag{B.4}$$

and chose a prescribed buoyncy force $\Theta\mathbf{r}$ of the form

$$\Theta = -\Theta_o r \cos^2\theta \tag{B.5}$$

such that the buoyancy force drives a differential rotation (or ω-effect) in the flow of the form $\omega = \Theta_o r$.

B.1.1 The Boundary Conditions.

At the core-mantle boundary, we have insulating boundary conditions on the field,

$$\mathbf{B} = \mathbf{B}^{(e)} \qquad \text{on} \quad r = r_o \tag{B.6}$$

where $\mathbf{B}^{(e)}$ is the external potential field. We have continuity conditions on the field at the inner core boundary as we assume a finitely conducting inner core.

$$\hat{\mathbf{B}} = \mathbf{B} \quad \text{and} \quad \hat{\mathbf{E}}_\perp = \mathbf{E}_\perp \qquad \text{on} \quad r = r_i \tag{B.7}$$

For the fluid we assume no-slip conditions on the inner core and core mantle boundaries, thus

$$U_r, U_\theta = 0 \quad , \quad U_\phi = \Omega_i r \sin\theta \qquad \text{at} \quad r = r_i \tag{B.8}$$

$$U_r, U_\theta, U_\phi = 0 \qquad \text{at} \quad r = r_o \tag{B.9}$$

B.2 Poloidal/Toroidal decomposition.

Since we have divergence free fields and flows, $\nabla \cdot \mathbf{B} = \nabla \cdot \mathbf{U} = 0$, the governing equations given in (B.1),(B.2) and (B.3) may be decomposed into poloidal and toroidal parts using

$$\mathbf{U} = \nabla \times (e\mathbf{e}_r) + \nabla \times \nabla \times (f\mathbf{e}_r) \tag{B.10}$$

$$\mathbf{B} = \nabla \times (g\mathbf{e}_r) + \nabla \times \nabla \times (h\mathbf{e}_r) \tag{B.11}$$

$$\hat{\mathbf{B}} = \nabla \times (\hat{g}\mathbf{e}_r) + \nabla \times \nabla \times (\hat{h}\mathbf{e}_r) \tag{B.12}$$

where $e, f, g, h, \hat{g}, \hat{h}$ are scalar functions of r, θ. More generally these may be assumed to be functions of r, θ, ϕ, however we are considering an axisymmetric model and so all quantities are independent of ϕ. The scalars $e, f, g, h, \hat{g}, \hat{h}$ may be expanded in spherical harmonics as,

$$e(r,\theta) = \sum_{l=1}^{LU} e_{kl}(r) P_l(\cos\theta), \qquad f(r,\theta) = \sum_{l=1}^{LU} f_{kl}(r) P_l(\cos\theta) \tag{B.13}$$

$$g(r,\theta) = \sum_{l=1}^{LB} g_{kl}(r) P_l(\cos\theta), \qquad h(r,\theta) = \sum_{l=1}^{LB} h_{kl}(r) P_l(\cos\theta) \tag{B.14}$$

$$\hat{g}(r,\theta) = \sum_{l=1}^{LB} \hat{g}_{kl}(r) P_l(\cos\theta), \qquad \hat{h}(r,\theta) = \sum_{l=1}^{LB} \hat{h}_{kl}(r) P_l(\cos\theta). \tag{B.15}$$

In Chapter 2, the decomposition we presented for the field and flow is given in (2.6) and (2.7). This decomposition is slightly different from the form we adopt here. However, these decompositions are entirely equivalent, and are related through the following expressions.

$$A = -\frac{1}{r}\frac{\partial h}{\partial \theta} \quad \& \quad B = -\frac{1}{r}\frac{\partial g}{\partial \theta}$$

$$\psi = -\frac{1}{r}\frac{\partial f}{\partial \theta} \quad \& \quad v = -\frac{1}{r}\frac{\partial e}{\partial \theta}$$

B.3 The Induction Equation Decomposition.

Applying the decompositions (B.15) to (B.1), the r component and the r component of the curl of (B.1) give,

$$\sum_{l=1}^{LB} \frac{l(l+1)}{r^2}\left[\frac{\partial}{\partial t} - L_l\right]\hat{h}_l(r) P_l(\cos\theta) = \mathbf{e}_r \cdot \nabla \times (\mathbf{u}_i \times \hat{\mathbf{B}}) \tag{B.16}$$

$$\sum_{l=1}^{LB} \frac{l(l+1)}{r^2}\left[\frac{\partial}{\partial t} - L_l\right]\hat{g}_l(r) P_l(\cos\theta) = \mathbf{e}_r \cdot \nabla \times \nabla \times (\mathbf{u}_i \times \hat{\mathbf{B}}) \tag{B.17}$$

where the operator L_l is defined as

$$L_l = \frac{\partial^2}{\partial r^2} - \frac{l(l+1)}{r^2} \tag{B.18}$$

As described in Chapter 2, we consider two types of dynamo model; the $\alpha^2\omega$-type model and the $\alpha\omega$-type model. In the $\alpha^2\omega$-type model, the prescribed α-effect acts on all components of the field, however in the $\alpha\omega$-type model, the α-effect is limited to act only upon the ϕ component of

the field. Therefore applying the decompositions (B.14), the r component and the r component of the curl of the induction equation, (B.2) are

$$\sum_{l=1}^{LB} \frac{l(l+1)}{r^2}\left[\frac{\partial}{\partial t} - L_l\right] h_l(r)P_l(\cos\theta) = \mathbf{e}_r \cdot \nabla \times (\mathbf{U}\times\mathbf{B} + \alpha\mathbf{B}) \quad \text{(B.19)}$$

$$\sum_{l=1}^{LB} \frac{l(l+1)}{r^2}\left[\frac{\partial}{\partial t} - L_l\right] g_l(r)P_l(\cos\theta) = \mathbf{e}_r \cdot \nabla \times \nabla \times (\mathbf{U}\times\mathbf{B} + \alpha\mathbf{B}) \quad \text{(B.20)}$$

in the $\alpha^2\omega$-type model, and

$$\sum_{l=1}^{LB} \frac{l(l+1)}{r^2}\left[\frac{\partial}{\partial t} - L_l\right] h_l(r)P_l(\cos\theta) = \mathbf{e}_r \cdot \nabla \times (\mathbf{U}\times\mathbf{B} + \alpha\mathbf{B}) \quad \text{(B.21)}$$

$$\sum_{l=1}^{LB} \frac{l(l+1)}{r^2}\left[\frac{\partial}{\partial t} - L_l\right] g_l(r)P_l(\cos\theta) = \mathbf{e}_r \cdot \nabla \times \nabla \times (\mathbf{U}\times\mathbf{B}) \quad \text{(B.22)}$$

in the $\alpha\omega$-type model.

B.3.1 The Spectral Boundary Conditions.

On the core mantle boundary, $r = r_o$, the insulating boundary conditions (B.6), written in spectral notation are simply,

$$g_l = \left(\frac{d}{dr} + \frac{l}{r}\right) h_l = 0 \quad \text{(B.23)}$$

The continuity conditions given in (B.7) can be rewritten in terms of the spectral coefficients $g_l, h_l, \hat{g}_l, \hat{h}_l$. Continuity of the magnetic field across the inner core boundary, gives

$$h_l = \hat{h}_l, \quad g_l = \hat{g}_l, \quad \frac{d}{dr}h_l = \frac{d}{dr}\hat{h}_l \quad \text{on } r = r_i \quad \text{(B.24)}$$

Continuity of the tangential component of the electric field is more tricky to deal with. The non-dimensionalised Ohm's Law is given as,

$$\mathbf{J} = \mathbf{E} + \mathbf{U}\times\mathbf{B}$$

Therefore, rearranging this equation for $\mathbf{E}$ and using $\mathbf{J} = \nabla\times\mathbf{B}$, we obtain,

$$\mathbf{E} = \nabla\times\mathbf{B} - \mathbf{U}\times\mathbf{B}$$

Now since we are generating the field through a prescribed α-effect, this may be more correctly written as

$$\mathbf{E} = \nabla\times\mathbf{B} - \mathbf{U}\times\mathbf{B} - \alpha\mathbf{B}. \quad \text{(B.25)}$$

Since both the field and flow are continuous across the inner core boundary, their cross product must also be continuous, and therefore for continuity we require that,

$$\mathbf{n} \times \hat{\mathbf{E}} = \mathbf{n} \times \mathbf{E} \tag{B.26}$$

$$\mathbf{n} \times (\nabla \times \hat{\mathbf{B}}) = \mathbf{n} \times (\nabla \times \mathbf{B} - \alpha \mathbf{B}) \tag{B.27}$$

$$(\nabla \times \hat{\mathbf{B}})_\theta = (\nabla \times \mathbf{B} - \alpha \mathbf{B})_\theta \tag{B.28}$$

Applying the decompositions (B.14) and (B.15), we obtain

$$\frac{d}{dr}\hat{g}_l = \frac{d}{dr} g_l - \alpha \frac{d}{dr} h_l \quad \text{on } r = r_i \tag{B.29}$$

Now, our prescribed α-effect given in (B.4), naturally goes to zero at $r = r_i$ and therefore, the final boundary condition is simply,

$$\frac{d}{dr}\hat{g}_l = \frac{d}{dr} g_l \quad \text{on } r = r_i \tag{B.30}$$

B.4 The Momentum Equation Decomposition.

The approach used in decomposing the momentum equation is different depending on whether the inertia term is included on the LHS of (B.3). The reasons for this lie in the stability of the code, see Hollerbach (2000) for further details.

B.4.1 Including Inertia.

We begin by taking the curl and the curl of the curl, of (B.3) in order to eliminate the pressure gradient term. Then, applying the decompositions (B.13, B.14), the r components of the curl and the curl of the curl give,

$$\sum_{l=1}^{LU} \frac{l(l+1)}{r^2} \left(Ro \frac{\partial}{\partial t} - EL_l \right) e_l(r) P_l(\cos\theta) = \mathbf{e}_r \cdot \nabla \times \mathbf{F}_1 \tag{B.31}$$

$$\sum_{l=1}^{LU} -\frac{l(l+1)}{r^2} \left(Ro \frac{\partial}{\partial t} - EL_l \right) L_l f_l(r) P_l(\cos\theta) = \mathbf{e}_r \cdot \nabla \times \nabla \times \mathbf{F}_1 \tag{B.32}$$

where $\mathbf{F}_1$ is,

$$\mathbf{F}_1 = -2\mathbf{k} \times \mathbf{U} - Ro(\mathbf{U} \cdot \nabla)\mathbf{U} + (\nabla \times \mathbf{B}) \times \mathbf{B} + \Theta \mathbf{r} \tag{B.33}$$

Now we can rewrite $(\mathbf{U}\cdot\nabla)\mathbf{U} = \nabla\left(\frac{|\mathbf{U}|^2}{2}\right) - \mathbf{U}\times(\nabla\times\mathbf{U})$, which upon taking the curl we see that the $\nabla\left(\frac{|\mathbf{U}|^2}{2}\right)$ will drop out. Therefore, we actually calculate

$$\mathbf{F}_1 = -2\mathbf{k}\times\mathbf{U} + Ro\mathbf{U}\times(\nabla\times\mathbf{U}) + (\nabla\times\mathbf{B})\times\mathbf{B} + \Theta\mathbf{r}. \tag{B.34}$$

B.4.2 Neglecting Inertia.

In the models considered in Chapters 3 and 5, we neglect the inertia term in (B.3), therefore taking the curl and the curl of the curl of (B.3), as before, the r components are then,

$$\sum_{l=1}^{LU} -\frac{l(l+1)}{r^2}EL_l e_l(r)P_l(\cos\theta) + \frac{2}{r^2}\left(\frac{l(l+1)}{r} - \frac{\partial}{\partial r}\right) f_l(r)\sin\theta\frac{d}{d\theta}P_l(\cos\theta)$$
$$+\frac{2l(l+1)}{r^2}\left(\frac{2}{r} - \frac{\partial}{\partial r}\right) f_l(r)\cos\theta\frac{d}{d\theta}P_l(\cos\theta) = \hat{\mathbf{e}}_r\cdot\nabla\times\mathbf{F}_2 \tag{B.35}$$

$$\sum_{l=1}^{LU} \frac{l(l+1)}{r^2}EL_l^2 f_l(r)P_l(\cos\theta) + \frac{2}{r^2}\left(\frac{l(l+1)}{r} - \frac{\partial}{\partial r}\right) e_l(r)\sin\theta\frac{d}{d\theta}P_l(\cos\theta)$$
$$+\frac{2l(l+1)}{r^2}\left(\frac{2}{r} - \frac{\partial}{\partial r}\right) e_l(r)\cos\theta\frac{d}{d\theta}P_l(\cos\theta) = \hat{\mathbf{e}}_r\cdot\nabla\times\nabla\times\mathbf{F}_2 \tag{B.36}$$

where $\mathbf{F}_2$ is,

$$\mathbf{F}_2 = (\nabla\times\mathbf{B})\times\mathbf{B} + \Theta\mathbf{r} \tag{B.37}$$

Using the recurrence relations (Abramowitz and Stegun, 1965)

$$\sin\theta\frac{d}{d\theta}P_l(\cos\theta) = \frac{l(l+1)}{2l+1}[P_{l+1}(\cos\theta) - P_{l-1}(\cos\theta)] \tag{B.38}$$
$$\cos\theta\frac{d}{d\theta}P_l(\cos\theta) = \frac{1}{2l+1}[(l+1)P_{l+1}(\cos\theta) + lP_{l-1}(\cos\theta)] \tag{B.39}$$

in (B.35) and (B.36) allows us to eliminate the derivatives in θ and replace them with expressions involving the spherical harmonics, thus

$$\sum_{l=1}^{LU} -\frac{l(l+1)}{r^2}EL_l e_l(r)P_l(\cos\theta) + \frac{2l(l+2)(l+1)}{2l+1}\left(\frac{(l+1)}{r^3} - \frac{1}{r^2}\frac{\partial}{\partial r}\right) f_l(r)P_{l+1}(\cos\theta)$$
$$-2\frac{l(l-1)(l+1)}{2l+1}\left(\frac{l}{r^3} + \frac{\partial}{\partial r}\right) f_l(r)P_{l-1}(\cos\theta) = \hat{\mathbf{r}}\cdot\nabla\times\mathbf{F}_2 \tag{B.40}$$

$$\sum_{l=1}^{LU} \frac{l(l+1)}{r^2} EL_l^2 f_l(r) P_l(\cos\theta) + \frac{2l(l+2)(l+1)}{2l+1}\left(\frac{(l+1)}{r^3} - \frac{1}{r^2}\frac{\partial}{\partial r}\right) e_l(r) P_{l+1}(\cos\theta)$$

$$-\frac{2l(l-1)(l+1)}{2l+1}\left(\frac{l}{r^3} + \frac{\partial}{\partial r}\right) e_l(r) P_{l-1}(\cos\theta) = \hat{\mathbf{r}} \cdot \nabla \times \nabla \times \mathbf{F}_2 \tag{B.41}$$

B.4.3 The Spectral Boundary Conditions.

Applying the decompositions (B.13) to our no-slip boundary conditions in (B.8, B.9) we find

$$e_1(r) = \Omega_i r^2, \quad f_l(r) = \frac{d}{dr} f_l(r) = 0 \quad \text{at} \quad r = r_i \tag{B.42}$$

$$e_l(r) = f_l(r) = \frac{d}{dr} f_l(r) = 0 \quad \text{at} \quad r = r_o \tag{B.43}$$

From (B.42) we see that the inner core rotation Ω_i depends only on the single mode, e_1, which needs to be determined as part of the solution. Now Ω_i is determined through the torque balance on the inner core, where we require that the total axial torque, Γ is given by,

$$CRo\frac{\partial \Omega_i}{\partial t} = \Gamma \tag{B.44}$$

where $C = \frac{8}{15}\pi r_i^5$ (for inner and outer cores of equal density) and Ro is the Rossby number. $CRo = 5.86 \times 10^{34} kgm^2$ is the polar moment of inertia of the inner core. The total torque on the inner core is balanced by the sum of electromagnetic and viscous torques, thus

$$\Gamma = \Gamma_B + \Gamma_\nu \tag{B.45}$$

where

$\Gamma_B = 2\pi r_i^3 \int_0^\pi B_\phi B_r \Big|_{r=r_i} \sin^2\theta d\theta$, is the electromagnetic torque and

$\Gamma_\nu = E2\pi r_i^3 \int_0^\pi r\frac{\partial}{\partial r}\left(\frac{U_\phi}{r}\right)\Big|_{r=r_i} \sin^2\theta d\theta$ is the viscous torque.

Including Inertia.

Thus, on the inner core boundary we have the following torque balance

$$E2\pi r_i^3 \int_0^\pi r\frac{\partial}{\partial r}\left(\frac{U_\phi}{r}\right)\Big|_{r=r_i} \sin^2\theta d\theta + 2\pi r_i^3 \int_0^\pi B_\phi B_r\Big|_{r=r_i} \sin^2\theta d\theta = CRo\frac{\partial \Omega_i}{\partial t}$$

$$E2\pi r_i^3 \int_0^\pi r\frac{\partial}{\partial r}\left(\frac{e_1}{r^2}\right)\Big|_{r=r_i} \sin^2\theta d\theta + 2\pi r_i^3 \int_0^\pi B_\phi B_r\Big|_{r=r_i} \sin^2\theta d\theta = CRo\frac{\partial \Omega_i}{\partial t} \tag{B.46}$$

Therefore, we timestep (B.44) along with the momentum equation to determine Ω_i at each timestep, which allows us to determine what the inhomogeneous boundary condition on $e_1(r)$ should be.

Neglecting Inertia.

In the absence of inertia, the integrated viscous torque, must be balanced by the electromagnetic torque,

$$E2\pi r_i^3 \int_0^\pi r\frac{\partial}{\partial r}\left(\frac{U_\phi}{r}\right)\Big|_{r=r_i} \sin^2\theta d\theta + 2\pi r_i^3 \int_0^\pi B_\phi B_r\Big|_{r=r_i} \sin^2\theta d\theta = 0 \tag{B.47}$$

i.e.

$$\frac{8\pi}{3}Er_i^4\frac{d}{dr}\left(\frac{e_1}{r^2}\right)\Big|_{r=r_i} = -\int_0^\pi B_\phi B_r\Big|_{r=r_i} \sin^2\theta d\theta \tag{B.48}$$

This therefore allows us to use this as our inhomogeneous boundary condition on e_1, since $\mathbf{B}$ is known at each timestep of the induction equation.

B.5 Radial Functions.

In the outer core we adopt the following radial decomposition for the scalar functions

$$e_l(r) = \sum_{k=1}^{KU+2} e_{kl}T_{k-1}(x), \qquad f_l(r) = \sum_{k=1}^{KU+4} f_{kl}T_{k-1}(x) \tag{B.49}$$

$$g_l(r) = \sum_{k=1}^{KB+2} g_{kl}T_{k-1}(x), \qquad h_l(r) = \sum_{k=1}^{KB+2} h_{kl}T_{k-1}(x) \tag{B.50}$$

where T_{k-1} are Chebyshev polynomials. Here we define x through the relation

$$r = \frac{r_o + r_i}{2} + \frac{r_o - r_i}{2}x \tag{B.51}$$

so that across the shell, $r_i \leq r \leq r_o$, x is normalised to $x \in [-1, 1]$. In all our models, we fix the ratio of inner to outer core radii, $\frac{r_i}{r_o} = \frac{1}{3}$. For the velocity coefficients, we have KU radial collocation points at which the spectral coefficients are evaluated. For the e_l functions we have 2 boundary conditions, and for the f_l functions we have 4 boundary conditions to be applied. For the field coefficients, we have KB radial collocation points at which the spectral coefficients are evaluated, with 2 boundary conditions on g and h. The truncations of the field and flow coefficients need not be the same, and can be varied as appropriate to the resolution of the solutions.

In the inner core, we can not apply the same radial decomposition to the field coefficients $\hat{g}$ and $\hat{h}$, since the radial distance now includes the origin. Now it can be shown that (see for example, Kerswell and Davey 1996), the following symmetries must hold

$$\hat{g}_l(-r) = (-1)^{l+1}\hat{g}_l(r) \quad \& \quad \hat{h}_l(-r) = (-1)^{l+1}\hat{h}_l(r) \tag{B.52}$$

From (B.52) we see that for l even, $\hat{g}, \hat{h}$ must tend to zero as quickly as r^2, and for l odd, $\hat{g}, \hat{h}$ must tend to zero as quickly as r^3.

Therefore, one possible expansion in keeping with these requirements is,

$$\hat{g}_l(r) = \sum_{k=1}^{KBI+1} \hat{g}_{kl} T_{2k-1}\left(\frac{r}{r_i}\right) r^{l'}, \qquad \hat{h}_l(r) = \sum_{k=1}^{KBI+1} \hat{h}_{kl} T_{2k-1}\left(\frac{r}{r_i}\right) r^{l'} \tag{B.53}$$

where

$$l' = \begin{cases} 1, & \text{for } l \text{ odd} \\ 2, & \text{for } l \text{ even} \end{cases} \tag{B.54}$$

The number of radial collocation points in the inner core is KBI, with an additional boundary condition to be applied for each $\hat{g}, \hat{h}$. Having adopted $T_{2k-1}(\frac{r}{r_i})$ as the radial decomposition, we note that for $0 \leq r \leq r_i$, the origin is not included as a collocation point, thus avoiding the coordinate singularity. The truncation of the field coefficients in the inner core is $KBI = KB/2$, so that we have the same radial resolution in the inner and outer cores.

B.6 Solution of the Induction Equation.

Now that we have set up our system of equations, we need to use a timestepping method in order to advance the spectral coefficients forward in time. To this, we use a second order Runge-Kutta method, which has been modified so that the diffusive terms may be treated implicitly. This method comprises of two steps

1. The Predictor Step.

Beginning with all the spectral coefficients at timestep n, we then evaluate the spectral coefficients of the forcing term $\mathbf{e}_r \cdot \nabla \times (\mathbf{U} \times \mathbf{B} + \alpha \mathbf{B})$ at timestep n. We then evaluate the forcing terms at each of the collocation points $x_j, j = 1, \cdots, KB$ and call them DG_j. Applying the time derivative, $\frac{\partial}{\partial t}$ and operator, L_l to q_{kl}, where q_{kl} represents the spectral coefficients, we have

$$\frac{\partial}{\partial t} q_{kl} = \frac{q_{kl}^{n+1} - q_{kl}^{n}}{\Delta t}, \quad L_l q_{kl} = L_l \frac{q_{kl}^{n+1} + q_{kl}^{n}}{2} \tag{B.55}$$

Therefore, enforcing (B.19) (or (B.21)) at the KB collocation points in the outer core, we obtain

$$\sum_{k=1}^{KB+2} \frac{l(l+1)}{r_j^2} \left[(\tilde{h}_{kl}^{n+1} - h_{kl}^{n}) - 0.5 \Delta t L_l (\tilde{h}_{kl}^{n+1} + h_{kl}^{n}) \right] T_{k-1}(x_j) \;=\; \Delta t DH_j \tag{B.56}$$

and at the KBI collocation points in the inner core,

$$\sum_{k=1}^{KBI+1} \frac{l(l+1)}{r_j^2}\left[(\tilde{\hat{h}}_{kl}^{n+1} - \hat{h}_{kl}^{n}) - 0.5\Delta t L_l(\tilde{\hat{h}}_{kl}^{n+1} + \hat{h}_{kl}^{n})\right] r^{l'} T_{2k-1}(x_j) \;=\; \Delta t \widehat{DH}_j \qquad \text{(B.57)}$$

Including the boundary conditions, this gives us an additional 3 equations which allow us to invert this system of equations for $\tilde{h}_{kl}^{n+1}$ and $\tilde{\hat{h}}_{kl}^{n+1}$.

Clearly this same procedure can be applied to (B.20) (or (B.22) in the $\alpha\omega$ case), and we will obtain the same form for the LHS, but now applied to the g_{kl} and $\hat{g}_{kl}$. The spectral form of the RHS, will of course be different, and we will come to a discussion on how these are calculated later.

2. The Corrector Step.

Now that we have this estimate of the coefficients at timestep $n+1$, we again evaluate the forcings at the collocation points and call them DH'_j. To obtain an improved estimate of the coefficients at timestep $n+1$, we then have the KB equations

$$\sum_{k=1}^{KB+2} \frac{l(l+1)}{r_j^2}\left[(h_{kl}^{n+1} - h_{kl}^{n}) - 0.5\Delta t L_l(h_{kl}^{n+1} + h_{kl}^{n})\right] T_{k-1}(x_j) \;=\; \frac{\Delta t}{2}(DH'_j + DH_j) \qquad \text{(B.58)}$$

and the KBI equations

$$\sum_{k=1}^{KBI+1} \frac{l(l+1)}{r_j^2}\left[(\hat{h}_{kl}^{n+1} - \hat{h}_{kl}^{n}) - 0.5\Delta t L_l(\hat{h}_{kl}^{n+1} + \hat{h}_{kl}^{n})\right] r^{l'} T_{2k-1}(x_j) \;=\; \frac{\Delta t}{2}(\widehat{DH'}_j + \widehat{DH}_j) \qquad \text{(B.59)}$$

which together with the boundary conditions allow these systems of equations to be inverted for h_{kl}^{n+1} and $\hat{h}_{kl}^{n+1}$ respectively.

The above system of equations (B.58) and (B.59) can be written in matrix form,

$$\mathbf{X}\tilde{\mathbf{h}}^{n+1} \;=\; \mathbf{Y}\mathbf{h}^{n} + \Delta t\mathbf{DH} \qquad \text{(B.60)}$$

$$\mathbf{X}\mathbf{h}^{n+1} \;=\; \mathbf{Y}\mathbf{h}^{n} + \frac{\Delta t}{2}(\mathbf{DH'} + \mathbf{DH}) \qquad \text{(B.61)}$$

where

$$\mathbf{h}^{n} \;=\; [h_{1l}^{n}, h_{2l}^{n}, \cdots, h_{(KB+2)l}^{n}, \hat{h}_{1l}^{n}, \hat{h}_{2l}^{n}, \cdots, \hat{h}_{(KBI+1)l}^{n}]^T$$

$$\mathbf{DH} \;=\; [DH_{1l}, DH_{2l}, \cdots, DH_{(KB)l}, 0, 0, \widehat{DH}_{1l}, \cdots, \widehat{DH}_{(KBI)l}, 0]^T$$

These square matrices, $\mathbf{X}, \mathbf{Y}$, are of dimension $KBDIM = KB + KBI + 3$. Their first KB rows are given as

$$X_{jk} = \frac{l(l+1)}{r_j^2}\left[1 - 0.5\Delta t L_l\right] T_{k-1}(x_j) \tag{B.62}$$

$$Y_{jk} = \frac{l(l+1)}{r_j^2}\left[1 + 0.5\Delta t L_l\right] T_{k-1}(x_j) \tag{B.63}$$

for $j = 1, \cdots, KB$. For $j = KB+3, \cdots, KBDIM$,

$$X_{jk} = \frac{l(l+1)}{r_j^2}\left[1 - 0.5\Delta t L_l\right] r^{l'} T_{2k-1}(x_j) \tag{B.64}$$

$$Y_{jk} = \frac{l(l+1)}{r_j^2}\left[1 + 0.5\Delta t L_l\right] r^{l'} T_{2k-1}(x_j) \tag{B.65}$$

The $KB+1, KB+2, KB+3$ rows of $\mathbf{X}$ are the boundary conditions on the field, given in equations (B.23), (B.24) and (B.30). The corresponding 3 rows of the matrix $\mathbf{Y}$ are zero.

Notice that equations (B.62), (B.63), (B.64) and (B.65) are independent of time and so will be the same at each timestep. Therefore, these matrices can be precomputed, as well as their product $\mathbf{X}^{-1}\mathbf{Y}$.

B.7 Solution of the Momentum Equation.

The approach adopted for solving the momentum equation, as indicated earlier in Section B.4, is different depending on whether we include the effect of inertia. The method of solution in each case is described below.

B.7.1 Including Inertial effects.

When we include the effect of inertia, we have the system of equations given in (B.31) and (B.32). Now in order to timestep these equations, we enforce them at the KU radial collocation points and then apply the second order Runge-Kutta predictor-corrector method, as used in Section B.6 to advance the coefficients from one timestep to the next.

1. The Predictor Step.

Following the the procedure described in Section B.6 for the induction equation, we calculate the spectral coefficients of the forcing terms $\mathbf{e}_r \cdot \nabla \times \mathbf{F}_1$ at timestep n, at each of the collocation

points $x_j, j = 1, \cdots, KU$, and call them DE_j.

Reinforcing (B.31) at these KU collocation points x_j gives

$$\sum_{k=1}^{KU+2} \frac{l(l+1)}{r_j^2}[Ro(\tilde{e}_{kl}^{n+1} - e_{kl}^n) - 0.5\Delta t EL_l(\tilde{e}_{kl}^{n+1} + e_{kl}^n)]T_{k-1}(x_j) = \Delta t DE_j \tag{B.66}$$

where we additionally include the two boundary conditions on e, as given in (B.42) and (B.43). Therefore we are able to invert this system for $\tilde{e}_{kl}^{n+1}$.

2. The Corrector Step.

Now we may use this estimate of $\tilde{e}_{kl}^{n+1}$ at timestep $n+1$, to obtain an improved estimate of the coefficients at timestep $n+1$. Evaluating the forcings again at the collocation points, x_j, and calling them DE_j', we then have the KU equations

$$\sum_{k=1}^{KU+2} \frac{l(l+1)}{r_j^2}[Ro(e_{kl}^{n+1} - e_{kl}^n) - 0.5\Delta t EL_l(e_{kl}^{n+1} + e_{kl}^n)]T_{k-1}(x_j) = \frac{\Delta t}{2}(DE_j' + DE_j) \tag{B.67}$$

which together with the two boundary conditions allows the system (B.67) to be inverted for e_{kl}^{n+1}.

The above system of equations, may then be written in matrix form as

$$\begin{aligned} \mathbf{X}\tilde{\mathbf{e}}^{n+1} &= \mathbf{Y}\mathbf{e}^n + \Delta t \mathbf{DE} \\ \mathbf{X}\mathbf{e}^{n+1} &= \mathbf{Y}\mathbf{e}^n + \frac{\Delta t}{2}(\mathbf{DE}' + \mathbf{DE}) \end{aligned}$$

where

$$\begin{aligned} \mathbf{e}^n &= [e_{1l}^n, e_{2l}^n, \cdots, e_{(KU+2)l}^n]^T \\ \mathbf{DE} &= [DE_{1l}, DE_{2l}, \cdots, DE_{(KU)l}, 0, 0]^T \end{aligned}$$

The first KU rows of $\mathbf{X}, \mathbf{Y}$ are given as

$$X_{jk} = \frac{l(l+1)}{r_j^2}\left[Ro - 0.5\Delta t EL_l\right] T_{k-1}(x_j) \tag{B.68}$$

$$Y_{jk} = \frac{l(l+1)}{r_j^2}\left[Ro + 0.5\Delta t EL_l\right] T_{k-1}(x_j) \tag{B.69}$$

for $j = 1, \cdots, KU$, whilst the final two rows of $\mathbf{X}$ implement the boundary conditions, and the final two rows of $\mathbf{Y}$ are zero.

The same procedure is applied to equation (B.32) at the same KU collocation points. From this analysis we obtain

$$\mathbf{X}\tilde{\mathbf{f}}^{n+1} = \mathbf{Y}\mathbf{f}^{n} + \Delta t\mathbf{DF} \tag{B.70}$$

$$\mathbf{X}\mathbf{f}^{n+1} = \mathbf{Y}\mathbf{f}^{n} + \frac{\Delta t}{2}(\mathbf{DF}' + \mathbf{DF}) \tag{B.71}$$

where

$$\mathbf{f}^{n} = [f_{1l}^{n}, f_{2l}^{n}, \cdots, f_{(KU+4)l}^{n}]^{T}$$

$$\mathbf{DF} = [DF_{1l}, DF_{2l}, \cdots, DF_{(KU)l}, 0, 0, 0, 0]^{T}$$

$$X_{jk} = -\frac{l(l+1)}{r_j^2}\left[Ro - 0.6\Delta t EL_l\right] L_l T_{k-1}(x_j) \tag{B.72}$$

$$Y_{jk} = -\frac{l(l+1)}{r_j^2}\left[Ro + 0.4\Delta t EL_l\right] L_l T_{k-1}(x_j) \tag{B.73}$$

Notice that the matrices $\mathbf{X}, \mathbf{Y}$, defined in (B.72) and (B.73) are slightly different from those derived for the e_{kl} in (B.68) and (B.69). Adopting matrices $\mathbf{X}, \mathbf{Y}$ in (B.68) and (B.69) with no-slip boundary conditions for the system of equations in (B.70) and (B.71) causes the equations to be unstable. By changing the weighting of the diffusive terms in (B.72) and (B.73), stabilizes the code, but results in a reduction in the accuracy of the diffusive terms. Weighting the known and unknown terms equally results in an accuracy of $O(\Delta t^2)$, but with any other weighting, the accuracy is only $O(\Delta t)$ with respect to the diffusive terms.

The boundary conditions are incorporated in the same way as in the case which neglects inertia, with the boundary condition on the inner core boundary simply given as

$$e_{(KU+1)1}(r) = \Omega_i r_i^2, \tag{B.74}$$

but since we are including inertia in both the inner and outer cores we must also timestep the torque balance equation (B.44) at the inner core boundary in order to determine Ω_i. Therefore, equation (B.44) may be written as

$$\Omega_i^{n+1} = \Omega_i^{n} + \frac{1}{CRo}(\Gamma^{n+1} + \Gamma^{n}) \tag{B.75}$$

Thus we may determine Ω_i from (B.75), so that we may determine the inhomogeneous boundary condition on $e_{(KU+1)1}(r)$. In this case, we suitably modify the corresponding column of $\mathbf{DE}$, by replacing 0 with $\Omega_i r_i^2$.

B.7.2 Neglecting Inertial effects.

Neglecting inertial effects, our system of equations is as given in (B.40) and (B.41). Since there is no time derivative appearing in these equations, we can solve these directly at each timestep.

We notice from these equations that e_l couples to $f_{l\pm1}$ and f_l couples to $e_{l\pm1}$. This poses no problems, as the equations separate into two symmetry classes; odd l for e_l and even l for f_l in one class, and even l for e_l and odd l for f_l in the other, which allows each case to be treated independently. The system of equations can then be written in matrix form, $\mathcal{A}\mathcal{X} = \mathcal{F}$ where $\mathcal{A}$ contains the details of (B.40) and (B.41), $\mathcal{X}$ contains the spectral coefficients for the appropriate symmetry class and $\mathcal{F}$ contains the r component of the first and second curls of the non-linear force term, F_2.

To obtain the spectral coefficients e and f, we need to invert the matrix $\mathcal{A}$. Fortunately, the matrix $\mathcal{A}$, takes a block tridiagonal form, which doesn't change with each timestep. Therefore, this matrix can be precomputed, along with their LU decomposition using the NAG routine F01NAF, and then efficiently inverted at each timestep using the NAG routine F04NAF. The non-linear forcings $\mathcal{F}$ are incorporated into the system via the pseudo-spectral method described in Section B.8. The dimensions of the block structure for $\mathcal{A}$, are determined by the angular truncation, LU - which gives the number of blocks, and *the size* of the blocks by the radial truncation KU. The blocks for the e spectral coefficients are $(KU+2)\times(KU+2)$, and $(KU+4)\times(KU+4)$ for the f coefficients, once the boundary conditions are included.

B.8 Nonlinear forcing and pseudo-spectral method.

In the previous sections we have presented the different systems of equations depending on which problem we are solving. In the inner core, the RHS of equations (B.16) and (B.17), are simply zero, as we only consider the axisymmetric case. The RHS of the equations which we must solve in the outer core, are less straightforward to deal with and so we use the pseudo-spectral method to evaluate these forcing terms. The pseudo-spectral method involves repeatedly switching back and forth between spectral and real space.

The first step in calculating the the non-linear forces on the RHS of the momentum and induc-

tion equations is to calculate in real space, the vector quantities $\mathbf{U}$, $\nabla \times \mathbf{U}$, $\mathbf{B}$, $\nabla \times \mathbf{B}$, etc. using the spectral coefficients. This procedure requires the spectral coefficients to be multiplied by terms involving $T_{k-1}(x)$ and its derivatives at radial collocation points KN, which are different from the timestepping matrix collocation points and these points are now uniformly spaced. Similarly, we multiply by appropriate terms in $P_l(\cos\theta)$ and its derivatives at angular collocation points LN. We take $KN = \frac{3}{2}\max\{KB, KU\} + 1$ and $LN = \frac{3}{2}\max\{LB, LU\} + 2$. The next step is also calculated in real space, and this simply involves calculating pointwise the required cross-products of terms, such as $\mathbf{U} \times \mathbf{B}$ in the induction equation, or $(\nabla \times \mathbf{B}) \times \mathbf{B}$ in the momentum equation.

In order to then calculate the first or second curls of the forcing terms we need to return to spectral space. For any vector, $\mathbf{V} = (V_r, V_\theta, V_\phi)$, we need to multiply by matrices in $T_{k-1}(x)$ and $P_l(\cos\theta)$ as follows,

$$V_r = \sum_{k,l} V_r^{kl} T_{k-1}(x) P_l(\cos\theta) \tag{B.76}$$

$$V_\theta = \sum_{k,l} V_\theta^{kl} T_{k-1}(x) \sin\theta P_l(\cos\theta) \tag{B.77}$$

$$V_\phi = \sum_{k,l} V_\phi^{kl} T_{k-1}(x) \sin\theta P_l(\cos\theta) \tag{B.78}$$

to obtain the vector in spectral space. To calculate $\nabla \times \mathbf{V}$, we need to multiply by more precomputed matrices. To calculate $\nabla \times \nabla \times \mathbf{V}$, we then simply repeat this process. The matrices that are precomputed for the timestepping procedure incorporate the necessary spectral to real conversion in r to get back the original KB collocation points at which the equations are evaluated.

It may seem immensely time consuming to be constantly switching between spectral and real space, but in fact this is a very efficient way to do the calculations. Since matrix multiplication is associative, the matrices may be calculated all together, so that only one multiplication within the actually code is required. Also, these matrices do not depend on time, and so are the same at each timestep, allowing all the matrices to precomputed prior to running the code.